Numerical Simulation of Non-Inductive Startup of the Pegasus Toroidal Experiment

By

John B. O'Bryan

A dissertation submitted in partial fulfillment of the
requirements for the degree of

Doctor of Philosophy
(Nuclear Engineering and Engineering Physics)

at the
UNIVERSITY OF WISCONSIN – MADISON
2014

Date of final oral examination: 5/30/2014

The dissertation is approved by the following members of the Final Oral Committee:
Carl R. Sovinec, Professor, Engineering Physics
Raymond J. Fonck, Professor, Engineering Physics
Chris C. Hegna, Professor, Engineering Physics
David T. Anderson, Professor, Electrical and Computer Engineering
Michael E. Plesha, Professor, Engineering Physics

Abstract

The dynamics and relaxation of magnetic flux ropes produced during non-inductive startup of the Pegasus Toroidal Experiment are simulated with nonlinear magnetohydrodynamic and two-fluid plasma models. A current filament is produced by a single injector and directed along multiple passes by toroidal and vertical vacuum magnetic field components. Adjacent passes of the current filament merge and reconnect, releasing an axisymmetric current ring from the driven channel. Squashing degree analysis indicates the presence of a quasi-separatrix layer (QSL) during ring formation, but the QSL does not solely correspond to magnetic reconnection. Chaotic scattering is also apparent from the distribution of magnetic field-line lengths. The merging of adjacent passes constitutes coherent dynamo action that affects the toroidally-averaged magnetic-field distribution. The MHD dynamo–primarily from the vertical displacement of the current channel–concentrates symmetric poloidal flux and transfers significant energy to the forming flux-rope ring. Accumulation of poloidal flux over many reconnection events contributes to the development of a poloidal magnetic field null near the central column that redirects the driven current filament, such that its path traces a toroidal surface. After cessation of the simulated current drive, temperature and current profiles broaden and closed flux surfaces form rapidly and encompass a large plasma volume. High toroidal-mode number harmonics of the magnetic energy decay preferentially, leaving a tokamak-like plasma suitable for transition to other forms of current drive. Computations with the two-fluid terms in Ohm's Law produce qualitatively similar plasma evolution to the MHD computations. However, for the computations with the two-fluid plasma model, the ion fluid significantly decouples from the electron fluid, weakening the dynamics during magnetic reconnection. This effect is quantified by comparing global and local plasma parameters in both sets of calculations. Synthetic Mirnov coils at the locations used in the experiment observe magnetic fluctuation amplitudes of order 5 % and significant activity in the 10-20 kHz range in agreement with experimental measurements. Based on the cross-power spectrograms, the two-fluid calculation more accurately reproduces the frequency response of the experimental dynamics.

Acknowledgements

I would like to express my appreciation toward my advisor, Carl Sovinec, for his assistance and patience over the years. Without his guidance in all aspects of my research and writing, this thesis would not have been possible. I would also like to thank Ray Fonck, Jayson Barr, Edward Hinson, Kathreen Thome, Justin Perry, Aaron Redd, Michael Bongard, David Schlossberg, Galen Burke and the rest of the Pegasus Team for many valuable discussions and insights throughout this process. The enthusiasm with which they have received my work has been greatly appreciated.

Additionally, this thesis would not have been possible without the immeasurable assistance, support, and friendship of my fellow graduate students and postdoctoral researchers in the Center for Plasma Theory and Computation. I would like to thank my current colleagues, including Eric Howell, Joshua Sauppe, Andrea Montgomery, Kyle Bunkers, Tyler Cote, and Jeffrey Kollash. I would also like to thank my colleagues who have since moved on with their careers, including Jacob King, Bonita Burke, Nicholas Murphy, Mark Schlutt, and Ping Zhu.

I would like to express my sincerest gratitude to all my family and friends who have supported me in so many ways throughout my life. Chief among these are my parents, William and Rebecca, and my sister, Katie, whose boundless love and encouragement have sustained me to an unparalleled degree. I would like to thank my maternal grandmother, Virginia, who has always and unquestionably believed in my ability to reach my aspirations. I also truly appreciate the nearly endless supply of support, distraction, and entertainment that my friend, Adam Squire, has provided over the years. Without these people, my sanity would have long ago been forfeit.

Finally, I would like to express my gratitude to those who have helped shape my life but are no longer here with me. My great aunts, Martha, Hazel, Bernadine, and Ermel, exemplified selfless love and support for family. My paternal grandmother, Daisy, nurtured and cared for me throughout much of my youth. I deeply miss our many summer afternoons spent together. My paternal grandfather, Herman, who along with my father, helped to inspire a lifelong passion for science and learning. I'm grateful that I could help you finally open up about your experiences. Finally, I would like to thank my maternal grandfather and namesake, John, whose boundless compassion and good humor have touched and shaped the lives of so many, even long after his passing.

Contents

List of Figures

List of Tables

Chapter 1

Introduction and Motivation

In this chapter, several methods of active and passive non-inductive current drive for spherical tokamak startup are discussed. Through this review, reasons why most forms of non-inductive drive are not suitable for spherical tokamak startup are noted to motivate study of one DC helicity injection scheme, which has potential. Then, the Pegasus Toroidal Experiment device and its operation are outlined, including a detailed description of the startup method using localized DC helicity injection from plasma guns. Some experimental results are presented. Finally, a detailed motivation for numerical simulation is given along with an overview of the relaxation phenomenology during localized DC helicity injection in the Pegasus computations.

1.1 Non-Inductive Current Drive

Most magnetic confinement devices require current drive to maintain a plasma current that produces the poloidal magnetic fields necessary for stable confinement. One notable exception is the stellarator. The most basic form of current drive is ohmic induction, where a time-varying magnetic field produces an electric field which drives plasma current via Faraday's Law of Induction, given in integral form in Equation 1.1. Ohmic induction is limited not only in terms of the amount of current that can be driven, but also in the amount of heating that can be provided as a result of the inverse temperature dependency of plasma resistivity, Equation 1.2. [1] Small aspect ratio tokamaks have particularly limited capacity for ohmic induction due to the size restrictions on the central solenoid.

$$\oint_{\partial S} \mathbf{E} \cdot d\mathbf{l} = -\frac{\partial}{\partial t} \int_S \mathbf{B} \cdot d\mathbf{S} \tag{1.1}$$

$$\eta_{\parallel} = 0.51 \frac{m_e}{n_e e^2 \tau_e} \ \propto \ T_e^{-3/2} \tag{1.2}$$

1.1.1 Passive Current Drive

Ideally, most, if not all, of the plasma current would be provided by passive current drive methods that utilize some physical mechanism to generate plasma current without requiring significant energy input to be effective. One of the most well-known means of passive current drive is the bootstrap current, which is considered essential for steady-state tokamak reactor operation.

Bootstrap Current

The bootstrap current is a neoclassical (i.e. toroidal geometry) effect and arises due to anisotropy in the electron pressure tensor. [2] The anisotropy results from differences in the diffusion of trapped and passing electrons in weakly collisional regimes (banana or plateau). The bootstrap current arises from the balance of momentum transfer between trapped and passing electrons with the momentum transfer between passing electrons and ions.

Particle trapping occurs as a result of the spatial variation of the magnetic field.

Particles with low $v_{||}$ become trapped in local magnetic wells, which are located on the outboard side of a tokamak. [3, Chap. 3] The projection of these trapped particle orbits on the poloidal plane has a characteristic banana shape, hence the moniker "banana orbits." The toroidal procession of the trapped particle orbits is small relative to the bounce motion.

The collisionality regime is given by the normalized bounce frequency ν_* (Equation 1.3) of a trapped particle, where $\epsilon = r/R$ is the inverse aspect ratio, q is the safety factor, R is the major radius, v_{th} is the thermal speed, and τ_{90} is the 90° deflection time (i.e. the time for effective 90° scattering) for a given flux surface.

$$\nu_* = \frac{qR}{v_{th}\tau_{90}\epsilon^{3/2}} \tag{1.3}$$

The three main neoclassical collisionality regimes are the banana (collisionless, $\nu_* \ll 1$), plateau (transitional, $1 \leq \nu_* \leq 1/\epsilon^{3/2}$), and Pfirsch-Schlüter (collisional, $\nu_* \gg 1$) regimes. The full expression for the trapping fraction f_t is given by Equation 1.4, where $\lambda = 1/B$. In the large aspect ratio limit, $f_t \simeq 1.46\sqrt{\epsilon}$.

$$f_t = 1 - \frac{3}{4}\langle B^2\rangle \int_0^{\frac{1}{B_{max}}} \frac{\lambda \, d\lambda}{\langle\sqrt{1 - \lambda B}\rangle} \tag{1.4}$$

The three main models for the bootstrap current are (1) the multi-ion-species collisional regime "Hirshman-Sigmar" model; (2) the single ion-species, collisionless regime "Hirshman" model; and (3) the single ion-species, collisional regime "Harris" model. In general, the Hirshman-Sigmar model is considered the most accurate method for thermal species. Unlike the collisionless Hirschman model, the collisional models never predict plasma current near the edge. Specific details of the three models are given in Reference [2].

The total toroidal bootstrap current is given by Equation 1.5, where the details of $\langle \mathbf{J} \cdot \mathbf{B} \rangle_{bs}$ are determined by the selected model. In the large aspect ratio and low pressure limit in the collisionless regime, the parallel bootstrap current density reduces to the form in Equation 1.6. Temperature gradient effects can cause the bootstrap current to become larger locally in the plateau collisionality regime than in the banana collisionality regime. The ratio of bootstrap current to plasma current can be expressed in the form given by Equation 1.7, where C_{bs} is a function of density, temperature, current profile, ion charge, collisionality, trapped particle fraction, and aspect ratio. The poloidal beta, β_p, is the ratio of the volume-averaged plasma pressure, $\langle p \rangle$, to the poloidal magnetic field pressure at the last closed flux surface, $B_p^2\left(a\right)/2\mu_0$.

$$I_\phi^{bs} = 2\pi \int d\psi \frac{q(\psi)}{\langle B^2 \rangle} \langle \mathbf{J} \cdot \mathbf{B} \rangle_{bs} \tag{1.5}$$

$$J_\parallel^{bs} \simeq -\sqrt{\epsilon} R \left(2.4 T \frac{dn}{d\psi} + 0.1 n \frac{dT}{d\psi} \right) \tag{1.6}$$

$$\frac{I_{bs}}{I_p} = C_{bs} \sqrt{\epsilon} \beta_p \tag{1.7}$$

The bootstrap current is always hollow, meaning that in the absence of an on-axis current source, the safety factor profile will have an off-axis minimum. Temperature in experiments typically decreases from the plasma center outward, meaning that the bootstrap current typically appears at the plasma edge first and develops inward. At equilibrium, broad pressure profiles cause the bootstrap current to peak near the plasma edge, while peaked pressure profiles cause the bootstrap current to peak closer toz the magnetic axis.

A large bootstrap current fraction is desirable, but imposes additional constraints on plasma configurations. [2] The pressure profile must be properly aligned such that the resulting bootstrap current profile is locally less than the equilibrium current profile, i.e. $\langle \mathbf{J} \cdot \mathbf{B} \rangle_{bs} \leq \langle \mathbf{J} \cdot \mathbf{B} \rangle_{eq}$. Additionally, β_p must be constrained, such that $I_{bs} \leq I_p$, which can be more restrictive in limiting β than MHD stability. The bootstrap current can negatively impact plasma stability if large edge currents are produced, which are destabilizing to external kink modes.

Other Passive Methods

Other theoretical means of passive non-inductive current drive include asymmetric reflection of radiated electromagnetic energy from the plasma, synchrotron radiation in particular, and the thermoelectric effect. The asymmetric reflection method requires the vacuum vessel walls to preferentially reflect radiation in an asymmetric manner, such that the reflected radiation will sustain a current. [4] Though a completely passive current drive method, extremely high electron temperatures are required to generate significant plasma current. To sustain the plasma current in a tokamak reactor, electron temperatures $T_e \simeq 50\,\text{keV}$ are required, which are significantly higher than temperatures expected for a D-T reactor.

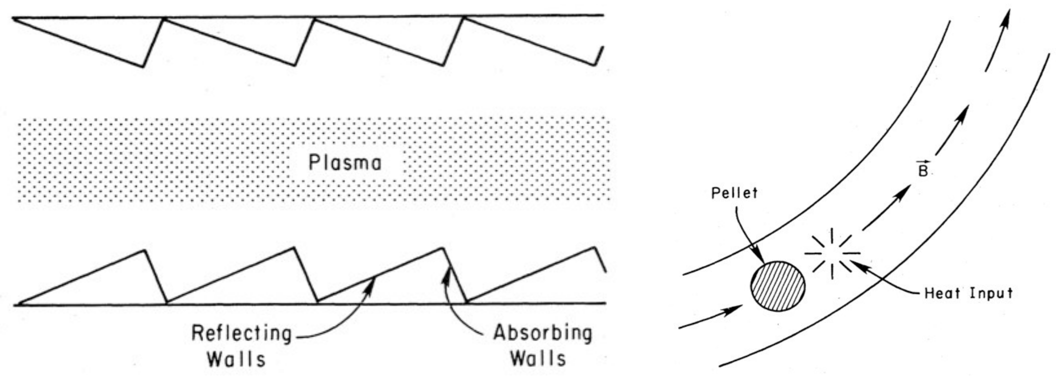

(a) Asymmetric Reflection (b) Thermoelectric Effect

Figure 1.1: Other passive methods of current drive [4]

In the thermoelectric method, frozen fuel pellets are injected into the plasma while the plasma is being heated on one side (with reference to magnetic field-lines). [4] The energetic electrons produced from heating stream in both directions along magnetic field lines, until impacting the fuel pellet, resulting in a net current from the electron deficit in the heated region and electron surplus in the pellet region. In principle, the pellets are injected in a phased manner to create a preferential current direction, in analogue to phased traffic lights on a single street favoring cars heading one direction versus the opposite. However, this method is not practical for high temperature plasmas as the fuel pellets will rapidly vaporize, requiring an exceedingly large amount of fuel to be injected into the plasma to generate plasma current. Such a large fuel input will result in a dramatic drop in plasma temperature.

1.1.2 Active Current Drive

To supplement passive current drive methods, a variety of active non-inductive current drive methods may be employed. The three most common forms of active current drive are neutral beam injection, radio frequency induction, and helicity injection.

Neutral Beam Injection

For current drive through neutral beam injection (NBI), beams of fast neutral atoms are injected into a plasma, as shown in Figure 1.2. The neutrals colliding with the plasma ionize and form an ion beam that toroidally circles the device. [4] To produce net toroidal current, disparate charge states are required between the plasma and beam ions. Otherwise, the frictional force will cause the electrons to rotate with the ions, canceling the ion current. The net current I_{net} from neutral beam injection is given by Equation 1.8, where I_f is the total ion current, Z_f is the beam ion charge, Z_{eff} is the effective plasma charge, v_e is the electron thermal speed, v_b is the beam velocity, and ϵ is the inverse aspect ratio of the torus. [5] Values of f, the ratio of the net current to the fast ion current, and A, a dimensionless coefficient defined in terms of the ratio of the trapped electron current to the current for no trapping, are computed in Reference [6]. The second and third terms on the right-hand side of Equation 1.8 correspond to the back electron current and electron trapping effects, respectively. In addition to current drive, beams also impart significant momentum into the plasma. For asymmetric beam injection, the imparted momentum gives rise to a radial electric field and causes the plasma to rotate toroidally.

$$I_{net} = I_f \left\{ 1 - \frac{Z_f}{Z_{eff}} \left[f\left(\frac{v_e}{v_b}\right) - A(Z_{eff})\epsilon^{1/2} \right] \right\} \tag{1.8}$$

An optimum beam energy will result in the deposition of as much power (and therefore current) as possible in the center of the plasma. Too much power will result in most of the neutral atoms passing through the plasma without ionizing. Too little power will result in most of the ionization and current drive at the plasma edge. Beams of energetic neutrals are typically produced by charge-exchange collisions between a beam of energetic ions (from an accelerator) and a neutral gas. The fraction of neutral atoms in the beam is determined by a balance between the charge-exchange and re-ionization interactions. As the beam particles will not efficiently collide with the plasma unless the plasma possesses sufficient density, i.e. an established plasma, neutral beam injection is not suitable for startup.

Radio Frequency Induction

All forms of radio-frequency (RF) induction couple wave energy to a specific resonance in the plasma, e.g. the ion cyclotron resonance, so that the wave energy is absorbed

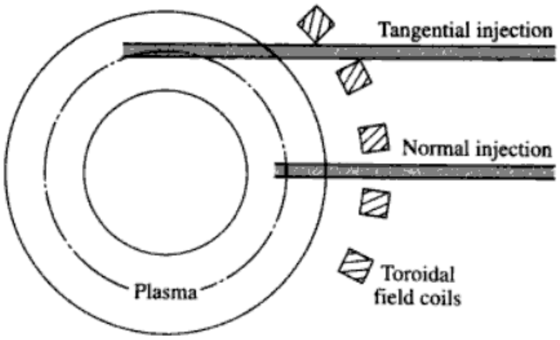

Figure 1.2: Neutral Beam Injection [3]

efficiently by either the ions or electrons. [3, Chaps. 3 & 5] As each resonance has dependency upon the magnetic field strength and/or plasma parameters, such as density and temperature, the energy deposition can be targeted toward specific locations within the plasma. Depending on the nature of the wave-particle interactions, the energy deposition leads to varying degrees of current drive and plasma heating, and though the current drive and heating are inseparable phenomena, the focus of this section will be on current drive.

As numerous normal modes exist within a plasma, particularly plasmas operating at reactor conditions, RF induction encompasses an expansive class of phenomena. In practice, the implementation of RF induction methods can vary significantly from class to class, with each method possessing its own advantages and disadvantages. The three most common types of RF current drive in tokamaks are ion cyclotron, lower hybrid, and electron cyclotron RF induction.

In ion cyclotron current drive (ICCD), fast magnetosonic waves are launched from the plasma edge. [7] Shear Alfvén waves are resonant at the ion cyclotron frequency, but are not suitable for current drive, as they cannot propagate when the wave frequency exceeds the local ion cyclotron frequency, $\omega_{ci} = Z_i eB/m_i$. Shear Alfvèn waves can be launched from the high magnetic-field side of the device, but will not penetrate the plasma edge, as they will mode convert into electrostatic waves. Therefore, the fast magnetosonic wave (also called the compressional Alfvén wave) must be used for effective ion cyclotron current drive. Damping of the wave at the fundamental resonance is weak as the electric field of the wave has opposite polarization relative to the wave gyromotion. However, damping at the second or higher harmonics is possible in a single species plasma with finite parallel wavenumber $k_\parallel$ or finite ion temperature T_i. Effects from the presence of a second ion species also allows wave damping.

For a minority ion concentration $\eta \lesssim 0.10\%$ where $\eta = n_{min}/n_{maj}$, the fast magnetosonic wave has weak damping at the minority fundamental resonance. [3, Chap. 5] When the minority concentration exceeds some critical value, a hybrid resonance occurs in the plasma. For a heavier minority species, a fast wave launched from the low field side will strongly reflect at the hybrid cutoff present on the low field side of the hybrid resonance. If the separation between the cutoff and resonance is small, the wave can tunnel through the evanescent region and mode convert into an electrostatic ion Bernstein wave (IBW) with a maximum conversion efficiency of 25%. [8] For a lighter minority species, the minority resonance is still accessible from the low field side. A fast wave launched from the high magnetic-field side will mode convert at the hybrid resonance frequency into an ion Bernstein wave. Ion Bernstein waves damp on electrons due to transit-time magnetic pumping (for sufficiently high β_e) and/or electron Landau damping. For high β plasmas, the damping remains very close to the hybrid layer.

As ion cyclotron waves possess large free-space wavelengths, an inductive loop antenna is often required for wave excitation, as opposed to rectangular waveguides. [7] The fast wave can only propagate at $\omega < \omega_{pe}$, meaning that the fast wave is evanescent in the plasma edge. Therefore, for efficient coupling, the antenna must be placed within a few centimeters of the cut-off electron density n_e.

For the lower hybrid current drive (LHCD) method, slow electromagnetic waves in the regime $\omega_{ci} \ll \omega \ll \omega_{ce}$ are launched from the plasma edge. [7] After tunneling through an evanescent layer at the plasma edge, the waves will propagate until encountering a lower hybrid resonance, $\omega_{LH}^{-2} = \left(\omega_{ci}\omega_{ce}\right)^{-1} + \omega_{pi}^{-2}$. At the lower hybrid resonance, the wave energy is imparted to electrons through electron Landau damping.

The ability of a slow wave to reach the lower hybrid resonance is subject to the Stix-Gallant accessibility condition, given by Equation 1.9. If the parallel index of refraction $n_\parallel$ drops below the critical value by even a few tenths of a percent, the slow wave will undergo total mode conversion into a fast wave. As the slow wave is a backward wave, i.e. the group and phase velocities have opposite signs, and the fast wave is a forward wave, mode conversion causes wave energy to reflect back out of the plasma. As the fast wave does not possess a resonance, it is not an effective means of current drive.

$$n_\parallel^2 > 1 + 2\frac{\omega_{pe}^2}{\omega_{ce}^2} - 2\frac{\omega_{pi}^2}{\omega^2} + 2\frac{\omega_{pe}}{\omega_{ce}}\left(1 + \frac{\omega_{pe}^2}{\omega_{ce}^2} - \frac{\omega_{pi}^2}{\omega^2}\right)^{1/2} \tag{1.9}$$

Slow electromagnetic waves may be generated by a rectangular waveguide operating in an appropriate transverse electric field (TE) mode, often the fundamental mode. [3, Chap. 5] Like fast magnetosonic waves, slow electromagnetic waves are evanescent at the plasma edge, as slow waves also can only propagate at $\omega < \omega_{pe}$. As for ion cyclotron current drive, the antenna must be placed close to the plasma edge for efficient coupling.

Electron cyclotron current drive (ECCD) can be achieved through either the ordinary (O) or extraordinary (X) plasma modes. Without hot particle effects, the O-mode does not possess a resonance and the X-mode only possesses a resonance at the upper hybrid frequency, $\omega_{UH}^2 = \omega_{pe}^2 + \omega_{ce}^2$. With the inclusion of hot particle and finite electron Larmor radius effects, resonances for both the O-mode and X-mode appear at $\omega \approx l\omega_{ce}$, with the cutoff conditions of $\omega_{pe}^2/\omega_{ce}^2 = l^2$ for the O-mode and $\omega_{pe}^2/\omega_{ce}^2 = l(l \pm 1)(1 - n_{\parallel}^2)$ for the X-mode. [3, Chap. 5]

Fundamental X-modes are not able to effectively produce current drive, as a fundamental X-mode launched from the low field side will encounter a low density cutoff and reflect. Though the wave may be able to tunnel and reach the upper hybrid resonance, wave transmission (for large tokamaks in particular) is often negligible. Fundamental X-modes launched from the high field side are able to reach the fundamental electron cyclotron and upper hybrid resonances. However, the placement of an antenna array on the inboard side of a tokamak (i.e. the high-field side) is problematic, especially for spherical tokamaks. Additionally, fundamental X-modes have the incorrect polarization to damp on electrons, though some damping occurs through finite parallel wavenumber $k_{\parallel}$ and ion temperature T_i effects. [7]

A second harmonic X-mode launched from the low field side is able to reach the second harmonic resonance, but not the upper hybrid resonance. Provided the density exceeds cutoff values, the fundamental O-mode is able to penetrate freely. Both the fundamental O-mode and second harmonic X-mode are strongly damped in the electron cyclotron region from relativistic variation of electron mass with speed, even for electrons with temperatures as low as 1 keV. [3, Chap. 5] Higher electron temperatures produce stronger wave absorption. The relativistic effects prevent reflection of incident waves launched from the low field side.

For devices with over-dense plasmas ($\omega_{pe}^2 \gg \omega_{ce}^2$), e.g. spherical tokamaks, the fundamental O-mode and second harmonic X-mode are not able to penetrate to the center of the discharge. Higher harmonics are still accessible to the center, but are only weakly damped. Therefore, devices with $\omega_{pe}^2 \gg \omega_{ce}^2$ must often rely on conversion into electrostatic electron Bernstein waves (EBWs) to provide effective current drive.

Electron Bernstein waves do not have density limits and all harmonics are strongly damped. Two distinct schemes are available for current drive through electron Bernstein waves: O-X-EBW and X-EBW. In the O-X-EWB scheme, a launched O-mode undergoes mode conversion into an X-mode when the parallel wave index $n_{\|}$ has the critical value n_c, where $n_c^2 = \omega_{ce}/(\omega + \omega_{ce})$. The X-mode then propagates into a lower density region, and upon encountering the upper hybrid resonance, mode converts into an electron Bernstein wave. The electron Bernstein wave undergoes total absorption at the first encountered electron cyclotron resonance. Near total mode conversion from O-mode to slow X-mode is possible when the O-mode and low density X-mode cutoffs are degenerate within the plasma core, where weaker plasma density gradients cause the degenerate cutoffs to be close to the high density X-mode cutoff. However, near the plasma edge, where density gradients are larger, the separation between the degenerate cutoffs (O-mode and low density X-mode) and high density X-mode cutoff increases rapidly, reducing mode conversion efficiency.

The X-EBW scheme requires two ion species and sufficiently steep edge density gradients, such that the X-mode low density cutoff, upper hybrid resonance, and X-mode high density cutoff form a triplet of critical points. [9] Upon encountering the triplet, an X-mode undergoes total mode conversion into an electron Bernstein wave and is totally absorbed at the first encountered electron cyclotron resonance.

For electron cyclotron current drive, a waveguide operating in the hybrid electric (HE) mode is frequently used to launch waves into the plasma. [3, Chap. 5] The hybrid electric mode, which only exists in a corrugated waveguide, is almost ideally suited for coupling to the plasma. The mode has an exact linear polarization; and the plane of polarization can be set to that of either the O-mode or X-mode. Unlike the waves used for ion cyclotron or low hybrid current drive, the waves used for electron cyclotron current drive are not evanescent between the antenna and plasma. Therefore, ECCD is suitable for pre-ionization and startup. [3, 10]

To summarize, the drawbacks possessed by the ICCD and LHCD prevent either from being an effective current drive scheme on the Pegasus Toroidal Experiment. The waves used for both ICCD and LHCD are evanescent at the plasma edge, meaning that neither method is effective for startup. For an established plasma, the antenna must be placed within a few centimeters of the cutoff electron density for efficient coupling. Passing through even a small evanescent region results in significant loss of transmitted power. Also, positioning the antenna in close proximity to the plasma edge will expose it to higher thermal, radiative, and mechanical stresses, significantly reducing its operational lifetime and potentially hindering overall device operation as contact between with energetic particles in a plasma results in antenna material sputtering into the vacuum vessel. The waves used for ECCD are not evanescent near the plasma edge, so ECCD is a suitable method for pre-ionization and startup.

Helicity Injection

Helicity injection is the application of a voltage across electrodes that are linked by magnetic flux. The resulting current flows along the magnetic field lines connecting the anode and cathode. Schemes that use helicity injection for sustainment of a plasma rely on the tendency of plasmas to relax into configurations with less overall transport than the direct parallel losses present in the original open field-line configuration. One of the most well-known theories of plasma relaxation is Taylor relaxation, in which the total magnetic energy is minimized given the constraint of the total magnetic helicity (Equation 1.10) being conserved.

$$K = \int_V \mathbf{A} \cdot \mathbf{B} \, d\mathbf{x} \tag{1.10}$$

Evaluating the temporal derivative of helicity provides an evolution equation with physically identifiable contributions. As the injected helicity from the third term of Equation 1.11 can be expressed as $2V_{loop}\Phi_T$, where V_{loop} is the toroidal loop voltage and Φ_T is the toroidal magnetic flux, ohmic induction can be viewed as a method of AC helicity injection. Other methods of AC helicity injection have been proposed that include both an oscillatory toroidal loop voltage and an oscillatory toroidal magnetic flux that are phased such that the time averaged product is non-zero. [11] The Steady Induction Helicity Injection Torus (HIT-SI) experiment at the University of Washington–shown in Figure 1.3–is a spheromak formed and sustained using non-axisymmetric AC helicity injection. [12] [13]

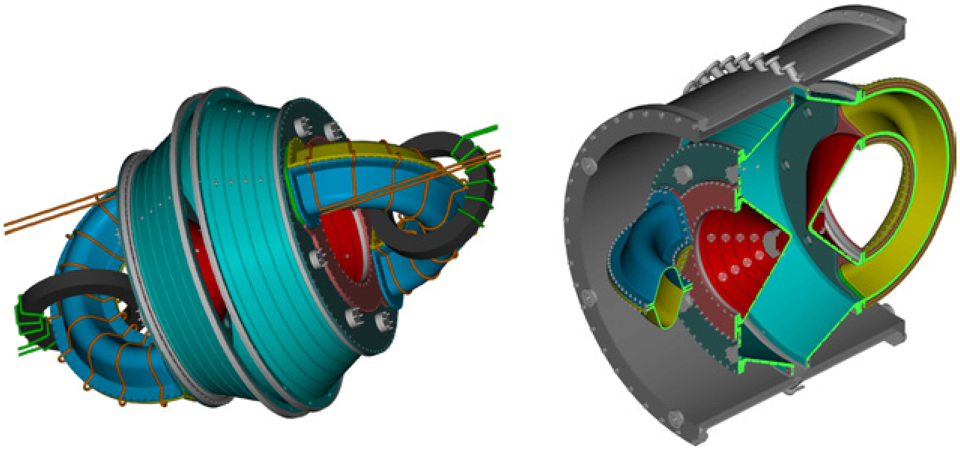

Figure 1.3: The HIT-SI experiment. [13] The left figure shows the electrical connections to the machine. The green wires drive the primary of the injector loop voltage V_{inj} driving the plasma secondary current I_{inj}. The brown wires supply the injector flux ψ_{inj}. The right figure shows a cutaway of the vacuum vessel.

$$\frac{\partial K}{\partial t} + \oint_{\partial V} d\mathbf{S} \cdot (\phi_{el}\mathbf{B} + \mathbf{E} \times \mathbf{A}) = -2\eta \int_V \mathbf{J} \cdot \mathbf{B} \, d\mathbf{x} \tag{1.11}$$

For the DC Helicity Injection method, a voltage bias is applied across open magnetic field-lines, which effectively drives plasma current along those field lines. DC helicity injection schemes are generally classified by the localization of the electrodes: the most common being toroidally symmetric electrodes. One example of a DC helicity injection scheme with toroidally symmetric electrodes is coaxial helicity injection (CHI) on the National Spherical Tokamak eXperiment (NSTX). CHI operates by driving current across vacuum magnetic fields that connect the inner and outer divertor plates through the application of a voltage bias, as shown in Figure 1.4. [14] The upper and lower gaps serve respectively as absorber and injector. The direction of the $\mathbf{E} \times \mathbf{B}$ plasma drift is away from the injector and toward the absorber. As the Lorentz force exceeds the restraining force from the injector field lines, the injected field is pulled into the vessel. With transient CHI, axisymmetric flux expands into the vessel, and when the applied current drive is reduced, reconnects near the injector region, producing a closed flux region inside the vessel. This approach has also been explored on the Helicity Injected Torus (HIT [15] and HIT-II [16]) and the Helicity Injected Spherical Torus (HIST [17]).

An alternative method of helicity injection is being investigated on the Pegasus Toroidal Experiment, where plasma guns serve as localized electrodes. Non-axisymmetric DC helicity injection has been previously explored on the Current Drive Experiment (CDX) and the Continuous Current Tokamak (CCT) using emissive lanthanum hexaboride (LaB_6) electrodes as the cathode, shown in Figure 1.5. [18] CDX achieved plasmas currents $I_p = 100 - 300$ A with injected current $I_{inj} = 50 - 200$ A solely from helicity injection as CDX lacked an ohmic transformer. Without utilizing its ohmic transformer, CCT achieved plasma currents $I_p = 100 - 6000$ A with injected current $I_{inj} = 20 - 400$ A.

The radial profiles of the poloidal magnetic field in CDX discharges–antisymmetric

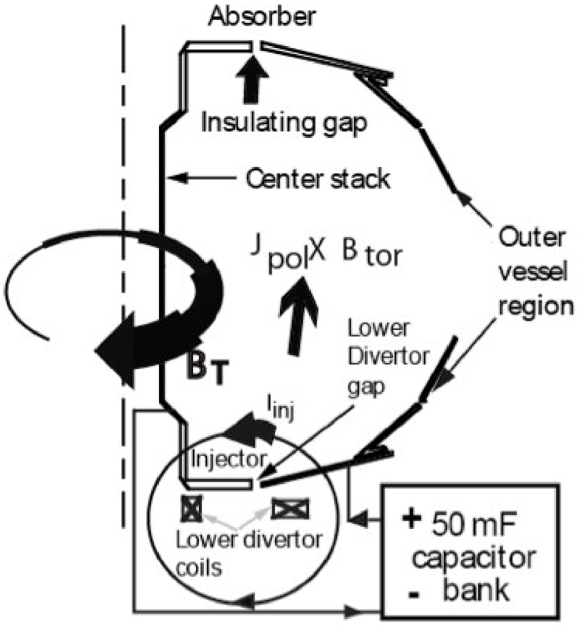

Figure 1.4: A cross-section of the CHI system on NSTX [14] A bias voltage drives current along the magnetic field lines connecting the inner and outer electrodes in the lower divertor region. When the $\mathbf{J}_{pol} \times \mathbf{B}_{tor}$ force from the injected current exceeds the restraining force from the injector field lines, the injected field is pulled into the vessel.

in proximity to a field null–are consistent with tokamak equilibria. [19] As the cathode provides edge current drive, centrally peaked current profiles in the relaxed plasma suggest a strong current transport mechanism. [18] Centrally peaked radial electron temperature profiles ($T_{e,0} \simeq 25$eV) in CDX discharges indicate good thermal confinement properties in the relaxed plasma state.

The Pegasus experiment and its implementation of non-axisymmetric DC helicity injection current drive are described in greater detail in the next section. Plasma relaxation and magnetic helicity are discussed in greater detail in Chapter 4.

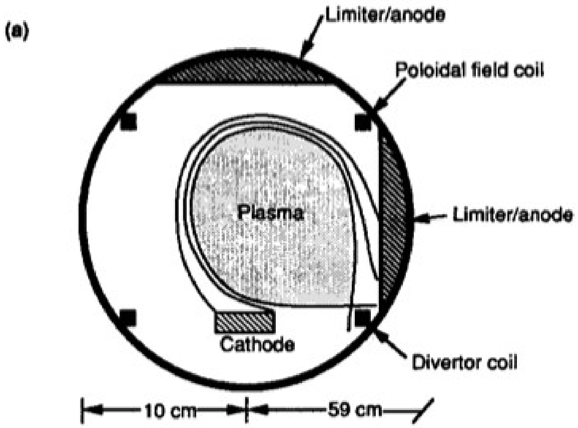

CDX Experimental Configuration

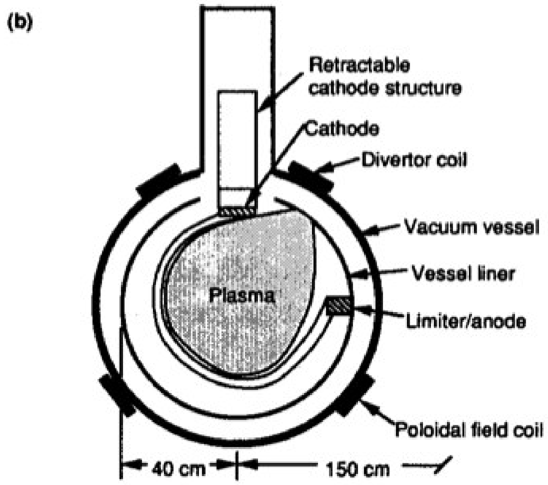

CCT Experimental Configuration

Figure 1.5: The CDX and CCT Experiments. [18] For both experiments, the cathodes are at a single toroidal location and emit in only one toroidal direction.

1.2 The Pegasus Toroidal Experiment

The Pegasus Toroidal Experiment is a spherical tokamak at the University of Wisconsin–Madison. The vacuum vessel (approximately 1.5 m-diameter by 1.5 m-height) is constructed of 0.64 cm-thickness stainless steel with no toroidal or poloidal electric breaks, and has twelve 46 cm-diameter ports encircling the midplane and six 20 cm diagnostic ports each on the top and bottom. [20] Neutral gas fueling is provided at an outboard midplane ($Z = -5.5\,\text{cm}$) port and/or an inboard injector near the central column ($Z = -30\,\text{cm}$). [21] Piezoelectric valves control the gas flow rate. Only outboard fueling was available for the experimental discharges discussed in this paper. Parameters typical of many Pegasus discharges are listed in Table 1.1.

The vacuum vessel is surrounded by 8 poloidal field (PF) coils, 12 ohmic trim coils, and 2 divertor coils, shown in Figure 1.6. [20] The ohmic trim coils are connected in series with the ohmic solenoid to exclude penetration of the fringe magnetic field from the solenoid into the plasma. The central solenoid of Pegasus was constructed by the National High Magnetic Field Laboratory. [23] The 10 cm-diameter center column consists of a central water cooling channel surrounded by twelve toroidal field (TF) conductors and the ohmic solenoid (OH). The twelve-turn, low-inductance (0.35 mH) toroidal field coil set is designed to carry up to 365 kA. The ohmic solenoid has a maximum current of 85 kA (magnetic field of 20 T) corresponding to a maximum inductive drive of approximately $154\,\text{mV}\cdot\text{s}$. The poloidal field coils are grouped into three independently driven sets: PF1-3, PF4-5, and PF6-8, shown in Figure 1.7. The poloidal field, toroidal field, and ohmic solenoid coil currents are programmed prior to a discharge, with pulse-width-modulated controllers and H-bridge power supplies providing real-time current feedback control. [20]

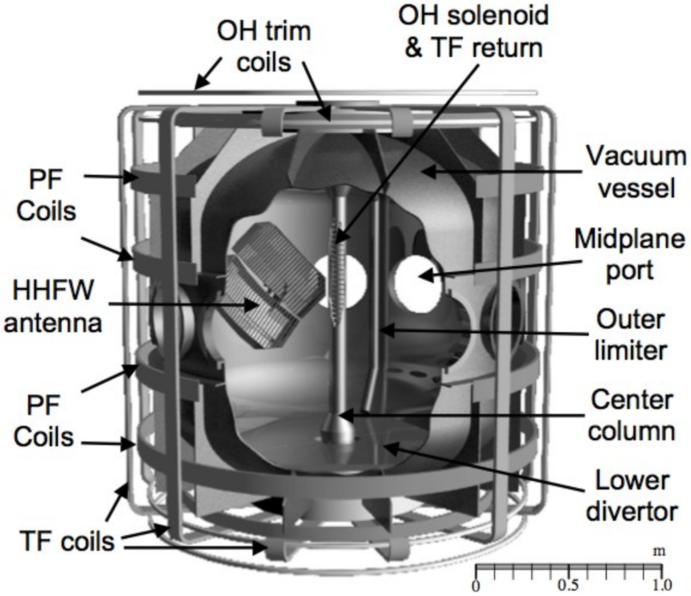

Figure 1.6: A cutaway view of the Pegasus Toroidal Experiment.

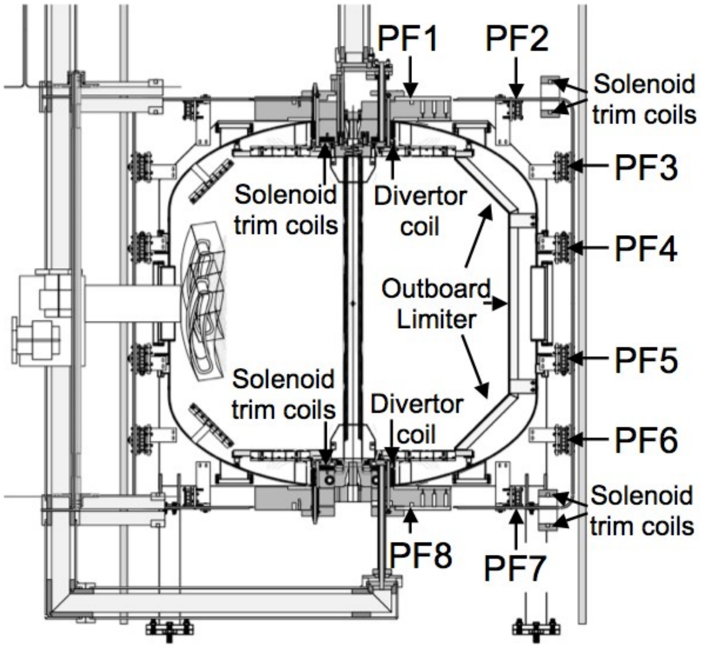

Figure 1.7: A cross-sectional view of the Pegasus Toroidal Experiment.

Table 1.1: Typical Pegasus discharge parameters

Parameter	Units	Achieved	Goal
A_r	-	1.15-1.3	1.12-1.3
R	m	0.2-0.45	0.2-0.45
I_p	MA	≤ 0.23	≤ 0.30
I_N	MA/T-m	6-14	6-20
RB_ϕ	T-m	≤ 0.06	≤ 0.10
κ	-	1.4-3.7	1.4-3.7
τ_{shot}	s	≤ 0.025	≤ 0.05
β_t	%	≤ 25	> 40

Achievements and goals current as of November 2013. [22]

Pegasus has multiple diagnostics for measuring the magnetic field and flux within the vacuum vessel. [24] Poloidally encircling the vacuum vessel are two Rogowski coils for measuring the total plasma current and two diamagnetic flux loops. Toroidally encircling the vacuum vessel are 26 internal and 6 external flux loops. Local magnetic field measurements are taken by 56 Mirnov coils. Some of the magnetic diagnostics are attached to the center column, but shielded from the plasma by a stainless steel shell. The magnetic measurements and the Grad-Shafranov solver KFIT have been used to produce reconstructions of plasma equilibria in Pegasus. [25]

Properties of the plasmas in Pegasus are characterized with additional diagnostics.

Line-integrated electron density and temperature are measured using a millimeter-wave heterodyne interferometer and soft x-ray pulse height analysis. The relative impurity content of the plasma relative to other discharges is measured using a vacuum ultraviolet spectrometer. Two D_α filterscopes qualitatively measure the deuterium fueling rate. Finally, a fast-frame (5140 fps) camera diagnostic is used to visualize the shape and location of a discharge plasma within the vacuum vessel.

1.2.1 Localized DC Helicity Injection

The small cross-section of the central solenoid limits the available inductive "ohmic" drive of toroidal plasma current. Therefore, non-inductive current drive is necessary to expand the available operational regime. On the Pegasus Toroidal Experiment, DC washer-gun plasma sources are being tested as a means of non-inductive current drive. [26] The washer-gun plasma sources are designed to be mounted through diagnostic ports, making installation, maintenance, removal, and reconfiguration relatively simple compared to other helicity injection schemes, e.g. Coaxial Helicity Injection.

Each plasma gun consists of a stack of alternating conducting and insulating washers, shown in Figure 1.8, which separate a molybdenum cathode cup from a molybdenum anode. Deuterium gas is puffed into the cathode cup from a 6.4 mm-diameter copper tube with the flow rate being controlled by a solenoidal gas valve. The copper tube also serves as the electrical connection for the cathode, and is electrically insulated from the gas supply system. A voltage bias (V_{arc}) is applied across the molybdenum anode and cathode and results in the formation of plasma within the plasma gun, which flows out of the gun. Another voltage bias (V_{inj}) is applied between the cathode and the anode external to the plasma gun and results in net current flowing into the gun.

The washer stack stabilizes the plasma arc and reduces the surface area of the gun

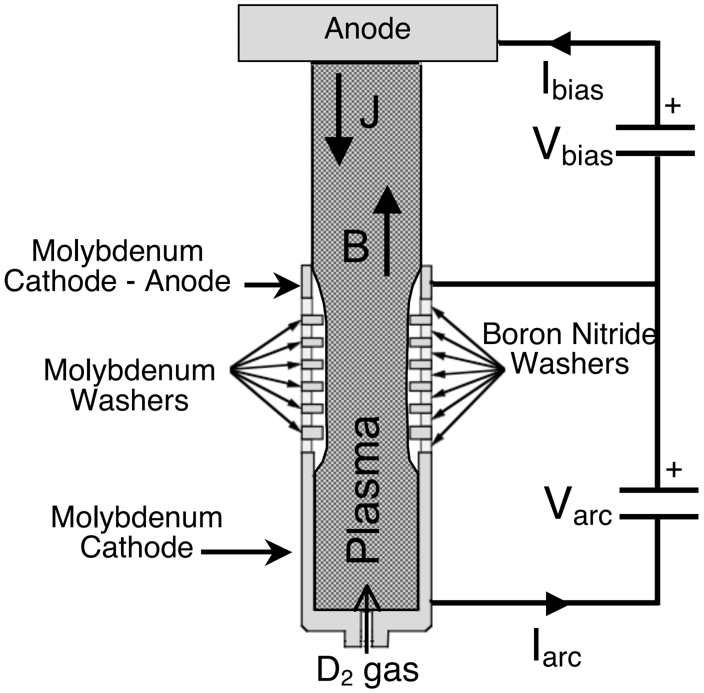

Figure 1.8: Schematic of a washer-gun plasma source [20]

material in contact with the plasma. As the current flows into plasma guns, most high-Z impurity ions, which produce significant radiative heat losses, will remained trapped within the gun aperture. The gun is encased in a boron nitride sleeve with a stainless steel tube connecting to the mounting structure within the vacuum vessel and a diagnostic port. The gun aperture and sleeve are approximately 0.625 in and 1.25 in in diameter, respectively. Test stand measurements in an expanding axial field reported electron density and temperatures of $n_e = (1\text{–}3) \times 10^{19}\,\mathrm{m}^{-3}$ and $T_e = 10\text{–}20\,\mathrm{eV}$, respectively, at the aperture of the plasma guns. [27] The initial diameter of an injected current filament was also observed to be comparable to the diameter of the aperture.

The plasma guns in the experiment have been operated in two primary configurations, which are shown in Figure 1.9. In the first configuration, the plasma guns are mounted in the lower divertor region at R = 0.16 m. [28] Experiments were run with either a single plasma gun or two guns mounted 180° apart. In the second configuration, an array of three plasma guns is mounted at the outboard side of the vacuum vessel, approximately 20–40 cm below the midplane and at a major radial position of $R = 70\,\mathrm{cm}$. [20] Each gun has a separate arc and bias circuit, and therefore, can be operated somewhat independently. However, all three guns in the array share a common valve for fueling. Both the position of the array below the midplane and its alignment with flux surfaces predicted by equilibrium reconstruction have been varied to improve discharge performance. [29] As the distance between the plasma gun and anode position limits the overall plasma size, a larger span between outboard injector and anode is being explored.

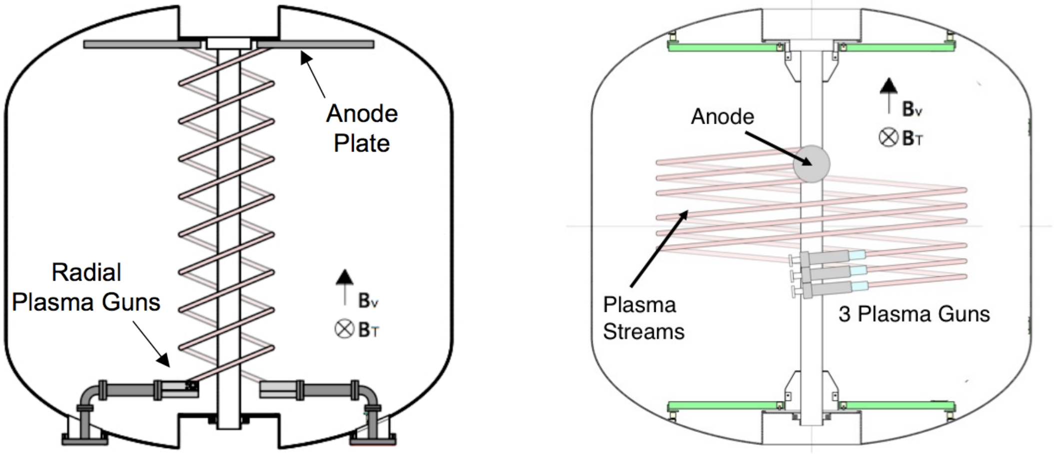

(a) Divertor guns [28] (b) Outboard guns [20]

Figure 1.9: Plasma gun configurations

For the outboard midplane configuration, a variety of anode configurations have been tested. These include a spherical anode and 2 in-diameter stainless steel pipe inserted a diagnostic port on the top of the vacuum vessel. The stainless steel pipe is bent such that it is roughly tangential to the reconstructed equilibrium flux surface shape. The design of the plasma guns has also been refined from early designs, in particular the cathode. [30] The objective is to increase the area of the cathode utilized for injecting current into the plasma and minimize deleterious plasma-material interaction: the formation of cathode spots reduces the utilized area and interaction of the cathode spots with the boron-nitride sleeve causes sputtering of impurity ions into the plasma, reducing overall discharge performance. Gas effused electrodes are being investigated that rely on the hollow cathode effect instead of an active arc circuit to provide greater injection area than currently possible with plasma guns.

The current filaments from the plasma guns undergo relaxation into a “tokamak-like” plasma, i.e. a plasma where the toroidally-averaged magnetic fields produce nested poloidal flux contours, like those for traditional tokamak equilibria, but the full three-dimensional magnetic field likely contains significant stochasticity. The evolution of plasma discharges for guns mounted in the lower divertor region has been captured across several discharges using a fast-frame camera, shown in Figure 1.10. Discrete current channels seen in Figure 1.10a coalesce into a current sheet that spans the height of the device, Figure 1.10b&c. Later, the plasma expands to fill much of the vacuum vessel and has a traditional spherical tokamak shape, as shown in Figure 1.10d.

During the relaxation process, the plasma current increases beyond that resulting from the geometric winding of the vacuum magnetic field, Figure 1.11. The center column poloidal flux also reverses in sign at the onset of relaxation. Solenoidal induction can be applied on the relaxing plasma to provide additional current drive. For the outboard midplane plasma gun configuration, poloidal flux compression of the relaxed plasma results in additional current amplification.

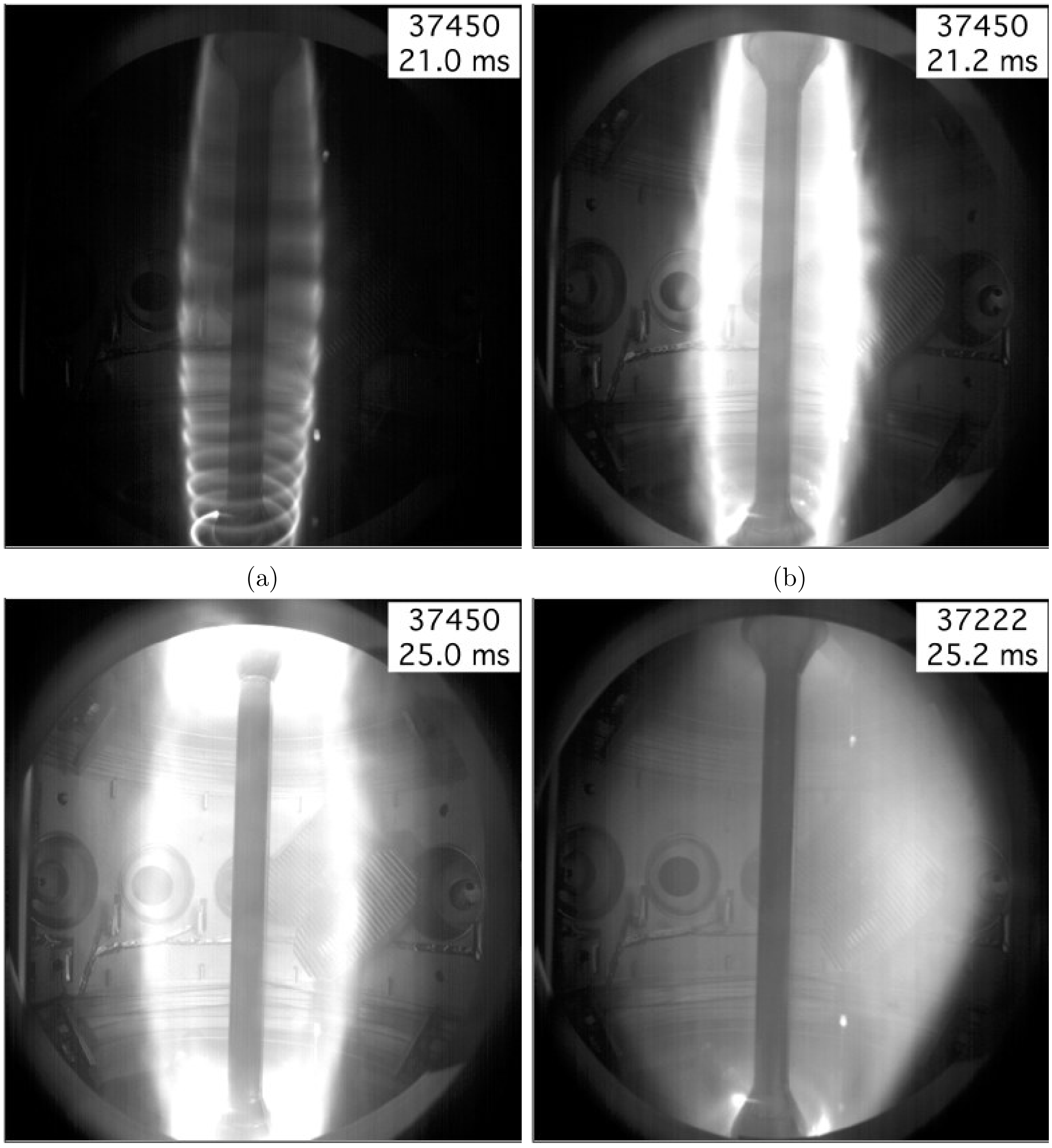

(a) (b)

(c) (d)

Figure 1.10: Visible light images showing the relaxation of divertor gun plasma filaments into a "tokamak-like" plasma [28]

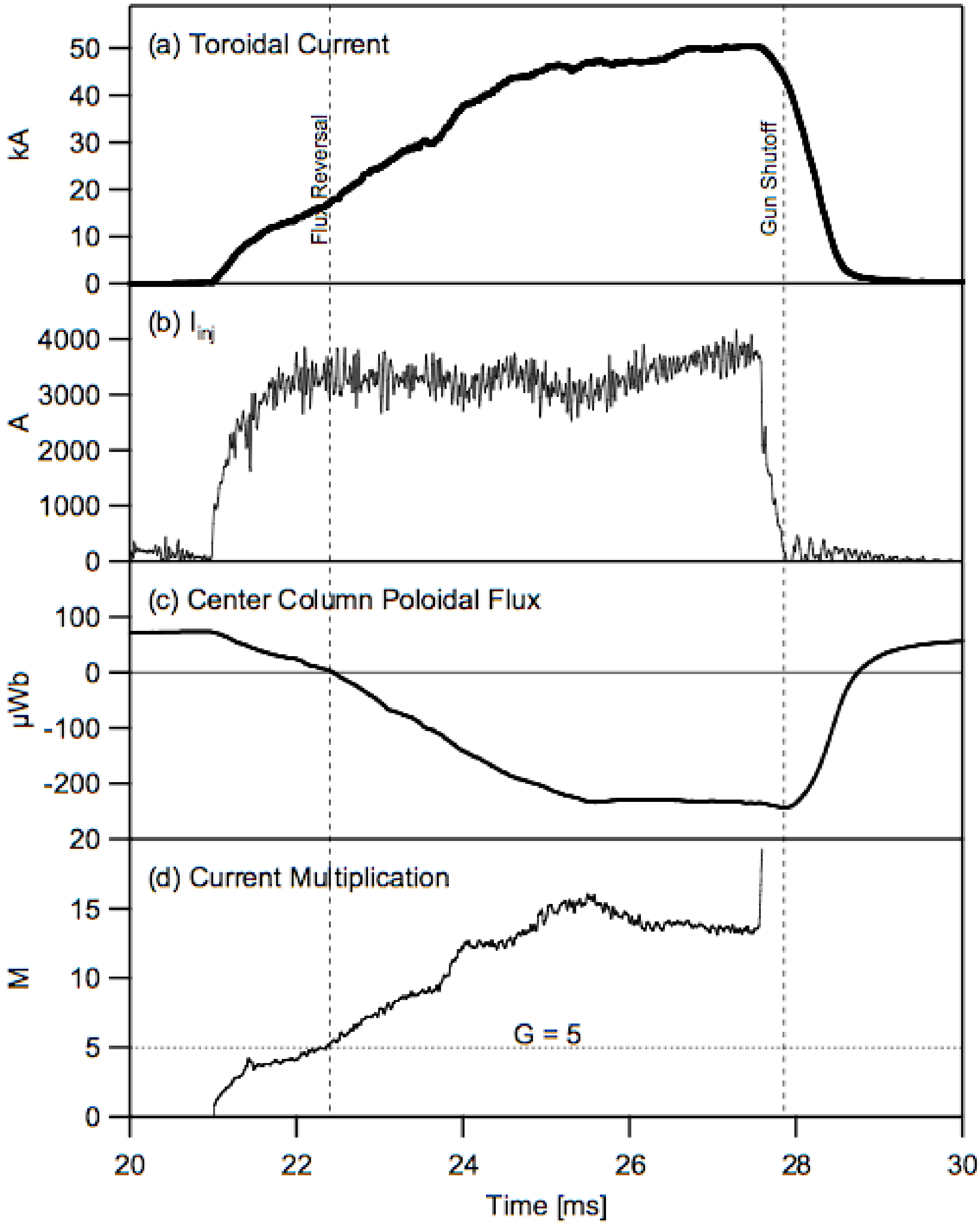

Figure 1.11: Diagnostic traces during the relaxation of divertor gun plasma filaments [28]

1.3 Numerical Simulation

Numerical computation has already proven itself a valuable tool for gaining insight into the plasma relaxation process in multiple devices and helicity injection schemes. Relaxation and flux amplification have been numerically investigated for the HIT experiment, which suggests incomplete relaxation and robust flux amplification and agrees with experiment observations of hollow current profiles. [31] Numerical computation has been used to explain how magnetic helicity can be transported through anti-dynamo electric fields from the open magnetic field lines connected to the electrodes to the amplified flux region during coaxial helicity injection on NSTX. [32] Numerical computation has also been used to investigate the entire evolution of spheromak plasma–including formation, current profile relaxation, and decay–using similar transport modeling to that used in this paper. [33–35]

While the initial helical plasma state and the final relaxed plasma state are well diagnosed in the experiment, the dynamics of the relaxation process have not been directly observed. Diagnostics that provide multidimensional information, such as the visible light Phantom camera, have yet to temporally resolve the interactions between the helical filaments. To date, ringlets have only been directly observable in experimental discharges operating near the relaxation threshold, thus slowing down the relaxation process. The vessel mounted magnetic diagnostics resolve fluctuations temporally, but are incapable of spatially resolving the fine-scale structure of the current filaments. A proposed insertable array of magnetic diagnostics may be able to overcome some of these limitations, as it can be placed in proximity to the location where the reconnection events occur. However, the array is still limited to a relative small poloidal region and cannot be placed too close to the filament without risking damage. Here, numerical computation is applied to investigate the details and provide a greater phenomenological understanding of the relaxation process that occurs in the Pegasus spherical tokamak. The temporal evolution of a three-dimensional current filament is modeled with the NIMROD code, starting from vacuum magnetic fields and progressing through relaxation into a tokamak-like state.

During formation with active helicity injection, the plasma evolves through a number of characteristic phases. The evolution is briefly described in this section with a more complete description given in Chapter 6. The plasma plasma current over the formation phase phase is displayed in Figure 1.12. The formation of a global poloidal magnetic field null near the central at $I_p \simeq 15\,\mathrm{kA}$ causes a dramatic change in magnetic topology and overall plasma evolution. During the interval $15 \leq I_p \leq 40\,\mathrm{kA}$, the plasma current increases much more rapidly than prior to the formation of the poloidal field null. The rate at which the plasma current increases is reduced for $I_p \geq 40\,\mathrm{kA}$.

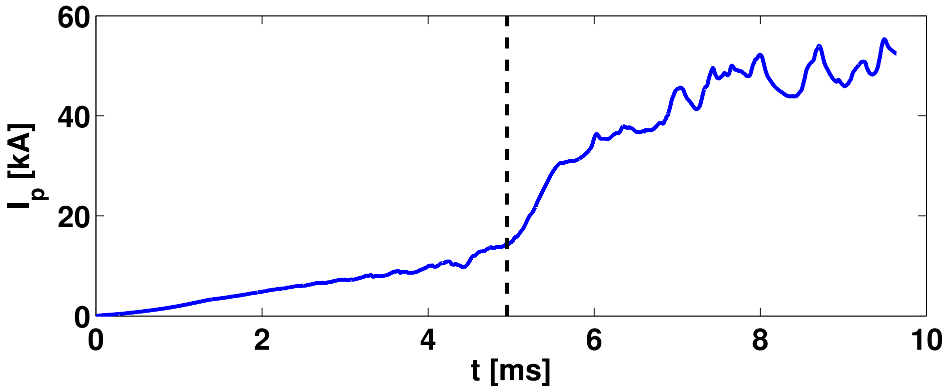

Figure 1.12: Plasma current during formation with localized helicity injection during the 2-fluid computation. The formation of a global poloidal magnetic field null near the central column is indicated by the dashed vertical line.

Early in the formation phase, the vacuum magnetic field directs the flux rope along several helical passes, as shown in Figure 1.13, and a helical current channel forms spanning the entire vertical extent of the domain. The initial formation of a current filament from the injector sources is described in Section 5.3.1.

After the self-induced magnetic field locally exceeds the vacuum magnetic field around the current channel, the attractive Lorentz force between adjacent passes of the current channel will periodically bring them into contact and drive reconnection. Eventually, with sufficient injected current, adjacent passes will fully reconnect and release axisymmetric current rings, shown in Figure 1.14 that form inboard of the driven current channel and slowly propagate vertically away from the location of helicity injection.

The formation of the current rings leads to the concentration of poloidal flux that accumulates over many reconnection events in the computation. The accumulation of poloidal flux contributes, in part, to the formation of a global poloidal magnetic field null forms near the central column. The poloidal field null redirects the current channel path so that it returns down the inboard side of the plasma. Initially, the current on the inboard side of the amplified flux region is diffuse, but coalesces at higher plasma current into a coherent channel that connects to the outboard driven current channel, and reconnection intermittently occurs between adjacent passes of the inboard portion of the current channel as it has for the outboard passes.

Reconnection and the formation of axisymmetric current rings continues after the poloidal field null forms, but as the plasma current increases, the rate at which adjacent passes of the outboard current channel reconnection decreases. This behavior continues until the eventual effective cessation of reconnection between adjacent passes of the outboard channel around $I_p \simeq 40\,\mathrm{kA}$, i.e. approximately the same time at which the rate at which the plasma current increases is reduced. The outboard portion of the current channel only makes a small number of toroidal transits for the entire vertical span, shown in Figure 1.15.

After the formation phase, the plasma is allowed to freely decay or an alternate form of current drive is applied, e.g. poloidal flux compression. For the computations modeled in Chapter 6, the plasma rapidly relaxes toward an convention, largely axisymmetric tokamak state, as shown in Figure 1.16. For computations where the plasma is allow to freely decay, closed flux surfaces form rapidly and encompass a significant plasma volume within a few milliseconds.

1.4 Outline of Dissertation

This dissertation is organized as follows:

In Chapter 2, the concept of magnetic helicity is introduced in order to provide a framework for the discussion on flux-rope interactions in Chapter 3 and plasma relaxation in Chapter 4. A number of different definitions for magnetic helicity are described in detail, along with a discussion on their respective properties. In particular, the conditions for gauge invariance are noted.

In Chapter 3, magnetic flux ropes are introduced in order to provide a framework for the interactions between adjacent passes of the current filament. One-dimensional flux tube models are described, including the properties for both generic and specific models. A primer is given on magnetic reconnection, particularly focused on Sweet-Parker reconnection and Hall-reconnection. The different types of interactions typically occur between pairs of interacting flux ropes and the conditions under which they typically occur is also presented.

In Chapter 4, the concept of plasma relaxation is introduced as a framework for understanding the evolution of the current filament. A number of relaxation theories are presented, each of which is characterized by the quantities conserved during plasma motions and/or the minimization/maximization principles describing the final state.

Comparisons to experimental and computational results are provided where available to show the successes and limitations of the theories. The mechanisms through which magnetic helicity evolution and transport occur and factors that limit the range of accessible plasma states are also detailed.

In Chapter 5, the primary tool of the computational study, the NIMROD code, is introduced. First, the physics model is presented, including the equations evolved by the code and optional closure models. NIMROD possesses a two-dimensional finite element mesh and finite Fourier series in the periodic direction. Each method of spatial discretization and its convergence properties are listed. Equations are also listed for the implicit-leapfrog temporal advance, along with its convergence and stability properties. Finally, the modifications to the code necessary for the computational study are described.

In Chapter 6, the results of this computational study are presented and discussed. The different phases of current filament evolution are listed and characterized: from initial formation of the helical filament to relaxation into a tokamak-like plasma configuration. The merger and reconnection of adjacent passes of the current filament is observed to release current rings from the driven current filament. The evolution of the magnetic topology is characterized over such reconnection events using the trajectory, length, and squashing factor produced by many field-line traces. Significant poloidal flux is observed to accumulate over many reconnection events. After the formation of a large-scale poloidal magnetic field null near the central column, a hollow current profile forms, which later relaxes into a tokamak-like plasma state after current injection has ceased. Measurements made with a synthetic Mirnov coil array are in quantitative agreement with magnetic fluctuation amplitude and frequency spectra observed in the experiment. Comparisons to similar or related phenomena are interspersed among the computational results.

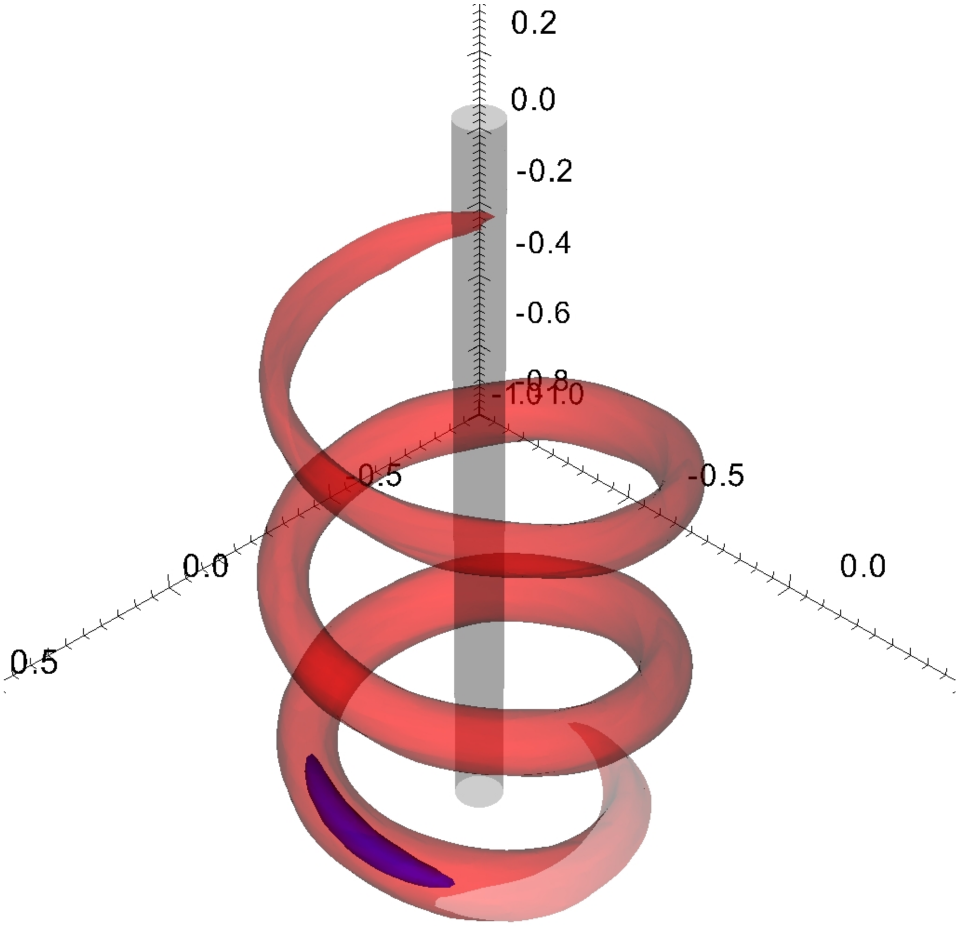

Figure 1.13: Early winding of the current filament along the helical vacuum magnetic field lines. The half-max shown of the injector shape function is shown in in blue. The isosurface $\lambda = 1.0\ \mathrm{m}^{-1}$ is shown in translucent red for the resulting current filament at $t = 0.6$ ms in the 2-fluid computation, when $I_p = 1.1$ kA . The central column is shown in gray for clarity.

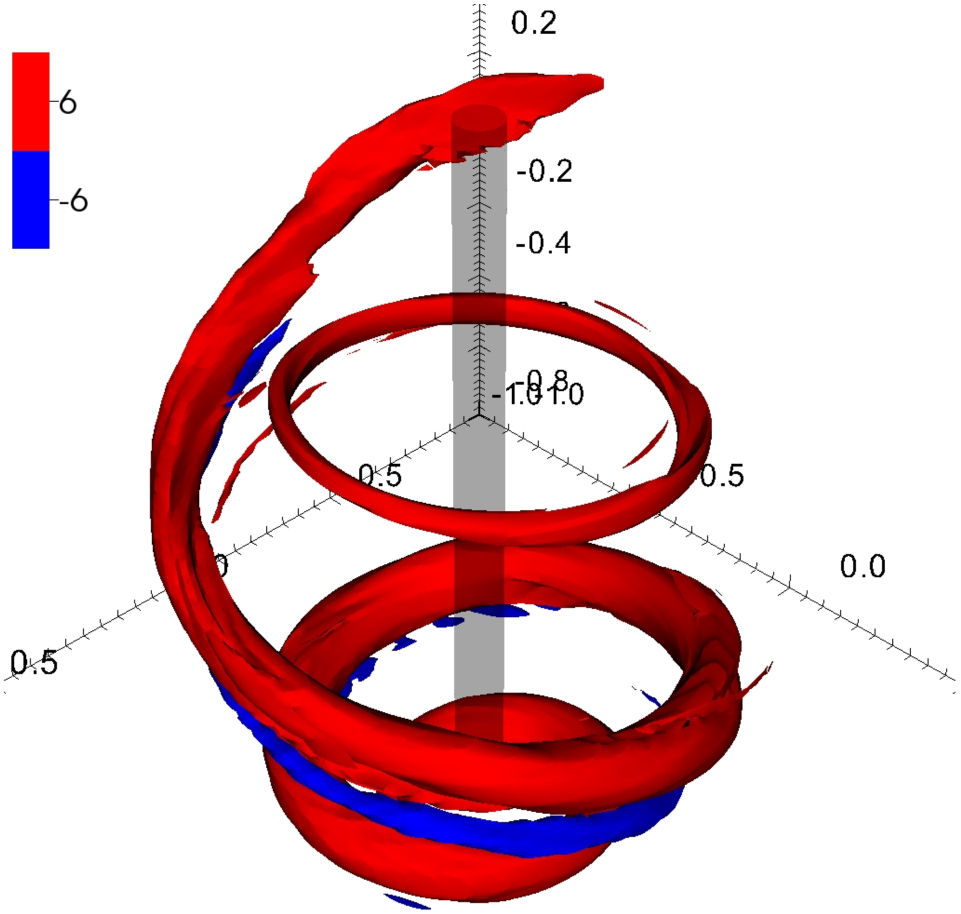

Figure 1.14: Reconnection releases an axisymmetric current ring (shown near the center of the figure) from the driven current channel plasma. Isosurfaces of $\lambda = \pm 6\,\mathrm{m}^{-1}$ are shown at $t = 2.95\,\mathrm{ms}$ in the 2-fluid computation, when $I_p \simeq 7\,\mathrm{kA}$. The central column is shown for reference.

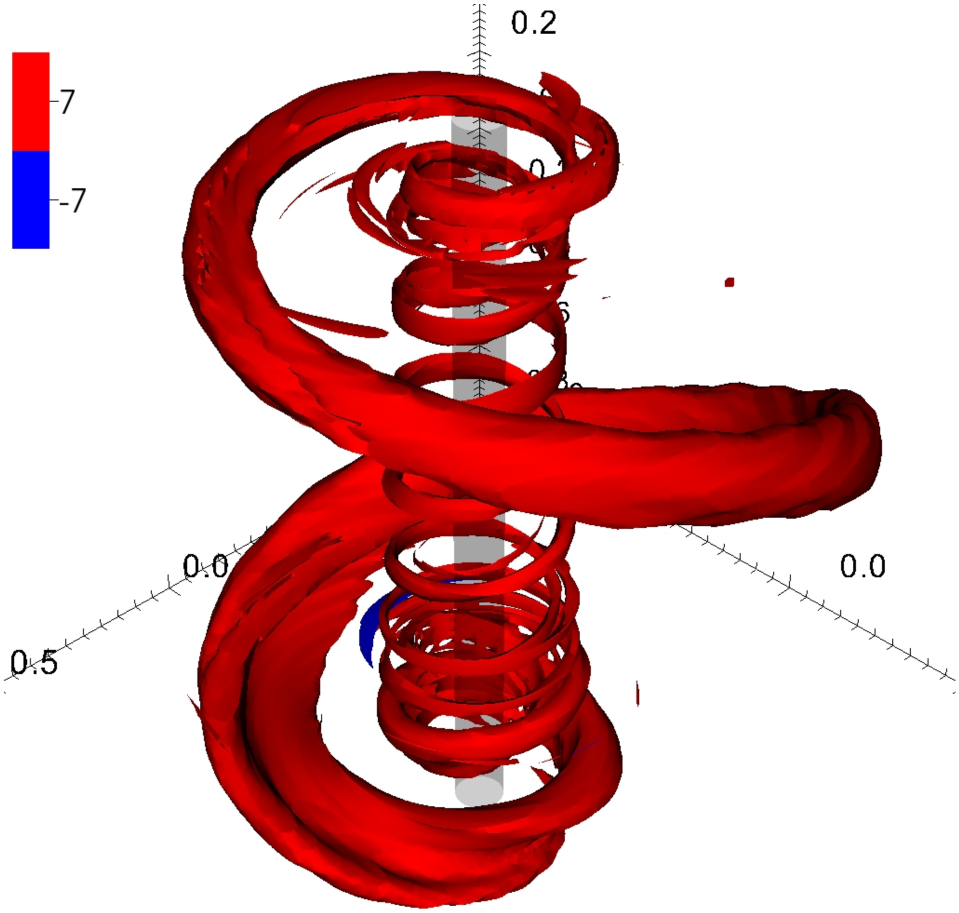

Figure 1.15: Late in the formation phase, the current channel forms a return path winding down the inboard side of the plasma near the central column. Isosurfaces of $\lambda = \pm 7\,\mathrm{m}^{-1}$ are shown $t = 8.51$ ms in the 2-fluid computation, when $I_p \simeq 45\,\mathrm{kA}$. The central column is shown for reference.

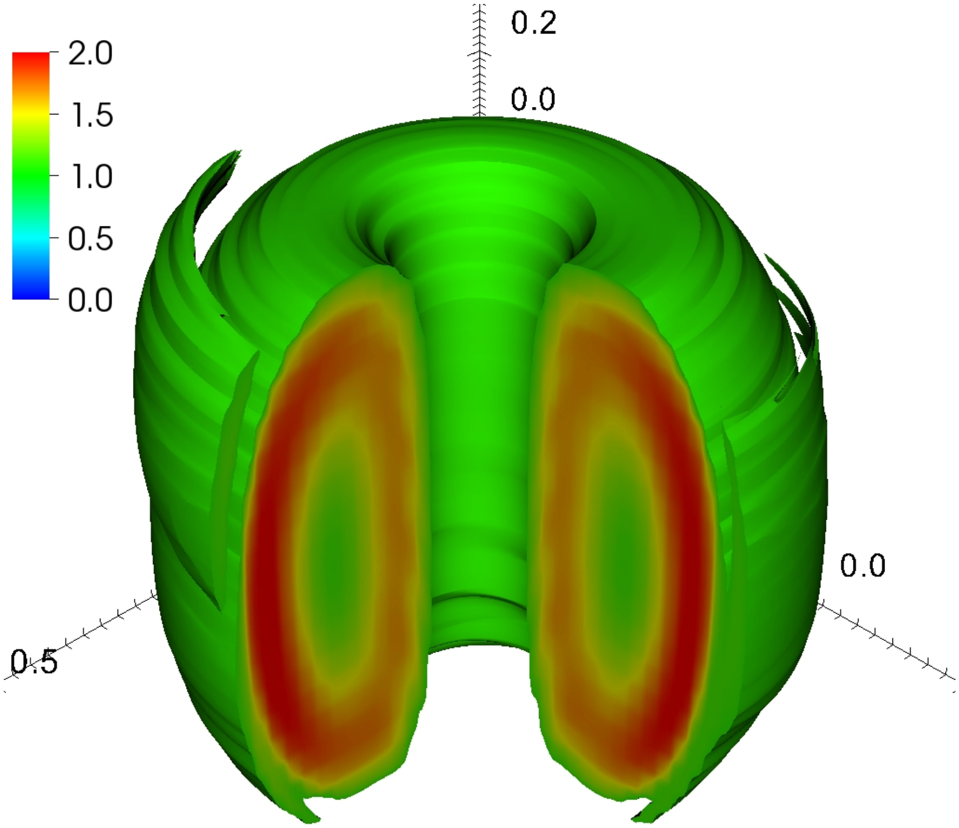

Figure 1.16: During free decay of the plasma after the formation phase, the plasma rapidly relaxes toward a conventional tokamak state. Contours of $1 \leq \lambda \leq 2$ $[\mathrm{m}]^{-1}$ are shown at 2 ms into the decay phase.

Chapter 2

Magnetic Helicity

Magnetic helicity is a measure of the extent to which magnetic field-lines within a volume wrap around themselves. The direction of writhe determines the sign of magnetic helicity, where right- and left-handed magnetic flux tubes have positive and negative magnetic helicity, respectively. Magnetic helicity is a generalization of the topological concept of linking number and essentially represents a flux-weighted sum of the linking numbers of pairs of magnetic field lines.

For a discrete set of flux tubes, magnetic helicity can be expressed as a linkage of magnetic fluxes. [36, 37] The total magnetic helicity for the set is the sum of all the contributions over all flux tubes as in Equation 2.1, where L_{ij} is the (integer) linking number between two flux tubes and ψ_i is the magnetic flux of an individual flux tube. The self ($i = j$) and mutual ($i \neq j$) helicity terms in Equation 2.1 are analogous to the magnetic energy from self and mutual inductance, respectively.

$$H = \sum_{i}^{N} \sum_{j}^{N} L_{ij} \psi_i \psi_j \tag{2.1}$$

Idealized flux tube linkages in Figures 2.1 & 2.2 independently illustrate the concept of self- and mutual-helicity. Self-helicity (or internal helicity) is the linking of magnetic flux with itself through a series of twists and kinks of the magnetic field. [36] Although the magnetic field line of the figure-8 knot in Figure 2.1a appears to be kinked but untwisted, the figure-8 knot is topologically equivalent to the twisted but unkinked magnetic field in the torus in Figure 2.1b. Both configurations have a magnetic helicity $H_{self} = +\psi^2$

In general, kinks and twists are not topologically equivalent operations. Therefore, the self-helicity contributions from kinks and twists must be considered independently. For example, a trefoil knot (not shown) with an untwisted magnetic field on the surface cannot be made topologically equivalent to a torus, but still possesses magnetic helicity $H_{self} = \pm 3\psi^2$. As only a single flux tube is present in each example in Figure 2.1, the mutual-helicity contribution is identically zero.

(a) Lemniscate

(b) Torus

Figure 2.1: Two flux-tube configurations with $H_{self} = +\psi^2$ demonstrate self-helicity through (a) kinks and (b) twists. A typical field line is traced on the surface of the flux tubes. The torus in (b) is translucent to show the full path of the magnetic field line.

Mutual-helicity is the linking of the magnetic flux of different flux tubes through non-topologically-trivial knots. The simplest example is a single linkage between two flux rings, as shown in Figure 2.2a. The mutual magnetic helicity of the rings (arbitrarily assigned labels 1 & 2) $H_{mutual} = +2\psi_1\psi_2$ from the symmetry of the linking number, i.e. $L_{1,2} = L_{2,1} = +1$. Although the Borromean rings in Figure 2.2b form a non-trivial magnetic topology, the mutual helicity contribution is identically zero. This can be demonstrated by ignoring any of the flux tubes: the remaining two flux tubes are not linked. As the examples in Figure 2.2 have unkinked and untwisted magnetic field lines, the self-helicity contribution is identically zero.

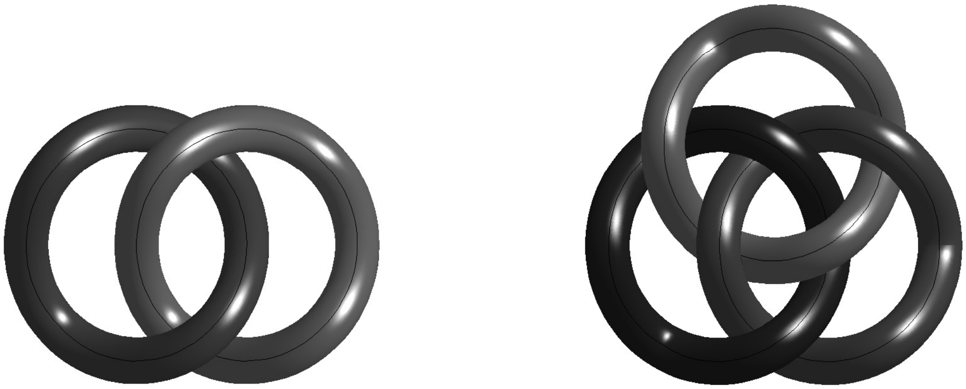

(a) Linked Rings

(b) Borromean Rings

Figure 2.2: Two flux-tube configurations demonstrate mutual-helicity through linking. For the two linked flux-tube rings in figure (a), $H_{mutual} = +2\psi_1\psi_2$. For the Borromean rings in figure (b), $H_{mutual} = 0$ as no pair of flux tubes is linked. A typical field line is traced on the surface of the flux tubes.

Higher-order linking integrals can distinguish between linked and unlinked configurations with zero net magnetic helicity, such as the Borromean rings in Figure 2.2b and three unlinked rings. However, these higher-order integrals are only defined for a finite number of discrete, non-intersecting flux tubes, and not continuum fields. For example, the third-order linking integral described in [38, 39] is only defined for three discrete flux tubes. The fourth-order linking integral described in [40] is defined for any arbitrary number of pairs of flux tubes. As both higher-order linking integrals are functions of the magnetic vector potential, any generalization to continuum fields would likely possess similar limitations on being well-defined and gauge invariant as those for magnetic helicity discussed later in this chapter.

The linking number L_{ij} is calculated for every pair of magnetic field lines, and therefore every pair of non-intersecting flux tubes, using the Gauss linking integral in Equation 2.2. [41] The positions along two field lines are parametrized such that $\mathbf{x} = \mathbf{x}(\tau)$, $\mathbf{x}' = \mathbf{x}'(\tau')$, and $\mathbf{r} = \mathbf{x}' - \mathbf{x}$.

$$L_{ij} = -\frac{1}{4\pi} \oint_{\tau} \oint_{\tau'} \frac{d\mathbf{x}}{d\tau} \cdot \frac{\mathbf{r}}{r^3} \times \frac{d\mathbf{x}'}{d\tau'} d\tau' d\tau \tag{2.2}$$

2.1 Classical Helicity

In the limit of infinitely many differential flux tubes ($\psi_i \to 0$), the total magnetic helicity reduces to the classical magnetic helicity formulation given by Equation 2.4. The Coulomb gauge vector potential $\mathbf{A}$ is given by Equation 2.3. For a given domain where magnetic helicity is well-defined, it is defined on every arbitrarily small flux tube–and therefore, closed magnetic field-line and surface–within a plasma.

$$\mathbf{A}(\mathbf{x}) = -\frac{1}{4\pi} \int \frac{\mathbf{r}}{r^3} \times \mathbf{B}\left(\mathbf{x}'\right) dx'^3 \tag{2.3}$$

$$H_C = \int_V \mathbf{A} \cdot \mathbf{B}\, d^3x \tag{2.4}$$

The gauge invariance for magnetic helicity is tested by defining a gauge transformation for vector potential, such that $\mathbf{A}' = \mathbf{A} + \nabla\chi$. As $\mathbf{B} = \nabla \times \mathbf{A}$, the magnetic field remains unchanged by this gauge transformation, i.e. $\mathbf{B}' = \mathbf{B}$. The resulting difference in magnetic helicity from the gauge transformation is given by Equation 2.5.

$$\Delta H \equiv \int_V \left(\mathbf{A}' \cdot \mathbf{B}' - \mathbf{A} \cdot \mathbf{B}\right) d^3x = \oint_{\partial V} \chi \mathbf{B} \cdot d\mathbf{S} \tag{2.5}$$

In a simply connected domain V, χ is single-valued on the domain boundary ∂V. By letting ∂V be a magnetic surface, i.e. $\mathbf{B} \cdot \hat{\mathbf{n}}|_{\partial V} = 0$, no change in magnetic helicity occurs as a result of the gauge transformation for a magnetic surface in a simply connected domain, i.e. $\Delta H = 0$. Therefore, the magnetic helicity of a closed field-line region is gauge invariant in a simply connected domain. Magnetic helicity is also well defined for toroidal geometries with continuous poloidal and toroidal flux across magnetic surfaces. [42]

2.2 Relative and Generalized Helicity Content

For open field-line configurations, the magnetic helicity can be defined relative to some reference region. [36] Relative helicity is illustrated in Figure 2.3, where a space V is subdivided into two simply connected regions V_a and V_b, which are separated by a boundary surface S. The magnetic field is represented by an ordered pair, $\mathbf{B} \equiv (\mathbf{B}_a, \mathbf{B}_b)$. To satisfy the divergence-free condition, the magnetic field defined in Equation 2.6 must satisfy $\mathbf{B}_a \cdot \hat{\mathbf{n}}|_S = \mathbf{B}_b \cdot \hat{\mathbf{n}}|_S$ where $\hat{\mathbf{n}} \equiv \hat{\mathbf{n}}_a = -\hat{\mathbf{n}}_b$. Relative helicity ΔH is considered for two magnetic fields that only vary in region V_a, i.e. $\mathbf{B}_1 = (\mathbf{B}_{a1}, \mathbf{B}_b)$ and $\mathbf{B}_2 = (\mathbf{B}_{a2}, \mathbf{B}_b)$.

$$\mathbf{B}(\mathbf{x}) = \begin{cases} \mathbf{B}_a(\mathbf{x}) & \text{if } \mathbf{x} \in V_a \\ \mathbf{B}_b(\mathbf{x}) & \text{if } \mathbf{x} \in V_b \end{cases} \tag{2.6}$$

$$\Delta H \equiv \int_V (\mathbf{A}_1 \cdot \mathbf{B}_1 - \mathbf{A}_2 \cdot \mathbf{B}_2)\, d^3x \tag{2.7a}$$

$$= \int_{V_a} (\mathbf{A}_1 - \mathbf{A}_2) \cdot (\mathbf{B}_{a1} + \mathbf{B}_{a2})\, d^3x - \oint_S \chi\, (\mathbf{B}_{a1} + \mathbf{B}_{a2}) \cdot d\mathbf{S} \tag{2.7b}$$

The total magnetic helicity of a system with open field-lines (i.e. $\mathbf{B} \cdot \hat{n} \neq 0$ on the

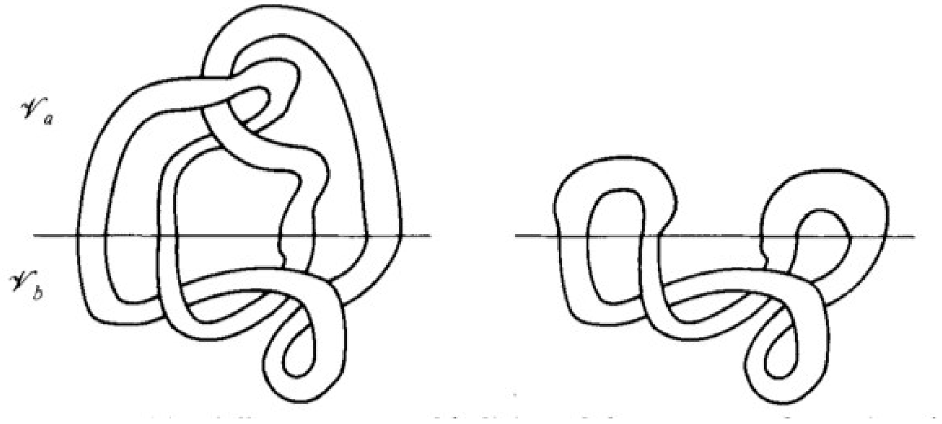

Figure 2.3: The difference in total helicity of these two configurations is independent of the field in region V_b. [36]

domain boundary) can be expressed in terms of self and mutual helicity contributions in an analogue to magnetic inductance, as shown in Equation 2.8, where the different components are integrated over the same spatial domain. [41] The magnetic field is decomposed into an open magnetic field ($\mathbf{B}_{vac}$) and closed magnetic field ($\mathbf{B}_{cl} = \mathbf{B} - \mathbf{B}_{vac}$) components. The closed magnetic field satisfies $\mathbf{B}_{cl} \cdot \hat{n} = 0$ on the domain boundary. The corresponding vector potential $\mathbf{A}_{cl} = \mathbf{A} - \mathbf{A}_{vac}$, such that $\mathbf{B}_{cl} = \nabla \times \mathbf{A}_{cl}$, satisfies $\mathbf{A}_{cl} \times \hat{n} = 0$ on the domain boundary. The vacuum magnetic field $\mathbf{B}_{vac}$ is assumed to possess no self helicity contribution as its magnetic helicity is ill-defined.

$$H_{self}\left(\mathbf{B}_{cl}\right) = \int \mathbf{A}_{cl} \cdot \mathbf{B}_{cl} \, d^3x \tag{2.8a}$$

$$H_{mutual}\left(\mathbf{B}_{cl}, \mathbf{B}_{vac}\right) = 2 \int \mathbf{A}_{vac} \cdot \mathbf{B}_{cl} \, d^3x \tag{2.8b}$$

$$H_{self}\left(\mathbf{B}_{vac}\right) = 0 \tag{2.8c}$$

The combination of the terms in Equation 2.8 yields the Finn-Antonsen relation, Equation 2.9, which is equivalent to the previously defined relative helicity in Equation 2.7 with the surface term neglected. This expression is applicable for any simply connected or toroidal geometry containing a closed-flux region V, under the same applicability conditions as classical helicity presented at the end of Section 2.1.

$$H_R = \int (\mathbf{A} + \mathbf{A}_{vac}) \cdot (\mathbf{B} - \mathbf{B}_{vac})\, d^3x \tag{2.9}$$

A generalized helicity content H_0, given in Equation 2.10, can be defined for an arbitrary, time-dependent, bounded region of space. [43] The first term of Equation 2.10 is the original classical helicity, and the second term is a product of a poloidal and toroidal loop integral of the vector potential of the bounding surface. For regions not bounded by a magnetic surface, helicity content and magnetic fluxes are still well-defined, but not gauge invariant. The generalized helicity content can be rewritten as a single volume integral of the poloidal (χ) and toroidal (ψ) fluxes, given Equation 2.11, where χ_B is the toroidal flux on the bounding surface. [44].

$$H_0 = \int_V \mathbf{A} \cdot \mathbf{B}\, dV - \oint \mathbf{A} \cdot d\mathbf{x}_\theta \oint \mathbf{A} \cdot d\mathbf{x}_\phi \tag{2.10}$$

$$H_0 = 2 \int_V (\chi_B - \chi) \left(\frac{\partial \psi}{\partial \rho} \right) dV \tag{2.11}$$

2.3 Helicity in Periodic Domains

Despite the utility of domains with a periodic poloidal plane to analytical and/or computational analysis, classical magnetic helicity is ill-defined in such domains. [45–47] For a configuration with a periodic mean field, such as the 2-torus in Figure 2.4, an ambiguity exists as how to define linking, as there is no longer a distinction between the inside and outside of a flux tube. As the sense of twist is positive about one area and negative about the other, summing over the entire domain can yield a trivial result for a nontrivial magnetic topology.

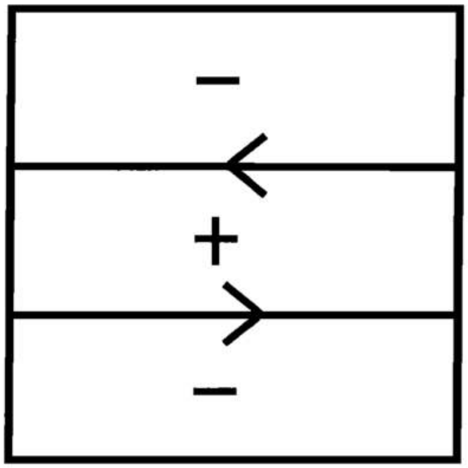

Figure 2.4: A periodic mean field configuration, where two periodic lines divide the poloidal plane into two pieces. [46]

Mapping the periodic poloidal plane to a topologically equivalent torus, Figure 2.5, demonstrates the out-of-plane component of the magnetic field in Figure 2.4 is equivalent to the magnetic field produced by a ring of magnetic monopole charges. [45] Magnetic vector potential, and therefore, classical magnetic helicity are only definite in divergence-free magnetic fields, i.e. in the absence of magnetic monopoles.

A helicity-like measure $\mathcal{H}$ can be defined for doubly periodic domains when the bounding box is a magnetic field line, Equation 2.12. [46] The periodic $\mathcal{H}$ does not in general reduce to the relative helicity H_R form in Equation 2.13: $\mathcal{H}$ and H_R are only equal when the flux on the bounding surface $\psi_B = (\psi_{\text{max}} - \psi_{\text{min}})/2$. [47] While $\mathcal{H}$ does not represent a true helicity and may differ in both sign and value from the relative helicity (if defined), it is an ideal invariant, and therefore, must be related to the topology of the field. The helicity-like measure $\mathcal{H}$ can detect changes in the polarization or mirror

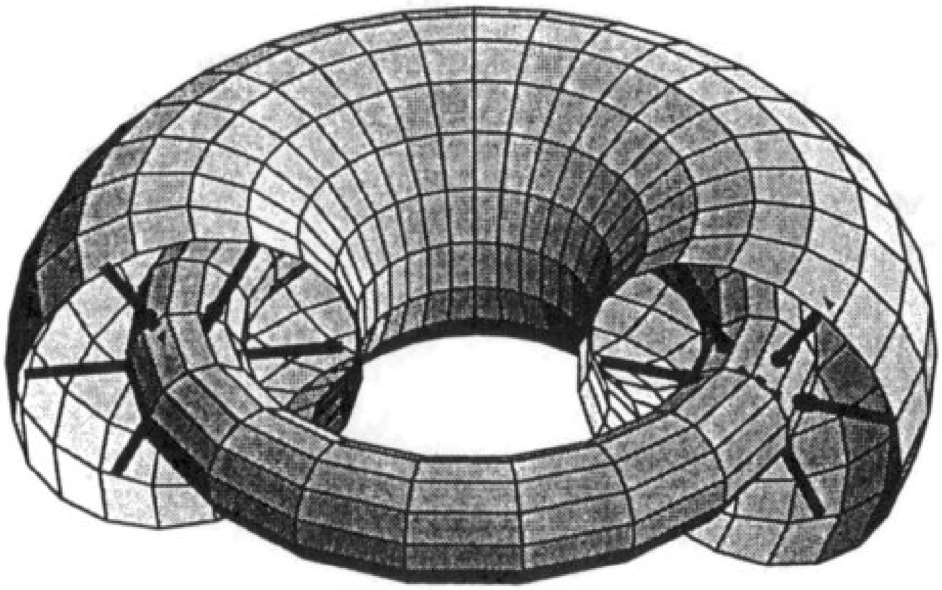

Figure 2.5: The topology of a periodic mean-field configuration is topologically equivalent to a torus with mean field lines pointing in the radial direction either toward or away from the axis of the torus. [45].

symmetry of the field.

$$\mathcal{H} = B_0 \int_V \left(2\psi - \psi_{\text{max}} - \psi_{\text{min}}\right) dV \tag{2.12}$$

$$H_R = 2B_0 \int_V \left(\psi - \psi_B\right) dV \tag{2.13}$$

Unlike confined or infinite geometries, magnetic flux tubes in doubly periodic domains–at least those of comparable size to the periodic lengths of the system–can convert right- or left-handed flux tube into its opposite. [45] This conversion is demonstrated by a flux tube reconnecting with itself in Figure 2.6. Note that while classical helicity is undefined in Figures 2.6 (c-e), both the starting (a & b) and ending (f) points have defined and oppositely signed magnetic helicities.

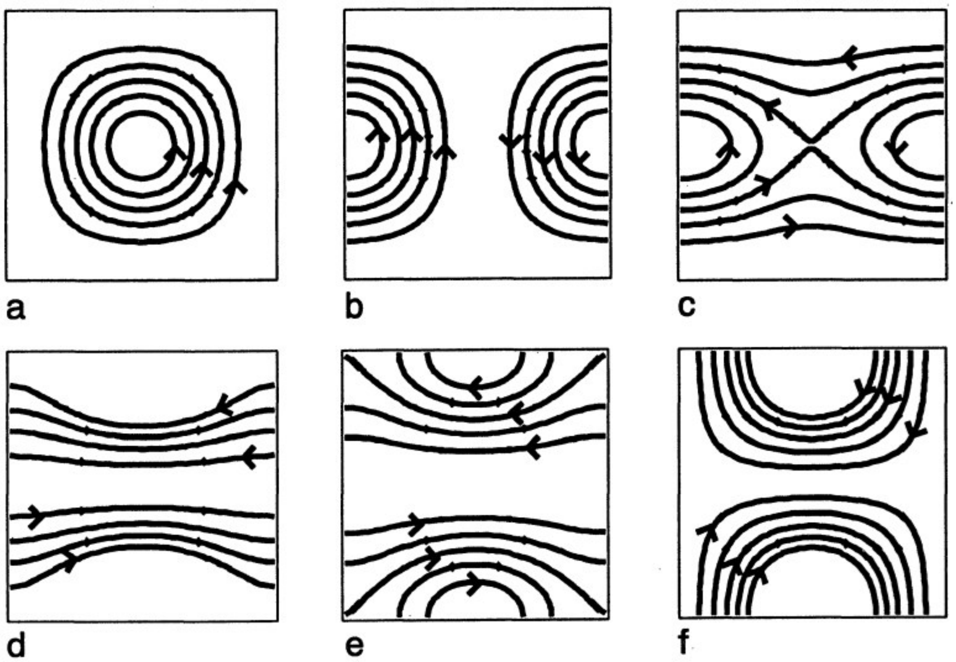

Figure 2.6: A sequence of reconnections which reverses the twist of a flux tube. [45]

Chapter 3

Flux Rope Reconnection

A flux rope is a topologically cylindrical region of space mapped out by a bundle of magnetic field lines that twist around a central magnetic axis. Surrounding the magnetic axis is a set of concentric surfaces defined by $\mathbf{B}\cdot\hat{n} = 0$, where $\hat{n}$ is the unit normal vector on a given surface. The outermost of these bounding surface typically determines the radial extent of the flux rope. Flux ropes also typically have a separation of scales, such that the axial length is much larger than the radial extent. Though the cross-sectional area, shape, and magnetic field of a flux rope may vary along its length, the magnetic flux Φ is constant through any surface normal to the magnetic axis.

$$\Phi = \int_S \mathbf{B} \cdot d\mathbf{S} \tag{3.1}$$

Flux ropes are often classified by the direction of magnetic field-line twist, as indicated by the sign of the field-line twist parameter τ for a given magnetic field configuration, where ϕ is the azimuthal angle, z is the axial coordinate, and $\langle\ \rangle$ indicates averaging over a field-line trajectory.

$$\tau \equiv \langle \frac{d\phi}{dz} \rangle \tag{3.2}$$

Flux ropes with $\tau > 0$ have a right-handed field-line twist relative to the direction of the axial magnetic field and are therefore called right-handed flux ropes. The axial current density J_z in a right-handed flux rope is parallel to the axial magnetic field B_z near the magnetic axis. Similarly, flux ropes with $\tau < 0$ are called left-handed flux ropes and have axial current density that is anti-parallel to the axial magnetic field near the magnetic axis. Magnetic flux ropes can possess either zero or non-zero net axial current I_z. Except for flux ropes sustained by external transform, non-zero axial current density J_z is required to produce field-line twist. While a flux rope with zero net axial current has reversed axial current density in its outer region, the field-line twist doesn't necessarily change sign in this region.

Magnetic flux ropes also have a defined magnetic helicity, a measure of the degree to which magnetic field lines wrap around themselves. The classical formulation of magnetic helicity is given in Equation 3.3, where $\mathbf{A}$ is the vector potential that satisfies $\mathbf{B} = \nabla \times \mathbf{A}$.

$$H = \int_V \mathbf{A} \cdot \mathbf{B} \, dV \tag{3.3}$$

As described in Chapter 2, classical helicity is not well-defined and gauge-invariant for all possible magnetic configurations, including open magnetic field configurations in particular. Therefore, relative magnetic helicity is often used as the metric of the helicity content of the system. As with the field-line twist parameter, right- and left-handed flux ropes possess positive and negative magnetic helicity content, respectively.

Interactions between multiple flux ropes are often characterized as co- or counter-helicity, corresponding to the relative sign of magnetic helicity between the interacting flux ropes. This classification is independent of the relative magnitude of the helicity content between flux ropes. For co-helicity interactions between two flux ropes, both flux ropes either have positive helicity content or both flux ropes have negative helicity content. For counter-helicity interactions between two flux ropes, one flux rope has positive helicity content, while the other has negative helicity content.

3.1 One-dimensional Flux Rope Models

In this section, a number of straight cylindrical flux rope models are presented that have a one-dimensional dependence on radius r. The magnetic field of these flux ropes has the general form

$$\mathbf{B}\left(\mathbf{r}\right) = B_{\phi}\left(r\right)\hat{\phi} + B_{z}\left(r\right)\hat{z} \tag{3.4}$$

For cylindrically symmetric flux ropes, the field-line twist parameter has the form

$$\tau = \frac{B_{\phi}}{rB_{z}} \tag{3.5}$$

In order to satisfy $\nabla\cdot\mathbf{B} = 0$, the radial component of the magnetic field must necessarily be zero. This magnetic field configuration is open as axial magnetic field penetrates any closed surface that surrounds a finite volume. By defining a reference magnetic field $\mathbf{B}_{ref}$ such that the helicity content of that field is zero, a relative magnetic helicity parameter is constructed using the Finn-Antonsen relation below. [41]

$$H_{R} = \int_{V}\left(\mathbf{A} + \mathbf{A}_{ref}\right)\cdot\left(\mathbf{B} - \mathbf{B}_{ref}\right)\, dV \tag{3.6}$$

By choosing the reference magnetic field $\mathbf{B}_{ref}\left(r\right) = B_{z}\left(r\right)\hat{z}$ with a corresponding reference vector potential $\mathbf{A}_{ref}\left(r\right) = A_{\phi}\left(r\right)\hat{\phi}$ that satisfies $\mathbf{B}_{ref} = \nabla\times\mathbf{A}_{ref}$ and satisfies $\mathbf{A}\times\hat{n} = \mathbf{A}_{ref}\times\hat{n}$ on the domain boundary, the expression for relative magnetic helicity per unit length reduces to the form

$$\frac{H_R}{L} = 4\pi \int_0^a A_\phi B_\phi r \, dr \tag{3.7}$$

The expression for magnetic energy per unit length has the form

$$\frac{E_M}{L} = \frac{\pi}{\mu_0} \int_0^a \left[B_\phi^2 + B_z^2\right] r \, dr \tag{3.8}$$

Parameters for three flux rope models are presented in Table 3.1. The first model presented is the linear force-free configuration, which satisfies the the force-free condition in Equation 3.9 with a uniform α. Taking the curl of Equation 3.9 and applying the condition $\nabla \cdot \mathbf{B} = 0$ results in the Helmholtz equation in Equation 3.10.

$$\mu_0 \mathbf{J} = \nabla \times \mathbf{B} = \alpha \mathbf{B} \tag{3.9}$$

$$\left(\nabla^2 + \alpha^2\right) \mathbf{B} = 0 \tag{3.10}$$

The force-free condition can be satisfied by the constant-α Chandrasekhar-Kendall modes in Reference [48]. However, in general, these solutions have variation in the azimuthal and axial directions. The special case solution in Equation 3.11 satisfies the force-free condition and has a one-dimensional dependence on radius.

$$\mathbf{B} = B_0 J_1 \left(\alpha r\right) \hat{\phi} + B_0 J_0 \left(\alpha r\right) \hat{z} \tag{3.11}$$

The second model presented is the Gold-Hoyle flux rope, which is a nonlinear force free configuration with a constant twist parameter τ_0. [49] The final model presented has a constant current density $\mathbf{J} = J_\phi \hat{\phi} + J_z \hat{z}$. [50] The constant current density model is not a force-free configuration. Although the constant current density profile is used as an analytical flux rope model, it fails to satisfy mathematical regularity as B_ϕ is non-zero as r approaches zero.

3.2 Magnetic Reconnection

Magnetic reconnection is a physical process by which the magnetic topology is rearranged in a highly conducting plasma. It is often conceptualized as the breaking of magnetic field-lines in the reconnection layer and rejoining them with a different connectivity. The process efficiently converts magnetic field energy into into kinetic energy, thermal energy, and particle acceleration. Magnetic reconnection occurs on an intermediate timescale between the magnetic diffusion (or resistive) timescale $\tau_R \equiv \mu_0 L^2/\eta$ and the Alfvén wave transit time $\tau_A \equiv L/v_A$, where η is the plasma resistivity, L is the characteristic length scale of the reconnection layer, and $v_A \equiv B/\sqrt{\mu_0 \rho}$ is the Alfvén speed. Magnetic reconnection is loosely defined as any process that is not globally diffusive and that drives a parallel electric field at a location that has an X-type topology in the magnetic field in a plane normal to that field-line, i.e. at a location with a local maximum in the magnetic shear. [51] This section includes select models of magnetic reconnection, focusing primarily on resistive and two-fluid reconnection models.

Sweet-Parker reconnection is the two-dimension, steady state reconnection of an incompressible, inviscid, resistive plasma. [52, 53] As shown in Figure 3.1, the reconnecting magnetic field B_{in} is anti-parallel about that reconnection layer. Resistivity is assumed to only affect plasma evolution within the shaded reconnection layer. Outside the reconnection layer, the plasma is assumed to be perfectly conducting. The derivation procedure for the reconnection rate in Reference [52] is repeated here.

From Ampere's law, the steady-state current density in the reconnection layer is $J_y \sim$

Table 3.1: One-dimensional flux rope models

Parameter	Linear force-free	Gold-Hoyle	Constant current
τ	$\dfrac{J_1(\alpha r)}{r J_0(\alpha r)}$	τ_0	$\dfrac{\tau_0}{1 - r/a}$
$\mathbf{A}$	$\alpha^{-1}\mathbf{B}$	$\dfrac{B_0}{2\tau_0^2 r} \ln\left(1 + \tau_0^2 r^2\right) \left(\hat{\phi} - \tau_0 r \hat{z}\right)$	$B_0 (r/a)(a/2 - r/3)\,\hat{\phi}$ $-B_0 \tau_0 (r^2/2)\,\hat{z}$
$\mathbf{B}/B_0$	$J_1(\alpha r)\,\hat{\phi} + J_0(\alpha r)\,\hat{z}$	$\dfrac{\tau_0 r \hat{\phi} + \hat{z}}{1 + \tau_0^2 r^2}$	$\tau_0 r \hat{\phi} + (1 - r/a)\,\hat{z}$
$\mathbf{J}$	$\alpha\mathbf{B}$	$\dfrac{2\tau_0}{1 + \tau_0^2 r^2}\mathbf{B}$	$J_\phi \hat{\phi} + J_z \hat{z}$
H_R/L	$\dfrac{4\pi B_0^2}{\alpha} \displaystyle\int_0^a J_1^2(\alpha r)\, r\, dr$	$\dfrac{\pi B_0^2}{2\tau_0^3} \ln^2\left(1 + \tau_0^2 a^2\right)$	$\dfrac{7\pi}{30} B_0^2 a^4 \tau_0$
E_M/L	$\dfrac{\pi B_0^2}{\mu_0} \displaystyle\int_0^a \left[J_0^2(\alpha r) + J_1^2(\alpha r)\right] r\, dr$	$\dfrac{\pi B_0^2}{2\tau_0^2 \mu_0} \ln\left(1 + \tau_0^2 a^2\right)$	$\dfrac{\pi B_0^2 a^2}{4\mu_0}\left(1 + \tau_0^2 a^2\right)$
$\dfrac{dp}{dr}$	0	0	$\dfrac{B_0^2}{\mu_0 a}\left[1 - \dfrac{r}{a}\left(1 + 2\tau_0^2 a^2\right)\right]$

The flux ropes are defined for $0 \leq r < a$. The magnetic vector potential and current density are defined as linear functions of the magnetic field where possible. B_0 and τ_0 are, respectively, the axial magnetic field and the field-line twist parameter at $r = 0$. For the constant current model, $B_0 = \mu_0 J_\phi a$ and $\tau_0 = J_z / (2 J_\phi a)$.

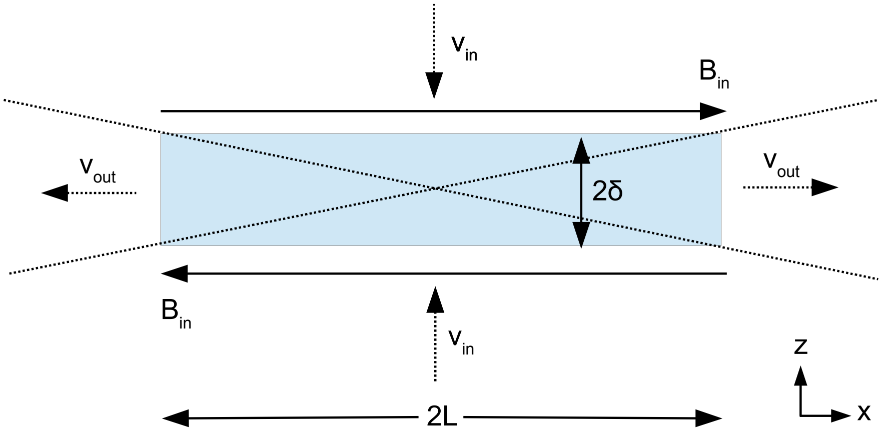

Figure 3.1: A Sweet-Parker reconnection layer of length $2L$ and thickness 2δ

$B_{in}/\mu_0\delta$, where B_{in} is the reconnecting field and δ is the reconnection layer half-thickness. From the ideal MHD Ohm's law ($\mathbf{E} + \mathbf{v} \times \mathbf{B} = 0$), the out-of-plane electric field E_y just outside the reconnection region is $E_y = v_{in}B_{in}$, where v_{in} is the inflow speed. Matching the out-of-plane electric field in the ideal outer region to that in the reconnection layer ($E_y = \eta J_y$) yields the inflow speed $v_{in} \sim \eta/\mu_0\delta$. Steady-state conditions and mass conservation yields a relation between inflow and outflow speeds, $v_{in}L = v_{out}\delta$, where v_{out} is the outflow speed and L is the reconnection layer half-length. Equating the magnetic energy flux into the reconnection layer with the kinetic energy flux out of the layer in Equation 3.12 yields the outflow rate $v_{out} \sim v_A$.

$$v_{in}L\left(\frac{B_{in}^2}{2\mu_0}\right) \sim v_{out}\delta\left(\frac{\rho v_{out}^2}{2}\right) \tag{3.12}$$

Thus, the dimensionless reconnection rate is $v_{in}/v_{out} \sim S^{-1/2}$, where $S \equiv \mu_0 L v_A/\eta$ is the Lundquist number.

The Sweet-Parker model predicts a reconnection rate much slower than that observed in many laboratory and astrophysical plasmas, e.g. reconnection in Earth's magnetotail.

[54] Hence, reconnection occurring at the rate predicted by the Sweet-Parker model is referred to as slow reconnection. Theoretical models that predict an enhanced reconnection rate relative to the Sweet-Parker model, "fast reconnection" models, have been the focus of much research. One of the earliest models attempting to resolve the discrepancy in the observed and predicted reconnection rates is the Petschek model, which introduces stationary slow mode shocks near the X-point. [55] While the Petschek model produces a much faster reconnection rate than the Sweet-Parker model, Petschek did not propose a mechanism for the origin of these shocks. In two-dimensional computational studies with resistivity enhanced around the central X-point of the current layer, shocks emerge at the point where resistivity is varying most rapidly. [56–58] With uniform plasma resistivity, shocks either do not appear at all [59], or when imposed [60], dissipate rapidly until the reconnection rate equilibrates with the value predicted by the Sweet-Parker model.

In many applications, the current layer thickness is smaller the the ion inertial length c/ω_{pi}. [54] The MHD model is not applicable as the electron and ion fluids decouple and behave as two separate fluids. In the two-fluid regime, whistler-wave physics allows the electron flow to deviate from the ion flow at small spatial scales. [61] Similarly, a combination of whistler and kinetic Alfvén waves drives reconnection in the two-fluid regime at large plasma-β. [62, 63]

Other fast reconnection models seek to enhance resistivity through plasma micro-instabilities and turbulence that occur when the relative electron flow velocity through the ions exceeds the sound velocity. [54] The limit on the relative drift speed of the electrons implies a lower limit to the current density, and therefore, an upper limit (of the ion skin depth) on the current layer thickness. A computational study predicts that when the current layer thickness is smaller than the ion inertial length the Hall effect still dominates even with localized enhancement of the resistivity through electron scattering and ion acoustic turbulence. [64] An enhanced resistivity with a strong dependence on the current density provides conditions favorable for the emergence of Petschek shocks. [65] Reference [54] provides a review of experimental observations of magnetic reconnection in many laboratory and astrophysical plasmas.

Magnetic reconnection can be verified using field-line trajectories. During reconnection in a two-dimensional system, the separatrix divides the domain into topologically distinct regions, such that the mapping of magnetic field-line trajectories is discontinuous across the separatrix curve. [66] When generalized to a three dimensional system, the separatrix forms a surface that also divides the domain into a number of topologically distinct regions defined by magnetic field-line connectivity: All field-lines originating within one source region, and only those field-lines, will all terminate within the same corresponding sink region. However, unlike two-dimensional reconnection, the mapping is generally continuous across the surface. Regions where reconnection occurs in three-dimensional and open field-line systems are identified by locating a quasi-separatrix layer (QSL), which is defined as a region of unusually large mapping distortion as quantified by the squashing degree Q. [66,67] For example, Reference [68] identifies QSLs in extensive probe data from LaPD to confirm and locate reconnection among flux ropes. The squashing degree Q is a measure of the gradients of the field-line mapping from the launch ($\mathbf{r}_0$) to the terminating ($\mathbf{r}_1$) positions, where J is the Jacobian matrix of the mapping $\mathbf{r}_0 \mapsto \mathbf{r}_1$.

$$Q = (\det J)^{-1} \sum_{ij} J_{ij}^2 \tag{3.13}$$

Conservation of magnetic flux along a field-line element connecting entry surface S_0

and exit surface S_1 implies that $B_1 dS_1 = B_0 dS_0$, where B_0 and B_1 are the magnetic field components normal to the entry and exit surfaces, respectively. As the surface element dS_0 in S_0 transforms to a surface element $dS_1 = \det J \; dS_0$ in S_1, $\det J = B_0/B_1$. In Section 6.2, Q is computed from Pegasus simulation results to assess the relevance of quasi-separatrix layers with respect to current-ring formation.

3.3 Flux rope Interactions

Generalizing to three dimensional systems, the magnetic field configuration between colliding flux ropes in Pegasus often produces conditions conductive for reconnection. To relate the Pegasus application with the referenced computational results, [69, 70] this section considers pairs of Gold-Hoyle flux ropes with a contact angle ϕ between the vertical reference flux rope and the rotated flux rope, as indicated in Figure 3.2. The flux ropes possess identical magnetic field strength, such that only the direction of the field line twist and not its magnitude differs between right- and left-handed flux ropes. These flux ropes do not contain net current, unlike the flux ropes in Pegasus.

With two types of flux-ropes (right-handed and left-handed), there are nominally four possible flux-rope pairs for each contact angle ϕ. A left-right pair (with the left-hand rope at the reference position) is equivalent to a right-left pair (with the right-hand rope at the reference position) through a coordinate rotation: rotating a left-right pair π about the z-axis and ϕ about the x-axis produces a right-left pair with the same contact angle ϕ as the original left-right pair. In an inertial frame as is assumed here, coordinate rotation has no effect on the interaction physics. The magnetic field of a left-left pair with a contact angle ϕ is mirror symmetric (about $x = 0$ in Figure 3.2) to the magnetic field of a right-right pair with a contact angle $-\phi$. The currents for a mirror-symmetric

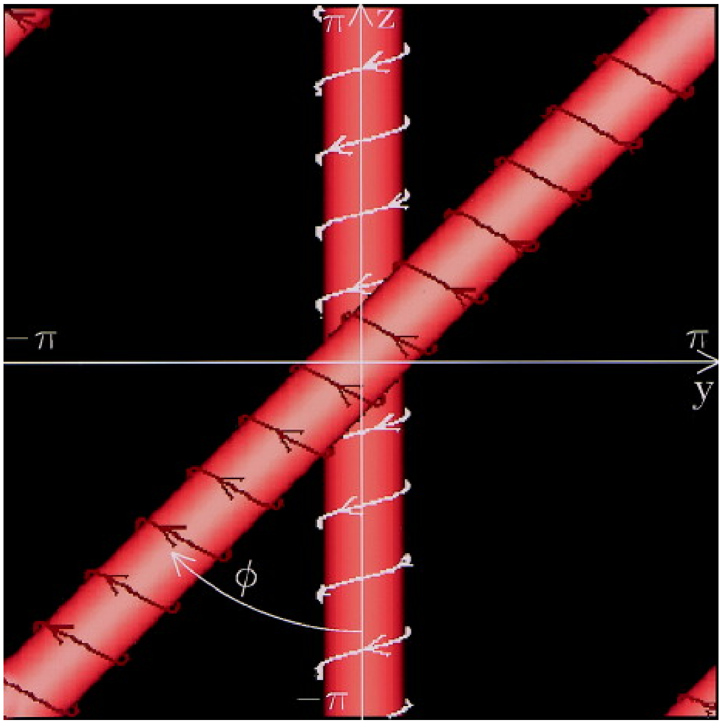

Figure 3.2: Contact angle between two identical interacting flux ropes. A pair of right-handed flux ropes are shown with a contact angle $\phi = \pi/4$ in a periodic cube of edge length 2π. [69]

magnetic field configuration are not mirror symmetric, but the resulting forces during flux-rope interaction are mirror symmetric. Therefore, the co-helicity right-right and counter-helicity right-left flux-rope pairs can capture the interaction dynamics of all four possible flux-rope pairs.

The vertical flux rope in the reference position is denoted by the subscript '1' and is always a right-handed flux rope. The rotated flux rope is denoted by the subscript '2' and may be either a right- or left-handed flux rope. The magnetic field for each flux rope is given below, where $s \equiv \mathrm{sgn}\tau = 1$ for a right-handed flux rope and $s = -1$ for a left-handed flux rope.

$$\mathbf{B}_1\left(r_1\right) = -\hat{z}B_z\left(r_1\right) - \hat{y}\tau r_1 B_z\left(r_1\right) \tag{3.14}$$

$$\mathbf{B}_2\left(r_2\right) = -B_z\left(r_2\right)\ \left(\hat{z}\cos\phi + \hat{y}\sin\phi\right)\ + s\tau r_2 B_z\left(r_2\right)\ \left(-\hat{z}\sin\phi + \hat{y}\cos\phi\right) \tag{3.15}$$

The angle θ at which the magnetic field-lines meet at the contact site $r \equiv r_1 = r_2$ is given below for a generic magnetic field configuration.

$$\cos\theta = \frac{\mathbf{B}_1\left(r\right)\cdot\mathbf{B}_2\left(r\right)}{|\mathbf{B}_1\left(r\right)||\mathbf{B}_2\left(r\right)|} \tag{3.16}$$

For a right-left flux-rope interaction, the magnetic field-lines meet at the contact site at the same angle as the colliding flux ropes themselves, i.e. $\theta = \phi$. For a right-right flux-rope interaction, the field-line contact angle is given by the expression below.

$$\cos\theta = \frac{\left(1 - \tau^2 r^2\right)\cos\phi + 2\tau r\sin\phi}{1 + \tau^2 r^2} \tag{3.17}$$

Except for the case where the the magnetic fields are perfectly aligned ($\theta = 0$), there exists some plane where the in-plane component of the magnetic field forms an X-type topology between two colliding flux ropes. However, depending on the contact angle ϕ, the magnetic field in that plane may be very weak compared to the total magnetic field strength, and therefore, the capacity for magnetic reconnection may be limited. The plane occurs at the angle $\alpha + \left(\pi + \theta\right)/2$ with the magnetic axis of the vertical flux rope, where $\alpha = \tan^{-1}\left[\tau r\right]$ is the angle that the magnetic field lines of the vertical flux rope forms with its magnetic axis at the contact site.

There are four fundamental types of flux rope interactions: merging, bouncing, tunneling, and slingshot. As reconnection progresses between a pair of flux ropes, the distance between the flux ropes decreases and magnetic field lines at smaller radii come into contact. The interaction type first depends on the contact angle θ of the magnetic field lines at the edge of the colliding flux ropes. Assuming that significant reconnection occurs at initial edge, the radial profile of the contact angle θ–particularly the angle ϕ

between the magnetic axes of the colliding flux ropes–determines the interaction type.

For a co-helicity flux-rope pair, the magnetic field-line contact angle θ, and therefore, the capacity for the magnetic reconnection is a function of radius. As a consequence, all four interaction types are possible for co-helicity flux-rope pairs, depending on the parameter regime. Deformation of the flux ropes from one interaction can change the contact angle θ of the magnetic field and allows multiple interactions to occur for a single co-helicity flux-rope configuration. For example, flux ropes can first bounce and then merge, [69] tunnel and then merge, or slingshot then tunnel then merge. [70] For a counter-helicity flux-rope pair, the magnetic field-line contact angle θ is independent of radius, such that the field-lines at the magnetic axes have the same capacity for magnetic reconnection as the magnetic field-lines at the initial edge of the colliding flux ropes. Therefore, only two interaction types are possible: bouncing when the flux ropes can only weakly reconnect and slingshot when they can strongly reconnect.

During a merger interaction, two separate flux ropes combine starting at the contact site. Reconnection proceeds along the length of the flux ropes forming a single flux rope, as visualized in Figure 3.3. Merger occurs when magnetic field are nearly anti-parallel in the outer shells of the colliding flux ropes, such that the magnetic field lines strongly reconnect at the edge of the flux ropes, but the field lines in the core are nearly parallel, and therefore, amenable to merger. Merger is only predicted for co-helicity flux rope interactions.

During a bounce interaction, two flux ropes come into contact at the reconnection site, but rather than merging, the flux ropes deflect away from each other, as visualized in Figure 3.4. Bouncing occurs when the magnetic field lines are nearly parallel in the outer shells of the colliding flux ropes. The magnetic field lines can, at best, only weakly reconnect and pile up in the interaction region, impeding further reconnection.

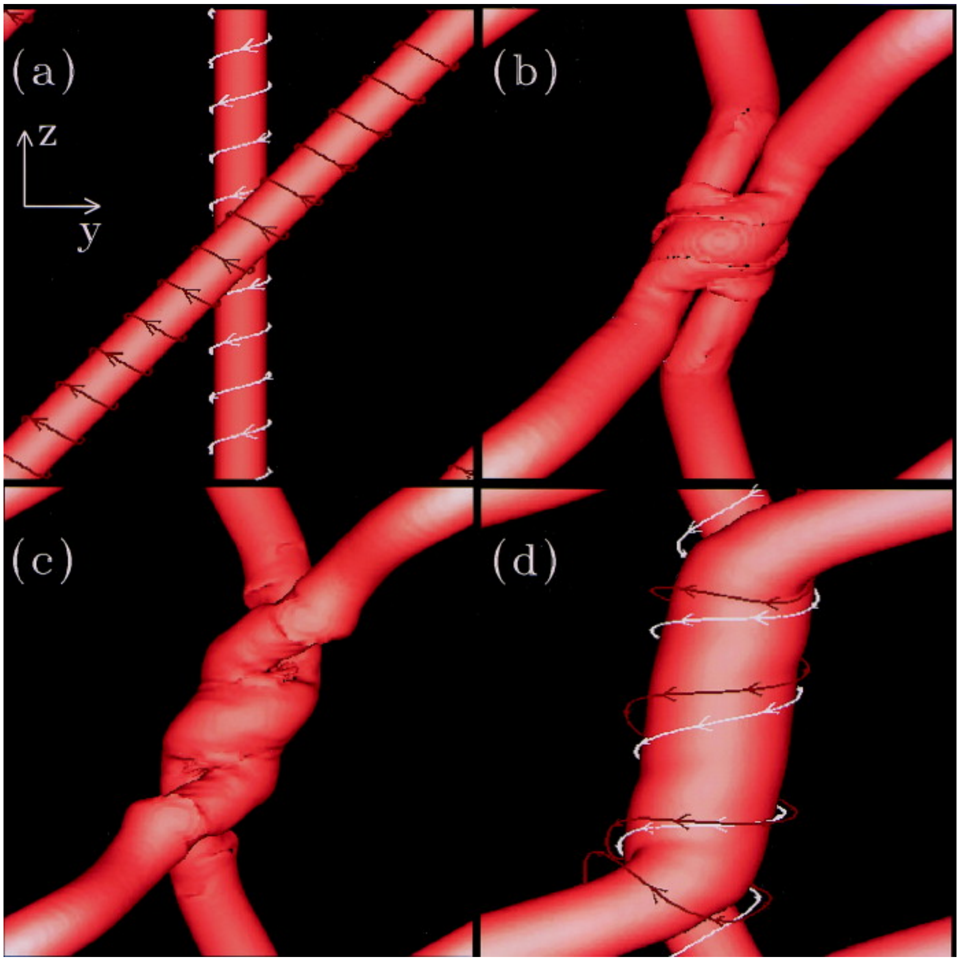

Figure 3.3: A merger interaction between a right-right flux rope pair with a contact angle $\phi = \pi/4$. Isosurfaces of $B_{max}/3$ and magnetic field lines are shown at (a-d) $tv_A/a = 0,\ 34,\ 51,\ \&\ 163$. [69]

As reconnection does not proceed past the outer shells of the flux ropes, the angle ϕ between the magnetic axes is irrelevant: bouncing occurs in a nearly identical manner for both anti-parallel right-right ($\phi = \pi$) pairs and parallel ($\phi = 0$) right-left pairs.

Bouncing also occurs between two flux ropes that would otherwise merge when the approach speed is outside some range critical for merger, i.e. the approach speed is either too low or too high. [71, 72] If the approach speed is too slow, the system is not driven hard enough for significant reconnection to occur. If the approach speed is too fast, magnetic flux builds up in the interaction region faster than it can can reconnect, slowing down the approach speed until the accumulated magnetic pressure causes them to move apart. The computations discussed in this section have an approach speed of $0.025v_A$. [69, 70]

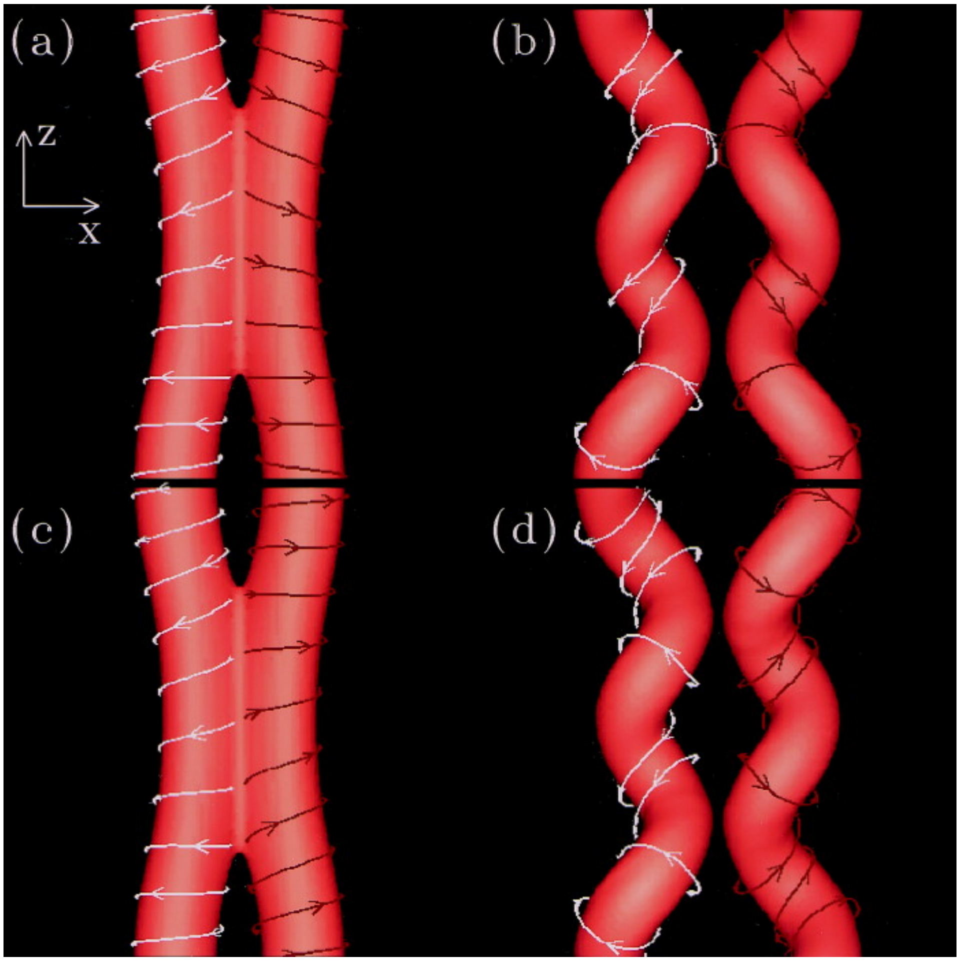

Figure 3.4: A bounce interaction between a right-left flux rope pair with a contact angle $\phi = 0$ at (a,b) $tv_A/a = 17,\ \&56$, and a bounce interaction between a right-right flux rope pair with a contact angle $\phi = \pi$ at (c,d) $tv_A/a = 17,\ 56$. Isosurfaces of $B_{max}/3$ and magnetic field lines are shown. [69]

During a slingshot interaction, reconnection occurring at the contact site changes the connectivity of the entire flux ropes, as visualized in Figure 3.5, much as reconnection does to pairs of magnetic field-lines. As θ is independent of contact radius for a counter-helicity flux-rope pair, any configuration that results in significant reconnection at the edge will inevitably result in significant annihilation of magnetic flux in the core of the flux ropes as well. This annihilation of magnetic flux facilitates the slingshot reaction. The slingshot interaction also occurs for co-helicity flux-rope interactions, but as discussed later, over a much more limited parameter regime.

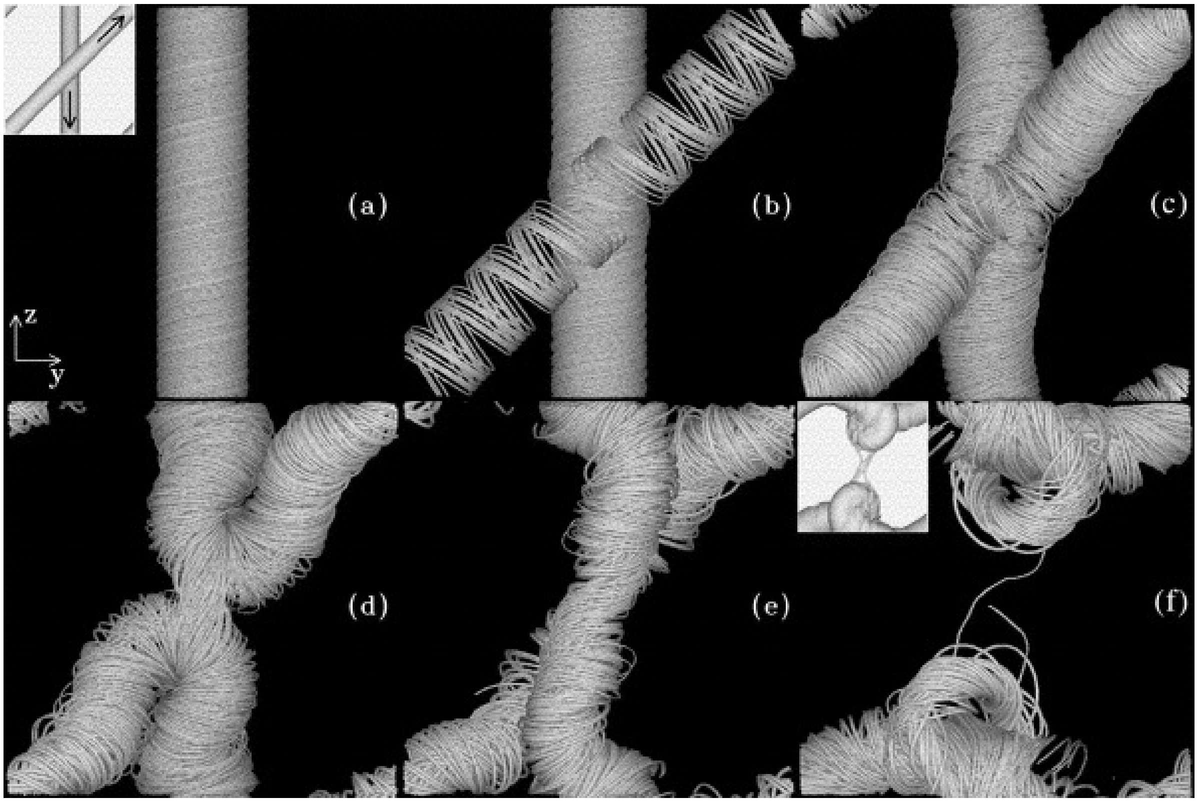

Figure 3.5: A slingshot interaction between a right-right flux rope pair with a contact angle $\phi = 3\pi/4$ and $2\pi\tau_0 L/2\pi = 7$. Magnetic field line trajectories are shown at (a-f) $tv_a/a = 0,\ 7,\ 32,\ 81,\ 125,\ \&\ 248$. [70]

During a tunneling interaction, the magnetic field-lines undergo two reconnections each allowing the flux ropes to pass through each other, as visualized in Figure 3.6. Tunnel is predicted to only occur during co-helicity flux rope interactions.

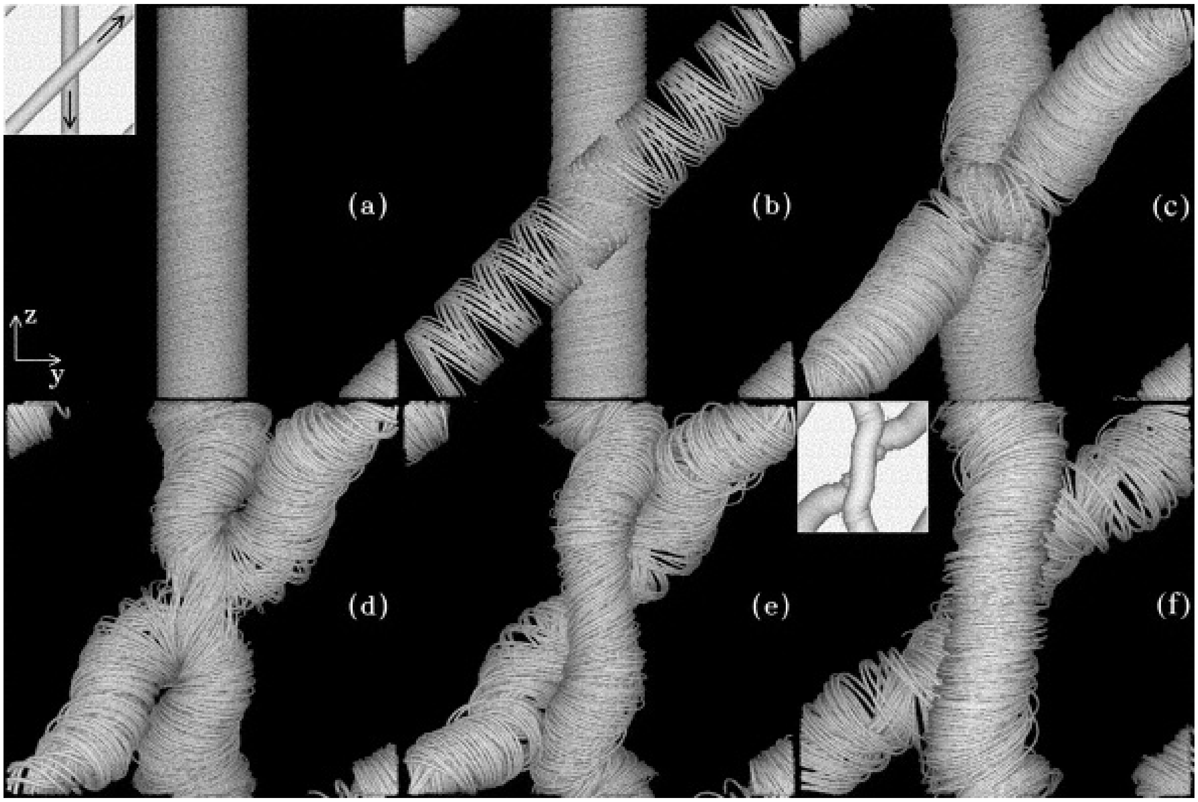

Figure 3.6: A tunneling interaction between a right-right flux rope pair with a contact angle $\phi = 3\pi/4$ and $\tau_0 L/2\pi = 7.5$. Magnetic field line trajectories are shown at (a-f) $tv_a/a = 0,\ 7,\ 32,\ 79,\ 106,\ \&\ 261$. [69]

As previously stated, the interaction type for co-helicity flux-rope interactions depends on the radial profile of the contact angle θ between magnetic field lines. This contact angle is a function the field-line twist parameter τ, and indeed, multiple interaction types are observed for otherwise identical flux rope configurations with different values of τ. With a contact angle $\phi = \pi/4$ between a right-right pair, a slingshot interaction occurs when $\tau_0 L/pi = 7$, shown Figure 3.5, where $\tau_0 L/2\pi$ is the number of times a field line winds about the flux rope axis over an axial distance L and L is the edge length of the periodic cubic domain. A tunneling interaction occurs for the same configuration when $\tau_0 \pi/L = 7.5$, shown in Figure 3.6. [70]

As indicated in Reference [70], the interaction type can change with resistivity. The computations in Reference [69] are globally more resistive but locally less so in the interaction region with a uniform $S = 2880$ than the computations in Reference [70], which have spatially varying resistive diffusion with $S = 57,600$ globally and $S = 567$ in the interaction region. For a right-right interaction with $\phi = 3\pi/4$, bouncing is observed with the uniform resistivity in Reference [69], but tunneling is observed with the resistive profile in Reference [70].

Chapter 4

Plasma Relaxation

Relaxation is the process by which a plasma undergoes rapid changes in magnetic topology in order to reach a more stable equilibrium configuration. One of the most well-known theories of relaxation–proposed by J.B. Taylor–postulates that the total magnetic energy of system is minimized subject to the constraint that the total magnetic helicity of the system is conserved. The magnetic energy and helicity of equilibria decay on the resistive timescale $\tau_R = L^2\mu_0/\eta$, where L is some characteristic length scale of the system. Relaxation occurs on a relatively fast timescale, often many times faster than the resistive timescale. Taylor's theory, which is described in greater detail in Section 4.1, produces a final force-free plasma state, i.e. $\mathbf{J} \times \mathbf{B} = \mathbf{0}$, as a result of minimization of magnetic energy. Theories of MHD relaxation generally produce a final equilibrium state.

Early work on plasma relaxation in astrophysical plasmas by S. Chandrasekhar and L. Woltjer considers the maximum total magnetic energy for a given mean-squared current density, $\int_V |\mathbf{J}|^2 d^3x$. [73] The solutions satisfy Equation 4.1 and include–but are not exclusive to–force-free configurations with constant α. By considering the Coulomb-gauge magnetic vector potential $\mathbf{A}$ in a simply connected domain, Woltjer demonstrates that force-free configurations with a constant α produce maximum magnetic energy for a given mean-square current density. [74]

$$\nabla \times \nabla \times \mathbf{B} = \alpha^2 \mathbf{B} \tag{4.1}$$

Chandrasekhar and Woltjer postulate that a non-force-free plasma will evolve until a force-free equilibrium is reached through dissipative mechanisms. However, the existence of force-free solutions to Equation 4.1 does not indicate whether a given plasma can reach those states. As this theory does not include conservation of magnetic flux, minimization of magnetic energy yields the trivial solution.

Woltjer proposed four invariants for plasma evolution in the absence of dissipative processes: total mass, angular momentum, cross-helicity (Equation 4.2), and magnetic helicity (Equation 4.3). [75] Later work by M.D. Kruskal and R.M. Kuslrud includes the conservation of toroidal and poloidal flux between every pair of flux surfaces during the minimization of magnetic energy for an ideal toroidal plasma with closed, nested flux surfaces, resulting in a infinite number of topological constraints. [76] The total toroidal current is not necessarily conserved under these conditions, and $\mathbf{J}_\perp$ may be nonzero for non-uniform pressure profiles.

$$H_C = \int_V \mathbf{v} \cdot \mathbf{B} \, dV \tag{4.2}$$

$$H_M = \int_V \mathbf{A} \cdot \mathbf{B} \, dV \tag{4.3}$$

4.1 Taylor Relaxation

Taylor considered plasma evolution in the ZETA toroidal pinch, which was operated from 1954-1958 in the United Kingdom. An initially, violently unstable plasma evolves to a "quiescent," largely stable configuration, which is characterized by the pinch parameter ($\theta \equiv 2I/aB_0$) of the unrelaxed plasma. [77] When the pinch parameter exceeds some critical value θ_c the relaxed plasma exhibits reversal in toroidal magnetic field B_ϕ near the edge.

As described in Chapter 2, magnetic helicity can be defined for each flux tube of plasma, indicated by Equation 4.4. Similarly, the parallel current density $\lambda \equiv \mu_0 J_\parallel / B$, which describes a particular force-free plasma configuration, can be a function of field lines and satisfies $\nabla \cdot \mathbf{J} = 0$. λ in Equation 4.5 is defined for each field-line, where a, b are field-line labels.

$$K_i = \int_{V_i} \mathbf{A} \cdot \mathbf{B} d^3x \tag{4.4}$$

$$\nabla \times \mathbf{B} = \lambda(a, b)\mathbf{B} \tag{4.5}$$

When considering an ideal plasma ($E_\parallel = 0$), all topological properties of the magnetic field are invariant, referred to as the frozen-flux condition. The integrands in Equation 4.6 must vanish on each field line and magnetic surface, respectively, resulting in an infinite number of topological constraints on plasma evolution. These constraints result from the condition of no net $\mathbf{E} \cdot d\mathbf{l}$ on field-lines for an ideal plasma.

$$\oint \frac{dl}{B} \mathbf{B} \cdot \frac{\partial \mathbf{A}}{\partial t} \quad \text{and} \quad \oint \frac{dS}{|\nabla \Psi|} \mathbf{B} \cdot \frac{\partial \mathbf{A}}{\partial t} \tag{4.6}$$

For a non-ideal plasma ($E_\parallel \neq 0$), the topological properties of the magnetic field-lines are not preserved as the plasma relaxes. Therefore, only the total magnetic helicity of the system K_0 is used to characterize the system. Like Chandrasekhar and Woltjer, Taylor hypothesizes that a system relaxes to a single-valued λ_0, satisfying $\nabla \times \mathbf{B} = \lambda_0 \mathbf{B}$. The value of λ_0 for the relaxed plasma is given by the ratio K_0/Φ^2, where the quantity

K_0/Φ is proportional to the ratio of net poloidal flux to net toroidal flux (Ψ/Φ). Thus, Taylor predicts the final state is unique, depending only on K_0/Φ^2, or equivalently, θ.

Using the cylindrical approximation ($\epsilon \equiv a/R_0 \ll 1$, where a and R_0 and the minor and major radii, respectively) and assuming an axisymmetric solution, the magnetic field of the relaxed plasma has the following form: $B_\phi = B_0 J_0(\lambda_0 r)$, $B_\theta = B_0 J_1(\lambda_0 r)$. By this expression, reversal occurs when $\lambda_0 a > 2.402$ or when the pinch parameter $\theta > 1.202$. A helical relaxed plasma occurs when $\lambda_0 a > 3.11$ or when the pinch parameter $\theta > 1.6$, which corresponds to the boundary for a resistive instability of the axisymmetric, uniform-λ state. The structure of the relaxed plasma is then set by external mode helicity and is not axisymmetric.

A more general treatment is given by Taylor in his 1986 review article, including non-axisymmetric fields and the corresponding necessary boundary conditions. [78] Relaxation is considered in additional devices, including OHTE, ETA-BETA, and HBTX. Experimental results for plasma relaxation yields non-uniform λ profiles, which Taylor hypothesized was the result of incomplete relaxation. At the plasma edge, the (toroidal) inductive electric field is not aligned with the (poloidal) magnetic field, which does not allow for relaxation to a single-valued λ state.

4.2 Other Relaxation Principles

A system with symmetries that are maintained throughout all motions of the plasma possess additional invariants that characterize its evolution beyond those defined by Woltjer, Kruskal, and Kulsrud. A new class of invariants were formulated for the evolution of a single-helicity $q_s = m/n$ tearing mode, while maintaining the magnetic energy minimization principle postulated by Taylor. [79,80] Consistent with Kruskal and

Kulsrud, an infinite number of topological invariants (Equation 4.7) exist in an ideal MHD plasma, where $\omega\left(\Psi,\Phi\right)$ is an arbitrary function and V is any volume bounded by magnetic surfaces. [81, 82] With a small amount of resistive dissipation, the hierarchy of invariants in Equation 4.8 is still permitted, where $\alpha \in \mathbb{Z}^{+}$ and the helical flux function $\chi = q_s\Psi - \Phi$.

$$K\left[\omega\right] = \int_V d\tau\, \omega\left(\Psi,\Phi\right)\frac{\mathbf{A}\cdot\mathbf{B}}{2} \tag{4.7}$$

$$K_\alpha = \int_{V_0} \chi^\alpha \frac{\mathbf{A}\cdot\mathbf{B}}{2} \tag{4.8}$$

Taylor's relaxation theorem considers neither a dynamical nor thermodynamical description of the relaxation process, and therefore, cannot address the accessibility of the plasma states. A relaxation principle wherein the entropy production rate of the plasma is minimized (locally) addresses this limitation, as such a state is not only a steady state but also attracts neighboring states and brings about their relaxation as well. [83, 84] The entropy production integral is given by Equation 4.9, keeping only terms up to second order in $\delta\mathbf{B}$, where $\mathcal{E} = \left(\mathbf{v}_1 \times \mathbf{B}_1\right)_0$ is the mean dynamo emf and $\mathbf{E}_a$ is an applied electric field at $r = a$. The analysis only holds for small deviations from a steady state solution, and therefore, a multiplicity of relaxed states are allowed in principle.

$$\mathcal{J} \equiv \int d\tau\, \left[\tfrac{1}{2}\eta J^2 - \tfrac{1}{2}\mathcal{E}\cdot\mathbf{J} - \mathbf{E}_a\cdot\mathbf{J} + \tfrac{1}{2}\left(\mathcal{E}\cdot\mathbf{J}_0 - \mathcal{E}_0\cdot\mathbf{J}\right)\right] \tag{4.9}$$

A typical form of the turbulent dissipation is given in Equation 4.10, where α and β are positive constants and K^2 and L^2 are positive functions of $\mathbf{x}$ and $\mathbf{B}$. If either α or β is large, minimization of the entropy production integral produces a state such that

$|\nabla\lambda|$ or $|\nabla p|$ is small. Therefore, the limit of α, $\beta \to \infty$, such that $\nabla\lambda$, $\nabla p \to 0$ i.e. a highly dissipative system, must be a Taylor state.

$$-\int \mathcal{E} \cdot \mathbf{J}\, d\tau = \int \left(\alpha K^2 |\nabla\lambda|^2 + \beta L^2 |\nabla p|^2\right)\, d\tau \tag{4.10}$$

Numerical calculations suggest that either higher-order magnetic invariants (briefly discussed in Chapter 2) or local helicity content affect the decay rate of helical and non-helical magnetic knots. [85] Both the IUCAA knot (a quatrefoil knot) and Borromean rings decay more slowly than expected for configurations with zero net linking-number, as shown in Figure 4.1. Both configurations decay more slowly than the non-helical triple rings and faster than the helical triple rings, both of which contain non-zero net helicity content. While the total helicity content remains at or near zero in the IUCAA knot and the Borromean rings, regions of net helicity (often antisymmetric) form during decay.

4.3 Helicity Transport and Evolution

The evolution of total magnetic helicity and total magnetic energy are described by Equation 4.11 and Equation 4.12, respectively, where Φ is an applied electrostatic potential and ψ and χ are the poloidal and toroidal flux on the last closed flux surface, respectively. The first, second, and third terms on the right-hand side of Equation 4.11 are, respectively, the mechanisms for helicity dissipation, AC helicity injection, and DC helicity injection. Examples of AC helicity injection include the application of a toroidal loop voltage and the scheme used on the HIT-SI experiment. Examples of DC helicity injection include Coaxial Helicity Injection (CHI), such as that implemented on the National Spherical Torus eXperiment (NSTX), and Localized Helicity Injection

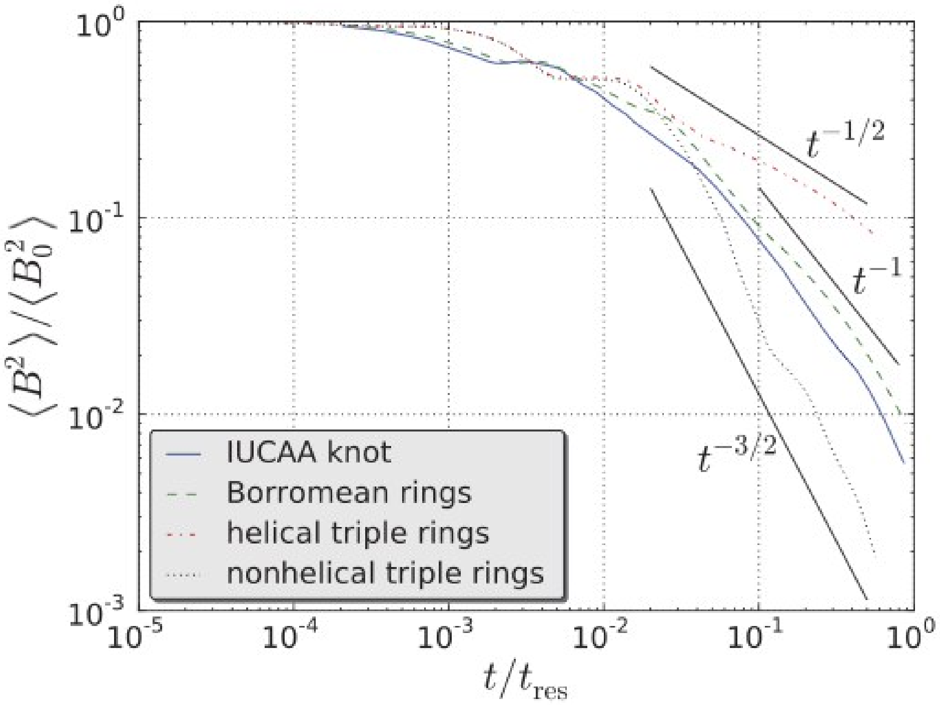

Figure 4.1: The rate of magnetic energy decay is displayed for different initial field configurations. [85] The IUCAA knot is a zero-linking-number 5-foil knot in the shape of the logo for the Inter-University Center for Astronomy and Astrophysics in Pune, India.

(LHI), which has been explored on the Current Drive Experiment (CDX), the Continuous Current Tokamak (CCT), and the Pegasus Toroidal Experiment. These helicity injection scheme were described in Chapter 1.

$$\frac{dK_0}{dt} = -2\int_V \mathbf{E}\cdot\mathbf{B}\,dV - 2\frac{\partial\psi}{\partial t}\chi + 2\int_{\partial V}\Phi\mathbf{B}\cdot d\mathbf{S} \tag{4.11}$$

$$\frac{dW_B}{dt} = -\int_V \mathbf{J}\cdot\mathbf{E} - \int_{\partial V}\frac{\mathbf{E}\times\mathbf{B}}{\mu_0}\cdot d\mathbf{S} \tag{4.12}$$

The presence of open magnetic field-lines, i.e. magnetic field-lines where $\mathbf{B}\cdot d\mathbf{S} \neq 0$ on the domain boundary, permits the transport of magnetic helicity into a plasma. [86] Some mechanism is required to transport magnetic energy and helicity from the open magnetic field lines where they are injected to a region of closed magnetic flux. Two computational studies of steady state DC helicity injection in resistive, pressure-less plasmas show relaxation through the MHD dynamo mechanism. [31, 32] In the first computational study of DC helicity injection, a hollow current profile is driven by a stead state, externally applied electrostatic potential, shown in Figure 4.2a. [31] The parallel current profile partially relaxes through the MHD dynamo effect to a state with closed poloidal flux contours and significant flux amplification.

Similarly, a later computational study of steady state CHI on NSTX shows formation and sustainment of an amplified magnetic flux region through the MHD dynamo effect. [32] For clarity the NSTX CHI system is shown again in Figure 4.2b. The injector current forms a hollow current profile as the injector flux expands into the vacuum vessel. In the computations, the peaked edge current profile drives a primary line-tied kink on the open magnetic field-line, which acts to reduce the current gradient. As such, the kink generates an anti-dynamo loop voltage on its originating flux surface, but generates a dynamo loop voltage as it penetrates into the high-q interior of the injector flux. The open field line kink with the largest saturation amplitude typically has the toroidal mode number $n = 1$. The dynamo electric field from the primarily open field-link kink mode drives parallel current, exciting secondary non-axisymmetric instabilities. These secondary modes then relax the current toward the magnetic axis. The secondary modes also have a different rotation speed from the open field-link kink.

Theoretical and computational turbulence models have been used to characterize the transfer of helicity between different length scales. Simulations of non-ideal turbulence in a cylindrical RFP have demonstrated an inverse cascade of magnetic helicity. [87, 88] The system relaxes toward a force-free state, i.e. the contribution of the dynamical pressure to the force balance is negligible, but not towards a single-valued λ Taylor

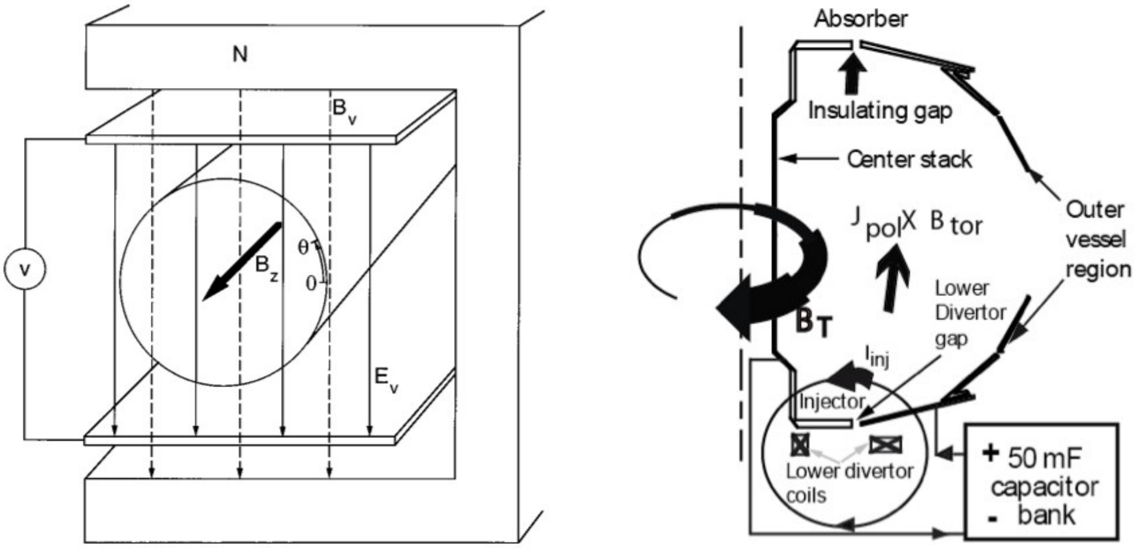

(a) A generalized DC Helicity Injection scheme for tokamaks [31]

(b) A cross-section of the CHI system on NSTX [14]

Figure 4.2: DC Helicity Injection Schemes

state. Thermal pressure is not evolved in the computations. Similarly, simulations of non-ideal, incompressible turbulence in a periodic cube have demonstrated an inverse cascade of magnetic helicity in both the presence and absence of a guide-field. [89] Helicity conservation differs slightly in that classical magnetic helicity is the conserved quantity in computations without a guide-field, while the generalized helicity content defined in Section 2.2 is the conserved quantity in computations with a guide-field. In both cases, however, helicity is non-dissipatively transferred to long wavelengths.

Closure theories indicate that for helicity-containing wavelengths, the kinetic and magnetic helicities will be brought into equipartition in a timescale on order of the Alfvén crossing time. [90–92] This is consistent with predictions and observations of significant magnetic relaxation occurring on dynamical timescales of the system. Computations of a driven dynamo also show that growing magnetic helicity fluctuations as the plasma relaxes produce a back reaction that suppresses, rather than driving, large-scale magnetic helicity growth. [92] While large-scale magnetic helicity reaches approximately half the strength of the injection-scale helicity in a dynamical timescale, the saturation values and timescale are determined by the magnetic Prandtl number and ratio of global and dissipation spatial scales.

The dissipation timescales have been computed for arbitrary power-law spectra of magnetic energy and magnetic helicity. [93] The magnetic energy M_k and magnetic helicity H_k spectra are given by Equations 4.13 & 4.14, respectively, where Ω_k is the solid angle in wave number space. The magnetic helicity spectrum is cast in terms of the magnetic energy spectrum via $f(k) \propto k^{-s}$, the assumed form of the fractional magnetic helicity as a function of k.

$$M_k \equiv \int |\tilde{\mathbf{B}}\,(\mathbf{k})|^2 k^2 \, d\Omega_k \;\propto\; k^{-q} \tag{4.13}$$

$$\begin{aligned} H_k &\equiv \tfrac{1}{2} \int \left[\tilde{\mathbf{A}}\,(\mathbf{k}) \cdot \tilde{\mathbf{B}}^*\,(\mathbf{k}) + \tilde{\mathbf{A}}^*\,(\mathbf{k}) \cdot \tilde{\mathbf{B}}\,(\mathbf{k}) \right] k^2 \, d\Omega_k \\ &= f\,(k)\, k^{-1} M_k \;\propto\; k^{-(q+s+1)} \end{aligned} \tag{4.14}$$

The magnetic energy decay timescale τ_M (assuming resistive decay) and the magnetic helicity decay timescale τ_H are then given by Equations 4.15 & 4.16, respectively. The power-law coefficients q and s for M_k and H_k are assumed to be independent of the wavenumber k for $k_L \leq k \leq k_\lambda$, where k_λ and k_L are the resistive wavenumber and the inverse of the system size, respectively.

$$\tau_M = \frac{-M}{\partial_t M} = \frac{\int_{k_L}^{k_\lambda} M_k \, dk}{2\,(\eta/\mu_0) \int_{k_L}^{k_\lambda} k^2 M_k \, dk} \tag{4.15}$$

$$\tau_H = \frac{-H}{\partial_t H} = \frac{\int_{k_L}^{k_\lambda} f\,(k)\, k^{-1} M_k \, dk}{2\,(\eta/\mu_0) \int_{k_L}^{k_\lambda} f\,(k)\, k M_k \, dk} \tag{4.16}$$

When $q \neq 1, 3$ and $q{+}s \neq 0, 2$, τ_M and τ_H reduce to the expressions in Equations 4.17 & 4.18, respectively. The regime $q > 1$ and $0 < q{+}s < 2$ corresponds to magnetic helicity decaying more slowly than magnetic energy, i.e. $R \equiv \tau_H/\tau_M < 1$, as is typically assumed for most relaxing plasmas.

$$\tau_H = \frac{(2-q-s)\left[k^{-(q+s)}\right]_{k_L}^{k_\lambda}}{2\left(\eta/\mu_0\right)(q+s)\left[k^{(2-q-s)}\right]_{k_L}^{k_\lambda}} \tag{4.17}$$

$$\tau_M = \frac{(3-q)\left[k^{1-q}\right]_{k_L}^{k_\lambda}}{2\left(\eta/\mu_0\right)(1-q)\left[k^{3-q}\right]_{k_L}^{k_\lambda}} \tag{4.18}$$

4.4 Helicity Limit

A limit for magnetic helicity is determined by considering a Taylor state plasma with an inhomogeneous magnetic field, i.e. $\mathbf{B} \cdot \hat{\mathbf{n}} \neq 0$ along the surface. [86] The requirement for a force-free equilibrium is given in Equation 4.19, where $\lambda = \mu_0 J_\parallel / B$. The vector potential $\mathbf{A}$ is decomposed into homogeneous and inhomogenous parts, Equation 4.20. The inhomogeneous part of $\mathbf{A}$, $\mathbf{A}_I$, must satisfy $\nabla \times \nabla \times \mathbf{A}_I = \mathbf{0}$ in the domain V and $\mathbf{A}_I = \mathbf{A}$ on ∂V. The solution satisfied by the eigenfunction $\mathbf{a}_\nu$ for the homogeneous part of the magnetic vector potential has the eigenvalue λ_ν for the parallel current density, shown in Equation 4.21. The relationship between total magnetic helicity K_c and the system eigenvalues is given by Equation 4.22, where I_ν is the coupling integral $I_\nu \equiv \int \mathbf{a}_\nu \cdot \nabla \times \mathbf{A}\, dV$. The equation for total magnetic helicity possesses resonances at $\lambda = \lambda_\nu$. While the boundary condition inhomogeneity imposes λ, the singularities arise from trying to relax the system to a single-value λ. The resonances being eigenvalues of the system are dependent upon the domain geometry.

$$\nabla \times \nabla \times \mathbf{A} + \lambda \nabla \times \mathbf{A} = \mathbf{0} \tag{4.19}$$

$$\mathbf{A} = \mathbf{A}_I + \sum_{\nu} \alpha_\nu \mathbf{a}_\nu \tag{4.20}$$

$$\nabla \times \nabla \times \mathbf{a}_\nu + \lambda_\nu \nabla \times \mathbf{a}_\nu = \mathbf{0} \tag{4.21}$$

$$K_c = \sum_{\nu} I_\nu^2 \frac{\lambda_\nu}{|\lambda_\nu|} \left(1 - \frac{\lambda_\nu^2}{(\lambda - \lambda_\nu)^2}\right) \tag{4.22}$$

Resonances in the total magnetic helicity K_c can act as effective barriers on the obtainable λ. This limit of λ does not preclude an increase in net current; but without crossing a resonance, net current cannot increase indefinitely without a simultaneous increase in the magnetic field. All relaxed states past the first resonance ($\lambda^2 > \lambda_1^2$) also have greater magnetic energy than those up to the first resonance ($\lambda^2 < \lambda_1^2$). Without resolving the singularities, Equation 4.22 implies that the necessary input power approaches infinite as $\lambda^2 \to \lambda_1^2$.

By allowing λ to be a function of poloidal flux ψ, the problem becomes nonlinear. This nonlinearity then allows for the regularization of the Jensen-Chu singularities, shown in Figure 4.3, which permits access to new branches of the relaxed state. [94] These states include doublets and the flipped spheromak configuration. The change to the eigenfuctions of the "Taylor state" resulting from regularization can be seen in Figure 4.5, where the original eigenfunctions are shown in Figure 4.4.

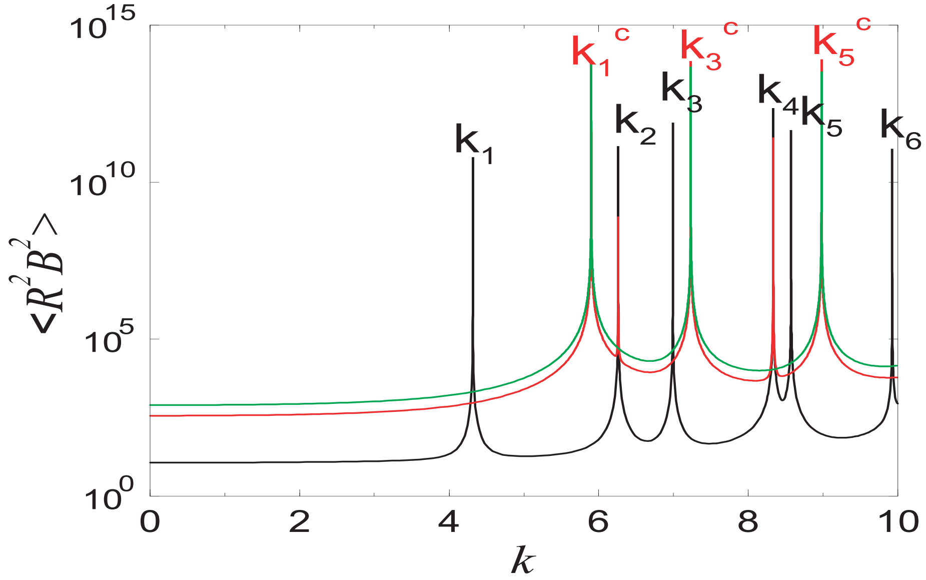

Figure 4.3: Resonances in λ. [95] The black line is for the Jensen-Chu curve, i.e. toroidal flux is not fixed. The red line is for fixed toroidal flux with the vacuum field producing normal flux through the boundary. The green line is for fixed toroidal flux without the vacuum field producing normal flux through the boundary. The torus has inner and outer radii of 0.2 and 1.2, respectively, and an elongation of 1.2.

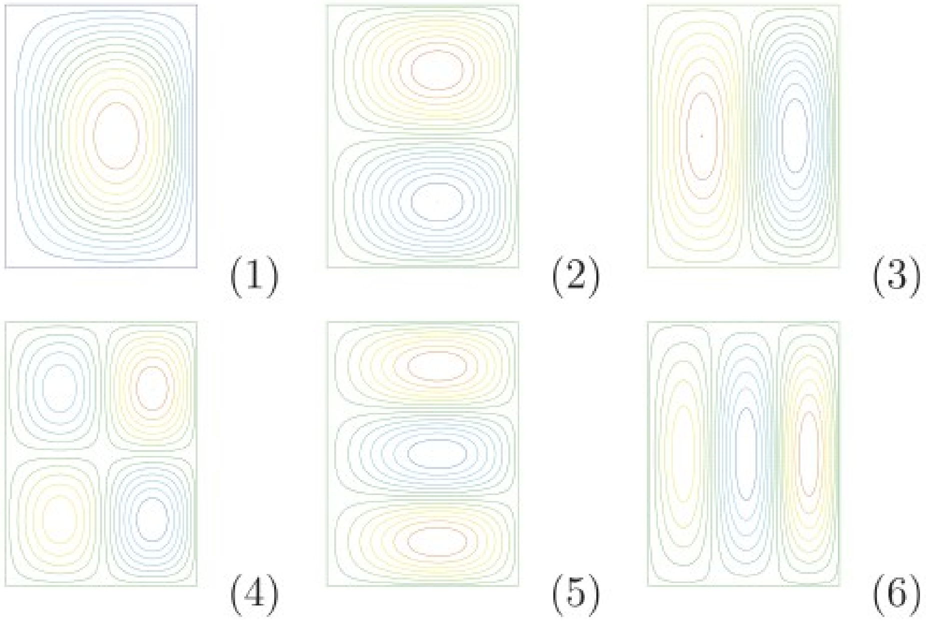

Figure 4.4: Axisymmetric Chandrasekar-Kendall modes for the first six Jensen-Chu resonances in λ. [95] The second and fourth are antisymmetric in the z direction, and therefore carry no net toroidal flux. Red and blue indicate opposite sign.

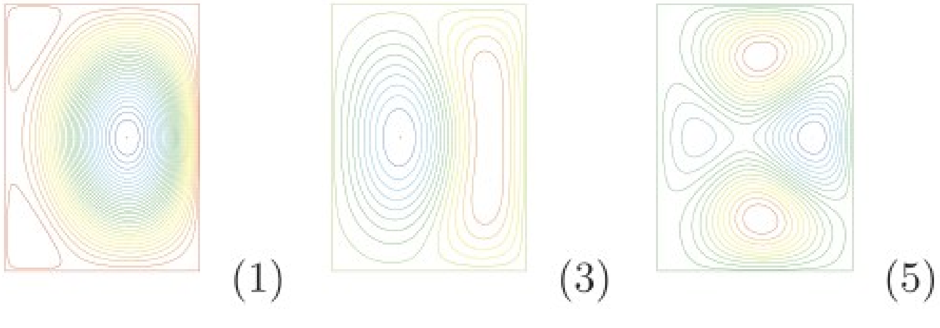

Figure 4.5: New resonant modes for resonances in λ. [95] The first, third, and fifth new resonant modes with the integral constraint of finite net toroidal flux. As the extra symmetry produces no net toroidal flux, the second and fourth fall on Jensen-Chu resonances.

Chapter 5

The NIMROD Code

The Non-Ideal Magnetohydrodynamics with Rotation, Open Discussion code (NIMROD) evolves the nonlinear, visco-resistive MHD equations in a finite domain with optional extensions to non-MHD effects through the closure relations. [96, 97] The three-dimensional spatial representation consists of two-dimensional Lagrange-type finite elements with a finite Fourier spectrum in the third dimension, which is assumed to be periodic and symmetric. This spatial representation encompasses toroidal, cylindrical, and periodic linear configurations with arbitrarily shaped cross-sections. An implicit leapfrog advance is implemented in NIMROD, which is stable for arbitrarily large time-steps and free of numerical dissipation when the advection and magnetic diffusion terms are time-centered. [98] The block-based preconditioning—to enhance convergence rate of the iterative linear solver—uses the SuperLU libraries of direct solvers. [99] The resulting matrices are then solved iteratively with the general minimum residual (GMRES) method. [98, 100]

5.1 Physics Model

NIMROD evolves number density n, center-of-mass flow velocity $\mathbf{v}$, magnetic field $\mathbf{B}$, and either a single temperature or separate electron and ion temperatures. [33,101] The physics model assumes charge neutrality throughout the domain, i.e. $n \equiv n_e \simeq n_i Z_{eff}$, resulting in divergence-free currents and a displacement-current-free or low frequency Ampere's Law, Equation 5.6. The bracketed terms in the magnetic field evolution equation, Equation 5.4, correspond to the electric field from an extended-MHD Ohm's Law. The two-fluid contributions from the Hall effect, electron pressure, and electron inertia are indicated. The ion and electron velocities used in the energy evolution equation (Eq. 5.3) are given by Equations 5.8 & 5.7, where $\nu \equiv Z_{eff} m_e/m_i$. The injector sources indicated in Equations 5.5 & 5.10 are described later in Section 5.3.1.

$$\frac{\partial n}{\partial t} + \nabla \cdot (n\mathbf{v}) = \nabla \cdot D_n \nabla n - \nabla \cdot D_h \nabla \nabla^2 n \tag{5.1}$$

$$\rho \left(\frac{\partial \mathbf{v}}{\partial t} + \mathbf{v} \cdot \nabla \mathbf{v} \right) = \mathbf{J} \times \mathbf{B} - \nabla p + \nabla \cdot \mathbf{\Pi} \tag{5.2}$$

$$\frac{n}{\gamma - 1} \left(\frac{\partial T_\alpha}{\partial t} + \mathbf{v}_\alpha \cdot \nabla T_\alpha \right) = -nT_\alpha \nabla \cdot \mathbf{v}_\alpha - \nabla \cdot \mathbf{q}_\alpha + Q_\alpha \tag{5.3}$$

$$\frac{\partial \mathbf{B}}{\partial t} + \nabla \times \mathbf{E} = \kappa_{\nabla \cdot \mathbf{B}} \nabla \nabla \cdot \mathbf{B} \tag{5.4}$$

$$\mathbf{E} = \left[\eta \mathbf{J} - \mathbf{v} \times \mathbf{B} - \underbrace{\frac{\eta \lambda_{inj} \mathbf{B}}{\mu_0}}_{\text{injector}} + \underbrace{\frac{\mathbf{J} \times \mathbf{B}}{n_e e} - \frac{\nabla p_e}{n_e e} + \frac{m_e}{n_e e^2} \frac{\partial \mathbf{J}}{\partial t}}_{\text{2-fluid}} \right] \tag{5.5}$$

$$\mu_0 \mathbf{J} = \nabla \times \mathbf{B} \tag{5.6}$$

$$\mathbf{v}_e = \mathbf{v} - (ne)^{-1} \mathbf{J} / (\nu + 1) \tag{5.7}$$

$$\mathbf{v}_i = \mathbf{v} + (ne)^{-1}\,\mathbf{J}\nu/\,(\nu+1) \tag{5.8}$$

For numerical stability, an artificial number diffusivity D_n, number hyper-diffusivity D_h, and magnetic-divergence conductivity $\kappa_{\nabla\cdot\mathbf{B}}$ are included in the model. The artificial number diffusivity and hyper-diffusivity are included to limit mesh-scale density perturbations, e.g. the formation of shocks, which cannot be handled by traditional finite element methods. [102] Additionally, being the lowest-order fluid moment, number density evolution greatly impacts the evolution of the other fluid equations. Magnetic-divergence cleaning is required, as $\nabla\cdot\mathbf{B}=0$ is not strictly enforced in NIMROD. When $\kappa_{\nabla\cdot\mathbf{B}}\neq 0$, magnetic-divergence diffuses out of the computational domain, as evident from the divergence of Equation 5.4 with the boundary conditions satisfying $\oint \mathbf{B}\cdot d\mathbf{S}=0$.

Expressions for the heat flux $\mathbf{q}_\alpha$, heat source Q_α, and stress tensor $\mathbf{\Pi}$ are given below, where $\mathbf{W}$ is the symmetric, traceless rate of strain tensor. Multiple closure relations are available in NIMROD, meaning that some or all of the contributions to $\mathbf{q}_\alpha$, Q_α, and $\mathbf{\Pi}$ may be neglected.

$$\mathbf{q}_\alpha = \nabla\cdot n\left[\left(\chi_{\parallel,\alpha}-\chi_{\perp,\alpha}\right)\mathbf{bb}+\chi_{\perp,\alpha}\mathbf{I}\right]\cdot\nabla T_\alpha \tag{5.9}$$

$$Q_i = n_e k_B (T_e - T_i)\frac{\nu_{T,eq}}{\gamma-1} - \mathbf{\Pi}:\nabla\mathbf{v} + \underbrace{Q_{inj}}_{\text{injector}} \tag{5.10}$$

$$Q_e = \eta J^2 - n_e k_B (T_e - T_i)\frac{\nu_{T,eq}}{\gamma-1} \tag{5.11}$$

$$\mathbf{W} = \nabla\mathbf{v} + (\nabla\mathbf{v})^T - \tfrac{2}{3}\mathbf{I}\,(\nabla\cdot\mathbf{v}) \tag{5.12}$$

$$\begin{aligned}\mathbf{\Pi} = &-\rho\left[\nu_{kin}\nabla\mathbf{v} + \nu_{iso}\mathbf{W} + \tfrac{3}{2}\nu_{par}\left(\mathbf{b}\cdot\mathbf{W}\cdot\mathbf{b}\right)\left(\mathbf{bb}-\tfrac{1}{3}\mathbf{I}\right)\right]\\ &+ (nT_i/4\omega_{ci})\left[(\mathbf{b}\times\mathbf{W})\cdot(\mathbf{I}+3\mathbf{bb}) - (\mathbf{I}+3\mathbf{bb})\cdot(\mathbf{W}\times\mathbf{b})\right]\end{aligned} \tag{5.13}$$

Modifications to the perpendicular thermal conduction are described in Section 5.3.2. The electron and ion heat sources (Q_e and Q_i) include contributions from ohmic heating, temperature equilibration between ions and electrons, and viscous heating. If a single fluid temperature model is used, $Q = Q_i + Q_e$. The temperature equilibration rate $\nu_{T,eq}$ may be treated as a constant for the entire plasma or locally computed, as described in Section 5.3.2. The last term of the stress tensor is the gyro-viscous contribution and is equivalent to the η_3^i and η_4^i terms in the high-magnetization limit ($\omega_{ci}\tau_i \gg 1$) of Braginskii's formulation. [1].

5.2 Numerical Representation

5.2.1 Spatial Discretization

The finite element method (FEM) is a numerical technique for solving systems of partial differential or integral equations. This method is applied to systems where computation of the analytic solution is intractable, e.g. systems with irregularly shaped domains and non-uniform boundary conditions. In the finite-element method, the domain is discretized, with the goal that increasing spatial and temporal resolution will not only cause convergence on a particular solution, but that the solution converged upon is the continuum solution. The evolution of the finite element method from mathematical techniques and previous numerical methods is described in Chapter 1 of [103].

For a one-dimensional element containing nodes x_i, the basis functions of a Lagrange-type finite element are given in Equation 5.14, where $\phi_i(x_j) = \delta_{ij}$, i.e. the expansion coefficients a_i for a Langrange-type finite element basis function are the values at the corresponding node. [104, Chap. 8] Fields within each element are described by the expansion coefficients and the finite element basis functions themselves, such that the numerical approximation $u(x,t)$ of the solution in the element is then given by Equation 5.15, where $u(x_i,t) = a_i(t)$.

$$\phi_i(x) = \prod_{j \neq i} \frac{x_j - x}{x_j - x_i} \tag{5.14}$$

$$u(x,t) = \sum_i a_i(t)\phi_i(x_i) \tag{5.15}$$

In general, a finite element method is characterized by how the residual $R(\mathbf{x}) = Du - f$ is handled, where $u(\mathbf{x})$ is numerical approximation to the equation $Dv - f = 0$, where $v(\mathbf{x})$ is the continuum solution. The three primary types of finite element methods are the collocation, least squares, and Galerkin methods. [104, Chap. 8] In the colocation method, $R(\mathbf{x}_i) = 0$, which is straightforward but does not address the error away from the nodes directly. For a sufficiently smooth solution, the error away from the nodes will decrease with resolution. In the least squares method, $\partial_{a_i} \int R^2(\mathbf{x}) d\mathbf{x} = 0$, where a_i are the expansion coefficients. In the Galerkin method, $\int R(\mathbf{x}) w_i(\mathbf{x}) d\mathbf{x} = 0$, where $w_i(\mathbf{x})$ are weighting functions used in evaluating the residual and are a basis for the space of functions used for the solution space. Thus, the Galerkin method is a weak formulation of the system.

The Galerkin method is analogous—but not always equivant—to a variational principle. In a variational principle such as the Rayleigh-Ritz method, some conserved integral quantity is formed, e.g. the strain energy $\Pi(\mathbf{u})$ for a series of beams. The solution of the continuum problem is the value of the function $\mathbf{u}$ that minimizes $\mathbf{\Pi}$. When a natural variational principle exists, the Galerkin method must necessarily yield the same result as the variational method. [103, Chap. 3] However, the Galerkin method is more flexible as it does not require the existence of a natural variational principle.

Numeric quadrature is used to perform the volume integrals required by the weak form of the equations. [33]

The finite element mesh in NIMROD is logically rectangular and uses isoparametric mapping to real-space coordinates (Figure 5.1), i.e the same order polynomials are used for both the dependent variables and the mapping itself. [103, Chap. 5] For a parametric mapping $x(\xi,\eta)$ and $y(\xi,\eta)$, where ξ and η are logical-space coordinates and x and y are real-space coordinates, the derivatives are recast in terms of the real-space variables. For the first-order derivatives, the chain-rule is applied to find the logical-space derivatives in terms of the real-space variables, Equation 5.16, where the matrix is the Jacobian of the mapping. The inverse of the Jacobian matrix casts the real-space derivatives in terms of the logical-space derivatives. Therefore, the finite element method provides a reliable way to achieve high-order convergence in domains with non-uniform shape.

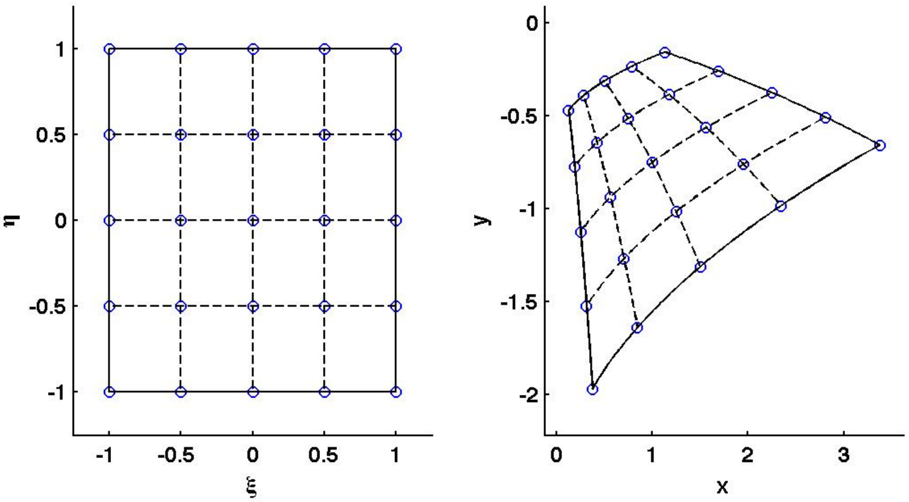

Figure 5.1: Isoparametric mapping of biquartic elements from logical coordinates ξ and η to real-space coordinates $x(\xi,\eta)$ and $y(\xi,\eta)$. Lines show constant values of either ξ or η.

$$\begin{bmatrix} \frac{\partial}{\partial \xi} \\ \frac{\partial}{\partial \eta} \end{bmatrix} = \begin{bmatrix} \frac{\partial x}{\partial \xi} & \frac{\partial x}{\partial \eta} \\ \frac{\partial y}{\partial \xi} & \frac{\partial y}{\partial \eta} \end{bmatrix} \begin{bmatrix} \frac{\partial}{\partial x} \\ \frac{\partial}{\partial y} \end{bmatrix} \tag{5.16}$$

An advantage of the finite element method is its ability to reproduce a higher-order solution with relatively few elements and/or nodes. The spatial convergence rate for the s^{th} derivative of the numerical solution is given by Equation 5.17, where the mesh spacing is given by h, the degree of the differential equations is $2m$, and the polynomial degree of the basis functions is $k-1$. [102] For $m \geq k$, the finite element method identically reproduces the continuum solution v. For $m \geq 2$, the finite element method has faster spatial convergence than a second-order finite difference method, which has the spatial convergence rate of $\|u - u^h\|^0 \sim O(h^2)$. Higher-order finite difference methods exist, but are difficult to apply to non-uniform domains. Convergence studies have shown that, in general, basis functions of polynomial degree $p \geq 3$ are required to accurately reproduce thermal conduction in NIMROD, including thermal conduction with a realistic degree of anisotropy ($\chi_\perp/\chi_\parallel \ll 1$) and without requiring alignment between the finite element mesh and the magnetic field. [101]

$$\|v - u^h\|^s \sim O(h^{k-s} + h^{2(k-m)}) \tag{5.17}$$

The number of cells in the periodic direction is given by $M = 2^p$, where $p \in [\mathbb{Z} \geq 0]$ is specified by the user. For a toroidal geometry with dealiasing, the total number of modes N represented by the finite Fourier series is $\lfloor M/3 \rfloor + 1$, inclusive of the non-harmonic $n = 0$ mode. Otherwise, the total number of modes is $\lfloor M/2 \rfloor + 1$. The fast Fourier transform (FFT) and the inverse fast Fourier transform (IFFT) are given by Equations 5.18 & 5.19, respectively. $R_j \in \mathbb{R}$ are the coefficients at the discrete spectral dimension locations, e.g. discrete toroidal angles for a toroidal geometry. $C_m \in \mathbb{C}$,

$\forall m \neq 0$ are the spectral mode amplitudes, with the non-harmonic mode amplitude $C_0 \in \mathbb{R}$.

$$C_n = \sum_{j=0}^{M-1} R_j \exp\left(\frac{-2\pi ijn}{N_\phi}\right) \tag{5.18}$$

$$R_j = C_0 + \sum_{m=1}^{N-1} \left[C_n \exp\left(\frac{2\pi ijn}{N_\phi}\right) + C_n^* \exp\left(\frac{-2\pi ijn}{N_\phi}\right) \right] \tag{5.19}$$

The coefficients D_n^s for the s^{th} derivate along the spectral dimension are given by Equation 5.20, where L_ϕ is the length of the periodic dimension. Thus, the wave number for the n^{th} spectral mode is given by $k_n = 2\pi/L_\phi$, which reduces to the familiar $k_n = n/R$ for toroidal geometries.

$$D_n^s = \left(\frac{-2\pi in}{L_\phi}\right)^s C_n \tag{5.20}$$

The converge of a spectral method depends upon discontinuities in the continuum solution. [105] For a continuum solution that is discontinuous in the s^{th} derivative, the max-norm (or ∞-norm) of the errors in the numerical solution will be $O(N^{-s})$ near the irregularity and $O(N^{-(s+1)})$ away from the irregularity, where N is the number of spectral modes. For an analytic solution without discontinuities, the max-norm of the errors in the numerical solution is e^{-cN}, where the coefficient $c > 0$.

5.2.2 Implicit Leapfrog Temporal Advance

All computations described in this paper use the implicit leapfrog temporal advance. The flow velocity $\mathbf{v}$ is staggered 1/2 time-step from n, $\mathbf{B}$, and T_α. The notation used is such that $\mathbf{v}$ is at integer time-steps, while the other fields are at half-integer time-steps. The Δ operator indicates the difference between successive timesteps, e.g. $\Delta\mathbf{v} = \mathbf{v}^{j+1} - \mathbf{v}^j$

and $\Delta n = n^{j+3/2} - n^{j+1/2}$. The bar operator indicates averaging over successive time-steps, e.g. $\bar{n} = \frac{1}{2}\left(n^{j+3/2} + n^{j+1/2}\right)$. The semi-discrete equations are given below, where $\mathbf{L}^{j+1/2}(\Delta\mathbf{v})$ contains the ideal MHD force operator, which has a coefficient of C_0. [98] C_1 is a coefficient for the Laplacian part with p_{nl} the 'nonlinear' pressure, which is typically orders of magnitude smaller than the total pressure.

$$
\begin{aligned}
& mn^{j+1/2}\left(\frac{\Delta\mathbf{v}}{\Delta t} + \frac{1}{2}\mathbf{v}^j\cdot\nabla\Delta\mathbf{v} + \frac{1}{2}\Delta\mathbf{v}\cdot\nabla\mathbf{v}^j + \frac{1}{4}\boldsymbol{\Delta}\mathbf{v}\cdot\nabla\boldsymbol{\Delta}\mathbf{v}\right) \\
&\quad - \Delta t\mathbf{L}^{j+1/2}(\Delta\mathbf{v}) + \nabla\cdot\mathbf{\Pi}^{j+1/2}(\Delta\mathbf{v}) = \mathbf{J}^{j+1/2}\times\mathbf{B}^{j+1/2} \\
&\quad - mn^{j+1/2}\mathbf{v}^j\cdot\nabla\mathbf{v}^j - \nabla p^{j+1/2} - \nabla\cdot\mathbf{\Pi}^{j+1/2}(\mathbf{v}^j)
\end{aligned}
\tag{5.21}
$$

$$
\begin{aligned}
& \frac{\Delta n}{\Delta t} + \frac{1}{2}\nabla\cdot\left(\mathbf{v}^{j+1}\Delta n\right) - \frac{1}{2}\nabla\cdot D_n\nabla\Delta n - \frac{1}{2}\nabla\cdot D_h\nabla\nabla^2\Delta n = \\
&\quad - \nabla\cdot\left(\mathbf{v}^{j+1}n^{j+1/2}\right) + \nabla\cdot D_n\nabla n^{j+1/2} + \nabla\cdot D_h\nabla\nabla^2\Delta n^{j+1/2}
\end{aligned}
\tag{5.22}
$$

$$
\begin{aligned}
& \frac{\bar{n}}{\gamma-1}\left(\frac{\Delta T_\alpha}{\Delta t} + \frac{1}{2}\mathbf{v}^{j+1}\cdot\nabla\Delta T_\alpha\right) + \frac{1}{2}\bar{n}\Delta T_\alpha\nabla\cdot\mathbf{v}^{j+1} + \frac{1}{2}\nabla\cdot\left[\mathbf{q}_\alpha(\Delta T_\alpha)\right] = \\
&\quad - \frac{\bar{n}}{\gamma-1}\mathbf{v}^{j+1}\cdot\nabla T_\alpha^{j+1/2} - \bar{n}T_\alpha^{j+1/2}\nabla\cdot\mathbf{v}^{j+1} - \nabla\cdot\left[\mathbf{q}_\alpha(T_\alpha^{j+1/2})\right] + Q_\alpha^{j+1/2}
\end{aligned}
\tag{5.23}
$$

$$
\begin{aligned}
& \frac{\Delta\mathbf{B}}{\Delta t} - \frac{1}{2}\nabla\times\left(\mathbf{v}^{j+1}\times\Delta\mathbf{B}\right) + \frac{1}{2}\nabla\times\eta\Delta\mathbf{J} + \nabla\times\left(\frac{m_e}{\mu_0\bar{n}e^2}\nabla\times\frac{\Delta\mathbf{B}}{\Delta t}\right) \\
&\quad + \nabla\times\frac{1}{\bar{n}e}\left(\frac{1}{2}\mathbf{J}^{j+1/2}\times\Delta\mathbf{B} + \frac{1}{2}\Delta\mathbf{J}\times\mathbf{B}^{j+1/2} + \frac{1}{4}\Delta\mathbf{J}\times\Delta\mathbf{B}\right) \\
&\quad - \frac{1}{2}\kappa_{\nabla\cdot\mathbf{B}}\nabla\nabla\cdot\Delta\mathbf{B} = \kappa_{\nabla\cdot\mathbf{B}}\nabla\nabla\cdot\mathbf{B}^{j+1/2} \\
&\quad - \nabla\times\left[\eta\mathbf{J}^{j+1/2} - \mathbf{v}^{j+1/2}\times\mathbf{B}^{j+1/2} + \frac{1}{\bar{n}e}\left(\mathbf{J}^{j+1/2}\times\mathbf{B}^{j+1/2} - \bar{T}_e\nabla\bar{n}\right)\right]
\end{aligned}
\tag{5.24}
$$

$$\begin{aligned}\mathbf{L}^{j+1/2}(\Delta\mathbf{v}) = C_0 \Big\{ &\tfrac{1}{\mu_0} \left[\nabla \times \nabla \times \left(\Delta\mathbf{v} \times \mathbf{B}^{j+1/2}\right)\right] \times \mathbf{B}^{j+1/2} \\ &+ \mathbf{J}^{j+1/2} \times \nabla \times \left(\Delta\mathbf{v} \times \mathbf{B}^{j+1/2}\right) + \nabla\left(\Delta\mathbf{v} \cdot \nabla p^{j+1/2} + \gamma p^{j+1/2} \nabla \cdot \Delta\mathbf{v}\right)\Big\} \\ &+ C_1 p_{nl}^{j+1/2} \nabla^2 \Delta\mathbf{v}\end{aligned} \tag{5.25}$$

All temporal centering coefficients for advection and resistivity are 1/2 in the semi-discrete equations shown, which, as stated previously, is required for numerical stability at arbitrarily large time-steps. Further, $C_0 > 1/4$ is also required for numerical stability at arbitrarily large time-steps. The only nonlinear implicit terms are in Equation 5.21 & 5.24. The terms are quadratic in terms of $\Delta\mathbf{v}$ and $\Delta\mathbf{B}$, respectively, which makes Newton iteration straightforward. Electron inertia—a symmetric contribution to the **B**-advance—can increase numeric convergence rates by limiting the frequency spectrum at large wave-numbers, i.e. the ω_{ce} resonance. [98] With the previously given constraints, the convergence rate for the implicit leapfrog advance is the same as for the Crank-Nicolson method (Equation 5.26), where k is the time-step and v is the continuum solution.

$$\|v - u_k\|_0 \sim O(k^2) \tag{5.26}$$

5.3 Code Development

This section describes a number of modifications made to the Nimrod code for this computational study. The motivation for and a description of each modification are described, though without the inclusion of source code.

5.3.1 Helicity Injector

As it is not computationally tractable to model the helicity injector in detail within a global-scale computation of relaxation, the injector is modeled as a combination of localized, volumetric current and ion heating sources. The source terms are indicated in the model equations in Section 5.1. The shape function (Γ) for both the injector current and heating sources is given in Equation 5.27, where Z_{inj} is defined in Equation 5.28 for $\phi \in [-\pi, \pi)$. The computations in Chapter 6 use parameters of $R_{inj} = 0.35$ m, $Z_{inj} = -0.70$ m, and $n_{inj} = 4$. The corresponding shape function is plotted in Figure 5.2.

$$\Gamma = \exp\left[-\left(\frac{R - R_{inj}}{w_{inj}}\right)^2 - \left(\frac{Z - Z_{inj}\left(\phi\right)}{w_{inj}}\right)^2 - \left(\frac{n_{inj}\phi}{\pi}\right)^2\right] \tag{5.27}$$

$$Z_{inj}\left(\phi\right) = Z_{inj,0} + \phi \left.\frac{RB_{Z,vac}}{B_{\phi,vac}}\right|_{R=R_{inj}} \tag{5.28}$$

The injector electric field is defined in Equation 5.29, where η is the electric resistivity. The amplitude $\lambda_0\left(t\right)$ is increased linearly in time at a constant rate of 200 m^{-1}/ms, allowing a more gradual current development than the sudden application of injector voltage in the experiment. This is done to avoid Alfvénic transients in the simulations, which would require extremely small time-steps to resolve: the sudden application of a high-amplitude injector electric field causes local density evacuation, which causes the Alfvén speed to become very large locally. As the purpose of this paper is to characterize the evolution and relaxation of the current filaments and not their initial formation, this should be an acceptable departure from experimental procedure. Additionally, without a precise match between the helicity injection rates in the experiment and in the computations, the plasma current evolution will necessarily differ.

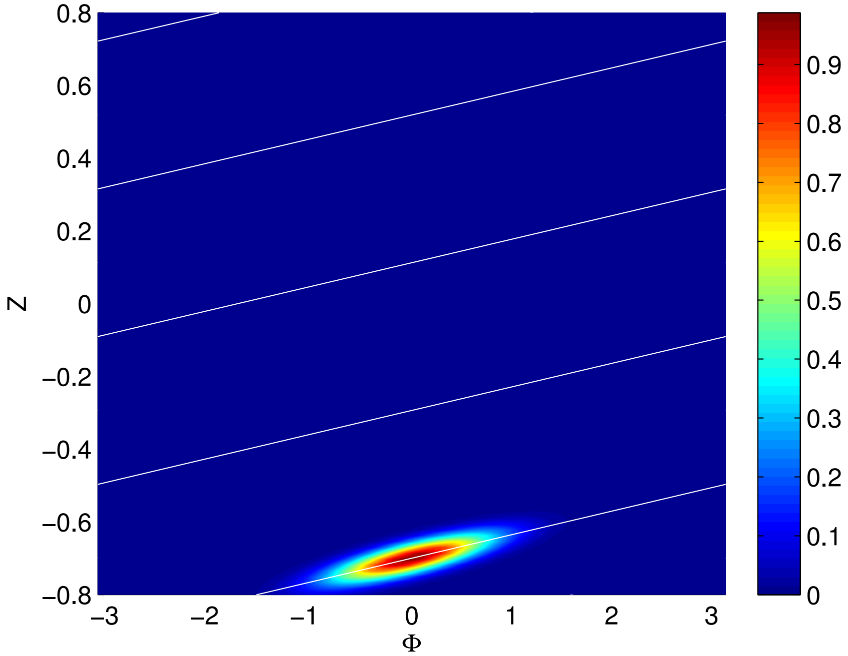

Figure 5.2: The helicity injector shape function is displayed at $R = R_{inj}$. A vacuum magnetic field trajectory that passes through the center of the injector is traced in white.

$$\mathbf{E}_{inj} = \eta\mu_0^{-1}\lambda_{inj}\left(t\right)\mathbf{B}\Gamma \tag{5.29}$$

The volumetric injector ion heat source is defined in Equation 5.30. The amplitude $Q_0\left(t\right)$ is increased linearly in time from 8.3 kW/m^3 at $t = 0$ to 50 kW/m^3 at $t \geq 5$ ms. The ion heating source precedes the injector electric field to establish a conducting path for the current. Even though the heating source is strictly on the ions, the high rate ($\nu_{T,eq} = 2.0 \times 10^6$ s^{-1}) of thermal equilibration at the initial plasma temperature will rapidly warm the electrons. Anisotropic conduction of the electron thermal energy then forms the electrically conducting helical path. Later, both ohmic heating from the injector current and the ion heating source contribute to lengthening the current-conducting path of the filament until it spans the entire vertical extent of the domain.

$$Q_{inj} = Q_0\left(t\right)\Gamma \tag{5.30}$$

The current source is a localized force density acting on the electrons, expressed here as the injector electric field $\mathbf{E}_{inj}$. From Faraday's Law, the application of a localized electric field source directly induces a ring of azimuthal magnetic flux around the source region. The azimuthal magnetic field (B_θ) adds a twist to the magnetic field lines in the injector region. Associated with the azimuthal magnetic field is a current toroid that loops around the azimuthal magnetic field. The Lorentz force between the azimuthal magnetic field and the radial current density at the ends of the toroid excite propagation of torsional Alfvén waves, which act to redistribute the helical twisting along the length of the magnetic field lines. Perpendicular resistive diffusion of the unsupported reverse current results in net current. The formation of a current filament from the injector electric field is visualized in Figure 5.3. In the computations, the unsupported reversed current quickly diffuses through the cold regions surrounding the modeled helical current filament, leaving a flux rope with net current.

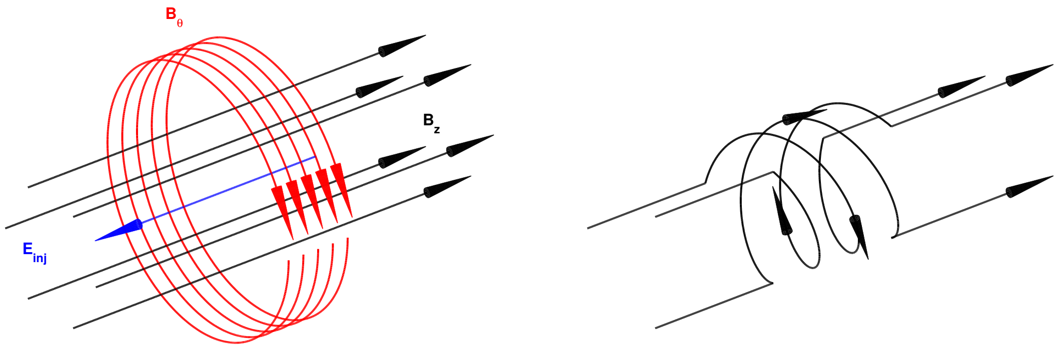

(a) E_{inj} induces B_θ

(b) B_θ adds a twist to magnetic field

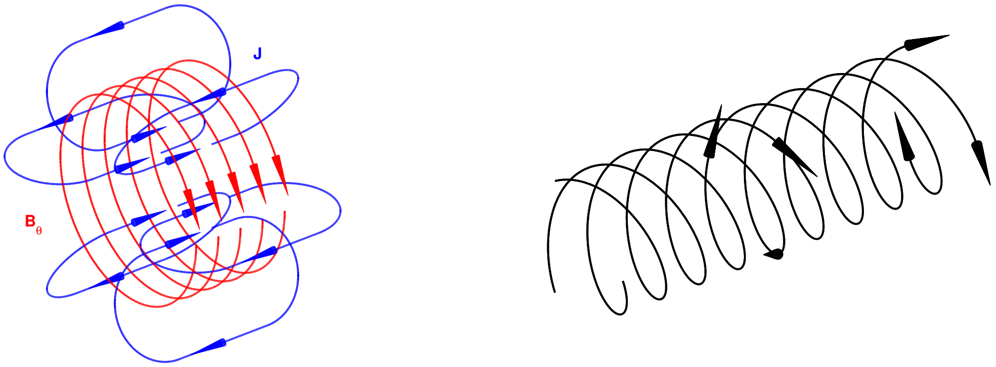

(c) The $J_r \times B_z$ Lorentz force at the ends launches torsional Alfvén waves

(d) With diffusion, a flux tube with net current forms

Figure 5.3: The formation of a current filament from $\mathbf{E}_{inj}$

5.3.2 Thermal Transport

In this section, a brief description is given of modifications to the thermal transport routines, as well as the motivation for the modifications. In particular, the perpendicular thermal diffusivity and thermal equilibration between ions and electrons have been updated to now include locally computed, temperature-dependent coefficients. All transport coefficients are computed from the Braginskii closure model in Reference [1]. For the rest of this section, the following characteristic times are used:

$$\tau_i = \sqrt{2}\tau_{ii} \tag{5.31}$$

$$\tau_e = \tau_{ei} \tag{5.32}$$

where $\tau_{\alpha\beta}$ is the scattering time of a test particle α off a field particle β, given in Equation 5.33. The Coulomb logarithm ($\log\Lambda_{\alpha\beta}$) in Equation 5.33 may be treated as a constant for the entire plasma or locally computed using the plasma parameter $\Lambda_{\alpha\beta}$ and Debye length λ_D in Equations 5.34 & 5.35, respectively. As the predicted value of the Coulomb logarithm does not vary greatly over the expected temperature range–$\log\Lambda \simeq 8$–12 from $T = 1$–10 eV, respectively–a constant value of $\log\Lambda = 10$ is used in the computations presented in Chapter 6.

$$\tau_{\alpha\beta} = \frac{6\sqrt{2}\pi^{3/2}\epsilon_0^2\sqrt{m_\alpha}\left(k_B T_\alpha\right)^{3/2}}{n_\beta q_\alpha^2 q_\beta^2 \log\Lambda_{\alpha\beta}} \tag{5.33}$$

$$\Lambda_{\alpha\beta} = \frac{12\pi\epsilon_0 k_B}{q_\alpha q_\beta}\frac{m_\beta T_\alpha + m_\alpha T_\beta}{m_\alpha + m_\beta}\lambda_D \tag{5.34}$$

$$\lambda_D = \left[\frac{n_e e^2}{\epsilon_0 k_B}\left(\frac{1}{T_e} + \frac{Z_{eff}}{T_i}\right)\right]^{-1/2} \tag{5.35}$$

The original perpendicular thermal diffusivity $\chi_\perp$ implemented in NIMROD was the high-magnetization limit ($x_s = \omega_{cs}\tau_s \gg 1$) of the Braginskii closure model for thermal conduction. [1] In regions of low temperature where $x_s < 1$, the high magnetization formulation over-predicts perpendicular thermal transport, Figure 5.4, leading to an artificial loss of thermal confinement. The computations presented in Chapter 6, which are initialized with a low, uniform plasma temperature, are susceptible to this issue. At the initial temperature, the ions are effectively unmagnetized with an ion magnetization parameter (x_i) of 0.0345, resulting in nearly isotropic ion thermal conductivity $\kappa_{\perp,i}/\kappa_{\parallel,i} = 0.996$. The electrons are moderately magnetized with an electron magnetization parameter (x_e) of 1.48, resulting in significant anisotropization ($\kappa_{\perp,e}/\kappa_{\parallel,e} = 0.171$) of the electron thermal conductivity. Therefore, the full Braginskii formulation [1] was implemented into NIMROD to reproduce realistic thermal transport across a wide range of values for the magnetization parameter x_s.

$$x_s = \omega_{cs}\tau_s \tag{5.36}$$

$$\kappa_{\parallel,s} = \frac{n_s T_s \tau_s}{m_s}\frac{\gamma_{0,s}}{\delta_{0,s}} \tag{5.37}$$

$$\kappa_{\perp,s} = \frac{n_s T_s \tau_s}{m_s}\frac{\gamma_{1,s}x_s^2 + \gamma_{0,s}}{x_s^4 + \delta_{1,s}x_s^2 + \delta_{0,s}} \tag{5.38}$$

$$\lim_{x\ll 1}\kappa_{\perp,s} = \kappa_{\parallel,s} \propto T_s^{5/2} \tag{5.39}$$

$$\lim_{x\gg 1}\kappa_{\perp,s} = \frac{n_s T_s \tau_s}{m_s}\frac{\gamma_{1,s}}{x_s^2} \propto T_s^{-1/2}B^{-2} \tag{5.40}$$

The new implementation of the full Braginksii perpendicular thermal conduction in NIMROD is benchmarked in Appendix A by investigating sound and compressional Alfvén wave damping with finite thermal conduction. The typical dispersion relations for these two types of waves are purely oscillatory for both the adiabatic ($\gamma = 5/3$) and isothermal ($\gamma = 1$) limits. By introducing finite thermal conduction, the

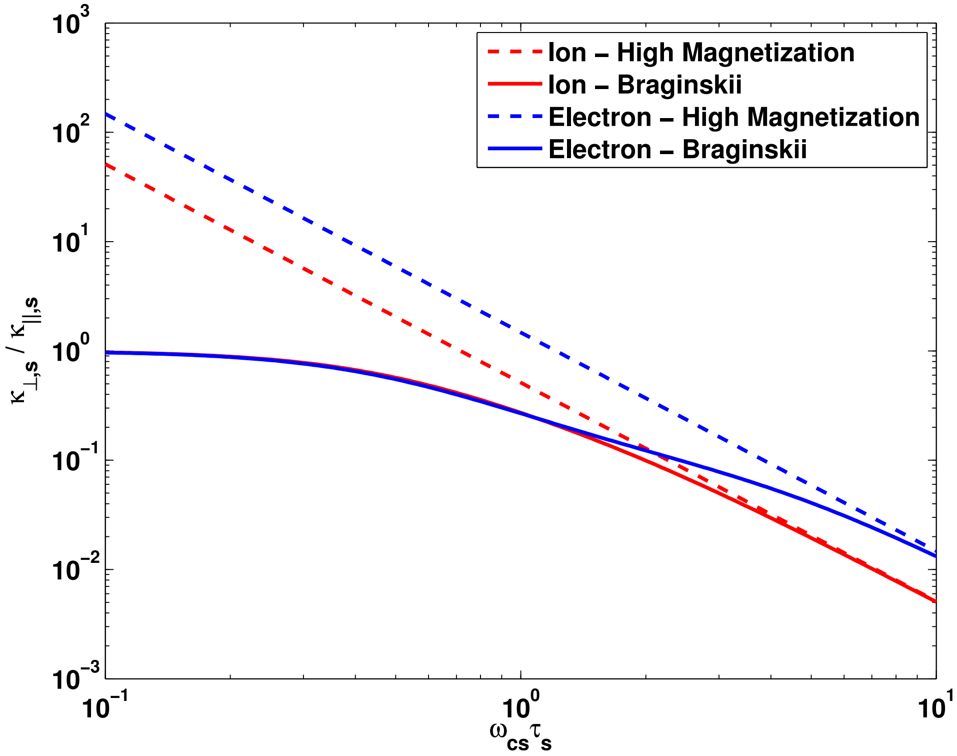

Figure 5.4: Scaling of the ratio of perpendicular-to-parallel thermal diffusivity with magnetization parameter $\omega_{cs}\tau_s$ for a $Z = 1$ plasma.

modified dispersion relations have strong damping at intermediate values of thermal conduction, while capturing both the adiabatic and isothermal oscillation frequencies in the appropriate limits.

NIMROD also previously utilized a toroidally symmetric perpendicular thermal diffusivity computed from toroidally averaged values of the density, temperatures, and magnetic field. However, the plasma temperature during the early, helical phase of current filament evolution has a strong toroidal dependence, meaning that locally-computed, temperature-dependent transport coefficients should also have a strong toroidal dependence. Therefore, NIMROD was updated to include a three-dimensional implementation of $\chi_\perp$.

In NIMROD, thermal equilibration between ions and electrons is applied at the end of the thermal advance in each time-step, applying a numerical time-splitting approach. In the separate step, simplified versions of the energy equation are solved (Equations 5.41 & 5.42), containing only the contribution from thermal equilibration between species. The rate of thermal equilibration, $\nu_{T,eq}$, may be treated as a constant for the entire plasma or locally computed from Equation 5.43.

$$n_i \frac{\partial T_i}{\partial t} + \ldots = \nu_{T,eq} \left(T_e - T_i\right) \tag{5.41}$$

$$n_e \frac{\partial T_e}{\partial t} + \ldots = \nu_{T,eq} \left(T_i - T_e\right) \tag{5.42}$$

$$\nu_{T,eq} = \frac{3m_e}{\tau_e m_i} \tag{5.43}$$

Casting the continuum equations above in terms of a discrete time-step Δt yields the discrete thermal equilibration equations below, where T_s^* is the temperature after the contributions of thermal conduction, ohmic and viscous heating, etc. have been applied, and T_s^{n+1} is the temperature at the end of the time-step after thermal equilibration.

$$(\Delta t)^{-1}\left(T_i^{n+1} - T_i^*\right) = Z_{eff}\nu_{T,eq}\left(T_e^{n+1} - T_i^{n+1}\right) \tag{5.44}$$

$$(\Delta t)^{-1}\left(T_e^{n+1} - T_e^*\right) = \nu_{T,eq}\left(T_i^{n+1} - T_e^{n+1}\right) \tag{5.45}$$

Energy conservation and the quasi-neutrality condition, $n_e \approx Z_{eft}n_i$, yield a relation between the ion and electron temperatures, given by Equation 5.46. Inserting the relation into the evolution equations above yields the ion and electron temperatures after thermal equilibration. The ion temperature is computed first, overwriting the original values. Then, electron temperature is computed using the T_i^{n+1} instead of T_i^*.

$$T_e^{n+1} - T_e^* = Z_{eff}^{-1}\left(T_i^{n+1} - T_i^*\right) \tag{5.46}$$

$$T_i^{n+1} = \left(\frac{1 + \nu_{T,eq}\Delta t}{1 + \nu_{T,eq}\Delta t\left(Z_{eff} + 1\right)}\right)T_i^* + \left(\frac{Z_{eff}\nu_{T,eq}\Delta t}{1 + \nu_{T,eq}\Delta t\left(Z_{eff} + 1\right)}\right)T_e^* \tag{5.47}$$

$$T_e^{n+1} = \left(\frac{1}{1 + \nu_{T,eq}\Delta t}\right)T_e^* + \left(\frac{\nu_{T,eq}\Delta t}{1 + \nu_{T,eq}\Delta t}\right)T_i^{n+1} \tag{5.48}$$

By construction, this implementation of thermal equilibration is both implicit and energy conserving, and it is a strictly local computation for each point in space. The time-splitting implies $\mathcal{O}\left(\Delta t^1\right)$ truncation errors, however. The computations described in Chapter 6 use locally computed, temperature-dependent coefficients of $\nu_{T,eq}$. At the initial temperature of $T_e = T_i = 0.24$ eV, the ions and electrons undergo rapid thermal equilibration with $\nu_{T,eq} = 2.0 \times 10^6$ s^{-1}. For T_e & $T_i \approx 10$ eV, thermal equilibration between ions and electrons is still significant at $\nu_{T,eq} = 7.5 \times 10^3$ s^{-1}. However, this rate falls within the range of significant MHD activity ($f \simeq$ 3–20 kHz) observed during the computations presented in Chapter 6, so other processes may have comparable or even greater impact on thermal transport.

5.3.3 Boundary Conditions

The helical conducting current filament forms part of the overall electrical circuit through which the injected current flows. In order for the plasma current to reach the surface and complete the circuit, the region at the ends of the current filament must possess sufficient electrical conductivity. With uniform, fixed boundary conditions on temperature, current forms an annular return path through the plasma that surrounds the driven current in the filament, as shown in Figure 5.5. The return current is anti-parallel to the current in the filament, partially shielding the attractive Lorentz force between adjacent passes of the current filament and delaying their eventual merger.

The surface at the ends of the current filament corresponds to the electrode surfaces in the experiment. Increasing the temperature in this region to be comparable to that in the current filament itself creates sufficient electrical conductivity for current to reach the surface. However, the remainder of the domain boundary corresponds to the vacuum vessel, and should therefore possess significantly lower temperature (and consequently, higher resistivity) than the electrode region. The ends of the current filament are also not restricted and–the upper end of the current filament, in particular–move during the computations. Rather than specifying a temperature profile on the domain boundary consistent with the movements of the current filament, a thermally insulating boundary condition is applied with a linear relaxation term. The thermal relaxation is expressed as differential equation below:

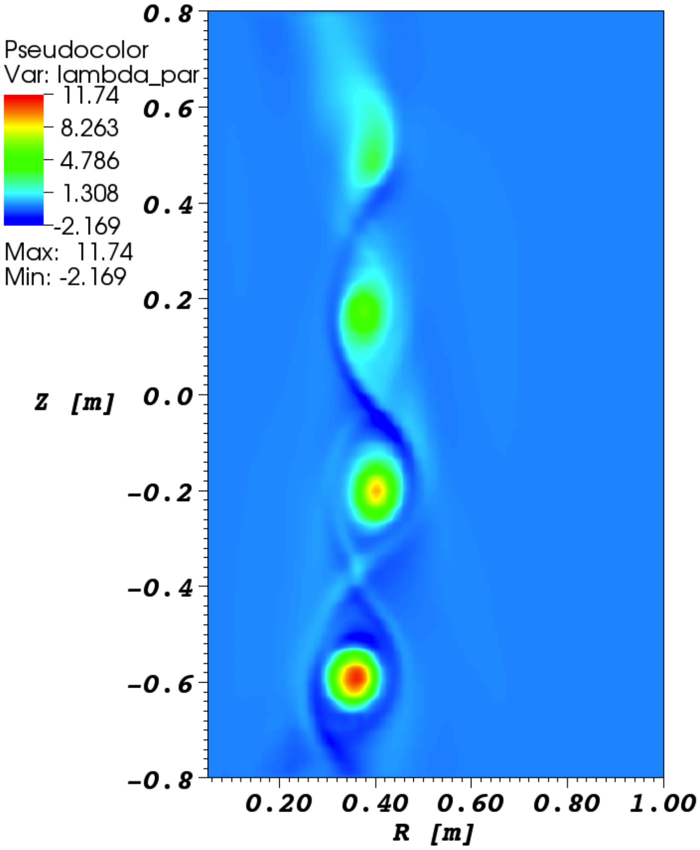

Figure 5.5: The plasma current forms a return path through the plasma with fixed boundary conditions on temperature. The temperature on the entire domain boundary is fixed at the initial temperature $T_e = T_i = 0.24$ eV.

$$\frac{\partial T_s}{\partial t} = -\alpha_{T,s}\left(T_s - T_{s,0}\right) \tag{5.49}$$

where values of the relaxation rates $\alpha_{T,i} = (1 - -1.5) \times 10^4 \text{ s}^{-1}$ and $\alpha_{T,e} = (1 - -2.5) \times 10^5 \text{ s}^{-1}$ are used in the computations.

The Pegasus vessel allows magnetic diffusion on the time-scale of the discharges. Modeling the chamber with an ideally conducting wall leads to an unphysical outward shift of toroidal flux that impedes the development of axial current. Alternatively, holding the toroidal magnetic field on the inboard and outboard surfaces fixed leads to a series of Alfvénic transients that are also unphysical. Instead, by relaxing the toroidal magnetic field along the inboard and outboard surfaces, the computations avoids the unphysical shift and represents a resistive-wall in a very approximate way. The relaxation of the toroidal magnetic field is expressed as a differential equation below:

$$\frac{\partial B_\phi}{\partial t} = -\alpha_\eta\left(B_\phi - B_{\phi,vac}\right) \tag{5.50}$$

where values of the relaxation rates $\alpha_\eta = (1\text{–}10) \times 10^9 \text{ s}^{-1}$ are used in the computations. Generally, α_η is chosen to be as large as possible but to still satisfy $\alpha_\eta \Delta t \ll 1$ for numerical stability.

Minor modifications must also be made to the magnetic field boundary conditions to model the poloidal flux compression phase. During the formation phase and prior to poloidal flux compression, the computations use the typical conducting boundary conditions, i.e. $\tilde{\mathbf{B}} \cdot \hat{n} = 0$, where $\tilde{\mathbf{B}}$ is the evolving part of the magnetic field. The tangential component of the magnetic field evolves consistently with the evolution equation in Section 5.1. During poloidal flux compression, the value of $\tilde{B}_Z$ on the surfaces $Z = Z_{min}$, Z_{max} is specified by the piecewise linear function in Equation 5.51.

The conditions on other components of the magnetic field and other surfaces remain unchanged.

$$\tilde{B}_Z(t) = \begin{cases} 0 & t < t_0 \\ \dot{B}_Z(t - t_0) & t_0 \leq t < t_1 \\ \dot{B}_Z(t_1 - t_0) & t \geq t_1 \end{cases} \tag{5.51}$$

For the resulting tangential electric field to be consistent with a conducting center column like in the experiment, $E_\phi = 0$ at $R = R_{min}$. This produces a toroidal electric field of the form:

$$E_\phi = \dot{B}_Z \left(\frac{R^2 - R_{min}^2}{2R} \right) \tag{5.52}$$

During the poloidal flux compression phase, a uniform rate of poloidal flux compression ($\dot{B}_Z = 1$ mT/ms) is specified in the computations presented in Chapter 6.

5.3.4 Synthetic Mirnov Diagnostic

The experiment relies heavily on a set of magnetic diagnostics to characterize plasma evolution during localized helicity injection. [20, 28] In order to make quantitative comparisons with the experimental measurements, an array of synthetic Mirnov coils has been implemented into NIMROD. First, a list of coil positions is read into NIMROD and the logical positions are found in an inversion of mapping done in Section 5.2.1. Then, the logical positions are used to solve for the magnetic field at each coil position and write it to a file at a user-specified stride in the number of time-steps. The analysis in Chapter 6 focuses on the Mirnov coils at the inboard and outboard midplane, rather than the entire set of Mirnov coils listed in Reference [106]. Those coil positions are listed in Table 5.1. The experimental and synthetic Mirnov coils possess identical poloidal positions and the same toroidal spacing relative to each other.

Spectrograms (Chapter 6) are produced from the 'raw' synthetic outer toroidal Mirnov coil signals through a multi-step analysis method. NIMROD uses an adaptive time-stepping algorithm, resulting in a non-uniform sampling of the synthetic Mirnov coil signals. To simplify analysis, each 'raw' signal is interpolated using a cubic spine onto an oversampled uniform time-step domain with a total number of samples $N_1 = 2 \wedge (\lfloor \log_2 \lfloor \Delta t_{sim} / \min(dt_0) \rfloor \rfloor + 1)$, where $\min(dt_0)$ is the smallest time-step from the original dataset and Δt_{sim} is the total length of time for the data being analyzed. The uniform time-step of the interpolated data is therefore $dt_1 = \Delta t_{sim}/(N_1 - 1)$. The peak frequency (50 kHz) of the spectrogram is well below the frequency corresponding to the maximum time-step in the simulations ($1/\max(dt_0) \sim 10$ MHz). Therefore, the error introduced by interpolation of the original signals would be far outside the frequency range of interest.

To isolate the sinusoidal part ($\tilde{y}$) of each signal, a running average is computed for a nominal window width $\Delta t_{win} = 0.5$ ms and subtracted from the original part (y) of the signal, as in Equation 5.53, where $N_{win} = \lfloor \Delta t_{win}/dt_1 + 0.5 \rfloor$ is the number of samples in each window and $y[n] = 0$ for $n < 1$ and $n > N_1$. The final analysis only considers the valid sample of $\tilde{y}$, i.e. $1 + \lfloor (N_1 - N_{win})/2 \rfloor \leq n \leq N_1 - \lfloor (N_1 - N_{win})/2 + 0.5 \rfloor$. The sinusoidal part of each signal is then divided into a series of overlapping windows of width $\Delta t_{win} = 0.5$ ms with a stride of 0.1 ms. A Hann window (Eq. 5.54) is applied to reduce edge effects, as the signal at the ends of any given window is not necessarily periodic.

$$\tilde{y}[n] = y[n] - \sum_{m=1}^{N_{win}} \frac{y[n-m]}{N_{win}} \tag{5.53}$$

Table 5.1: Mirnov coil positions

name	R (cm)	Z (cm)	Φ (degrees)
OT1	88.2	-17.00	301.7
OT2	90.5	-16.25	329.8
OT3	89.2	-34.75	344.9
OT4	88.2	-17.25	31.5
OT5	91.2	-16.70	122.3
OT6	90.2	-16.9	210.7
CT1	5.445	0	293.1
CT2	5.445	0	344.5
CT3	5.445	0	36.0
CT4	5.445	0	87.4
CT5	5.445	0	241.7
HR11	5.445	0	138.82

Positions are list for a selected set of Mirnov coils in the Pegasus Toroidal Experiment. [106] The first set is designated the outboard toroidal (OT) array, while the second set is designated the inboard toroid (CT) array. The toroidal angle Φ is relative to the inboard limiter in the experiment and relative to the center of the injector in the computations.

$$w\left(n\right) = 0.5\left[1 - \cos\left(\frac{2\pi n}{N-1}\right)\right] \tag{5.54}$$

For each unique pair of Mirnov signals x and y, the cross-power spectral density is computed using the Welch's averaged, modified periodogram method of spectral estimation, Equation 5.55, where R_{xy} is the cross correlation sequence (Eq. 5.56) and $E\left\{.\right\}$ is the expected value operator. The root-mean-square average is taken of the cross-power spectral density for all unique pairs of outboard toroidal Mirnov array signals. Frequencies of a few kilohertz are filtered from the experimental diagnostics. Therefore, the average amplitude is attenuated by (f/10 kHz) for $f \leq 10$ kHz to diminish, but not entirely eliminate, the contribution of lower-frequency dynamics.

$$P_{xy}\left(\omega\right) = \sum_{m=-\infty}^{\infty} R_{xy}\left(m\right) e^{-j\omega m} \tag{5.55}$$

$$R_{xy}\left(m\right) = E\left\{x_{n+m} y_n^*\right\} = E\left\{x_n y_{n-m}^*\right\} \tag{5.56}$$

Chapter 6

Results and Discussion

In this chapter, the results of two sets of computations are presented and discussed: one that evolves the MHD Ohm's law and another that evolves the two-fluid Ohm's law defined in Chapter 5. A large Hall parameter (δ_i/r_c) indicates that the electron fluid can significantly decouple from the ion fluid, affecting current-filament motion and interaction. The experimentally measured electron density $n_e \simeq 5 \times 10^{18}$ m^{-3} during a typical plasma produced by localized helicity injection [107] produces a Hall parameter of 3.6 for a channel width (r_c) of 4 cm, where δ_i is the ion skin depth. Therefore, two-fluid effects were anticipated, and now confirmed, to significantly affect current filament evolution. Through the use of separate calculations with and without the two-fluid terms in Ohm's Law, the effect of those terms is to some degree quantified. As both sets of computations exhibit the same qualitative behavior throughout much of the evolution, only one set of results (usually those with the two-fluid effects) is discussed, unless making specific comparisons.

The computations start from vacuum magnetic fields and progress through relaxation into a tokamak-like state. The vacuum magnetic field has the form

$$\mathbf{B}_{vac} = (I/R)\,\hat{\phi} + B_Z\hat{Z} \tag{6.1}$$

with a uniform $I \equiv RB_\phi$ of 0.007 $\text{m} \cdot \text{T}$ and axial magnetic field (B_Z) of 3.69 mT. The vacuum toroidal magnetic field corresponds to axial current through the central column of 35 kA. At the injection radius, $R = 35$ cm, the geometric winding number (Equation 6.2) of the vacuum field is 3.96.

$$G \equiv \frac{I \Delta Z}{2\pi R^2 B_Z} \tag{6.2}$$

The initial condition of the computations is treated as plasma with respect to transport properties, abeit at an unphysically low, uniform temperature $T_i = T_e = 0.24$ eV. The initial electron number density (n_e) is set uniformly to $1 \times 10^{19}\text{m}^{-3}$. Ionization, recombination, and neutral particle evolution are not considered in the modeling. However, transitions from unmagnetized transport properties to magnetized properties over the profile are important. Therefore, the Braginskii closure model for thermal conduction is used to reproduce the transition from unmagnetized ($x_i \ll 1$) to magnetized ($x_i \gg 1$) thermal conduction as the local plasma pressure increases, where $x_i \equiv \omega_{ci}\tau_i$ is the ion magnetization parameter. The physics model for these computations is discussed in greater detail in Chapter 5.

The computations have only one source region producing a single current filament, which is shown in Figure 6.1. The sources comprising the helicity injector are described in Section 5.3.1, including the initial formation of a current filament from those sources. The vacuum magnetic field, which is required for relaxation of the current filament into a tokamak-like configuration, directs the flux rope along several helical passes. [28] The current filament pierces each constant toroidal-angle plane in multiple locations. As the current crossing each plane is necessarily parallel, adjacent passes of the current filament will attract each other.

The self-induced magnetic field from the flux rope reduces the vertical field on the

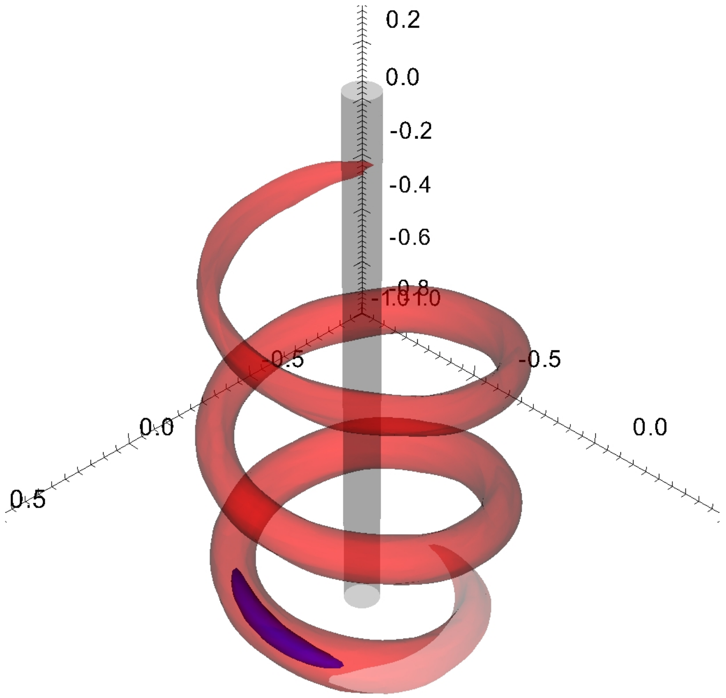

Figure 6.1: The spatial distribution of the injector sources and the resulting helical current filament. The half-max shown of the injector shape function is shown in in blue. The isosurface $\lambda = 1.0$ m^{-1} is shown in translucent red for the resulting current filament at $t = 0.6$ ms in the 2-fluid computation, when $I_p = 1.1$ kA . The central column is shown in gray for clarity.

inboard side of the rope and reinforces it on the outboard side. At low injected current, $I_p \lesssim 2$ kA, the self-induced magnetic-field from the flux rope is less than the axial vacuum magnetic field, and the current filament winds along the vacuum field as observed during the filamentary phase described in Reference [28]. With additional injected current, the magnetic field associated with the current filament locally exceeds the axial vacuum magnetic field, producing a local vertical magnetic field null inboard of the flux rope axis. With the local field null, the attractive Lorentz force between adjacent passes of the current filament then excites vertical oscillations in the helical channel.

6.1 Current Filament Merger and Reconnection

Interaction among adjacent passes intensifies over time with increasing channel current until they collide and merge via magnetic reconnection. When $I_p > 3$ kA, the localized merger releases a ring of net current that surrounds the central column. As shown in Figure 6.2, the merger geometry is nearly parallel, and adjacent passes are oriented in the co-helicity sense. The separated current rings form slightly inboard of the current-channel near the midplane and slowly propagate vertically away from the injector. Reconnection along the rope is, therefore, restricted by the source region, just as reconnection is restricted by the electrostatic plasma gun injectors in the Reconnection Scaling Experiment (RSX) [108] and the Large Plasma Device (LaPD) [109]. However, unlike Pegasus, the current filaments in RSX and LaPD are injected along straight axial magnetic fields.

When focusing on the region near the reconnection site, the two segments of the current filament that pass through this region can be considered as separate flux ropes. The parallel merger geometry between these segments appears similar to the RR0 configuration in Reference [69], in which two straight, parallel co-helicity flux tubes merge. Here, however, one of the ends of each segment curves away vertically to the ends of the current filament path. Unlike results for parallel co-helicity flux tubes, the current-channel passes in our simulations do not remain merged, but separate with a changed connectivity that severs an axisymmetric current loop, as shown in Figure 6.2, from a shortened driven current-channel path. An oblique contact angle between adjacent passes of the Pegasus current channel is insufficient to explain the eventual separation, as Reference [69] predicts coalescence over a significant range of contact angle between co-helicity flux tubes, $\Delta\phi \simeq \pi/4$ for merging only and $\Delta\phi \simeq \pi$ when allowing for other phenomena such as tunneling in addition to merging. Rather, the formation of the current ring resembles the slingshot interaction discussed in Chapter 3. The strong toroidal magnetic field, or more precisely, the relatively small field-line winding parameter for the current filament facilitates the slingshot interaction, as in Reference [70]. After reconnection and separation in the computations, only the helical path contains drive, while the symmetric ring freely decays.

Figure 6.3 shows that the cross-section of the reversed current density that is associated with reconnection has the characteristic S-shape for flux-rope merger, also reported in References [68, 110]. The periodic creation and spreading of flux-rope rings accumulate net axisymmetric poloidal flux as part of the magnetic relaxation process, [111] which is described later in the chapter. An early numerical study of the interaction of flux-ropes also finds conditions that produce a flux-rope ring [112]. In that case, the two distinct ropes carry net current but are driven by field-lines tied to foot-point motion, and a ring is produced in the attracting case with opposite helicity. Closed loops in the study of ropes without net current also form in cases of opposite helicity only. [69]

To characterize both the formation of the current loops and how they affect the global system, segments containing multiple successive reconnection events are examined in both the MHD and 2-fluid computations. These segments (Figures 6.4 & 6.5) are entirely prior to the formation of a global poloidal magnetic field null, when reconnection events occur frequently and the current filament dynamics dominate the system. In addition to the evolution of global quantities over the overlapping 0.8 ms segment from $2.4 \leq t \leq 3.2$ ms, comparisons are made between two merger events that occur at similar times in the MHD and 2-fluid computations. The time at which the greatest reconnection, i.e. reversed, current density occurs over the course of one such merger event–henceforth referred to as *peak reconnection*–occurs at $t = 2.97$ ms into the MHD

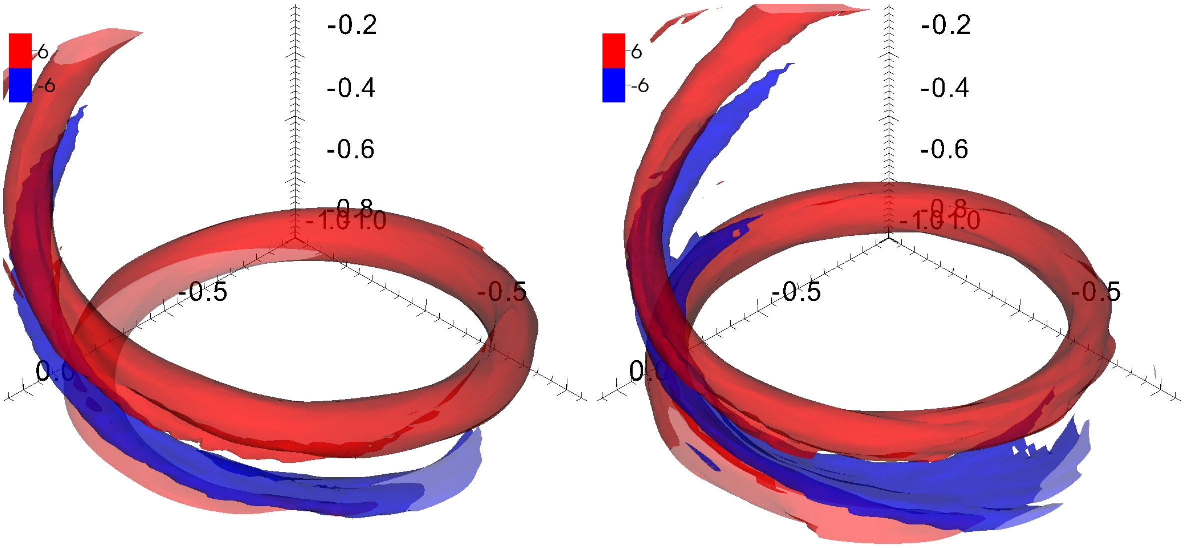

(a) $t = 2.91$ ms (b) $t = 2.93$ ms

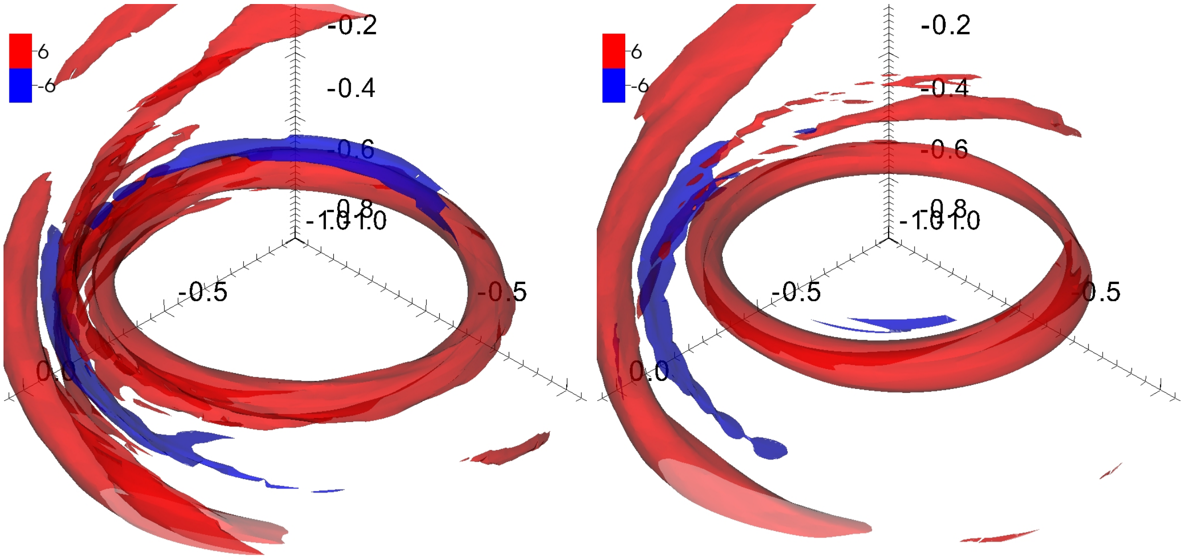

(c) $t = 2.94$ ms (d) $t = 2.95$ ms

Figure 6.2: The formation and release of a current ring. Isosurfaces of λ in units of m^{-1} are shown at different times in the 2-fluid computation. The positive-valued (red) isosurface shows current flowing from the source, and the negative-valued (blue) isosurface shows reversed current associated with reconnection.

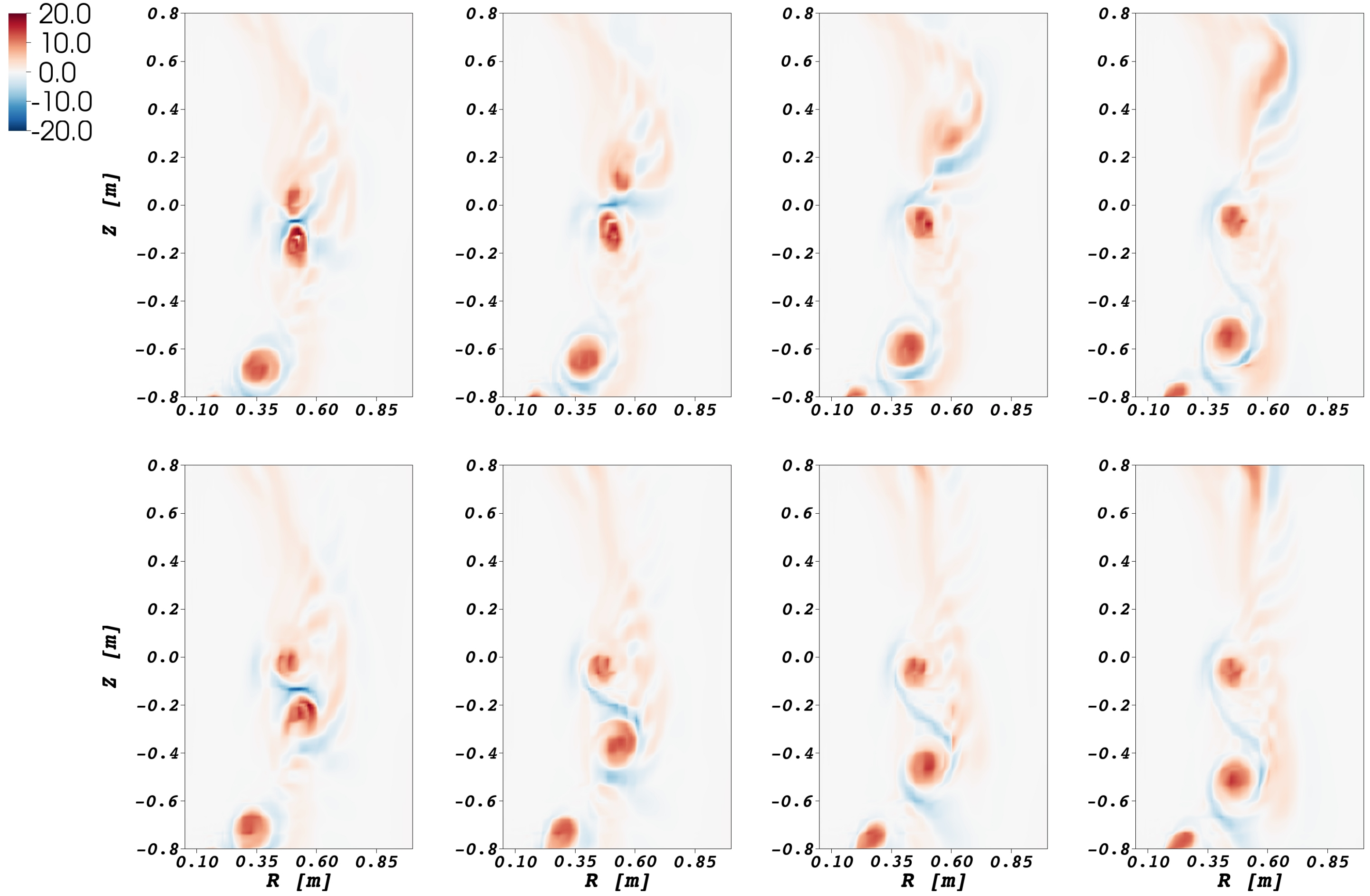

Figure 6.3: Slices of parallel current at different toroidal angles during magnetic reconnection. Contours of λ in units of m^{-1} are shown at different toroidal angles at $t = 2.93$ ms in the 2-fluid computations when $I_p = 7.2$kA. Clockwise from upper left, $\phi = 0$, $\pi/4$, $\pi/2$, etc., where the injector is centered at $\phi = 0$.

computation and at $t = 2.93$ ms into the 2-fluid computation.

Both the MHD and 2-fluid computations exhibit similar plasma properties at peak reconnection. The qualitative similarities between parallel current density and temperatures profiles are displayed in Figures 6.6 & 6.7. Quantitatively, peak values of these parameters vary by at most 6 % between the computations, as indicated in Table 6.1. However, global parameters exhibit significantly different evolution over the segment, indicated in Table 6.2. While the plasma current varies by a maximum of 7.6 % between the MHD and 2-fluid computation, it exhibits a much slow rate of increase in the 2-fluid computation, only approximately two-thirds of that in the MHD computation. Similarly, the rate of increase for both the electron and ion internal energies is approximately one-quarter slower in the 2-fluid computation. While the electron and ion internal energies vary by 20.8 % and 21.3 %, respectively, over the entire segment, they vary by only 2.0 % and 2.8 %, respectively, at the time of peak reconnection. The contention, here, is that the conditions between the computations are similar enough to allow for comparison, while simultaneously acknowledging that only exaggerated differences should be considered significant, as the computations have evolved from the beginning to these merger events either entirely with or without the 2-fluid terms in Ohm's law which would have some contribution to the plasma conditions at the time of the merger.

Figures 6.4 & 6.5 display diagnostic traces over three successive reconnection events for the MHD and 2-fluid computations, respectively. The inboard toroidal (CT) and outboard toroidal (OT) synthetic Mirnov arrays display qualitatively different behavior in the magnetic fluctuations prior to the formation of a poloidal magnetic field null near the central column. The outboard array consistently shows rotating mode behavior, indicated by the temporal phasing between the individual Mirnov signals. The inboard

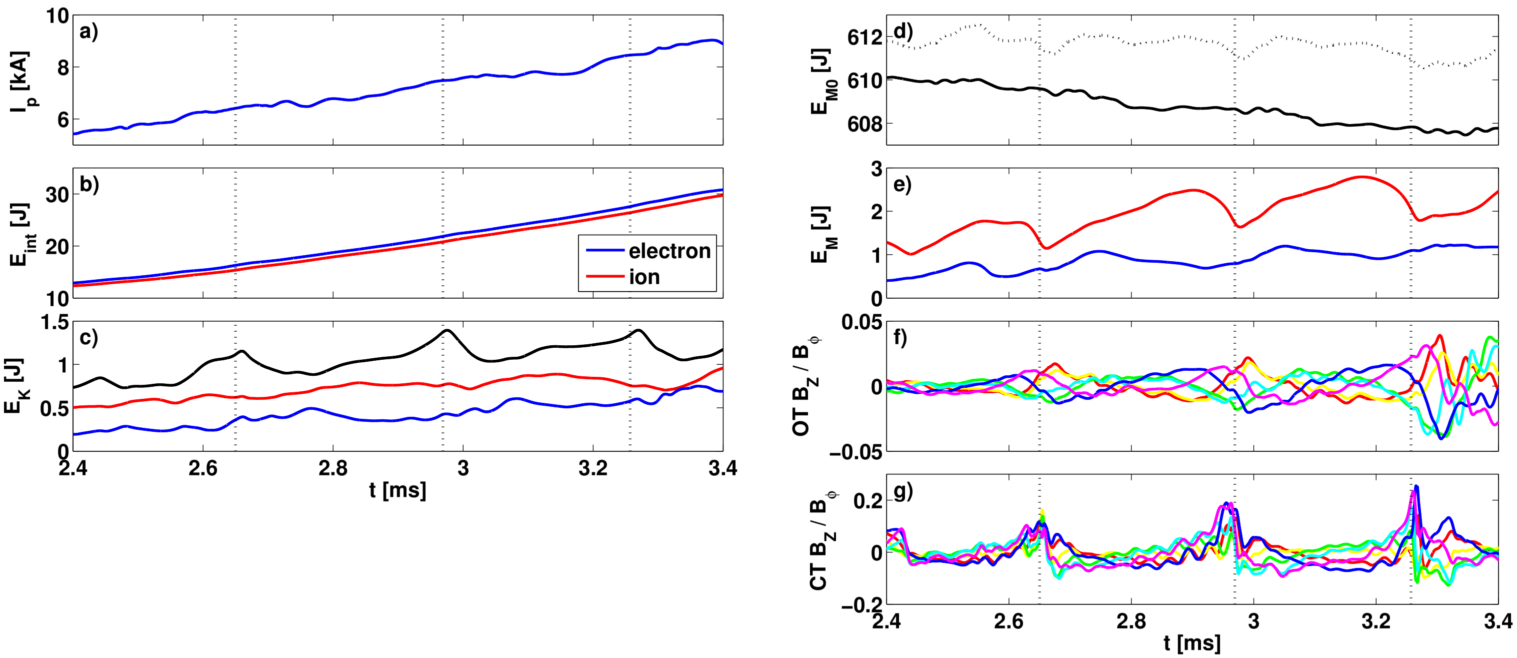

Figure 6.4: Diagnostic traces over three successive reconnection events in the MHD computation, including a) the plasma current, b) the ion and electron internal energies, c) the $n = 0$ (black), $n = 1$ (red), and the sum of the $n = 2 - 10$ (blue) components of the kinetic energy spectrum, d) the total (dashed) and $n = 0$ (solid) magnetic energies, e) the $n = 1$ (red) and the sum of the $n = 2 - 10$ (blue) components of the magnetic energy spectrum, and the magnetic signal measured by the synthetic f) outboard and g) inboard toroidal Mirnov arrays. The magnetic fluctuations in f) and g) are normalized to the vacuum toroidal field at the injector. The vertical dotted lines indicate the times at which peak reconnection occurs.

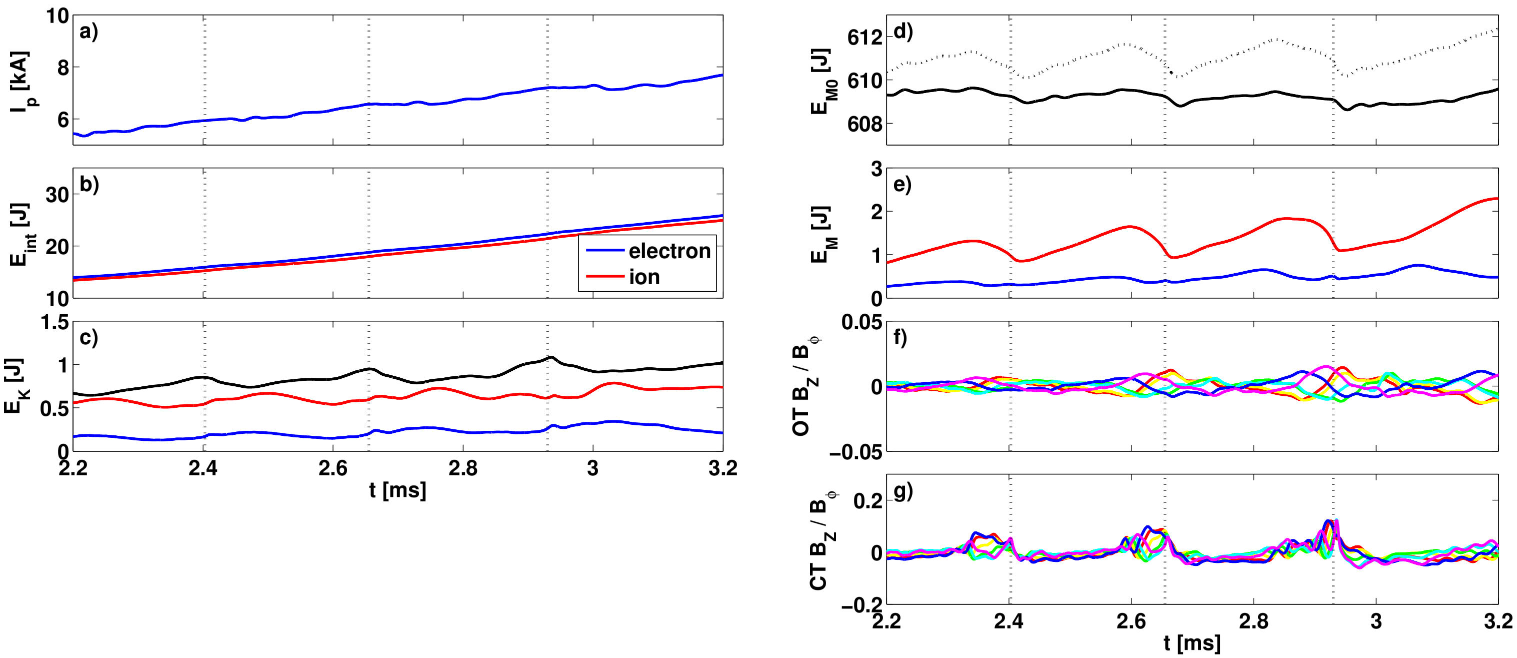

Figure 6.5: Diagnostic traces over three successive events in the 2-fluid computation, including a) the plasma current, b) the ion and electron internal energies, c) the $n = 0$ (black), $n = 1$ (red), and the sum of the $n = 2 - 10$ (blue) components of the kinetic energy spectrum, d) the total (dashed) and $n = 0$ (solid) magnetic energies, e) the $n = 1$ (red) and the sum of the $n = 2 - 10$ (blue) components of the magnetic energy spectrum, and the magnetic signal measured by the synthetic f) outboard and g) inboard toroidal Mirnov arrays. The magnetic fluctuations in f) and g) are normalized to the vacuum toroidal field at the injector. The vertical dotted lines indicate the times at which peak reconnection occurs.

Table 6.1: Plasma properties at peak reconnection

Quantity	MHD	2-fluid	Ratio
$\max\lambda\ [\mathrm{m}^{-1}]$	21.6	22.9	1.06
$\min\lambda\ [\mathrm{m}^{-1}]$	-21.3	-22.6	1.06
$\max T_e\ [eV]$	5.5	5.5	1.00
$\max T_i\ [eV]$	3.9	4.1	1.04

Local plasma properties near the reconnection region at $t = 2.97$ ms in the MHD computation and at $t = 2.93$ ms in the 2-fluid computation.

array, however, indicates a symmetric burst of MHD activity that correlates with the presence of the reversed current sheet during filament merger. The forward current in the driven current channel depresses the vertical vacuum magnetic field on the inboard side, so the reversed current sheet acts to oppose that depression. The forming current ring is in closer proximity to the central column than the outboard array. As each signal represents the superposition of the magnetic field contribution from current over the entire domain, the ability of the inboard array to directly infer current ring formation–while the outboard array is unable to–is unsurprising. As shown in Table 6.3, both the inboard toroidal synthetic Mirnov arrays display significantly smaller fluctuation amplitudes in the 2-fluid computation, indicating that the 2-fluid effects in Ohm's law are effectively weakening the dynamic response from reconnection.

Neither the electron nor the ion internal energy fluctuates significantly during a reconnection event, as indicated in Figures 6.4b & 6.5b. This result suggests that while active reconnection drives significant ohmic heating as a result of the high current

Table 6.2: Plasma properties in the overlapping segments

Quantity	MHD	2-fluid	Ratio
$\dot{I}_p$ [kA/ms]	3.18	2.13	0.67
$\dot{E}_{int,e}$ [J/ms]	17.1	12.8	0.74
$\dot{E}_{int,i}$ [J/ms]	16.6	12.5	0.75

Plasma properties obtained through linear regression over the segment $2.4 \leq t \leq 3.2$ ms in both the MHD and 2-fluid computations.

density in the reconnection current sheet, the ohmic heating is sufficiently balanced by thermal conduction to minimally affect the plasma temperature. Reconnection does not significantly alter the conditions or the length of the driven current channel over a reconnection event, and shortly after its creation, the current ring has similar properties to the driven channel, as confirmed in Figures 6.6 & 6.7 for both the MHD and 2-fluid computations. A significant drop in the temperature of either the driven current channel or the current ring would alter both its thermal conduction and ohmic heating properties, but this is not observed. Therefore, current filament merger redistributes thermal energy only insomuch as it separates a portion of the driven current channel that then decays freely, not through reconnective outflows or substantial loss of thermal confinement due to changing magnetic topology.

The fluctuations of the $n = 1$ harmonic of the magnetic energy spectrum is well correlated with the reconnection events, as shown in Figures 6.4e & 6.5e. The drop in $n = 1$ magnetic energy corresponding to the reconnection events may result from the tilting of a transit of the current filament into the horizontal plane that effectively

Table 6.3: Fluctuation amplitudes over successive reconnection events

Quantity	Calculation	MAX Amplitude	RMS Amplitude
$E_{K,0}$ $[J]$	MHD	2.79e-01	9.64e-02
	2-fluid	1.57e-01	5.09e-02
	Ratio	0.56	0.53
$E_{K,1}$ $[J]$	MHD	8.43e-02	3.03e-03
	2-fluid	8.74e-02	4.39e-02
	Ratio	1.04	1.45
$E_{M,0}$ $[J]$	MHD	3.16e-01	1.43e-01
	2-fluid	5.39e-01	2.07e-01
	Ratio	1.71	1.45
$E_{M,1}$ $[J]$	MHD	6.16e-01	2.46e-01
	2-fluid	4.86e-01	2.76e-01
	Ratio	0.79	1.12
OT B_Z $[mT]$	MHD	2.88e-01	1.20e-01
	2-fluid	1.91e-01	8.96e-02
	Ratio	0.66	0.75
CT B_Z $[mT]$	MHD	2.42e+00	7.93e-01
	2-fluid	1.81e+00	5.31e-01
	Ratio	0.75	0.67

Both the maximum and root-mean-squared temporal average fluctuation amplitudes are computed relative to a linear fit over the segment from $2.4 \leq t \leq 3.2$ ms in both the MHD and 2-fluid computations. The fluctuation amplitude for the outboard toroidal (OT) and inboard toroidal (CT) synthetic Mirnov array signals is computed for the root-mean-square average of the individual signals in each array.

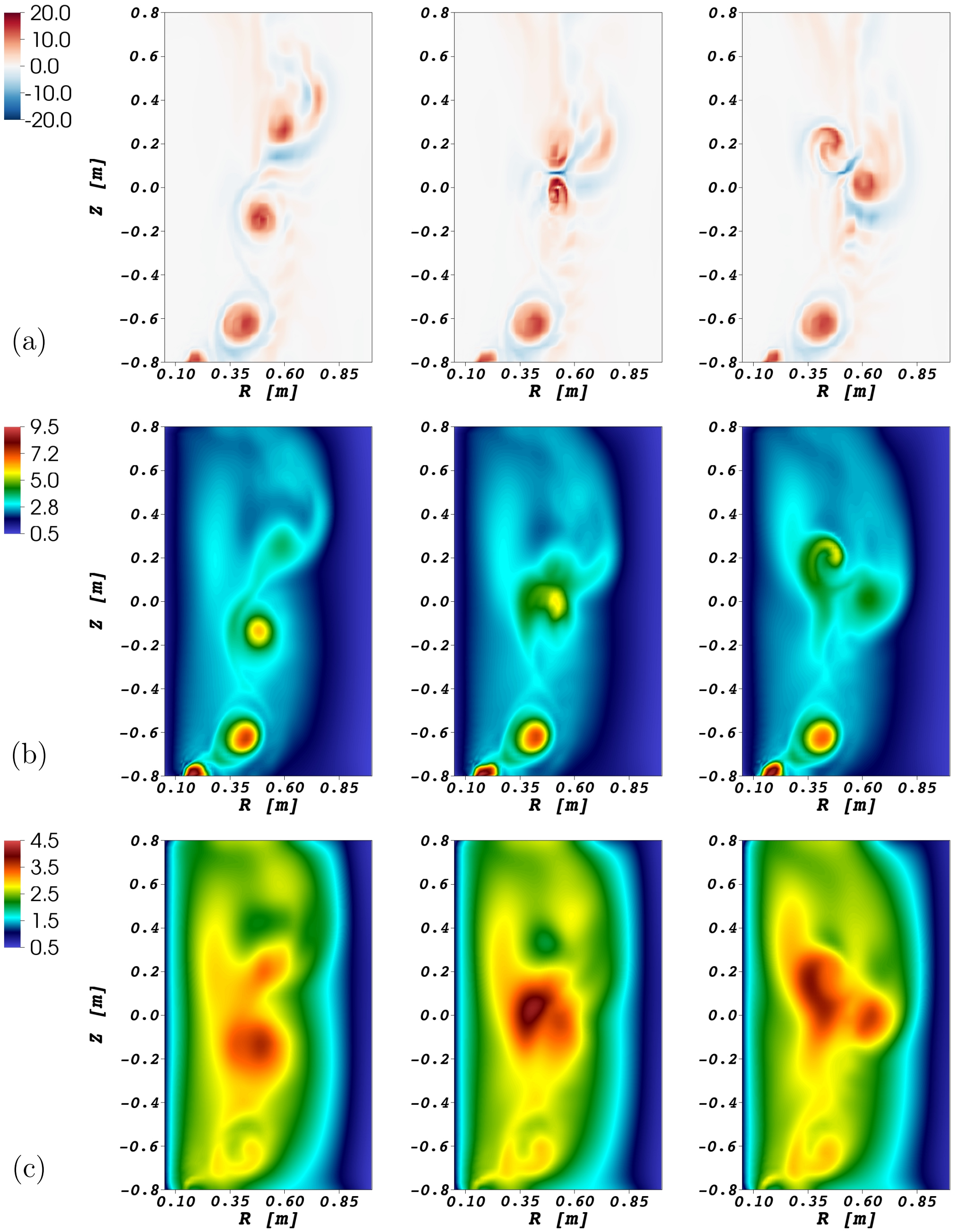

Figure 6.6: Plasma evolution over a reconnection event in the MHD computation. Contours of (a) λ in units of m^{-1} and (b) T_e & (c) T_i in units of eV at $t = 2.95$ (left), $t = 2.97$ (center), and $t = 2.99$ ms (right) for $\phi = \pi/6$.

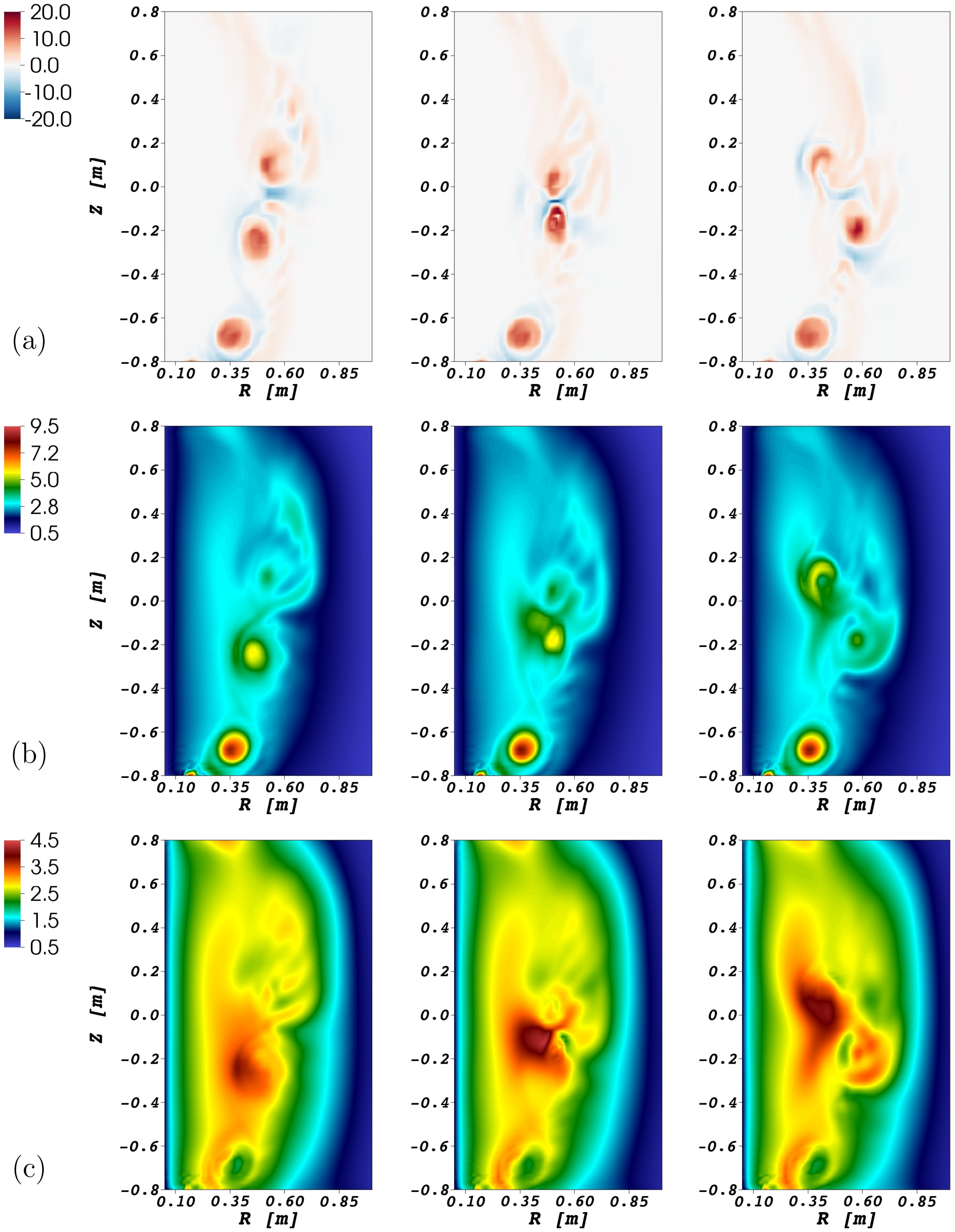

Figure 6.7: Plasma evolution over a reconnection event in the 2-fluid computation. Contours of (a) λ in units of m^{-1} and (b) T_e & (c) T_i in units of eV at $t = 2.91$ (left), $t = 2.93$ (center), and $t = 2.95$ ms (right) for $\phi = 0$.

converts the helical magnetic flux in the driven filament into poloidal magnetic flux in the current ring. A drop in the total magnetic energy suggests that conversion of magnetic energy to kinetic energy through reconnection is occurring at a faster rate than dynamo electric field (Section 6.3) is transferring energy to the mean field. While resistive dissipation also converts significant magnetic energy to thermal energy, the energy transfer rate is smaller than that for the dynamo electric fields. The fluctuations in magnetic energy are small relative to the vacuum magnetic field energy, $E_{M,vac} = 613.979$ J. The fluctuation amplitude of $n = 0$ magnetic energy (Table 6.3) is smaller in the 2-fluid computation, which is consistent with the observation later of a smaller MHD dynamo electric field than in the MHD computation. Note that the $n = 0$ magnetic energy includes contributions from the vacuum magnetic field. The effect of the 2-fluid terms on the $n = 1$ magnetic energy fluctuation amplitudes is ambiguous: while the maximum amplitude is larger in the MHD computation, the root-mean-square temporal average amplitude is larger in the two-fluid computation.

Local minima in the $n = 1$ kinetic energy shortly precede local maxima in the $n = 0$ kinetic energy, Figures 6.4c & 6.5c. The minima correspond to the stagnation of the adjacent current filament passes as they merge. The current channel rotates very rapidly ($v > 20$ km/s) about its helical axis. The tilting of the current filament does not inherently alter this rotation, but changes its projection onto the different toroidal harmonics. The fluctuation amplitude of the $n = 0$ kinetic energy (Table 6.3) is much smaller in the 2-fluid computation than in the MHD computation. The root-mean-squared temporal average fluctuation amplitude of the $n = 1$ kinetic energy is significantly larger (45 % larger) in the 2-fluid computation, but the maximum fluctuation amplitude is comparable (only 4 % larger) to the MHD computation.

Prior to the formation of a global poloidal magnetic field null, significant thermal energy is transported to the bottom surface of the domain, which corresponds to the vacuum vessel in the experiment. This transport is particularly evident in Figures 6.9–6.12, in which maxima are located on the bottom surface for parallel electron, parallel ion, perpendicular electron, and perpendicular ion heat fluxes. While the electron and ion convective heat fluxes (Figures 6.13 & 6.14) are large just a few centimeters above the bottom surface, no-slip boundary condition causes the flux at the boundary to be identically zero and produces the resulting steep gradient. Formulas for the toroidally averaged parallel, perpendicular, and convective heat fluxes are given in Equations 6.3, 6.4, & 6.5, respectively, where the species velocity $\mathbf{v}_s$ is defined in Section 5.1.

$$\langle \mathbf{q}_{\parallel,s} \rangle = \tfrac{1}{2\pi} \int_{-\pi}^{\pi} d\phi \; n\chi_{\parallel,s} \mathbf{b}\mathbf{b} \cdot \nabla T_s \tag{6.3}$$

$$\langle \mathbf{q}_{\perp,s} \rangle = \tfrac{1}{2\pi} \int_{-\pi}^{\pi} d\phi \; n\chi_{\perp,s} \left(\mathbf{I} - \mathbf{b}\mathbf{b}\right) \cdot \nabla T_s \tag{6.4}$$

$$\langle \mathbf{q}_{\mathbf{v},s} \rangle = \tfrac{1}{2\pi} \int_{-\pi}^{\pi} d\phi \; n\mathbf{v}_s T_s \tag{6.5}$$

The parallel ion heat flux (Figure 6.10) is typically more than an order of magnitude larger than the parallel electron heat flux (Figure 6.9), which likely results from heat leaking onto adjacent field lines through perpendicular thermal conduction. At a given temperature, ions have a much larger perpendicular thermal diffusivity than electrons, so heat is transferred across magnetic field lines at a much faster rate for ions (Figure 6.12) than for electrons (Figure 6.11). Parallel thermal conduction then redistributes the thermal energy along the magnetic field lines. As parallel thermal diffusivities are at least as large as the perpendicular thermal diffusivities and typically much larger, the rate at which perpendicular thermal conduction leaks energy effectively limits the rate of parallel thermal conduction, so both the parallel and perpendicular thermal conduction rates are larger for ions than electrons.

The convective heat fluxes are also typically much larger than the parallel and perpendicular heat fluxes. The greatest contribution to the convective heat flux is the high speed rotation of the current filament about its helical axis, as shown in Figures 6.8. Despite its magnitude, the convective heat flux only has a small contribution to the overall temperature evolution, as the temperature variation is small along the direction of flow, i.e. $\mathbf{v}_{i/e} \cdot \nabla T_{i/e} / |\mathbf{v}_{i/e}||\nabla T_{i/e}| \ll 1$. Note that a flow speed on the order of tens of km/s represents a significant fraction of the Alfvén speed, which is on the order of 100 km/s at the injector radius.

During peak reconnection, significant enhancement of all components of both the electron and ion heat fluxes is observed (Figures 6.9–6.14), as gauged by comparing the heat fluxes at 50 μs prior to peak reconnection–corresponding to $t = 2.92$ ms in the MHD computation and to $t = 2.88$ ms in the 2-fluid computation–to the heat fluxes at peak reconnection. The parallel electron, parallel ion, convective electron, and convective ion heat fluxes are all comparable (at most an 8 % variation) between the MHD and 2-fluid computations at 50 μs prior to peak reconnection, as indicated in Table 6.4. The perpendicular electron and perpendicular ion heat fluxes prior to peak reconnection are, respectively, somewhat smaller and larger in the 2-fluid computation than the MHD computation. However, during peak reconnection the perpendicular heat fluxes are comparable with a less than 1 % variation in the perpendicular electron and 12 % variation in the perpendicular ion heat fluxes. The parallel electron and parallel ion heat fluxes display significantly larger enhancement in the 2-fluid computation than the MHD computation with the parallel ion heat flux reaching a maximum nearly triple that in the MHD computation. This results from the effect that the 2-fluid terms in Ohm's law have on the magnetic field-line topology, which are characterized fully in the next

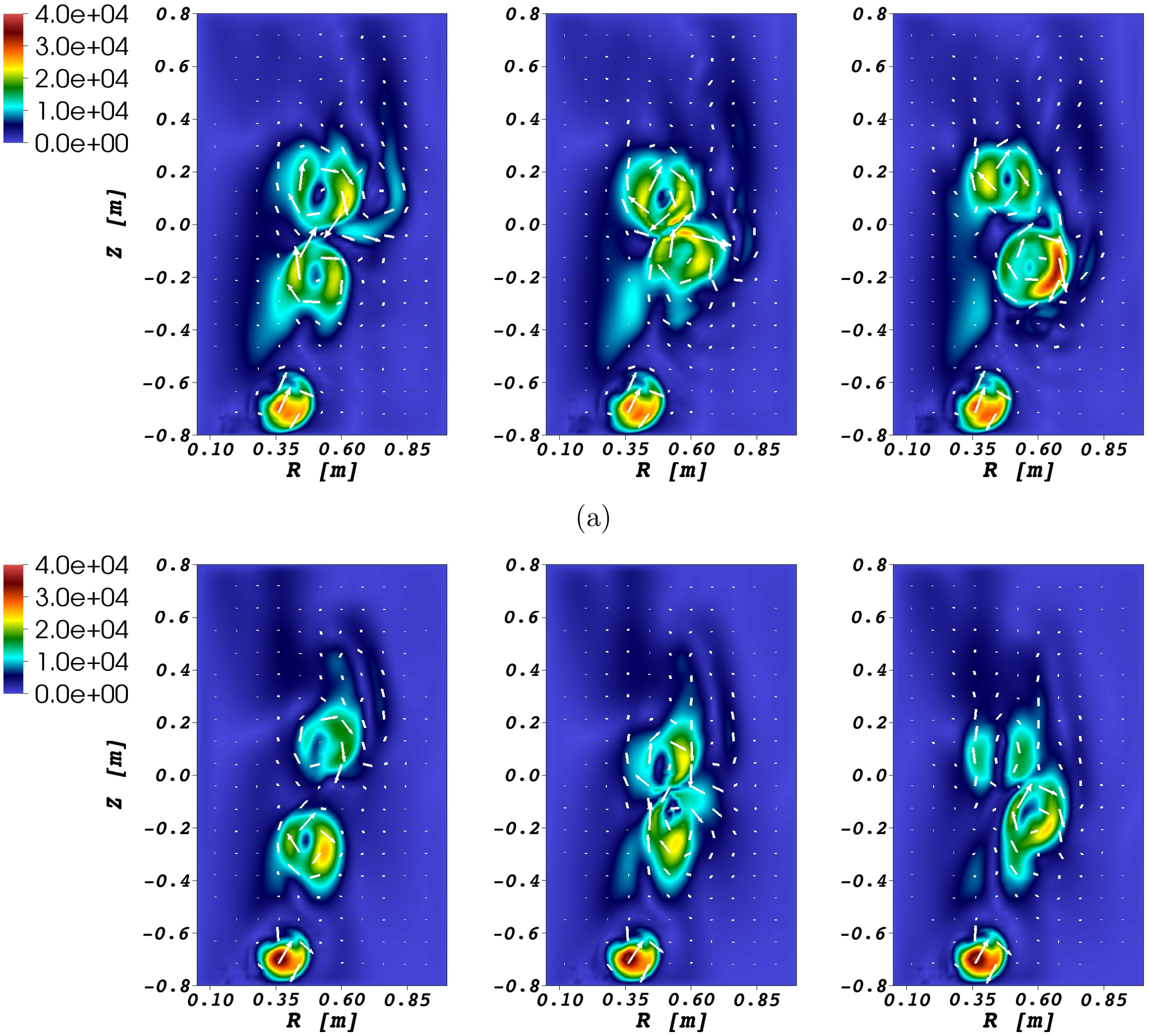

(a)

(b)

Figure 6.8: Contours of the magnitude of the plasma flow velocity, $|\mathbf{v}|$, in units of m/s for $\phi = 0$ (a) in the MHD computation at $t = 2.95$ (left), $t = 2.97$ (center), and $t = 2.99$ ms (right) and (b) in the 2-fluid computation at $t = 2.91$ (left), $t = 2.93$ (center), and $t = 2.95$ ms (right) in the MHD computation. Overlaid arrows indicate the direction of the flow velocity.

section. To preview here though, the magnetic field-lines experience greater deformation in the 2-fluid computations, but that deformation is limited to smaller spatial scale, as evidenced by larger values of the squashing factor and magnetic field-line lengths over smaller spatial scales. Both the toroidally-averaged electron and ion convective heat fluxes are smaller in the 2-fluid computation, which is consistent with observations of smaller $n = 0$ kinetic energy fluctuations over a reconnection event.

Table 6.4: Toroidally-averaged heat fluxes over a reconnection event

Quantity	Calculation	Off-Peak	Peak	Peak/Off-Peak
$\left\|\langle \mathbf{q}_{\parallel,e} \rangle\right\|$	MHD	5.03e+01	9.23e+01	1.83
	2-fluid	5.43e+01	1.27e+02	2.33
	Ratio	1.08	1.37	
$\left\|\langle \mathbf{q}_{\parallel,i} \rangle\right\|$	MHD	6.46e+02	1.51e+03	2.34
	2-fluid	6.25e+02	4.33e+03	6.93
	Ratio	0.97	2.86	
$\|\langle \mathbf{q}_{\perp,e} \rangle\|$	MHD	5.91e+02	1.07e+03	1.81
	2-fluid	4.98e+02	1.08e+03	2.16
	Ratio	0.84	1.00	
$\|\langle \mathbf{q}_{\perp,i} \rangle\|$	MHD	2.38e+03	7.01e+03	2.95
	2-fluid	2.87e+03	7.92e+03	2.76
	Ratio	1.21	1.12	
$\|\langle \mathbf{q}_{\mathbf{v},e} \rangle\|$	MHD	7.02e+04	1.19e+05	1.69
	2-fluid	7.43e+04	9.89e+04	1.33
	Ratio	1.06	0.83	
$\|\langle \mathbf{q}_{\mathbf{v},i} \rangle\|$	MHD	6.09e+04	1.00e+05	1.64
	2-fluid	6.09e+04	8.90e+04	1.46
	Ratio	1.00	0.89	

The magnitude of the toroidally averaged heat fluxes is displayed in units W/m^2. The column “Off-peak” refers to the heat fluxes 50 μs prior to peak reconnection.

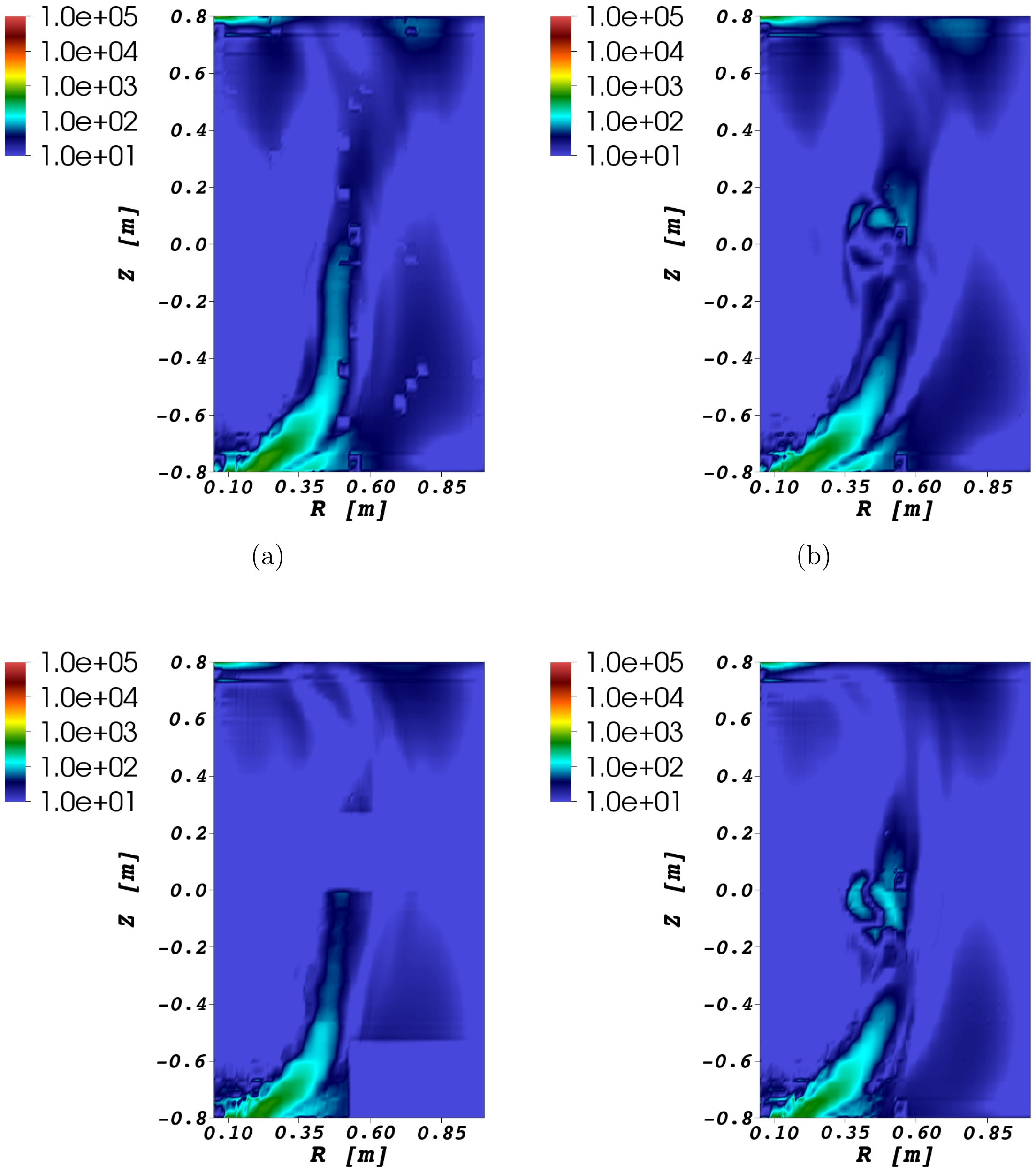

(a) (b)

(c) (d)

Figure 6.9: The magnitude of the toroidally-averaged parallel electron heat flux in units of W/m^2 is plotted for the MHD computation at (a) $t = 2.92$ & (b) $t = 2.97$ ms and for the 2-fluid computation at (c) $t = 2.88$ & (d) $t = 2.93$ ms.

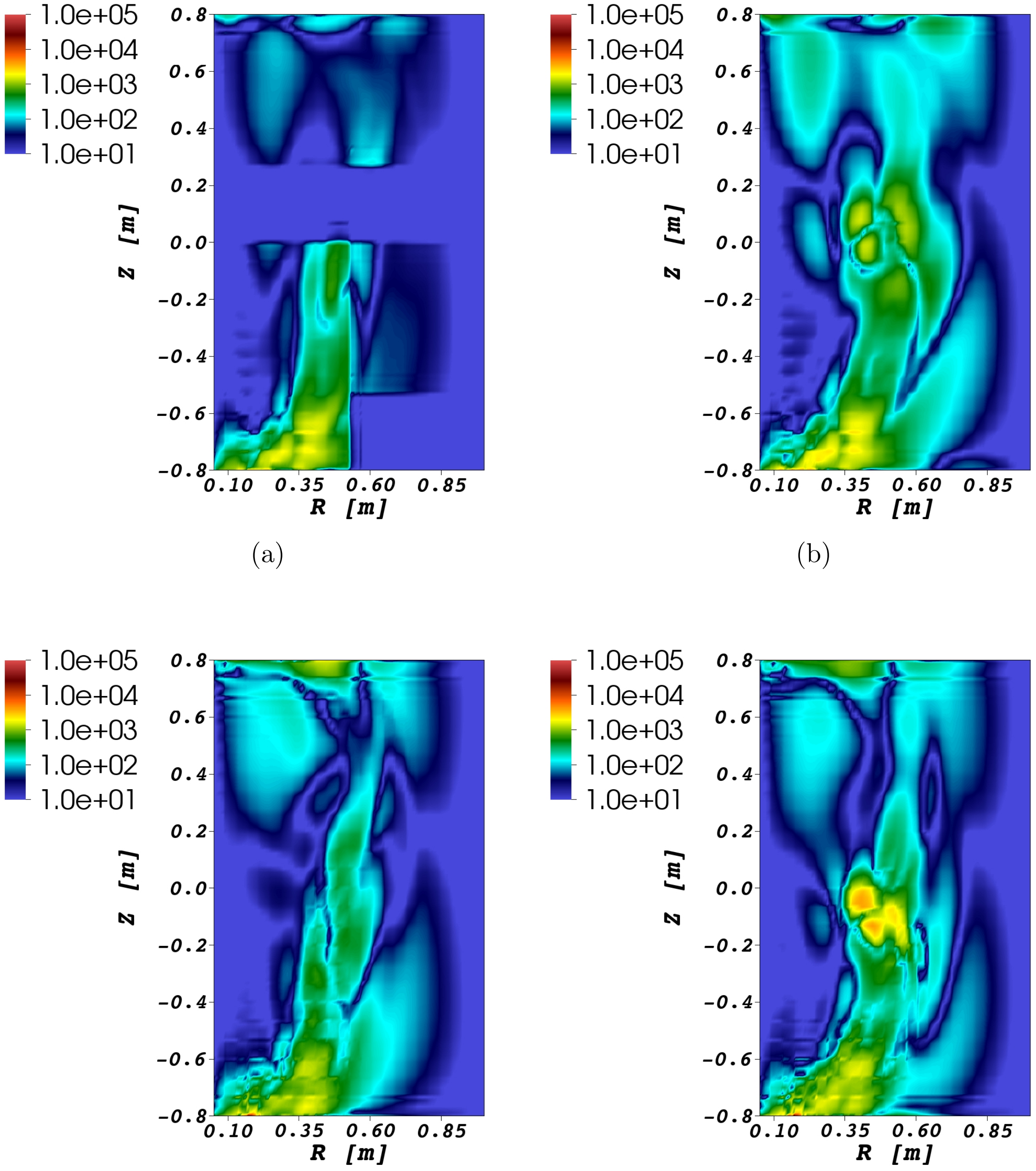

(a) (b)

(c) (d)

Figure 6.10: The magnitude of the toroidally-averaged parallel ion heat flux in units of W/m^2 is plotted for the MHD computation at (a) $t = 2.92$ & (b) $t = 2.97$ ms and for the 2-fluid computation at (c) $t = 2.88$ & (d) $t = 2.93$ ms.

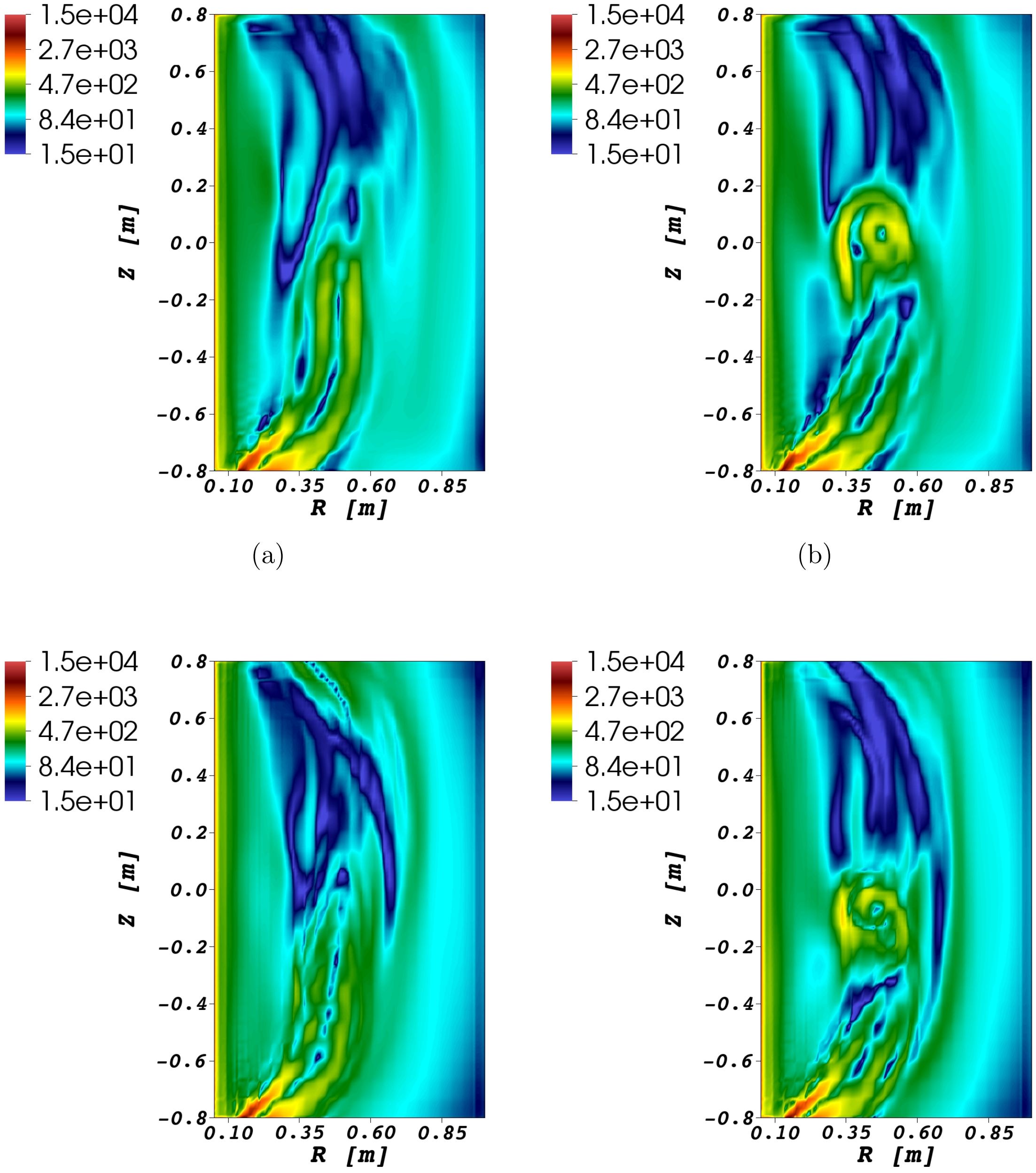

(a)

(b)

(c)

(d)

Figure 6.11: The magnitude of the toroidally-averaged perpendicular electron heat flux in units of W/m^2 is plotted for the MHD computation at (a) $t = 2.92$ & (b) $t = 2.97$ ms and for the 2-fluid computation at (c) $t = 2.88$ & (d) $t = 2.93$ ms.

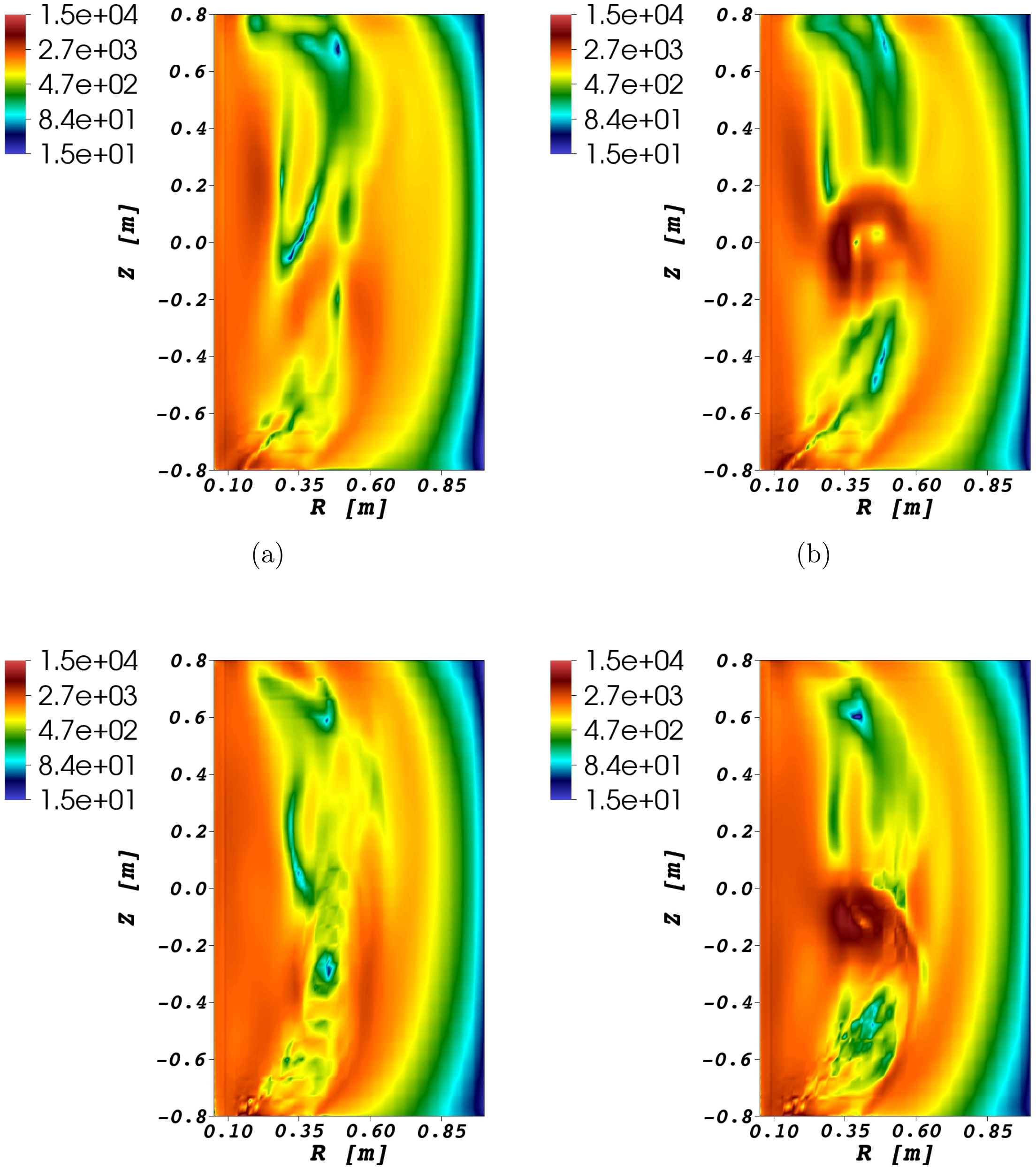

(a)

(b)

(c)

(d)

Figure 6.12: The magnitude of the toroidally-averaged perpendicular ion heat flux in units of W/m^2 is plotted for the MHD computation at (a) $t = 2.92$ & (b) $t = 2.97$ ms and for the 2-fluid computation at (c) $t = 2.88$ & (d) $t = 2.93$ ms.

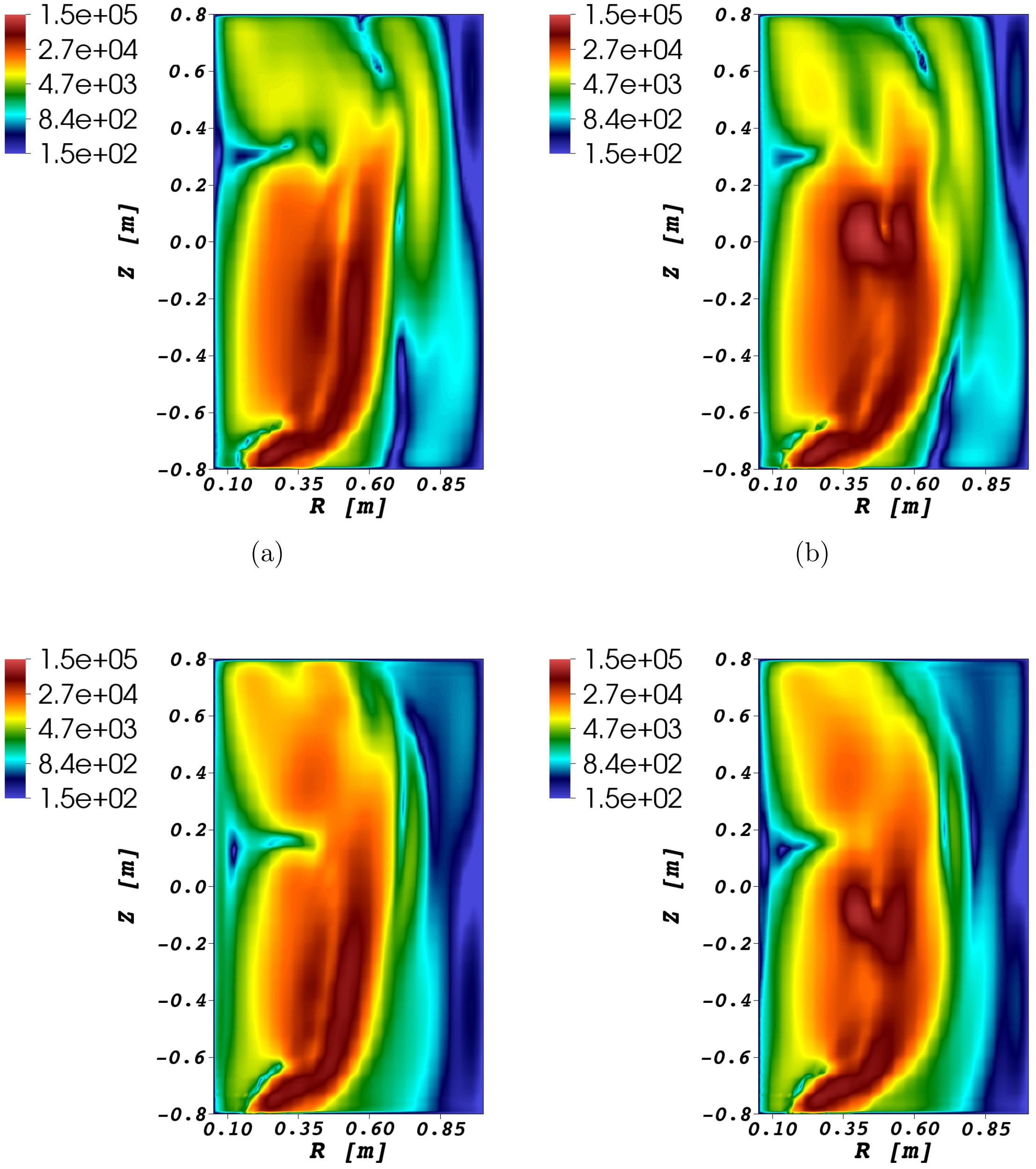

(a) (b)

(c) (d)

Figure 6.13: The magnitude of the toroidally-averaged convective electron heat flux in units of W/m^2 is plotted for the MHD computation at (a) $t = 2.92$ & (b) $t = 2.97$ ms and for the 2-fluid computation at (c) $t = 2.88$ & (d) $t = 2.93$ ms.

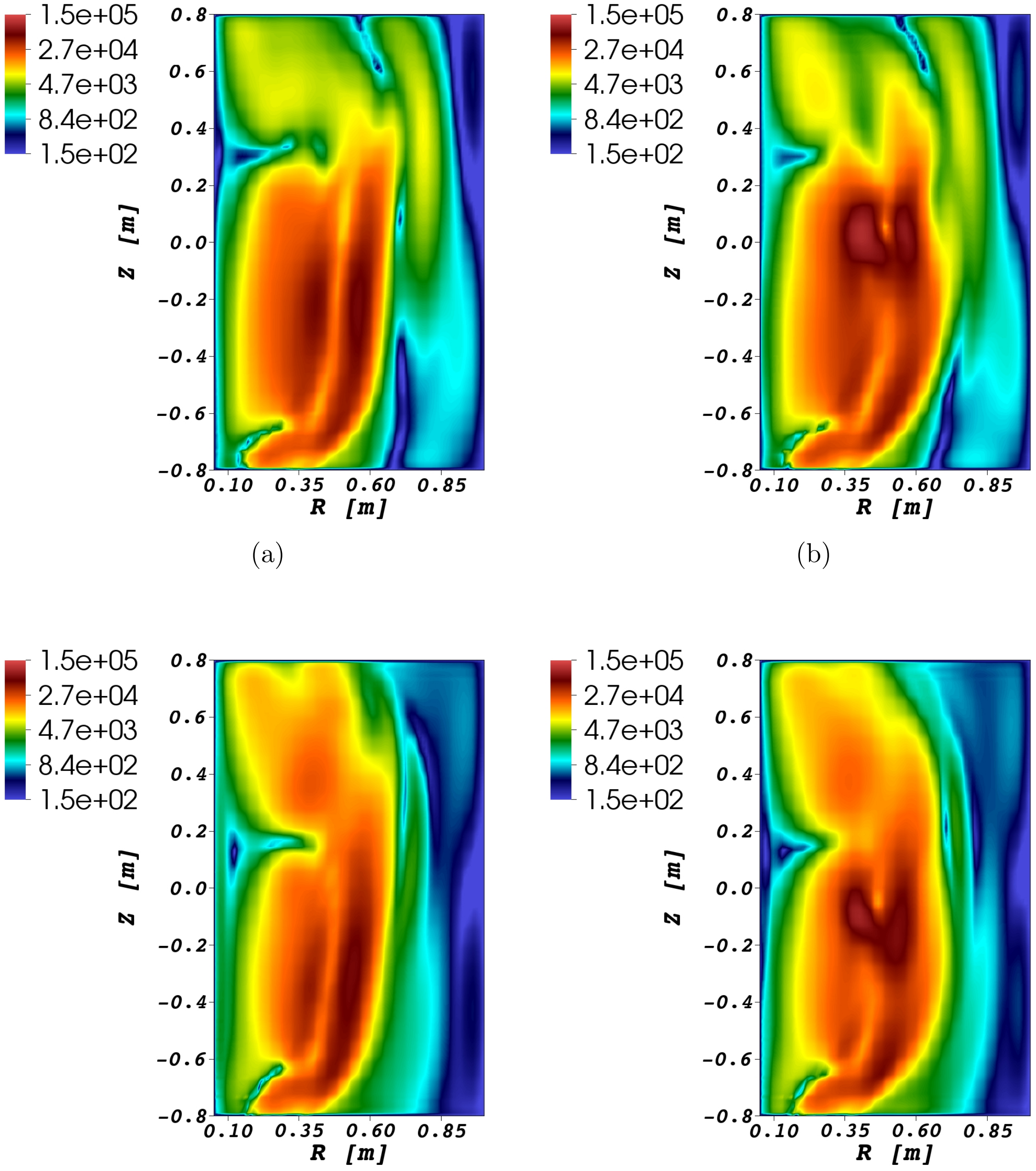

(a)

(b)

(c)

(d)

Figure 6.14: The magnitude of the toroidally-averaged convective ion heat flux in units of W/m^2 is plotted for the MHD computation at (a) $t = 2.92$ & (b) $t = 2.97$ ms and for the 2-fluid computation at (c) $t = 2.88$ & (d) $t = 2.93$ ms.

6.2 Characterization of Magnetic Topology Evolution

The formation of a current ring represents a distinct change in the magnetic field-line topology. In this section, the magnetic field-line topology is characterized through a number of techniques rooted in field-line integration. Magnetic field-line trajectories are launched from an initial position ($\mathbf{r}_0$) and integrated to a terminal position ($\mathbf{r}_1$) where the magnetic field-line intersects the domain boundary.

$$\mathbf{r}_1 = \mathbf{r}_0 + \int_0^L ds\ \hat{\mathbf{b}} \tag{6.6}$$

In general, the length of the field-line trajectory (L) is not known *a prior*, and therefore, must also computed through field-line integration. The radial magnetic field specified ($B_R = 0$) on the inboard and outboard surfaces causes both ends of all open magnetic field-line trajectories to intersect the top and bottom surfaces of the domain. Figure 6.15 shows one such trajectory entering the domain through the bottom ($Z = -0.8$ m) surface and exiting through the top ($Z = +0.8$ m). Magnetic field-line integration is performed numerically using the NIMFL diagnostic included with the NIMROD code.

Figure 6.17 shows parallel and anti-parallel trajectories launched from a grid of points (Figure 6.16) that covers the source region. Magnetic field-lines are traced in both directions from the injector, and then, the parallel and anti-parallel trajectories are combined into a single trajectory spanning from $-0.8 \leq Z \leq 0.8$ m. The two times shown in the figure represent a small fraction of the ring formation in Figure 6.2. At the earlier time in Figure 6.17a, the traces are topologically unchanged from conditions before the start of the reconnection event: the trajectories make at most a single pass around the forming current ring. Only a few field-line trajectories at this time bypass the forming flux-rope ring, while most pass through it.

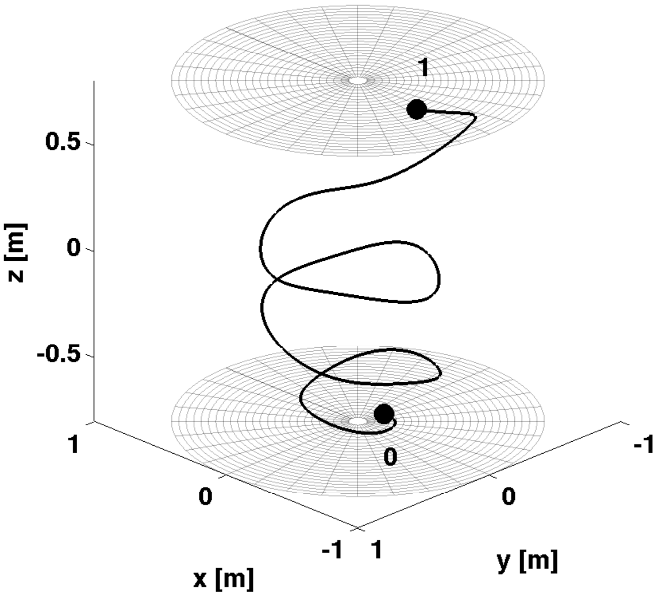

Figure 6.15: Field-line mapping. A magnetic field-line trajectory is launched from the position (X_0, Y_0) on the plane $Z_0 = -0.8$ m and traced to the position (X_1, Y_1) on the plane $Z_1 = +0.8$ m.

Shortly thereafter ($\Delta t = 10\ \mu$s), one of the trajectories makes multiple passes around the ring region before progressing to the top of the domain, as evident in Figure 6.17b. Only a single trajectory now passes through the forming flux-rope ring, indicating a decoupling of the forming flux-rope ring from the injector. As reconnection continues, the ring completely separates from the driven flux rope.

As discussed in Chapter 3, the location of magnetic reconnection in a three-dimensional system can be identified by finding a surface of large squashing degree (Q). As all magnetic field-line trajectories in the computations intersect both the top and bottom surfaces of the domain, the squashing degree analysis is readily applied to the simulation data. A 5000×256 (radial x azimuthal) mesh of launch points provides a discrete representation of the field-line mapping functions, $X_1(X_0, Y_0)$ and $Y_1(X_0, Y_0)$,

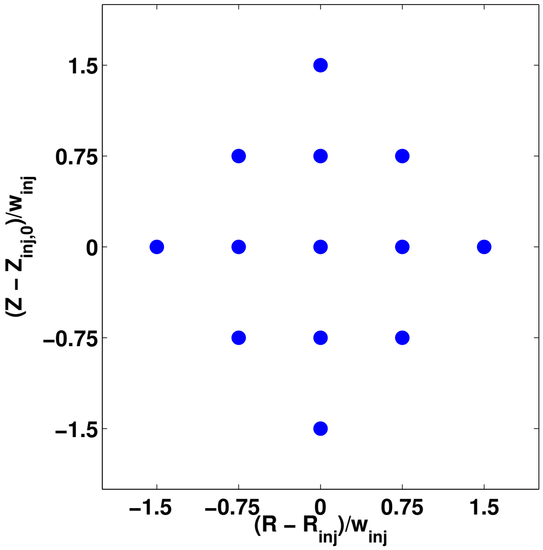

Figure 6.16: Launch points for field-line trajectories that cover the source region. The launch positions are relative to the center of the injector $R_{inj} = 35$ cm and $Z_{inj,0} = -70$ cm at $\phi = 0$.

where X and Y are Cartesian coordinates in the constant Z-planes of the bottom ("0" subscript) and top ("1" subscript) surfaces. Thus, the squashing degree has the form

$$Q = \frac{1}{J}\left[\left(\frac{\partial X_1}{\partial X_0}\right)^2 + \left(\frac{\partial Y_1}{\partial Y_0}\right)^2 + \left(\frac{\partial Y_1}{\partial X_0}\right)^2 + \left(\frac{\partial X_1}{\partial Y_0}\right)^2\right] \tag{6.7}$$

where J is the Jacobian determinant. In the computations, $\mathbf{B} \cdot \hat{\mathbf{n}}$ is uniform on the top and bottom surfaces, so the Jacobian determinant reduces to $J = 1$ and Q is identically the square of the norm of the mapping.

The launch points have $R_0 > 0.1$ m to avoid the large values of Q near the central column from the externally sourced vacuum field. Uniform values of $I = RB_\phi$ and B_Z in the vacuum magnetic field produce a mapping (Equation 6.8) with a one-dimensional dependency on the major radial coordinate of the launch position (R_0). The corresponding squashing degree ($Q \propto R_0^{-4}$) becomes exceedingly large near the

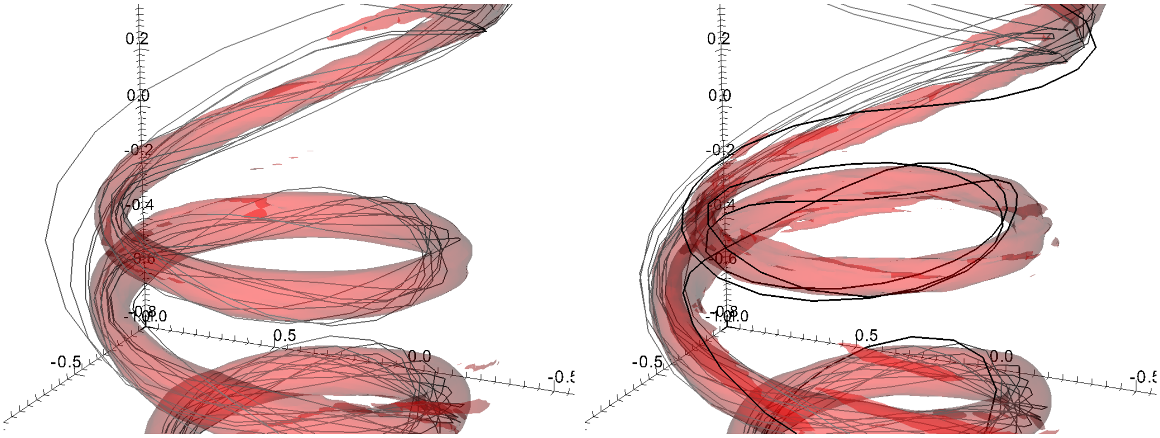

(a) $t = 2.925$ μs (b) $t = 2.935$ μs

Figure 6.17: Field-line trajectories launched from a grid of 13 positions covering the source region pass through the forming flux-rope ring in the two-fluid computation. The darkened trace accentuates a trajectory that makes more than one pass through the forming ring.

central column, up to $Q = 5.88 \times 10^6$ at $R_0 = 0.05$ m. The length of the vacuum magnetic field-lines (L) also becomes large near the central column, up to $L = 60.6$ m at $R_0 = 0.05$ m.

$$R_1 = R_0 \tag{6.8a}$$

$$\phi_1 = \phi_0 + I\Delta Z / R_0^2 B_Z \tag{6.8b}$$

$$Q = 2 + 4\left(I\Delta Z / R_0^2 B_Z\right)^2 \tag{6.9}$$

$$L = \Delta Z\sqrt{1 + \left(I / R_0 B_Z\right)^2} \tag{6.10}$$

Contours of the squashing factor, $\sqrt{Q}$, are computed from finite differences of the discrete mapping information at peak reconnection in both the MHD and 2-fluid computations, and are plotted with respect to launch positions in Figures 6.18 a & b. During the simulated flux-rope merging, large Q-values appear as rolled surfaces, as indicated by their projection onto the Z_0 plane. The existence of a quasi-separatrix layer along these surfaces is inferred. Corresponding rolled surfaces are observed for the magnetic field-line length plotted as function of launch position, Figures 6.18 c & d, where the largest field-line lengths correlate with the largest values of squashing factor for $R_0 > 0.15$ m. Like the squashing factor, the magnetic field-line lengths become large near the center column as a results of the externally applied vacuum field structure. The maximum values of the squashing factor and magnetic field-line length are 2958.7 and 83.4 m, respectively for the MHD computation and 2769.1 and 98.5 m, respectively, for the 2-fluid computation. In general, the 2-fluid computation experiences finer spatial scale variation in the two quantities and larger values of both quantities occupy a greater fraction of the domain than in the MHD computations.

To determine whether the rolled surfaces of large-Q indicate the formation of a QSL related to magnetic reconnection, the location where the large-Q trajectories intercept the $\phi = 0$ plane is considered relative to the location of the reversed current sheet. Figures 6.19 a & b shows this information with Poincaré plots for trajectories with large values of Q and $R_0 > 0.2$ m overlaid on contours of the parallel current parameter λ in the MHD and 2-fluid computations, respectively. As these trajectories progress upward from the launch positions, they track along the inboard side of the next pass of the current channel and then bifurcate at $Z \approx -0.5$ m. Some of the trajectories continue along the inboard side of the next current channel pass, while other trajectories continue along its outboard side. The trajectories on the inboard side bifurcate a second time at $Z \approx -0.05$ m, which is the reconnection site, as indicated by the large negative values of λ. This second bifurcation is consistent with the relation between QSLs and magnetic reconnection presented in References [68, 112].

The first bifurcation is caused by a X-point like behavior between the adjacent

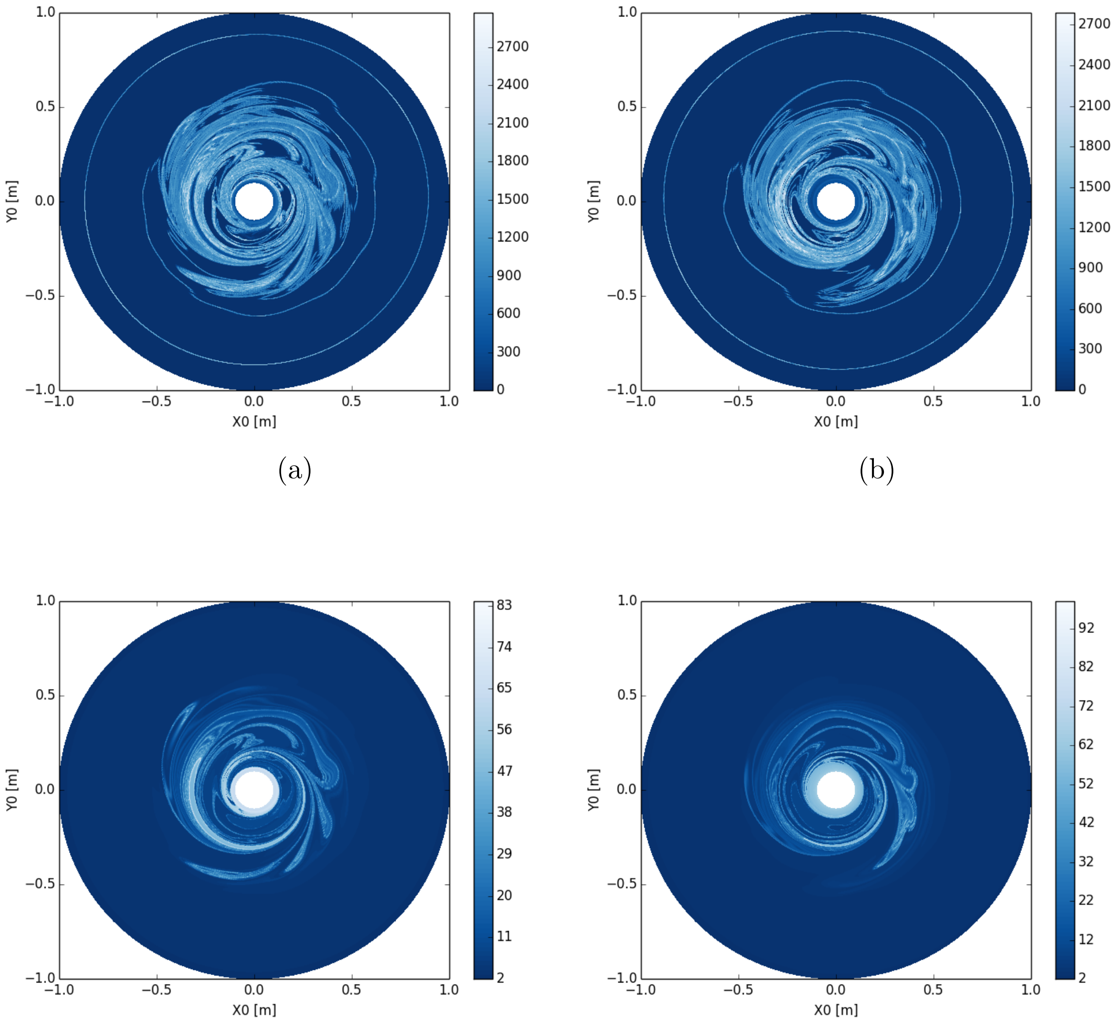

(a) (b) (c) (d)

Figure 6.18: Squashing factor and magnetic field-line length as a function of launch position. The squashing factor is plotted at (a) $t = 2.97$ ms in the MHD computation and (b) $t = 2.93$ ms in the 2-fluid computation. The corresponding magnetic field-line lengths are plotted in Figures (c) for the MHD computation and (d) for the 2-fluid computation.

passes, but not from magnetic reconnection reconnection. [113] As the magnetic field-distribution during merger resembles the classic description of island-coalescence instability in Reference [114], an analogy can be drawn between the first bifurcation and the X-point away from the merger location during island coalescence instability. Magnetic island chains from tearing can form in magnetically sheared periodic systems along a resonant surface, where $\mathbf{B} \cdot \mathbf{k} = 0$ with $\mathbf{k}$ being the helical wavenumber vector. During island coalescence instability, the distance between some adjacent O-points decreases, while the distance between others increases.

For small-amplitude, helically symmetric perturbations, the X-points of the magnetic separatrix remain on the resonant surface, and both X- and O-points can be identified by nulls of the helical field $\mathbf{B}_h = B_R\hat{\mathbf{R}} + \mathbf{B} \cdot \hat{\mathbf{k}}\hat{\mathbf{k}}$. The analogy considers the cylindrical surface $R = R_{inj}$ in Pegasus to be similar to the resonant surface in a periodic system, where $\mathbf{k} = 2\pi G \Delta z^{-1}\hat{\mathbf{z}} - R_{inj}^{-1}\hat{\phi}$ with $G = 3.96$ for the geometric winding of the vacuum field at the injector location. The magnitude of this $\mathbf{B}_h$ is plotted in Figures 6.19 c & d for the MHD and 2-fluid computations with the same magnetic punctures shown in Figures 6.19 a & b. The overlays show that the first bifurcation is near the minimum in $|\mathbf{B}_h|$ between the lowest two passes of the flux rope, and the second bifurcation is near the minimum in $|\mathbf{B}_h|$ between the second and third passes, where reconnection is occurring. Unlike the magnetic field-distribution for the island-coalescence instability, the loose-solenoid equilibrium in the computations is neither sinusoidal nor periodic, and the source ties the structure near one end.

Large Q-values can be expected more generally from chaotic scattering of trajectories around the forming ring, and chaotic scattering is evident from the plots of field-line length in Figure 6.20. With chaotic scattering, regions where long trajectories rise above a background with the longest values appearing at the edge of each region. i.e. castle-like structures, appear across different spatial scales in R. These castle structures indicate chaotic scattering around magnetic structures and have been identified previously in both the flux-rope simulations of Reference [112] and in weakly driven conditions for spheromaks in Reference [115]. Chaotic field-line scattering also occurs between reconnection events, Figures 6.20 a & b, but has a less pronounced effect than during a reconnection event, Figure 6.20c.

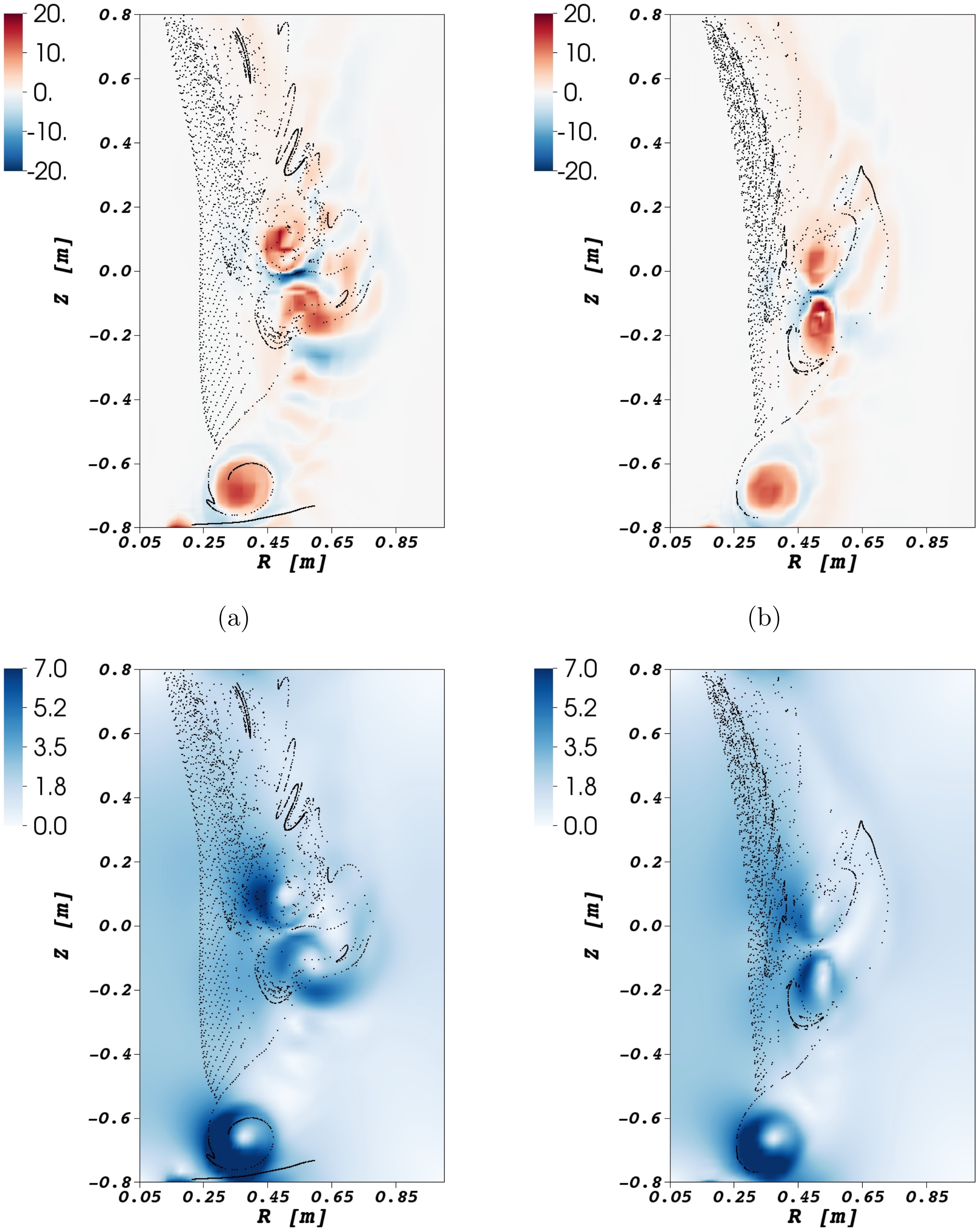

(a) (b)

(c) (d)

Figure 6.19: Puncture plots of magnetic field-lines with large squashing degree. Puncture plots for magnetic field-lines with $\log Q \geq 15$ and $R_0 \geq 20$ cm are overlaid (a-b) on contours of λ in units of m^{-1} and (c-d) on contours of $|\mathbf{B}_h|$ in units of mT at (a,c) $t = 2.97$ ms in the MHD computation and (b,d) $t = 2.93$ ms in the 2-fluid computation.

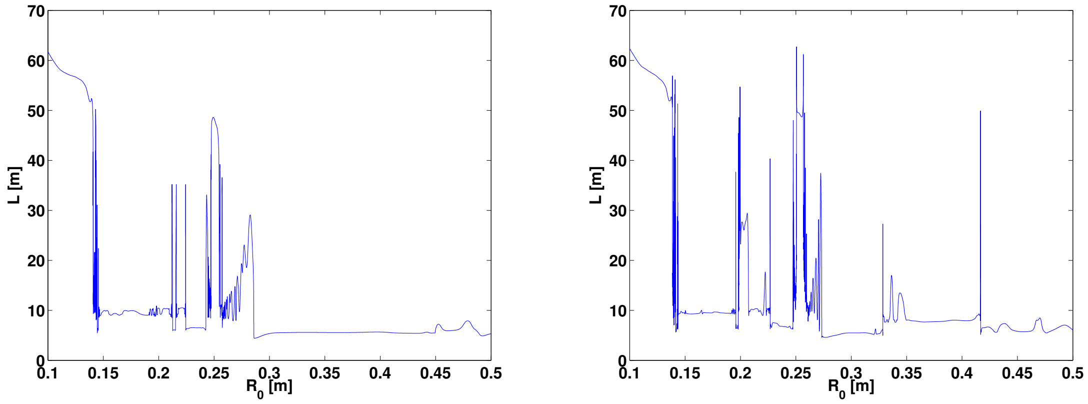

(a) $t = 2.89$ ms

(b) $t = 2.91$ ms

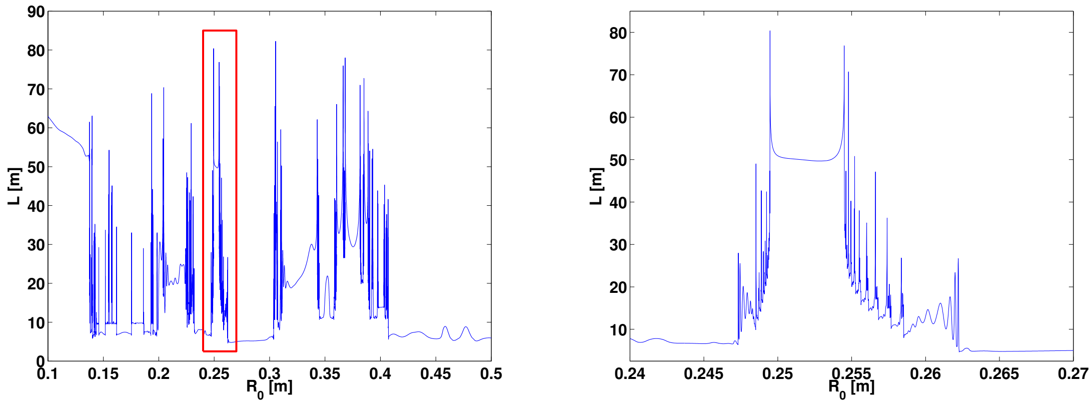

(c) $t = 2.93$ ms

(d) $t = 2.93$ ms

Figure 6.20: Field-line length as a function of launch position. 50,000 field-line trajectories are launched at the times indicated in the two-fluid computation along a radial chord, 0.1 m $\leq R \leq$ 0.5m, with $Z = -0.8$ m and $\phi = 0$. Figure (d) is zoomed in to highlight a castle-like structure in the boxed region of (c). Figures (b) & (c) correspond to the times shown in Figures 6.2 (a) & (b), respectively.

6.3 Development of Poloidal Magnetic Flux

While the helicity source in our simulations directly induces poloidal magnetic flux, as $\oint \mathbf{E}_{inj} \cdot \hat{\phi}\, d\phi \neq 0$, wave propagation and macroscopic dynamics are required of the system to develop a tokamak-like current distribution. During the merger process, a transit of the current filament tilts into a horizontal plane–visualized in Figure 6.21, where the images shown correspond to the same times as the images in Figure 6.2. While the driven current filament is only constrained by the source region, the endpoints of the filament are essentially unchanged on the time-scale of the current filament merger and reconnection.

The tilting of a transit of the current filament into the horizontal plane constitutes coherent dynamo action that affects the global distribution. The evolution of the mean-field magnetic field energy, $\langle B\rangle^2/2\mu_0$, is described by the mean-field Poynting's theorem in Equation 6.11, where $\langle\ \rangle$ indicates toroidal averaging. The mean-field Poynting's theorem is constructed by taking the scalar product of the toroidally averaged magnetic field with the toroidally averaged Maxwell-Faraday equation and using $\mu_0\langle \mathbf{J}\rangle = \nabla \times \langle \mathbf{B}\rangle$

$$\frac{1}{2\mu_0}\frac{\partial \langle B\rangle^2}{\partial t} + \nabla \cdot \left[\frac{\langle \mathbf{E}\rangle \times \langle \mathbf{B}\rangle}{\mu_0}\right] = -\langle \mathbf{E}\rangle \cdot \langle \mathbf{J}\rangle \tag{6.11}$$

Energy is transferred to the mean-field fluctuations when $\langle \mathbf{J}\rangle \cdot \langle \mathbf{E}\rangle < 0$. Correlations of asymmetric fluctuations of velocity $\tilde{\mathbf{v}}$ and current density $\tilde{\mathbf{J}}$ with fluctuations of magnetic field $\tilde{\mathbf{B}}$, drive mean toroidal electric fields through both the MHD contribution, $-\langle \tilde{\mathbf{v}} \times \tilde{\mathbf{B}}\rangle_\phi$, and the Hall contribution, $\langle \tilde{\mathbf{J}} \times \tilde{\mathbf{B}}\rangle_\phi/ne$.

Significant magnetic energy is dissipated through ohmic heating, as shown in Figure 6.22. However, significant energy is transferred to the mean-field magnetic field energy through the MHD and Hall dynamo electric fields. The MHD dynamo electric

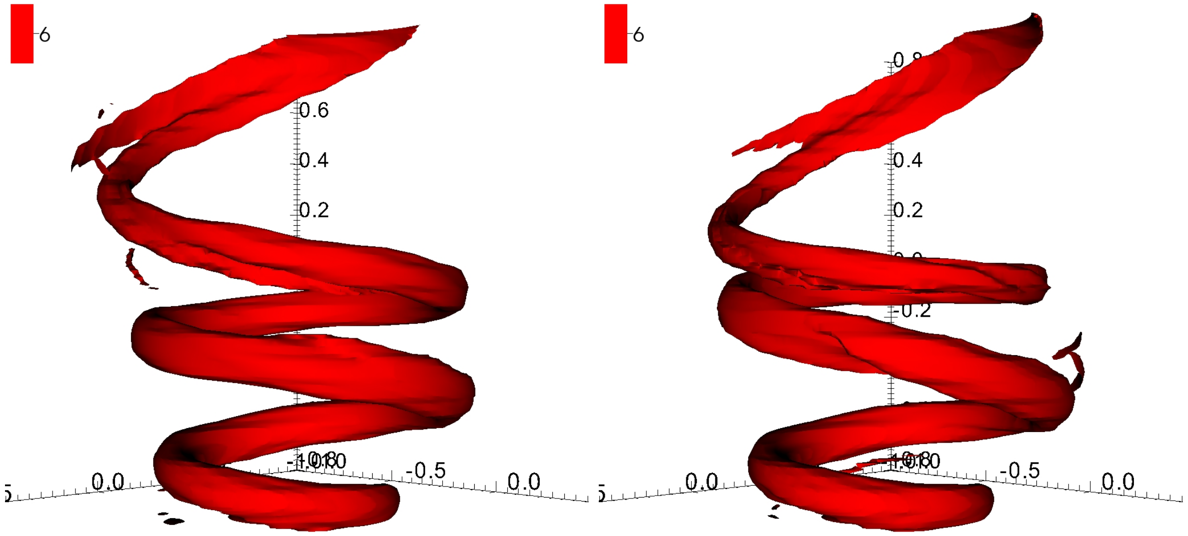

(a) $t = 2.91$ ms (b) $t = 2.93$ ms

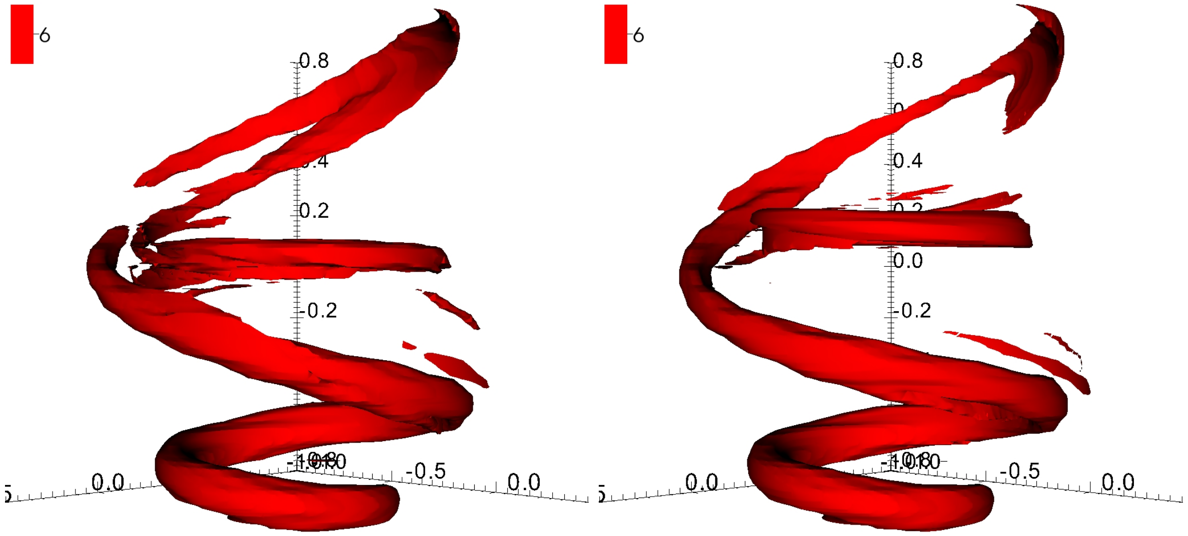

(c) $t = 2.94$ ms (d) $t = 2.95$ ms

Figure 6.21: A winding of the current filament tilts into the horizontal plane and is released. An isosurface of λ in units of m^{-1} with a horizontal view at the midplane ($Z = 0$ m) in the 2-fluid computation. A winding of the current channel is rotated into the horizontal plane (c) and released (d) from the driven current channel.

field energy transfer rate, $-\langle\tilde{\mathbf{v}}\times\tilde{\mathbf{B}}\rangle\cdot\langle\mathbf{J}\rangle$–displayed in Figures 6.23a & 6.24a for the MHD and 2-fluid computations, respectively–exceeds the energy dissipation rate by ohmic heating at the location where the current ring forms. The Hall dynamo electric field energy transfer rate, $\langle\tilde{\mathbf{J}}\times\tilde{\mathbf{B}}\rangle/ne\cdot\langle\mathbf{J}\rangle$–displayed in Figure 6.25a–is also larger than the ohmic dissipation rate.

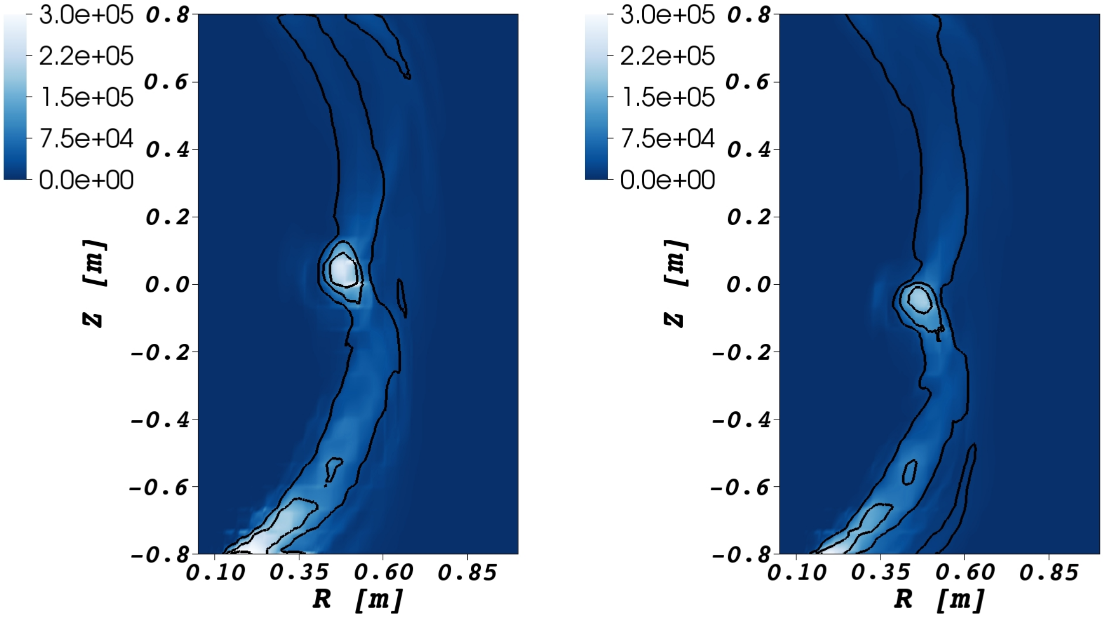

(a) (b)

Figure 6.22: Color contours of the toroidally averaged ohmic heating, $\langle\eta J^2\rangle$, in units of W/m^3 (a) $t = 2.97$ ms in the MHD computation and (b) $t = 2.91$ ms in the 2-fluid computation. The black contours show the toroidally averaged parallel current density, $\langle\lambda\rangle > 0$.

Figures 6.23 & 6.24 display the toroidal MHD dynamo electric field expressed as an effective loop voltage, $-2\pi R\langle\tilde{\mathbf{v}}\times\tilde{\mathbf{B}}\rangle_\phi$, in the MHD and 2-fluid computations, respectively. In both computations, the largest contribution to the total toroidal MHD dynamo electric field, Figures 6.23b & 6.24b, at the location of current filament merger, is driven by the vertical displacement of the current filament, Figures 6.23d & 6.24d. The radial flows, Figures 6.23c & 6.24c, do not provide as much of a contribution to current ring formation. The MHD dynamo effect is responsible for the significant transfer of energy to the current ring, as $-2\pi R\langle\tilde{\mathbf{v}} \times \tilde{\mathbf{B}}\rangle_\phi < 0$ and $\langle\lambda\rangle > 0$ at the location of current ring formation, where $\lambda > 0$ necessarily implies $J_\phi > 0$.

The toroidal MHD dynamo electric field is qualitatively similar in both the MHD and 2-fluid computations. However, the MHD dynamo electric field has a significantly greater contribution in the MHD computation with minimum loop voltage of approximately -17.4 V than in the 2-fluid computation with a minimum loop voltage of approximately -10.3 V. This result is consistent with observations above that the two-fluid effects in Ohm's law weakens the dynamic response from reconnection. In the two-fluid computations, the ion fluid decouples from the electron fluid. Therefore, the ion fluid–which is the dominant contribution to the center-of-mass flow velocity–is not driven to as small spatial scale during reconnection as in the MHD computation, producing a smaller MHD dynamo electric field. Summing the MHD and Hall dynamo electric fields in the two-fluid computation results in a smaller total dynamo electric field than in the MHD computation.

Figure 6.25 displays the toroidal Hall dynamo electric field expressed as an effective loop voltage, $+2\pi R\langle\tilde{\mathbf{J}} \times \tilde{\mathbf{B}}\rangle_\phi/ne$, in the two-fluid computation. The vertical current fluctuations have the largest contribution to the total toroidal Hall dynamo electric field, Figure 6.25d, at the location of current filament merger. The Hall dynamo effect acts over a much smaller region than the MHD dynamo and is antisymmetric about the forming flux-rope ring. Therefore, the Hall dynamo primarily contributes to the shaping of the current ring.

Figure 6.26 demonstrates the conversion of helical flux in the driven current channel to poloidal flux as a transit of the current filament rotates in the horizontal plane. As the current ring decays, the amplified flux then diffuses into the surrounding plasma.

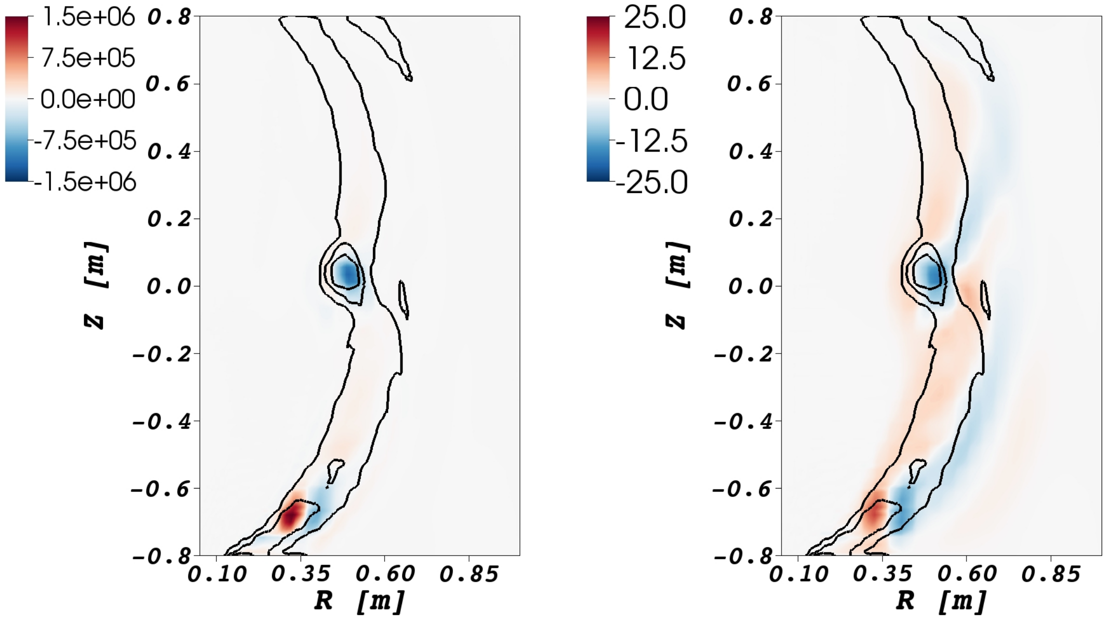

(a) $-\langle \tilde{\mathbf{v}} \times \tilde{\mathbf{B}} \rangle \cdot \langle \mathbf{J} \rangle$ (b) $-2\pi R \langle \tilde{\mathbf{v}} \times \tilde{\mathbf{B}} \rangle_{\phi}$

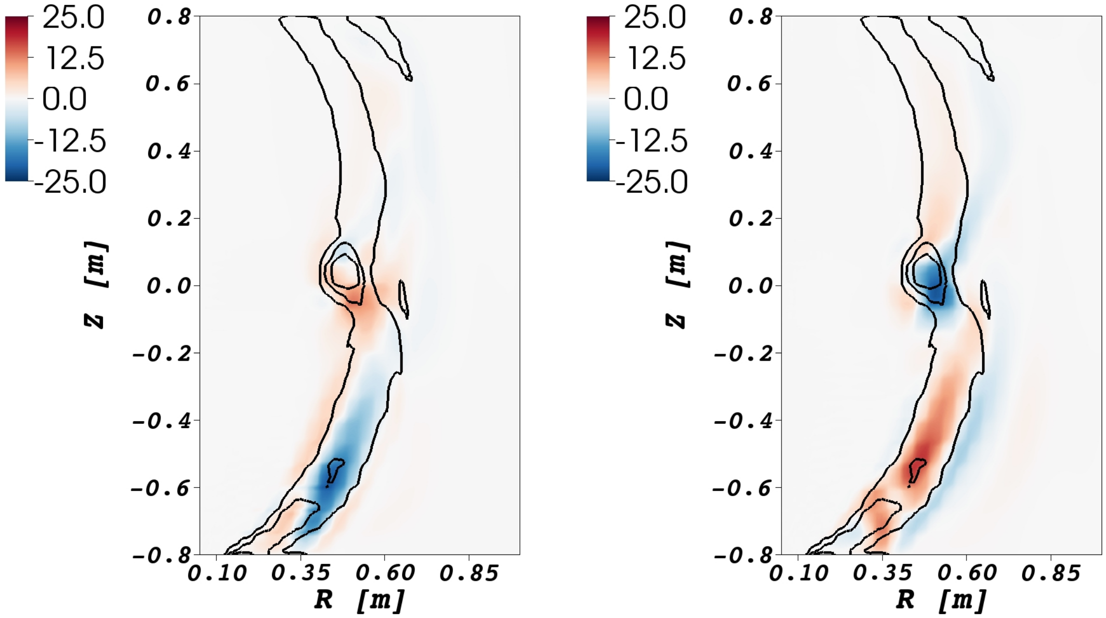

(c) $-2\pi R \langle \tilde{v}_R \tilde{B}_Z \rangle_{\phi}$ (d) $+2\pi R \langle \tilde{v}_Z \tilde{B}_R \rangle_{\phi}$

Figure 6.23: MHD dynamo electric field in the MHD computation. Color contours of (a) the energy transfer rate of the MHD dynamo electric field in units of W/m^3 and (b-d) the toroidal MHD dynamo electric field (total and its components) are expressed as an effective loop voltage in units of V at $t = 2.97$ ms in the MHD computation. The black contours show positive values of the toroidally averaged parallel current density, i.e. $\langle \lambda \rangle > 0$.

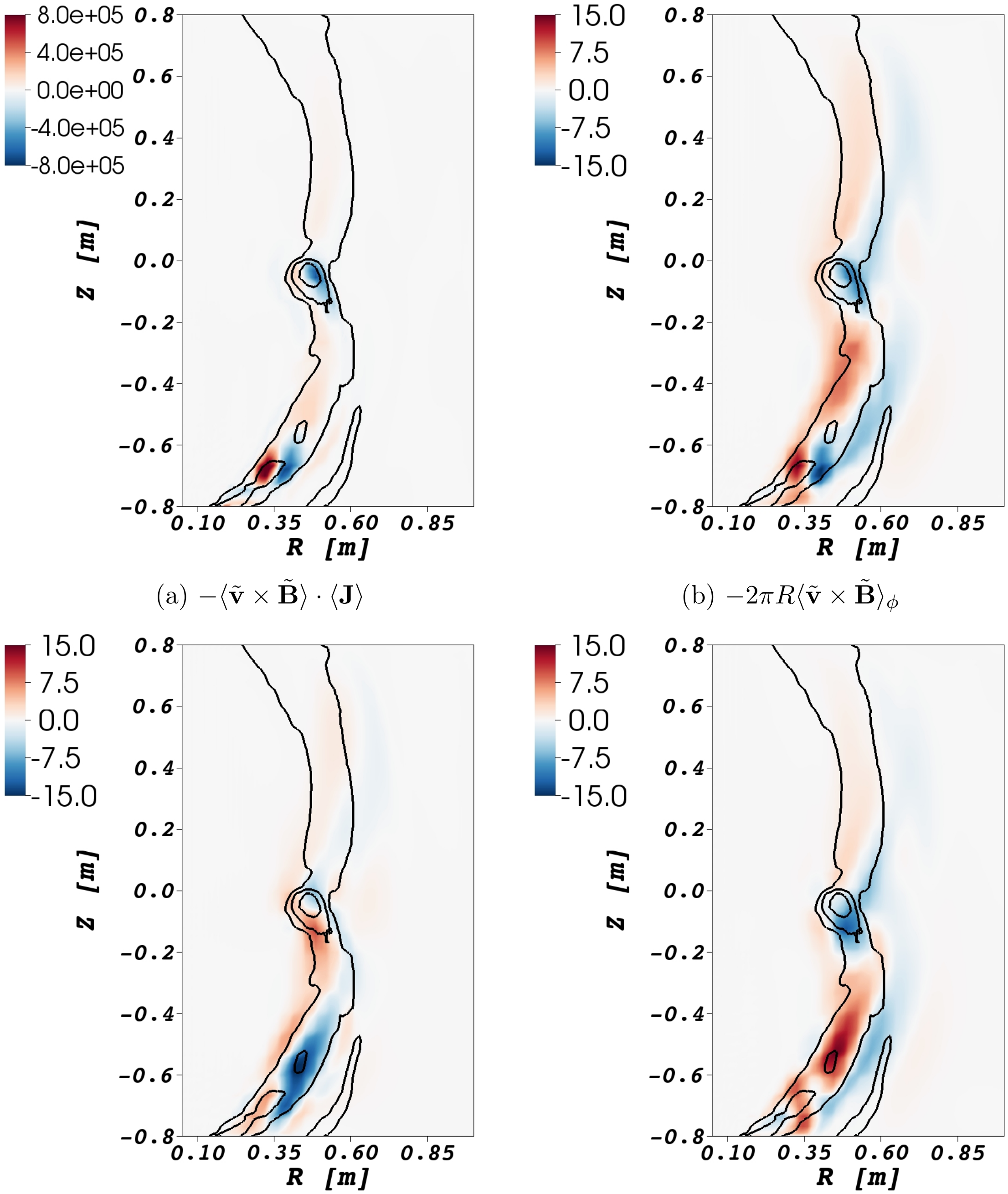

(a) $-\langle \tilde{\mathbf{v}} \times \tilde{\mathbf{B}} \rangle \cdot \langle \mathbf{J} \rangle$

(b) $-2\pi R \langle \tilde{\mathbf{v}} \times \tilde{\mathbf{B}} \rangle_\phi$

(c) $-2\pi R \langle \tilde{v}_R \tilde{B}_Z \rangle_\phi$

(d) $+2\pi R \langle \tilde{v}_Z \tilde{B}_R \rangle_\phi$

Figure 6.24: MHD dynamo electric field in the 2-fluid computation. Color contours of (a) the energy transfer rate of the MHD dynamo electric field in units of W/m^3 and (b-d) the toroidal MHD dynamo electric field (total and its components) are expressed as an effective loop voltage in units of V at $t = 2.93$ ms in the 2-fluid computation. The black contours show positive values of the toroidally averaged parallel current density, i.e. $\langle \lambda \rangle > 0$.

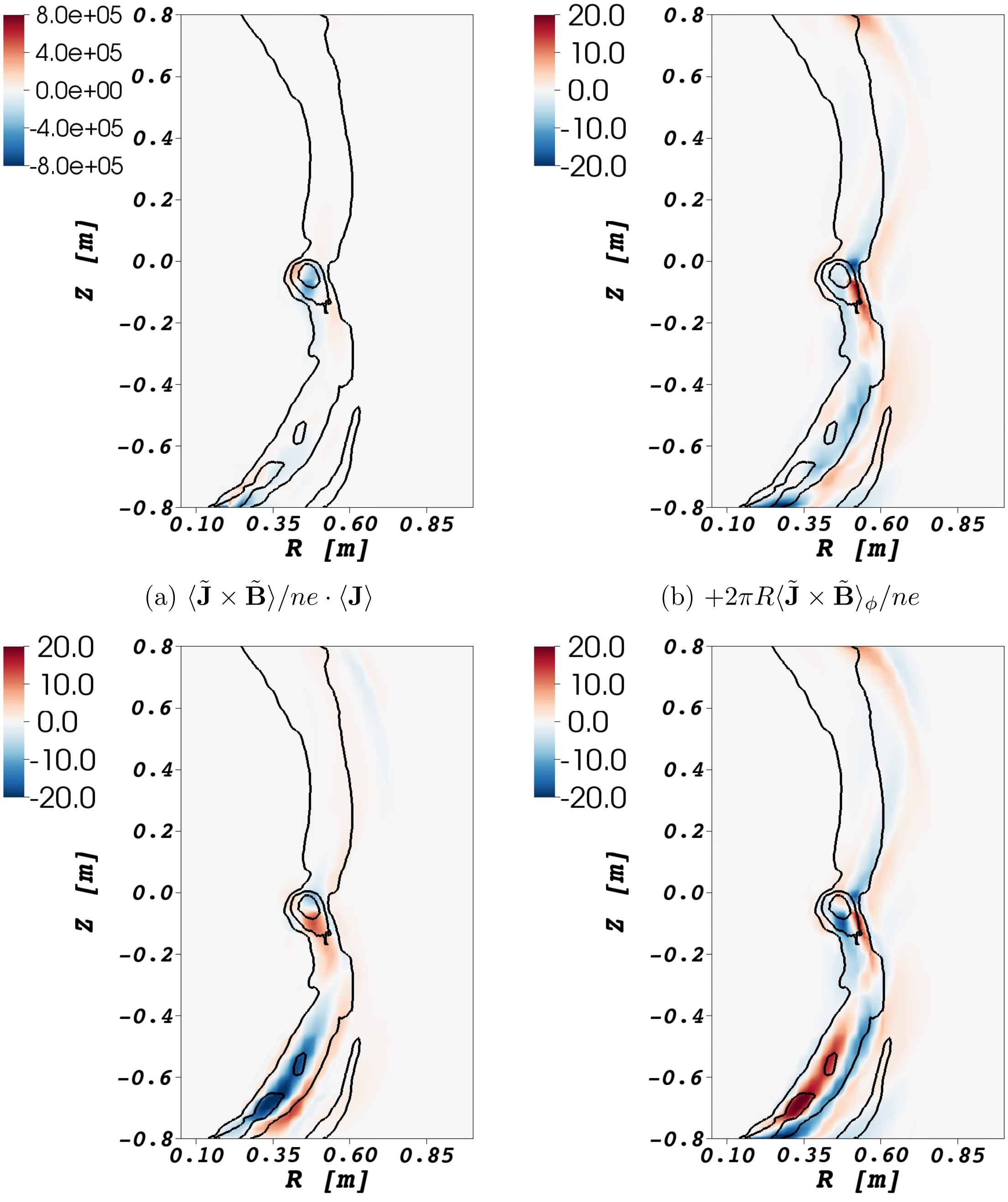

(a) $\langle \tilde{\mathbf{J}} \times \tilde{\mathbf{B}} \rangle / ne \cdot \langle \mathbf{J} \rangle$

(b) $+2\pi R \langle \tilde{\mathbf{J}} \times \tilde{\mathbf{B}} \rangle_\phi / ne$

(c) $+2\pi R \langle \tilde{J}_R \tilde{B}_Z \rangle_\phi / ne$

(d) $-2\pi R \langle \tilde{J}_Z \tilde{B}_R \rangle_\phi / ne$

Figure 6.25: Hall dynamo electric field in the 2-fluid computation. Color contours of (a) the energy transfer rate of the Hall dynamo electric field in units of W/m^3 and (b-d) the toroidal Hall dynamo electric field (total and its components) are expressed as an effective loop voltage in units of V at $t = 2.93$ ms in the 2-fluid computation. The black contours show positive values of the toroidally averaged parallel current density, i.e. $\langle \lambda \rangle > 0$.

While local poloidal flux amplification occurs, the flux amplification resulting from a single reconnection event is small, even with significant channel current, shown in Figure 6.26d. Therefore, significant poloidal flux amplification must accumulate over multiple reconnection events.

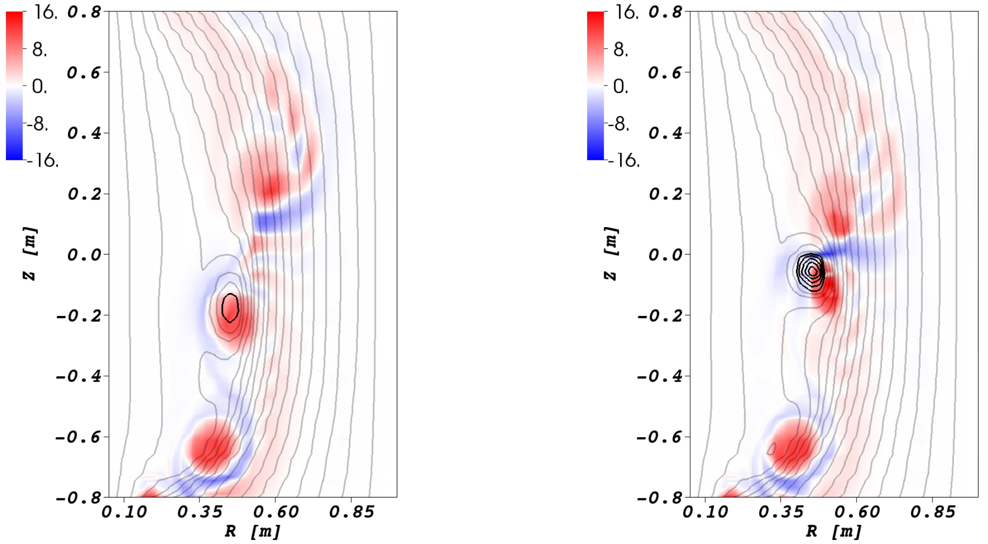

(a) $t = 2.91$ ms

(b) $t = 2.93$ ms

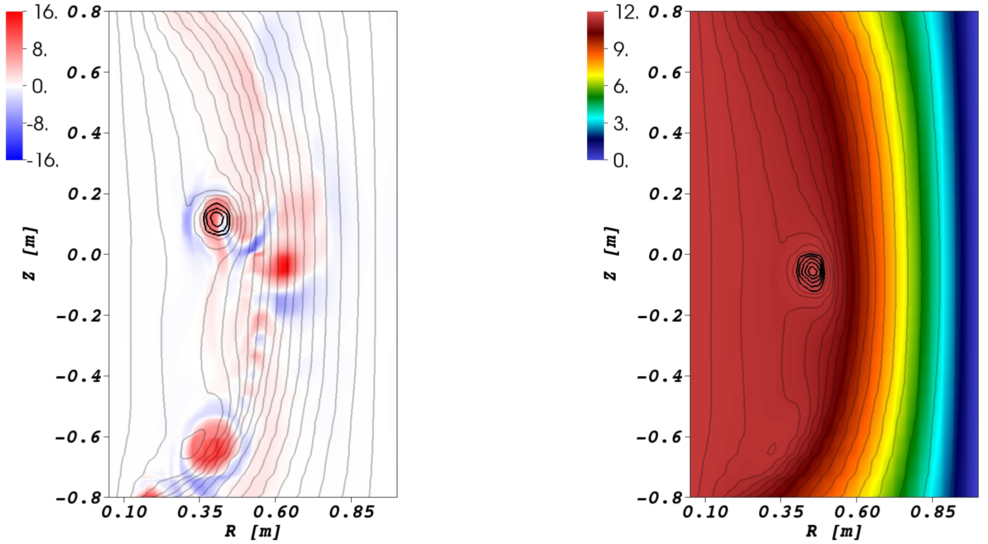

(c) $t = 2.95$ ms

(d) $t = 2.93$ ms

Figure 6.26: Conversion of helical flux to poloidal flux. (a-c) Color contours of λ at $\phi = 0$ in units of m^{-1} and (d) color contours of toroidally-averaged poloidal flux in units of mWb are overlaid with logarithmic contours of toroidally-averaged poloidal flux in the two-fluid computation. The darker poloidal flux contours indicate values of poloidal flux that exceed that maximum value of the vacuum poloidal flux.

6.4 Global Evolution of the Plasma during the Formation Phase

Each computation evolves from vacuum fields either entirely with or entirely without the two-fluid terms in Ohm's law. Just as poloidal magnetic flux accumulates over many reconnection events, the contribution of the two-fluid effects accumulates over the plasma evolution, affecting not only local plasma conditions, but the global plasma evolution as well. Thus, comparisons between the evolution of global quantities provide information that is complementary to the single-event comparisons of the previous sections from the MHD and 2-fluid computations. Figures 6.27 & 6.28 display diagnostic traces over the entire formation phase for the MHD and 2-fluid computations, respectively.

As stated previously, a global-scale poloidal magnetic field null forms near the central column when $I_p \simeq 15$ kA in both the experiment and the computations. The formation of the poloidal magnetic field null represents a dramatic change in the magnetic topology and global plasma evolution. It occurs at $\tau_{null} = 4.26$ ms into the MHD computation and $\tau_{null} = 4.85$ ms into the 2-fluid computation. Prior to the formation of the poloidal field null, between $1 \leq t \leq \tau_{null} - 1$ ms, the plasma experiences exponential growth for the internal energies, magnetic energy spectrum (except for the $n = 0$ component), and the kinetic energy spectrum. As indicated in Table 6.6 and Figure 6.29, the global parameters evolve at significantly different rates for this phase in the MHD and two-fluid computations.

Consistent with the results in Section 6.1, the configuration develops faster in the MHD computation than in the two-fluid computation. In particular, the rate at which the $n = 0$ magnetic energy grows and the growth rate for the ion and electron internal energies in the MHD computations are triple of those in the two-fluid computation. The

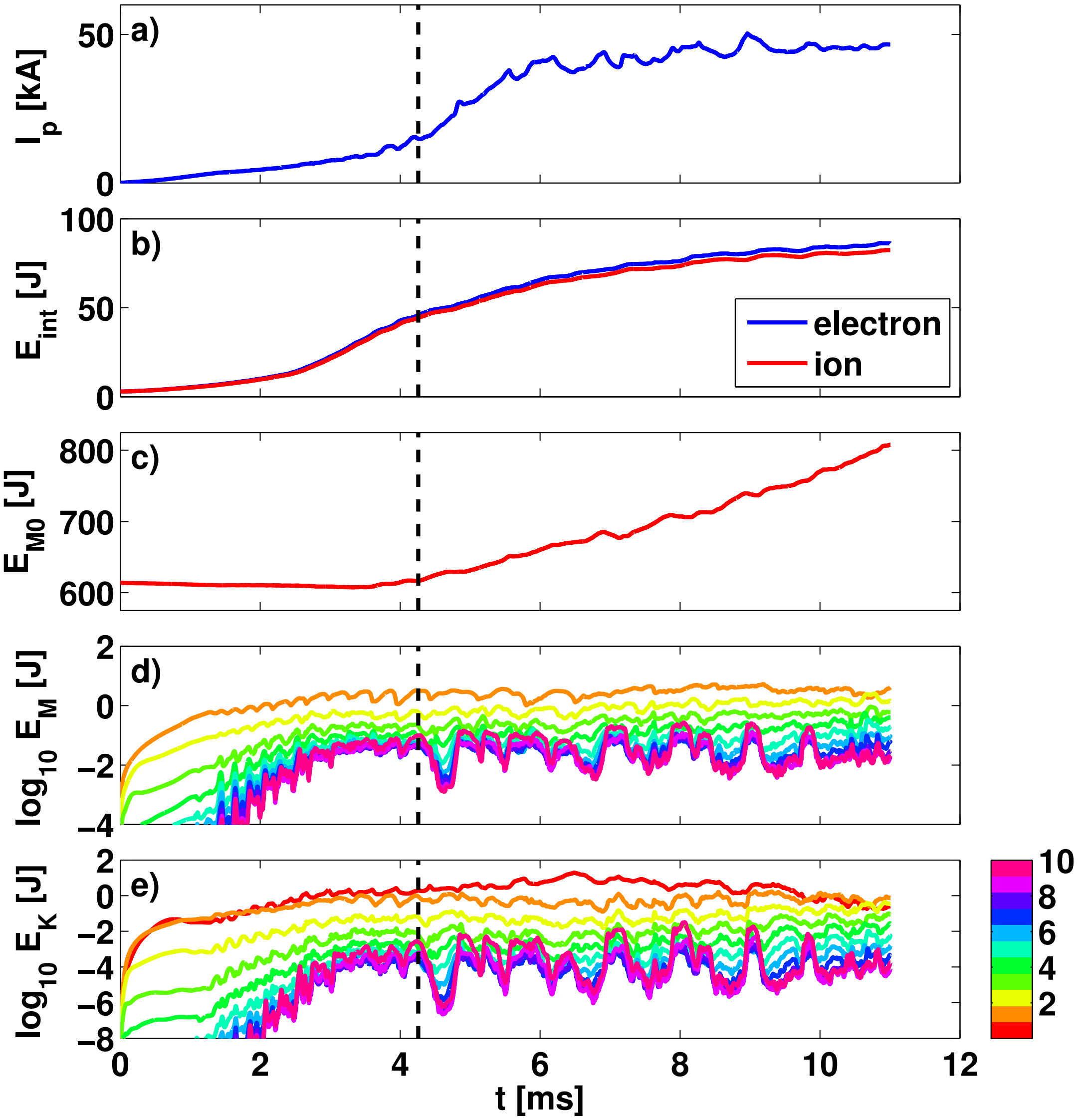

Figure 6.27: Diagnostic traces over the entire formation phase in the MHD computation, including a) the plasma current, b) the ion and electron internal energies, c) the $n = 0$ magnetic energy, d) the $n = 1-10$ magnetic energy spectrum, and e) the kinetic energy spectrum. The magnetic and kinetic energy spectra are colored according to the color bar at the lower right. The vertical dotted line indicates the time at which the poloidal magnetic field null forms.

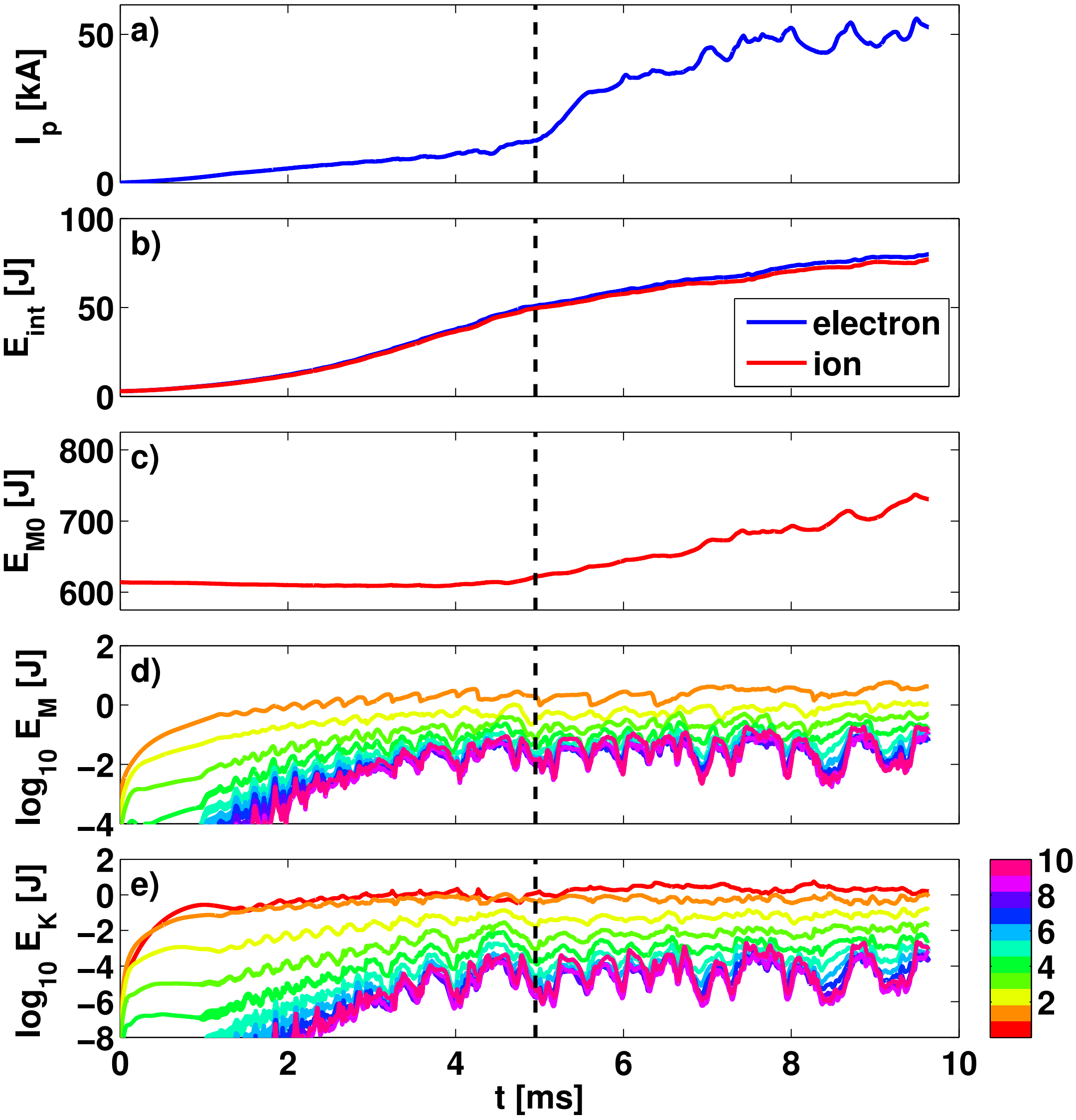

Figure 6.28: Diagnostic traces over the entire formation phase in the 2-fluid computation, including a) the plasma current, b) the ion and electron internal energies, c) the $n = 0$ magnetic energy, d) the $n = 1-10$ magnetic energy spectrum, and e) the kinetic energy spectrum. The magnetic and kinetic energy spectra are colored according to the color bar at the lower right. The vertical dotted line indicates the time at which the poloidal magnetic field null forms.

growth rates for both the magnetic and kinetic energy spectra follow the same general trend in the MHD and 2-fluid computations. However, for the $n \geq 5$ toroidal mode number components, the kinetic energy spectrum in the MHD computation consistently grows at roughly double the rate in the 2-fluid computation. Faster growth in the higher toroidal mode number components of the flow is consistent with a larger MHD dynamo electric field being observed in the MHD computation than in the 2-fluid computation, as discussed in Section 6.3.

Table 6.5: Plasma properties in the growth phase

Quantity	MHD	2-fluid	Ratio
$\dot{I}_p$ [kA/ms]	2.91	2.28	0.78
$\partial_t \log E_{int,e}$ [ms^{-1}]	1.08	0.36	0.34
$\partial_t \log E_{int,i}$ [ms^{-1}]	1.12	0.38	0.34
$\dot{E_{M0}}$ [J/ms]	-1.90	-0.61	0.32

Plasma properties over the segment $1 \leq t \leq \tau_{null} - 1$ ms, where $\tau_{null} = 4.26$ ms for the MHD computation and $\tau_{null} = 4.85$ ms for the 2-fluid computation.

After the formation of the poloidal field null, the plasma current rapidly increases and the plasma undergoes a rapid change in magnetic topology. The current filament path is redirected down the inboard side of the plasma near the central column. Shortly after the formation of the poloidal field null, the inboard current is diffuse, as shown in Figure 6.30a. As the plasma current increases, the inboard current coalesces into a coherent channel that connects to the driven outboard current filament, as shown in Figure 6.30b. As long as helicity injection remains active, the plasma retains its

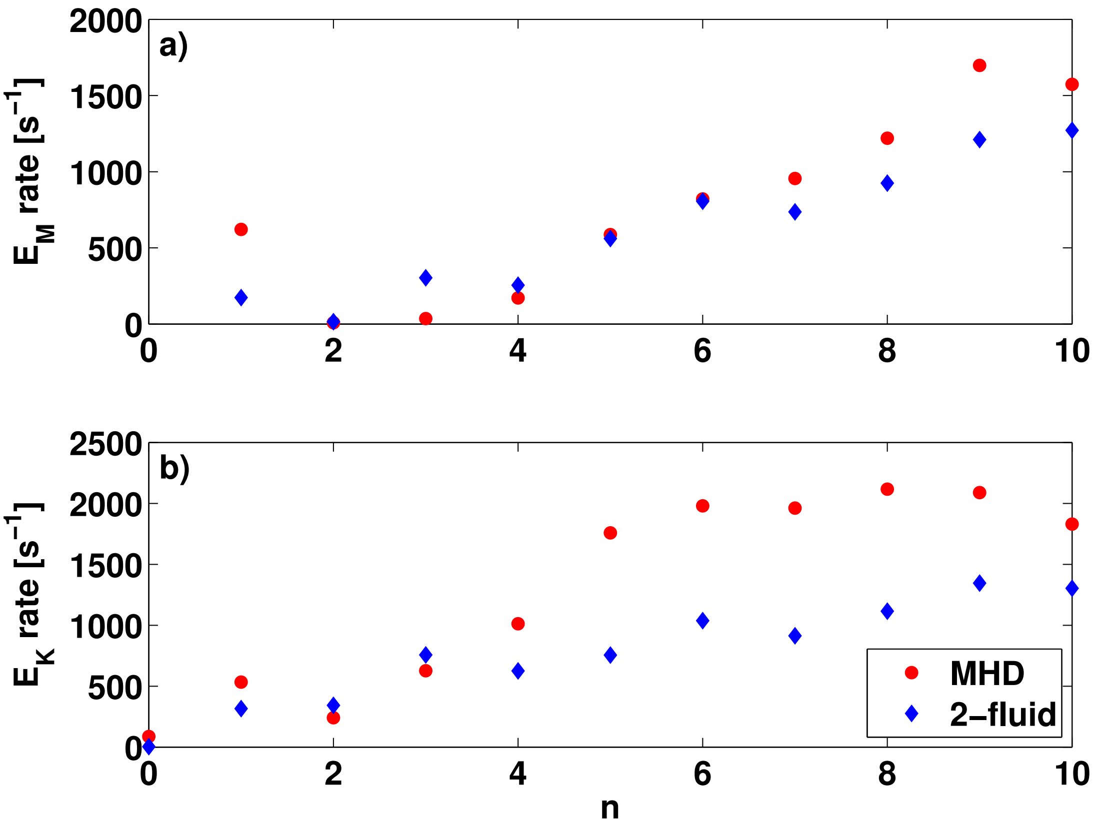

Figure 6.29: The (a) magnetic and (b) kinetic energy spectra growth rates during the growth phase as a function of toroidal mode number n.

three-dimensional filamentary structure, even late in the formation phase. However, a significant portion of the plasma current can flow outside the main current filament structure, as shown by the translucent green contours of normalized parallel current in Figure 6.31.

Prior to the formation of the poloidal field null, much of the thermal energy is transported to the vacuum vessel, as shown at the end of Section 6.1. After the formation of the poloidal field null, a significant fraction of the thermal energy recirculates in the amplified flux region, as shown in Figure 6.32. The formation of many current rings over many reconnection events leads to the redistribution of thermal energy from the driven

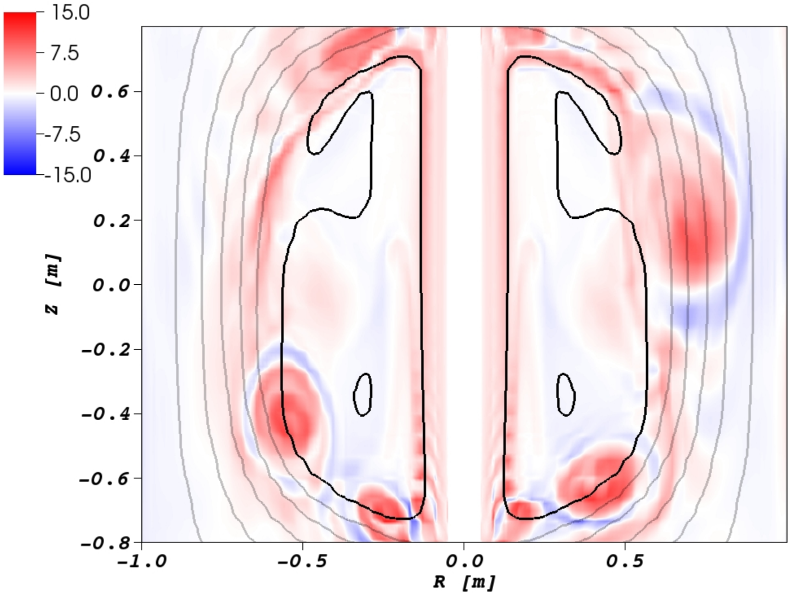

(a)

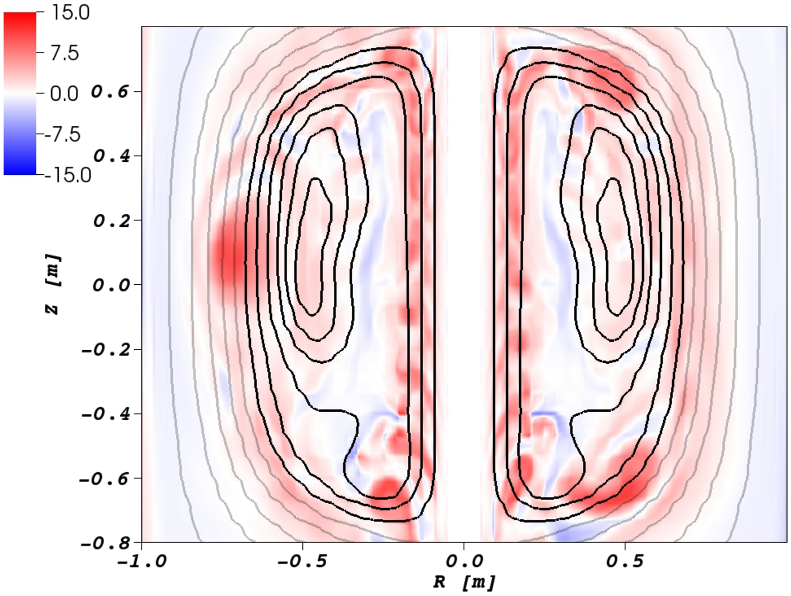

(b)

Figure 6.30: Hollow current profiles after the formation of a poloidal magnetic-field null. Color contours of λ in units of m^{-1} with overlaid logarithmic contours of poloidal flux in the two-fluid computation. The current on the inboard side is (a) diffuse at $t = 5.50$ ms when $I_p \simeq 29$ kA and (b) forms a coherent channel at $t = 8.51$ ms when $I_p \simeq 46$ kA. The darker poloidal flux contours indicate values of poloidal flux that exceed that maximum value of the vacuum poloidal flux.

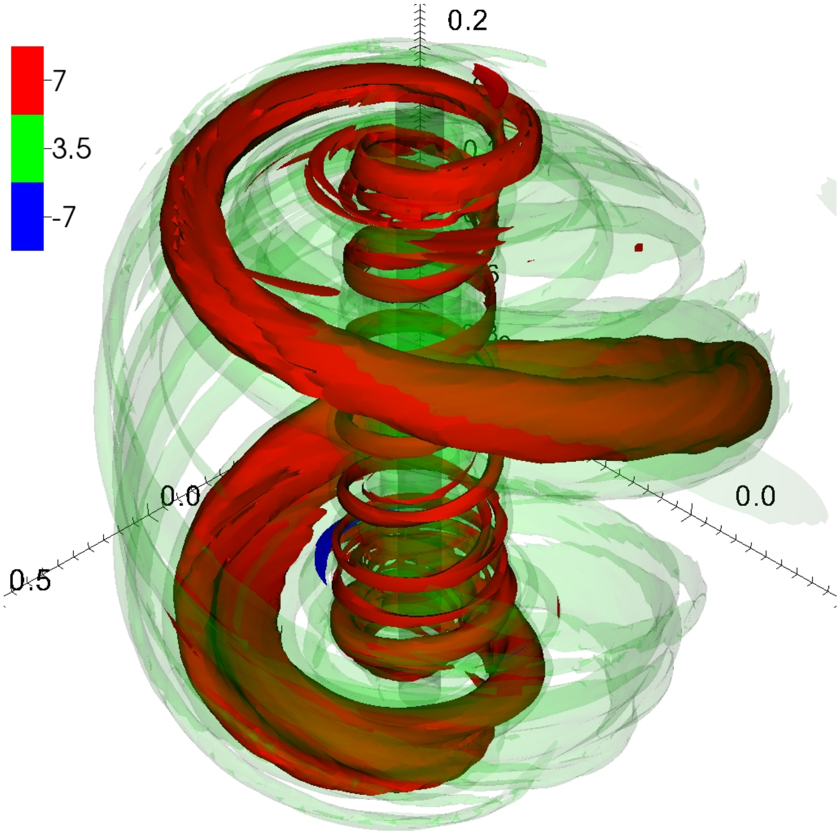

Figure 6.31: The plasma retains its three-dimensional filamentary structure late in the formation phase. Isosurfaces of the parallel current parameter λ in units of m^{-1} at $t = 8.51$ ms in the 2-fluid computation.

current channel into the amplified flux region.

A few milliseconds after the formation of the poloidal field null, the plasma current still increases with time, but the rate at which it increases stagnates compared to immediately after the formation of the poloidal field null. To compute the time at which the plasma current stagnates, the plasma current is fit to a line for a segment where the plasma current rises most rapidly ($20 \leq I_p \leq 35$ kA) and for a segment well into the stagnation phase ($7 \leq t \leq 9$ ms). The extrapolated intercept between the linear fits is taken as the stagnation time, which occurs at $\tau_{stag} = 5.53$ ms into the MHD computation and $\tau_{stag} = 6.65$ ms into the 2-fluid computation.

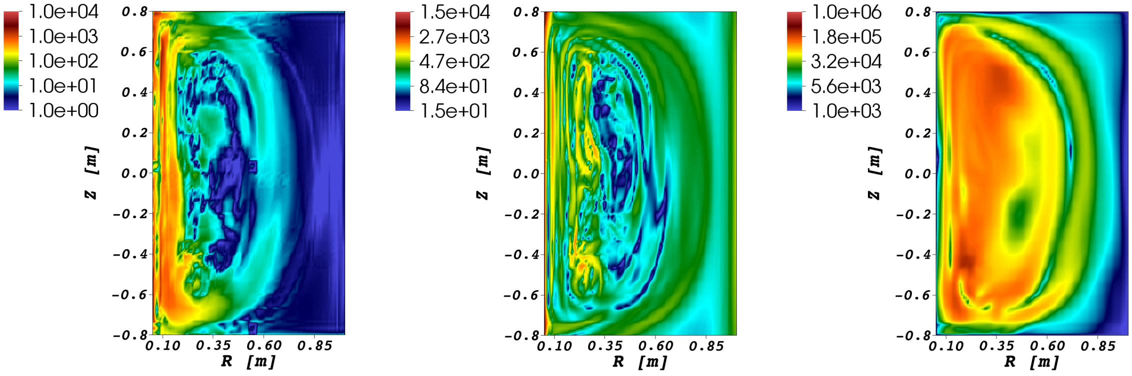

(a) $|\langle \mathbf{q}_{\|,e} \rangle|$ (b) $|\langle \mathbf{q}_{\perp,e} \rangle|$ (c) $|\langle \mathbf{q}_{\mathbf{v},e} \rangle|$

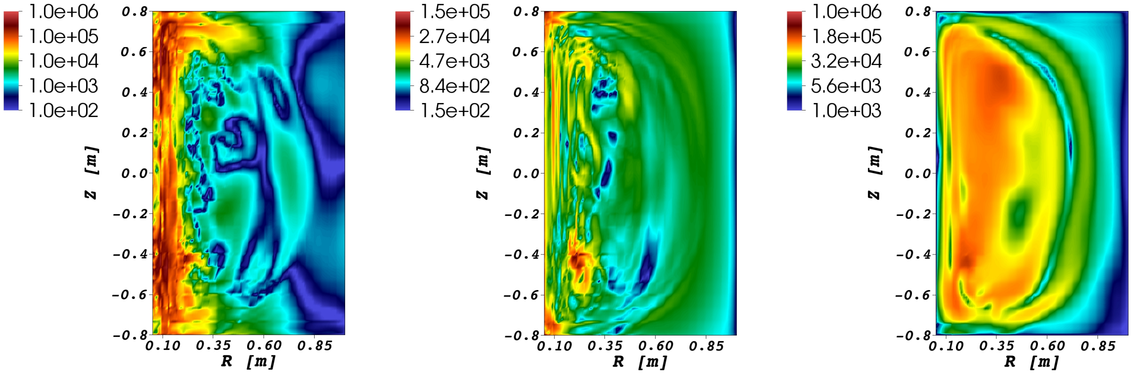

(d) $|\langle \mathbf{q}_{\|,i} \rangle|$ (e) $|\langle \mathbf{q}_{\perp,i} \rangle|$ (f) $|\langle \mathbf{q}_{\mathbf{v},i} \rangle|$

Figure 6.32: Toroidally averaged heat fluxes in units of W/m^2 at $t = 8.51$ m/s in the 2-fluid computation, after the formation of a poloidal field null.

Tables 6.6 lists the rates for a number of global parameter in the MHD and two-fluid computations. The plasma current is still increasing during this saturated growth phase, but the rate at which it increases is less than half that during the exponential growth phase. The ion and electron internal energies are assumed to approach some value via the form in Equation 6.12, where c_n are fitting parameters. Consistent with previous results, the saturation values of the ion and electron internal energies are smaller and the $n = 0$ magnetic energy increases at a slower rate in the two-fluid computation than in the MHD computation. However, the ion and electron internal energies equilibrate much more rapidly in the two-fluid computation than in the MHD computation, and the plasma currents now rise at comparable rates. The magnitude of the rate of change of the $n = 0$ magnetic energy is also much greater in the saturated growth phase than in the growth phase, and is now positive.

$$y = c_0 + c_1 \left[1 - \exp\left(-c_2 t\right)\right] \tag{6.12}$$

Table 6.6: Plasma properties late in the formation phase

Quantity	MHD	2-fluid	Ratio
$\dot{I}_p$ [kA/ms]	1.36	1.39	1.03
$\partial_t \log E_{int,e}$ [ms^{-1}]	0.316	0.757	2.45
$\partial_t \log E_{int,i}$ [ms^{-1}]	0.378	0.747	1.97
saturation $E_{int,e}$ [J]	91.1	81.8	0.90
saturation $E_{int,i}$ [J]	8.53	7.47	0.92
$\dot{E_{M0}}$ [J/ms]	30.2	26.2	0.87

Plasma properties late in the formation phase, over the segment $t > \tau_{stag} + 1$ ms, where $\tau_{stag} = 5.53$ ms in the MHD computation and $\tau_{stag} = 6.65$ ms in the 2-fluid computation.

The magnetic (except the $n = 0$ component) and kinetic energy spectra experience little, if any, growth late in the formation phase. The maximum and mean amplitudes for the spectra are similar between the MHD and two-fluid computations, as shown in Figure 6.33. The amplitudes are generally somewhat larger for the MHD computation than for the two-fluid computation.

To test this predicted model of filament relaxation, synthetic Mirnov array signals in

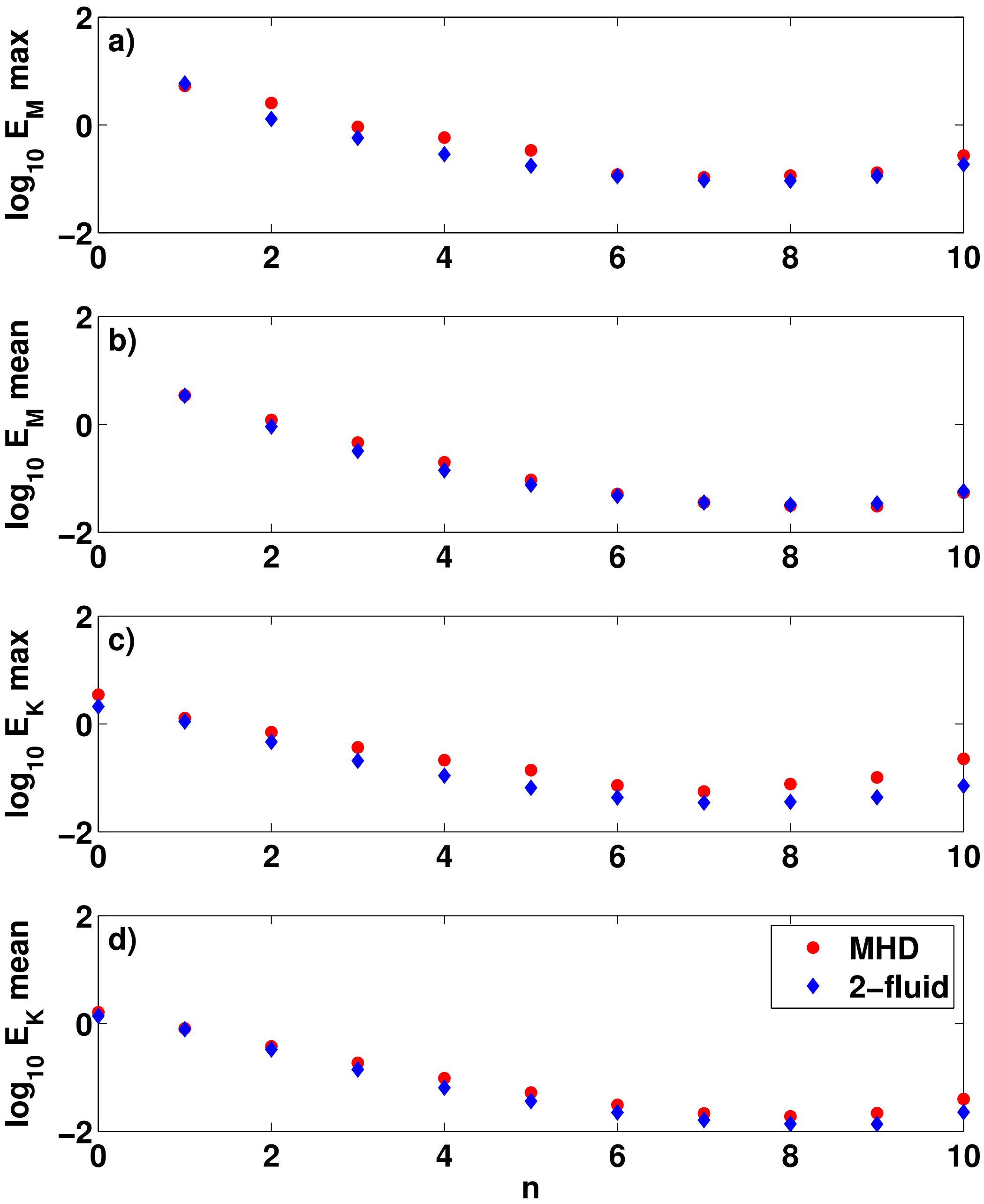

Figure 6.33: Fluctuation amplitudes of the (a) maximum and (b) mean magnetic energy spectrum and the (c) maximum and (b) mean kinetic energy spectrum as function of toroidal mode number n late in the formation phase, over the segment $t > \tau_{stag} + 1$ ms, where $\tau_{stag} = 5.53$ ms in the MHD computation and $\tau_{stag} = 6.65$ ms in the 2-fluid computation.

the computations are compared to laboratory observations for a experimental discharges described in Reference [28]. The synthetic Mirnov diagnostic signal are analyzed using the procedure outlined in Section 5.3.4. As the computations have a more gradual rate of helicity injection than the experiment, comparisons focus on after the formation of a global poloidal magnetic field null, which is indicated by the vertical red lines in Figure 6.34. The plasma current is shown in the top panels of Figures 6.34 (a-c) for reference and reaches comparable values after the poloidal field null forms in the experimental discharge and in the MHD and 2-fluid computations.

The experimental outboard toroidal Mirnov array observed normalized magnetic fluctuation amplitudes of order 5 %, shown in the middle panel of Figure 6.34a. The synthetic outboard toroidal Mirnov diagnostic also observes normalized magnetic fluctuation amplitudes of order 5 % in both the MHD and two-fluid computations, shown in the middle panels of Figures 6.34 b & c, respectively.

The spectrogram of the cross-spectral power for the experimental Mirnov array in the lower panel of Figure 6.34a shows significant activity in the $f \simeq 3-20$ kHz range. Both the MHD and 2-fluid computations also have significant activity for $f \sim 10$ kHz, shown in the bottom panels of Figures 6.34 b &c. In the computations, the MHD activity at $f \sim 10$ kHz corresponds the reconnection event causing abrupt changes in the current channel winding, described in Section 6.1. The frequency $f \sim 10$ kHz is also significant as it corresponds to the time for an Alfvén wave to propagate along the helical current filament path. The computational spectrograms also show significant MHD activity at lower frequencies, $f \sim 3$ kHz, which corresponds to the slower timescale recovery of a winding of the driven current filament shed during after the formation and release of a current ring.

The spectrogram for the MHD computation shows significant MHD activity at higher frequencies up to 50 kHz that is not present in the spectrograms for the experimental discharge or the two-fluid computations. Therefore, in addition to damping the amplitude of magnetic fluctuations, as discussed in Section 6.1, two-fluid effects are also avoid higher frequency activity. In the experiment, the cross-spectral power density is filtered for frequencies below a few kilohertz.

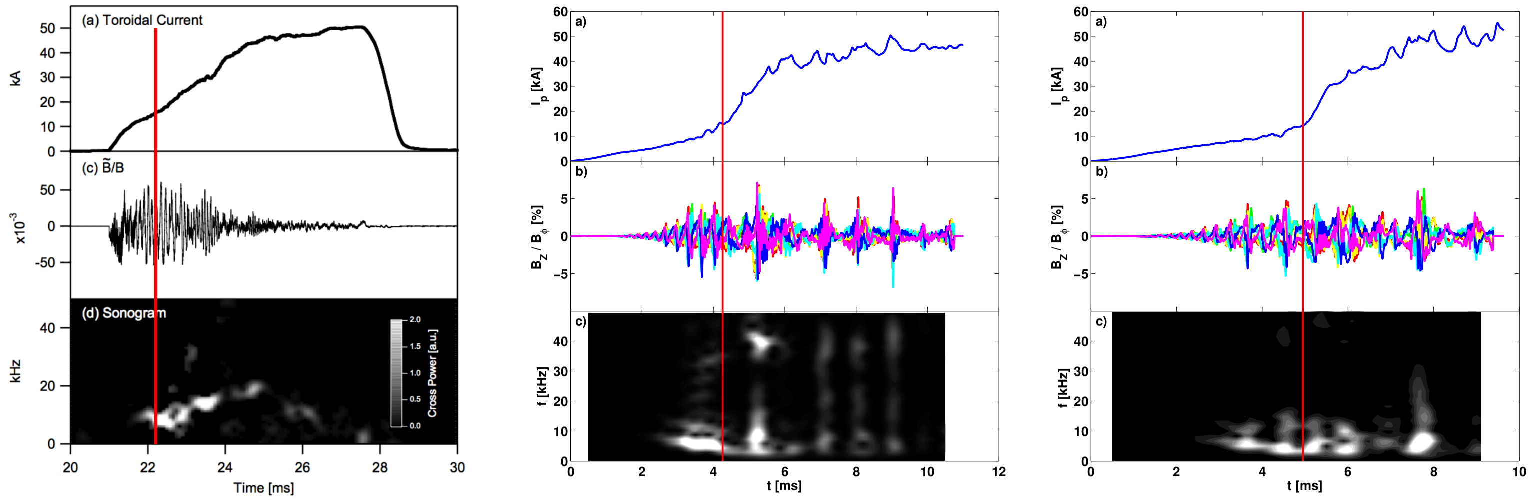

(a) (b) (c)

Figure 6.34: Spectrograms of the cross-spectral power density for signals measured by the outboard toroidal Mirnov array. Figure (a) shows a spectrogram for experimental measurements during a Pegasus discharge, taken from Reference [28]. Figures (b) & (c) use the procedure outline in Section 5.3.4 and correspond to MHD and 2-fluid computations, respectively. The vertical red line in each figure corresponds to the formation of the poloidal magnetic field null.

6.5 Symmetrization of the Plasma Toward a Tokamak Equilibrium State

Plasmas formed through localized helicity injection are intended to transition to other forms of current drive. Therefore, the ability of said plasmas to relax into a configuration with closed flux surfaces–and therefore, good confinement–is critical. As discussed in the previous section, the global parameters evolve at different rates in the saturated growth phase in the MHD and 2-fluid computations. Therefore, to compare free decay during the MHD and 2-fluid computations, the helicity injector sources are instantaneously turned off for plasma configurations with the same plasma current ($I_p \simeq 55$ kA) in both the MHD and 2-fluid computations. Despite having approximately the same plasma plasma current, the plasmas have different ion and electron internal energies in the MHD and 2-fluid computations. The electron internal energy at the end of the formation phase is 93 J in the MHD computation and 79 J in the 2-fluid computation. Likewise, the ion internal energy at the end of the formation phase is 89 J in the MHD computation and 75 J in the 2-fluid computation.

After cessation of current drive in the computations, closed flux surfaces form rapidly and encompass a large plasma volume through decay toward a conventional, axisymmetric tokamak equilibrium state, as shown in Figures 6.35 & 6.36. Closed surfaces enclose a larger plasma volume in the 2-fluid computation, which likely results from the faster decay of higher toroidal mode number harmonics of magnetic energy in the 2-fluid computation than in the MHD computation. The current profile of the relaxing plasma remains hollow, but the pressure profile relaxes to a centrally peaked configuration. The hollow current profile is consistent with the off-axis peaked current profile observed in equilibrium reconstructions of experimental discharges. [28]

Figures 6.37 & 6.38 show diagnostic traces over the free-decay phase in the MHD and 2-fluid computations, respectively. The plasma current and internal energies decay more rapidly in the 2-fluid computation than in the MHD computation. At $\Delta t = 2$ ms into the free-decay phase, $I_p = 39$ kA in the MHD computation and $I_p = 33$ kA in the 2-fluid computation. The decay rate of the magnetic and kinetic energy spectra depends on the toroidal mode number, such that the highest toroidal mode number harmonics decay the most rapidly. In both the MHD and 2-fluid computations, the magnetic energy of a given toroidal mode number harmonic is comparable to the kinetic energy of the same toroidal mode number harmonic, i.e. $E_{M,n} \sim E_{K,n}$. The magnetic energy and kinetic energy spectra also decay more rapidly in the 2-fluid computation than in the MHD computation. For example, the $n = 10$ harmonic of magnetic and kinetic energy reaches 1 eV at $\Delta t \approx 5$ ms into the MHD and $\Delta t \approx 3$ ms into the 2-fluid computation.

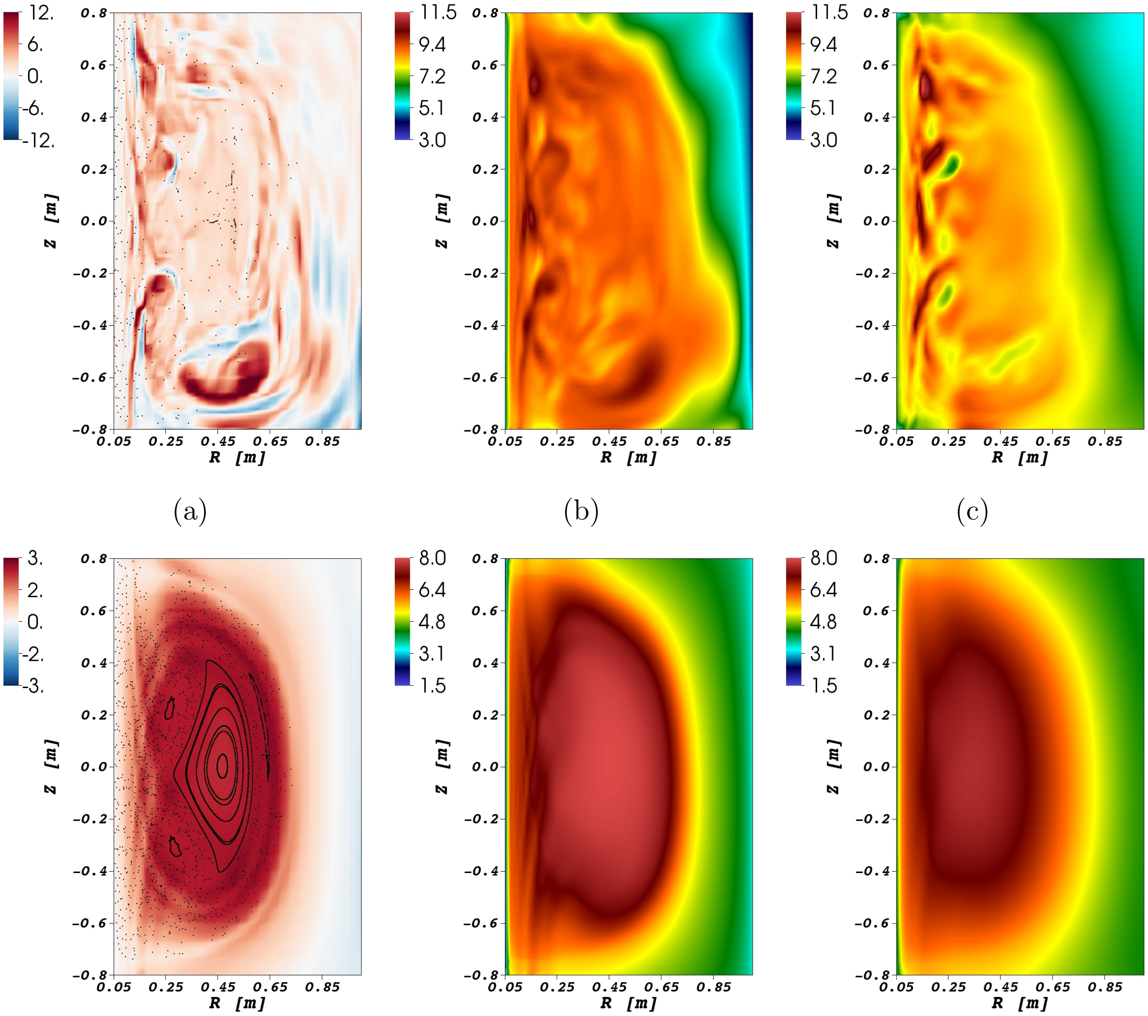

(a) (b) (c)

(d) (e) (f)

Figure 6.35: Plasma evolution during free-decay phase in the MHD computation. Contours of (a,d) λ in units of m^{-1} and (b,e) T_e & (c,f) T_i in units of eV for $\phi = 0$ at (a-c) the end of the formation phase and (d-f) 2 ms into the free decay phase. Figures a & d are overlaid with magnetic field-line punctures.

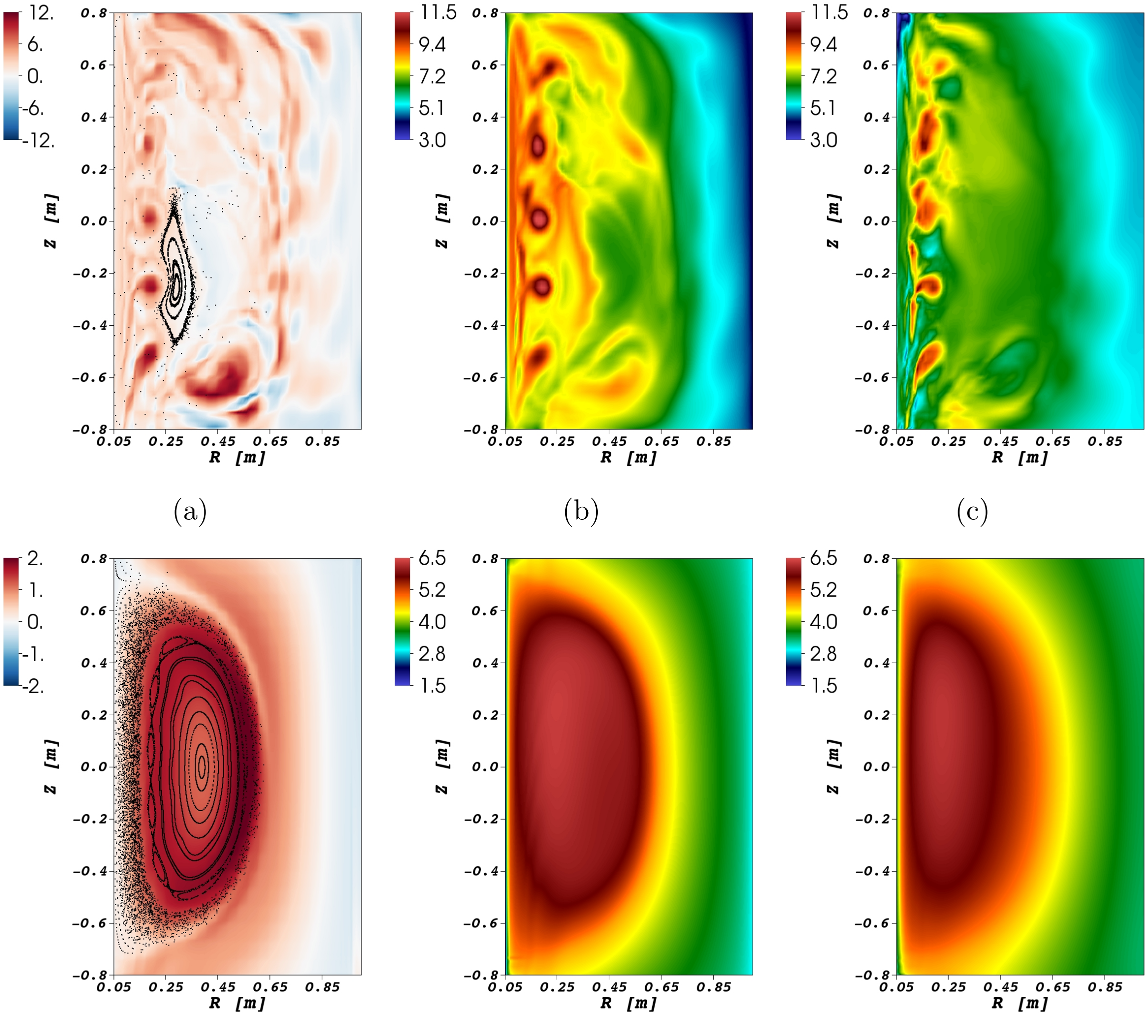

(a) (b) (c)

(d) (e) (f)

Figure 6.36: Plasma evolution during the free-decay phase in the 2-fluid computation. Contours of (a,d) λ in units of m^{-1} and (b,e) T_e & (c,f) T_i in units of eV for $\phi = 0$ at (a-c) the end of the formation phase and (d-f) 2 ms into the free decay phase. Figures a & d are overlaid with magnetic field-line punctures.

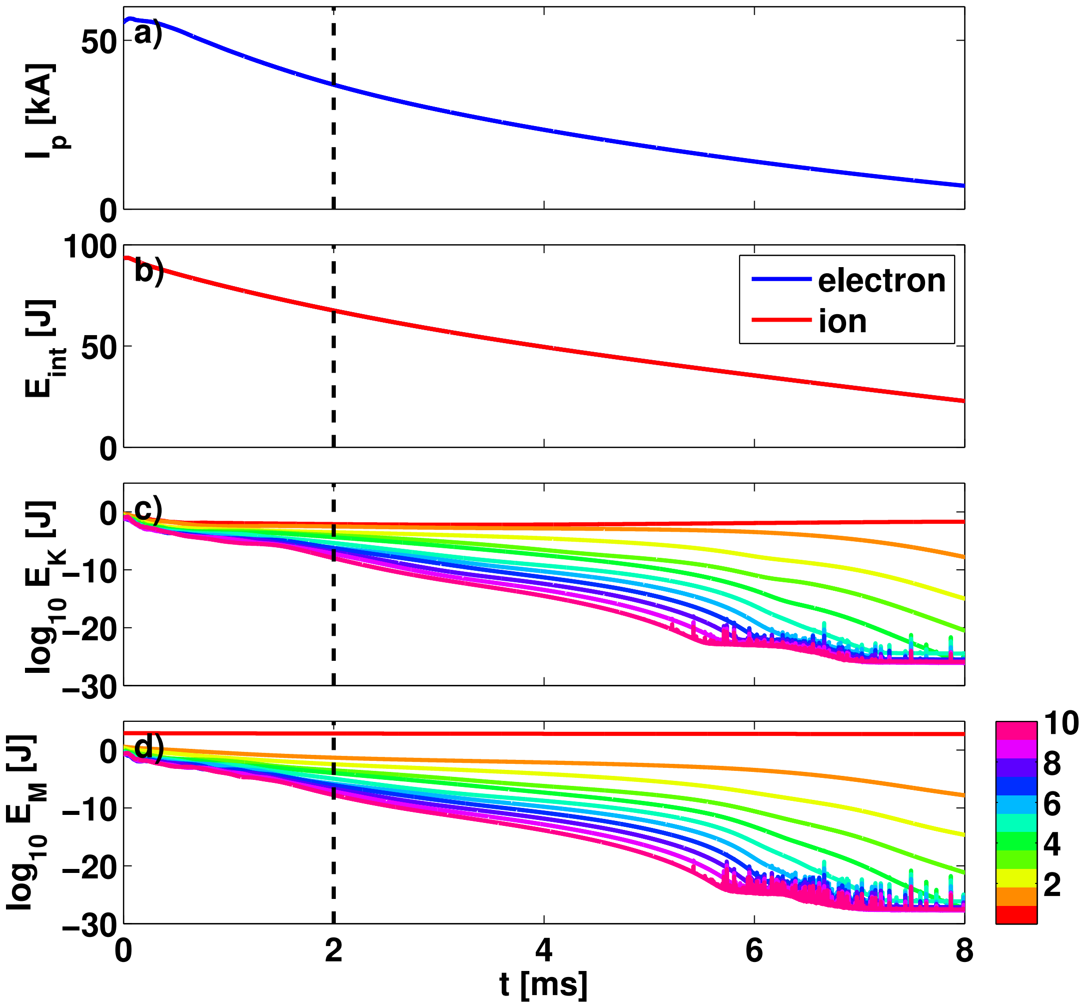

Figure 6.37: Diagnostic traces during free-decay in the MHD computation, including a) the plasma current, b) the ion and electron internal energies, c) the magnetic energy spectrum and d) the kinetic energy spectrum. The magnetic and kinetic energy spectra are colored according to the color bar at the lower right. The time indicated by the vertical dotted line corresponds contours in Figure 6.35.

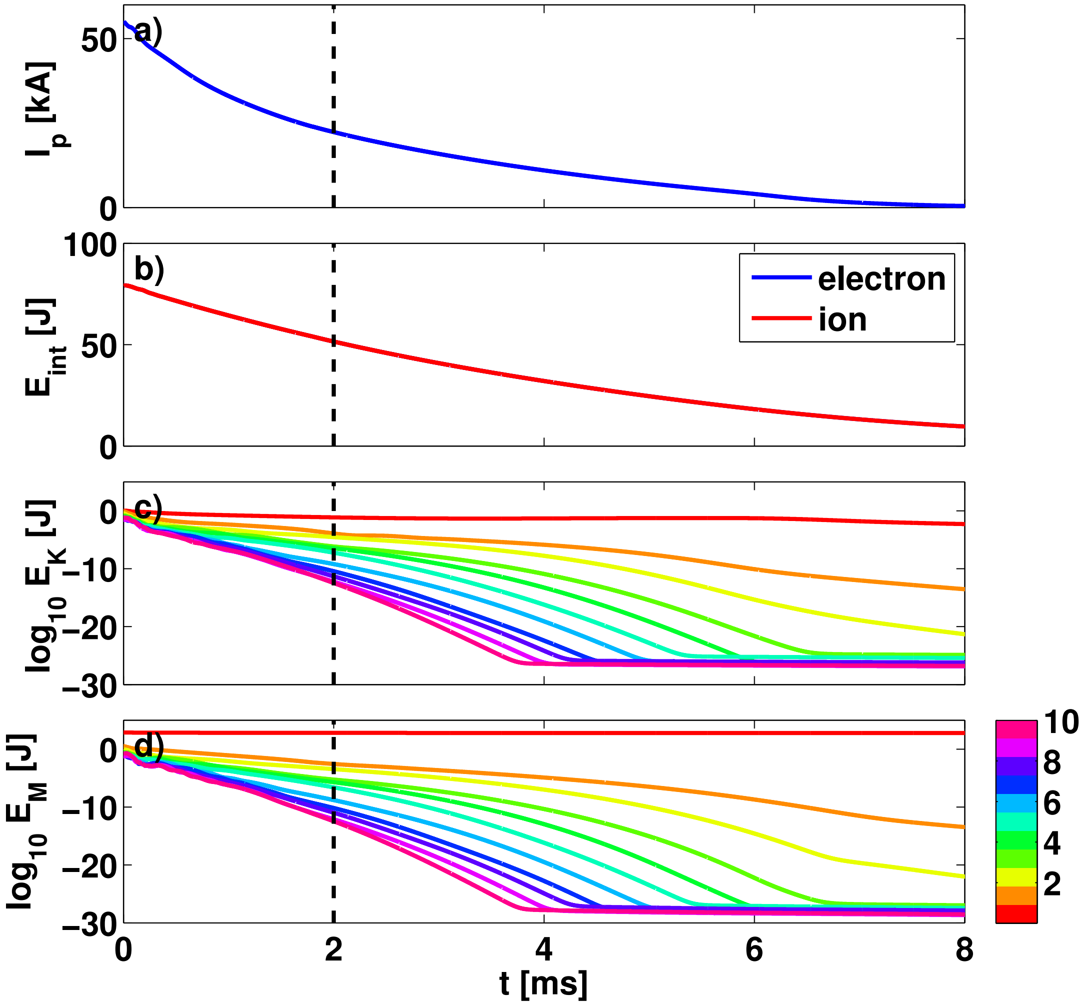

Figure 6.38: Diagnostic traces during free-decay in the MHD computation, including a) the plasma current, b) the ion and electron internal energies, c) the magnetic energy spectrum and d) the kinetic energy spectrum. The magnetic and kinetic energy spectra are colored according to the color bar at the lower right. The time indicated by the vertical dotted line corresponds to the contours in Figure 6.36.

Chapter 7

Summary and Conclusions

Spherical tokamaks have limited capacity for ohmic induction due to geometric constraints on the central solenoid, which motivates the use of non-inductive current drive technique to expand their operational regimes. Experiments on Pegasus have investigated non-inductive startup with localized helicity injectors in the form of electrostatic plasma guns. [107, 116] The injectors generate current-carrying magnetic flux ropes, which are directed along multiple passes by the toroidal and axial vacuum magnetic field components. With sufficient plasma current, $I_p \simeq 15$ kA, a global poloidal magnetic field null forms and the flux ropes relax towards an axisymmetric tokamak equilibrium state. While the initial helical plasma state and final relaxed state are well diagnosed in the experiment, the dynamics of the relaxation process have yet to be directly observed. Therefore, numerical computation has been applied in this thesis to investigate the details and provide a greater phenomenological understanding of the unique relaxation process that occurs during startup with localized helicity injection in the Pegasus spherical tokamak.

The numerical simulations provide a detailed self-consistent description of the evolution. The entire evolution of a single three-dimensional current filament has been modeled with the NIMROD code, starting from vacuum magnetic fields and progressing through relaxation toward a conventional tokamak equilibrium. Only the localized helicity injector current and heat sources are prescribed in the computations: the plasma dynamics follow self-consistently from the physics model. The computations are initialized with a uniform density and temperature, 'cold' fluid and rely on realistic, evolving, and locally-computed transport to form a conducting path for the current filament.

The injector electric field induces a twist in the magnetic field lines in the injector region. Torsional Alfvén waves redistribute the helical twisting along the length of the magnetic field lines, and perpendicular resistive diffusion of the unsupported reverse current results in net current. At low injected current, the current filament winds along the vacuum magnetic field lines.

7.1 Summary of Numerical Results

The attractive Lorentz force between adjacent passes of current filament excites vertical oscillations in the flux rope. With sufficient injected current, adjacent passes of the driven channel repeatedly merge and reconnect, releasing axisymmetric current rings that then freely decay. As reconnection progresses through a single reconnection event, magnetic field-line trajectories show the decoupling of the forming flux-rope ring from the injector and the change in magnetic topology. Prior to the formation of a poloidal magnetic field null, reconnection events occur frequently and the current filament dynamics dominate the system. Poloidal magnetic flux accumulates over many reconnection events in the computations and contributes to the formation of a poloidal magnetic-field null near the central column.

The poloidal magnetic field null redirects the current filament path, so that current flows down the inboard side of the amplified flux region. The current on the inboard side is initially diffuse, but coalesces into a coherent channel as the plasma current increases. The plasma current increases much more rapidly after the formation of the poloidal field null. The rate at which reconnection events occur decreases, and eventually adjacent passes of the outboard part of the current channel cease to merge. The plasma current still increases late into the formation phase, but the rate at which it increases is even lower than during the early growth phase. Even late into the formation phase, the simulated plasma retains its filamentary structure as long as helicity injection remains active. When current injection ceases, high toroidal mode number harmonics of magnetic energy preferentially decay leaving good flux surfaces that encompass a large volume of the decaying plasma.

The tilting of a transit of the current filament into the horizontal plane as adjacent passes merge and reconnect constitutes coherent dynamo action that contributes to the evolution of the toroidally-averaged magnetic field. At the location where the current ring forms, the MHD and Hall dynamo electric fields transfer energy to the toroidally-averaged magnetic field at a faster rate than ohmic heating dissipates energy from it. The MHD dynamo acts on a scale comparable to that of the forming flux-rope ring, where the largest contribution to the MHD dynamo electric field is the toroidally asymmetric vertical flow from the tilting motion. The Hall dynamo acts on a smaller spatial scale than the MHD dynamo and is anti-symmetric about the forming flux-rope ring. The dynamo action concentrates poloidal magnetic flux at the location of current ring formation, which then diffuses into the surrounding plasma.

The squashing degree, which is computed from field-line trajectories launched from a grid on the bottom surface of the domain, shows evidence of quasi-separatrix layers that appear as rolled surfaces when plotted as a function of launch position. The quasi-separatrix layers in the computations show separatrix-like behavior that does not solely correspond to magnetic reconnection: Field-line trajectories with large values of the squashing degree bifurcate between both the reconnecting and non-reconnecting passes of the current filament. Large values of the squashing degree result from chaotic scattering of field-line trajectories around the forming current ring, where the largest values of the squashing degree correlate well with the longest values of magnetic field-line length. Chaotic field-line scattering also occurs between reconnection events, but it is less a pronounced effect than during a reconnection event.

The width of the current channel is larger than the ion skin depth, which indicates that the electron fluid significantly decouples from the ion fluid, even for small gyro-radii. Therefore, the Hall term provides a significant contribution to Ohm's Law, and two-fluid terms are expected to significantly affect current channel evolution. During reconnection, flows are not driven to as small spatial scale, producing smaller fluctuation amplitudes in the kinetic energy. The reduced flow activity during reconnection translates into the smaller observed MHD dynamo electric field during the two-fluid computation than during the MHD computation. As a result, less energy is transferred to the toroidally-averaged magnetic field, which corresponds to smaller fluctuations in the magnetic energy and smaller magnetic fluctuations being observed by the synthetic Mirnov array. The effect of the two-fluid terms on the flow is inferred, as the high speed rotational flow of the current channel about its helical axis obscures the flows resulting from magnetic reconnection.

While the two-fluid terms in Ohm's law provide a significant quantitative contribution to the evolution of the current filaments, the evolution computed with these terms is qualitatively similar to the evolution in computations without them. The small quantitative contributions accumulate over the formation phase, much as poloidal flux accumulates over multiple reconnection events. Even though the evolution is qualitatively similar, there are significant differences between the plasma states late in the formation phase and during the decay phase in the MHD and two-fluid computations.

Synthetic Mirnov coils at the locations used in the experiment are used to test this model of filament relaxation. Magnetic fluctuation amplitudes of order 5 % are observed by both the experimental and computational outboard toroidal Mirnov arrays. Based on the cross-power spectrograms, the two-fluid calculation more accurately reproduces the frequency response of the experimental dynamics.

7.2 Outstanding Questions and Future Direction

Several possible avenues for future research into this non-inductive startup method exist:

First, computations could be used to verify whether this model of filament relaxation reproduces the plasma current (I_p) scaling relations observed in the experiment: $I_p \sim \sqrt{I_{inj} I_{TF}/R}$ in Reference [20], where I_{TF} is the toroidal field current through the central column, I_{inj} is the injector current, and R is the radial position of the plasma centroid. With the current implementation of the injector in the computations, current is not driven through an electrostatic potential difference, but rather through an applied, inductive source that couples to the MHD electric field ($-\mathbf{v} \times \mathbf{B}$) and drives torsional Alfvén waves. As a result, varying the drive parameter λ_{inj} for the injector electric field ($\mathbf{E}_{inj} \sim \eta \mu_0^{-1} \lambda_{inj} \mathbf{B}$) does not produce the same effect on injector current as varying the bias voltage for plasma guns in the experiment. Even though the injector electric field drive is linearly increased throughout the entire formation phase, the injected current rapidly asymptotes to some value. Therefore, the computations would likely focus on scaling the toroidal magnetic field and the radial position of the plasma by varying the injector position.

In this thesis, the relaxation phenomenology has been studied using a single current filament. In the experiment, multiple helicity injectors are often used. Computations could be used to characterize the effect of having multiple injectors. Qualitatively similar behavior is anticipated with multiple current filaments, such as poloidal flux amplification through the formation of current rings and preferential decay of high toroidal mode number harmonics of magnetic energy during decay. However, multiple current carrying plasma filaments could result in braiding of the magnetic field lines, which could significantly impact reconnection during a merger event. Even if the effect of having multiple injectors is small over the course of a single reconnection event, the contribution could aggregate over longer timescales, much as poloidal flux accumulates over multiple reconnection events.

Further improvements could be made to the modeling to improve the predictive capability of the computations. In the experiment, the plasma guns themselves are a source of fueling in the experiment, as well as the outboard and inboard neutral gas injectors. Therefore, density sources and sinks could be added to the computations to approximate fueling in the experiment. Additionally, neutral particle effects (e.g. ionization and recombination) could be added to the physics model. These effects would be significant during the initial formation of the helical current filament path, as well as in the scrape off layer for the entire plasma evolution, and could provide a significant modification to the density and thermal transport.

7.3 Conclusions

The primary objective of this work has been to improve understanding of how current filaments relax into a tokamak-like discharge. The simulations show that the release of current rings from helical current filaments is the mechanism through which significant poloidal flux amplification occurs. The accumulation of poloidal flux from the rings contributes to the formation of a global poloidal magnetic field null near the central column and the (in a toroidally-averaged sense) hollow current profile surrounding the amplified flux region. As such, the current rings provide a new phenomenological understanding for filament relaxation in Pegasus.

The computations also provide physical intuition into what limits the plasma current with this non-inductive startup method. Late in the formation phase, the outboard part of the current channel only makes a few toroidal transits around the central column, so the distance between adjacent passes has significantly increased from the initial vacuum magnetic field winding. Adjacent passes of the outboard current channel cease to merge, and the plasma current increases at a much lower rate than shortly after the formation of the poloidal field null. Therefore, current injection is most effective after the formation of the poloidal magnetic field null, while outboard passes of the current channel are still merging.

A diffuse tokamak equilibrium with good flux surfaces forms rapidly after cessation of current drive, indicating that plasmas formed through this method of non-inductive startup should be able to effectively couple to other forms of current drive for sustainment. The preferential decay of high toroidal mode number harmonics of magnetic energy during decay occurs through MHD dynamics and is also observed in spheromak computations with a similar transport model as the one used in this thesis. [33–35].

Non-magnetohydrodynamic effects have been shown to quantitatively impact the current channel evolution, though the qualitative evolution remains the same. In fact, this model of filament relaxation in Pegasus has shown to be quite robust to additional contributions to the physics model. Computations with a single fluid temperature model and the MHD Ohm's law [111], with two fluid temperatures (ion and electron) and the MHD Ohm's law [113], and with two fluid temperatures and the 2-fluid Ohm's law all exhibit the same general evolution throughout the entire formation and decay phases.

Appendices

Appendix A

Benchmarking Thermal Diffusivity

In this section, the new implementation of the full Braginksii perpendicular thermal conduction (Section 5.3.2) is benchmarked by investigating sound and compressional Alfvén wave damping with finite thermal conduction. The typical dispersion relation for these two types of waves are purely oscillatory for both the adiabatic ($\gamma = 5/3$) and isothermal ($\gamma = 1$) limits. By introducing finite thermal conduction, the modified dispersion relations have strong damping at intermediate values of thermal conduction, while capturing both the adiabatic and isothermal oscillation frequencies in the appropriate limits.

To derive the dispersion relations, the fluid equations (and Ampere's Law for the compressional Alfvén waves) are linearized for plane waves in an infinite homogeneous plasma using the form shown in Equation A.1. Quantities denoted with subscript '0' are constant, uniform equilibrium fields, while a subscript of '1' denotes a perturbation amplitude of the indicated periodic form. Nonlinear terms and the equilibrium flow velocity v_0 are neglected. For simplicity, the wave vector is solely parallel to the magnetic field ($\mathbf{k} \parallel \mathbf{B}$) for sound waves and solely perpendicular to the magnetic field ($\mathbf{k} \perp \mathbf{B}$) for compressional Alfvén waves. The sound and compressional Alfvén wave dispersion relations are given by Equations A.2 & A.3, respectively.

$$\mathbf{v}(\mathbf{x},t) = \mathbf{v}_1 \exp^{i(\mathbf{k}\cdot\mathbf{x}-\omega t)} \tag{A.1}$$

$$\omega^2 = \frac{k^2 C_s^2}{\gamma}\left[1 + \frac{\gamma - 1}{1 + ik^2\left(\gamma - 1\right)\chi_{\parallel}/\omega}\right] \tag{A.2}$$

$$\omega^2 = k^2 V_A^2 + \frac{k^2 C_s^2}{\gamma}\left[1 + \frac{\gamma - 1}{1 + ik^2\left(\gamma - 1\right)\chi_{\perp}/\omega}\right] \tag{A.3}$$

Both dispersion relations are cubic with respect to frequency ω, resulting in three possible solutions for each type of wave. Two solutions of the dispersion relation are damped, counter-propagating waves. The third solution is purely damped with no flow ($v_1 = 0$), and is charactered by the expression $n_1 T_0 + n_0 T_1 = 0$. This third solution is not modeled computationally for this benchmarking procedure.

To benchmark the new thermal conductivity implementation with the traveling wave solutions, the initial conditions for number density and temperature–in addition to flow velocity–must be accurately represented for the tests using the perturbation amplitudes given by Equations A.4 & A.5. By combining the two traveling solutions with the same perturbation amplitude Equations A.6 & A.7, a standing wave solution is produced. The initial conditions for number density and temperature have the same form for both types of waves, though with different frequencies. Sample initial conditions for the standing wave are shown in Figure A.1 for number density, flow, and ion temperature for $\overline{\chi} = 1$, i.e. at the thermal diffusivity with the greatest damping ramp. In both the adiabatic ($\chi \to 0$) and isothermal ($\chi \to \infty$) limits, the initial perturbation amplitude limits to zero for both number density and temperature, i.e. Re $n_1, T_1 \to 0$. This assumes negligible damping, which is shown to be true.

$$\frac{n_1}{n_0} = \frac{\mathbf{k} \cdot \mathbf{v}_1}{\omega} \tag{A.4}$$

$$\frac{T_1}{T_0} = \frac{(\gamma - 1)\mathbf{k} \cdot \mathbf{v}_1}{\omega + i(\gamma - 1)k^2\chi} \tag{A.5}$$

$$\left.\frac{n_1}{n_0}\right|_{standing} = \frac{1}{2}\left(\left.\frac{n_1}{n_0}\right|_{\omega} + \left.\frac{n_1}{n_0}\right|_{-\omega^*}\right) = -i\mathbf{k} \cdot \mathbf{v}_1 \frac{\omega_I}{\omega_R^2 + \omega_I^2} \tag{A.6}$$

$$\begin{aligned} \left.\frac{T_1}{T_0}\right|_{standing} &= \frac{1}{2}\left(\left.\frac{T_1}{T_0}\right|_{\omega} + \left.\frac{T_1}{T_0}\right|_{-\omega^*}\right) \\ &= -i(\gamma - 1)\mathbf{k} \cdot \mathbf{v}_1 \frac{\omega_I + (\gamma - 1)k^2\chi}{\omega_R^2 + (\omega_I + (\gamma - 1)k^2\chi)^2} \end{aligned} \tag{A.7}$$

$$\overline{\chi} \equiv (\gamma - 1)k^2\chi/\omega_0 \tag{A.8}$$

For simplicity, a normalized thermal diffusivity is defined in Equation A.8, where ω_0 is the adiabatic oscillation frequency. For sound and compressional Alfvén waves, the thermal diffusivity χ refers to the parallel ($\chi_\parallel$) and perpendicular ($\chi_\perp$) thermal diffusivities, respectively. At low thermal diffusivity ($\overline{\chi} \ll 1$), the modified dispersion relations limit to the adiabatic dispersion relations. At large thermal diffusivity ($\overline{\chi} \gg 1$), the modified dispersion relations limit to the isothermal dispersion relations. In both the adiabatic and isothermal limits, minimal damping is observed. This behavior is illustrated in Figure A.2 for both sound and compressional Alfvén waves. The intermediate region ($\overline{\chi} \sim 1$) is where the transition between adiabatic and isothermal oscillation frequencies occur, as well as the region of peak damping.

For the benchmarking procedure, the magnetization $x_i \equiv \omega_{ci}\tau_i$ is varied logarithmically from 10^{-1} to 10^1. The value of parallel thermal diffusivity is set to produce the peak damping rate in the low magnetization limit ($x_i \ll 1$), i.e. $\lim_{x_i \ll 1} \overline{\chi} = 1$. For these computations, the sound speed c_s and Alfvén speed v_A are constant, i.e. T_i and the ratio B^2/n are constant. The plots in Figure A.3 indicate a good agreement between the

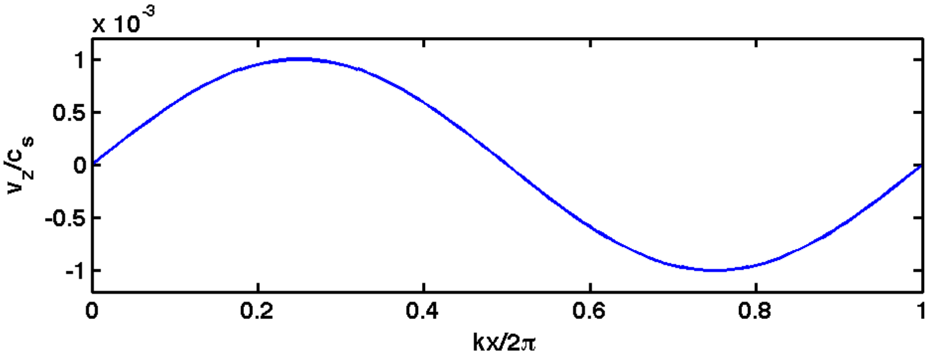

(a) velocity

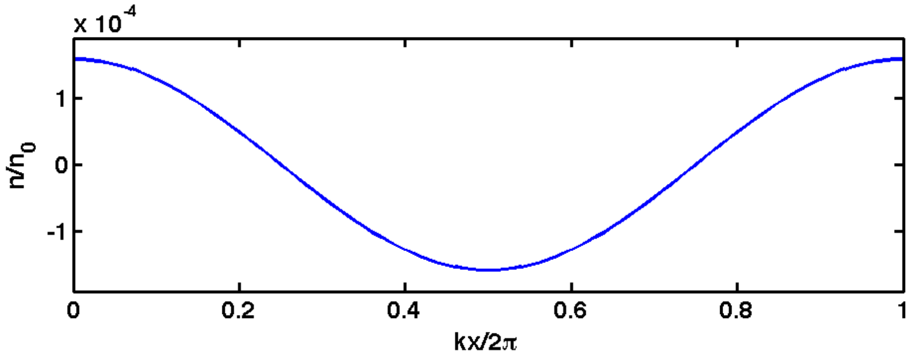

(b) density

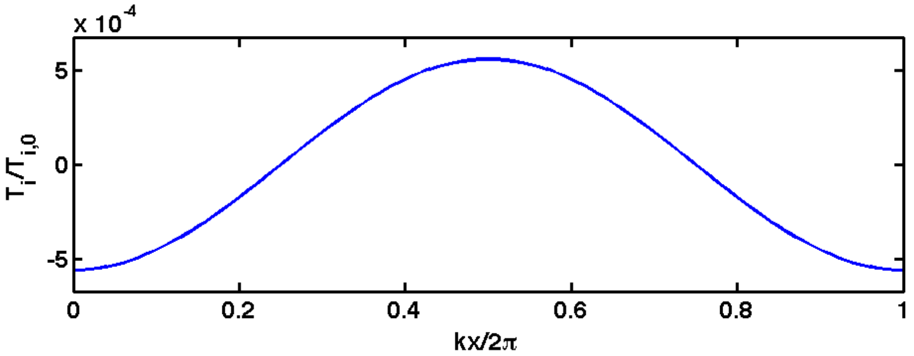

(c) ion temperature

Figure A.1: Sample initial conditions for testing a sound wave with perturbation amplitude $v_1/c_s = 10^{-3}$ and $\overline{\chi} = 1$

implemented full Braginskii perpendicular thermal conduction and analytic predictions. The figure also demonstrates the magnitude of error produced by inaccurately applying the high-magnetization formulation of perpendicular thermal diffusivity.

As sound waves depend upon parallel and not perpendicular thermal transport, the behavior of sound waves is independent of perpendicular thermal diffusivity. However, when $\chi_\perp$ exceeds $\chi_\|$ in NIMROD, the default thermal transport model becomes isotropic with $\chi_{iso} = \chi_\perp$, which causes the magnetization scan results for sound waves in Figure A.3 to depart from the analytic prediction.

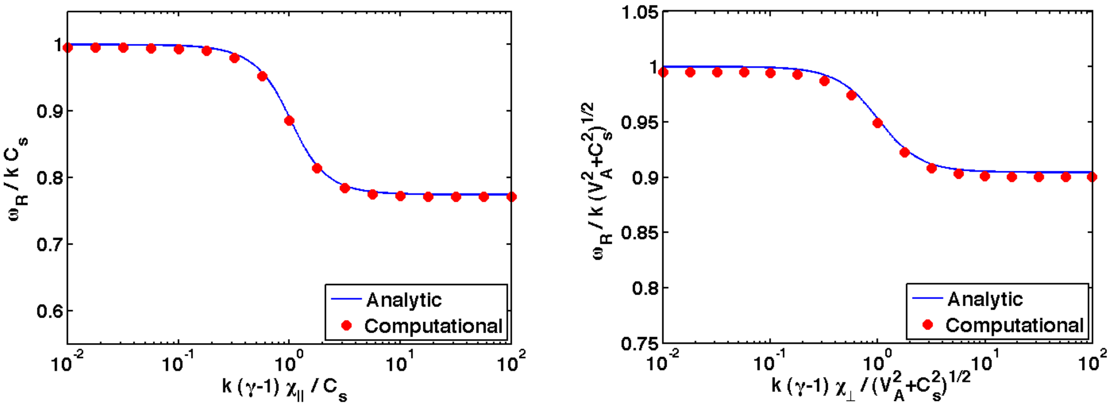

(a) Sound Wave, Re ω (b) Compressional Alfvén Waves, Re ω

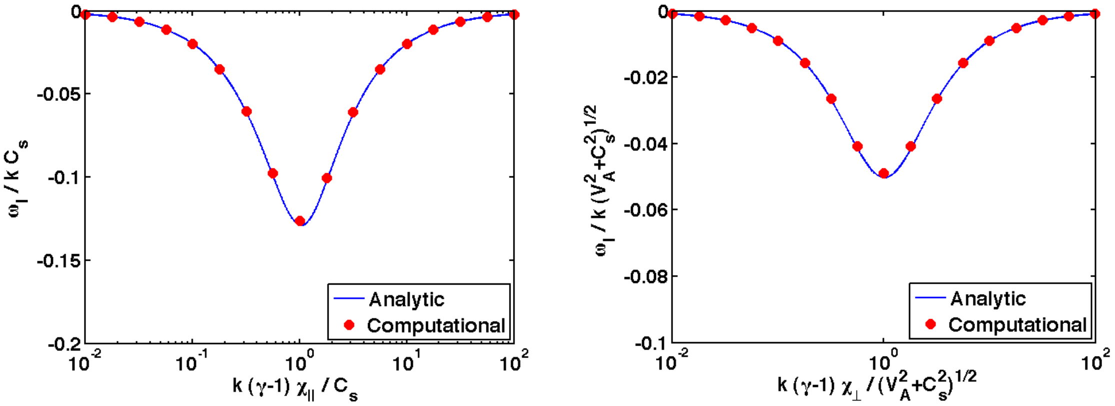

(c) Sound Wave, Im ω (d) Compressional Alfvén Waves, Im ω

Figure A.2: Numerical reproduction of sound and compressional Alfvén wave dispersion with isotropic thermal condition

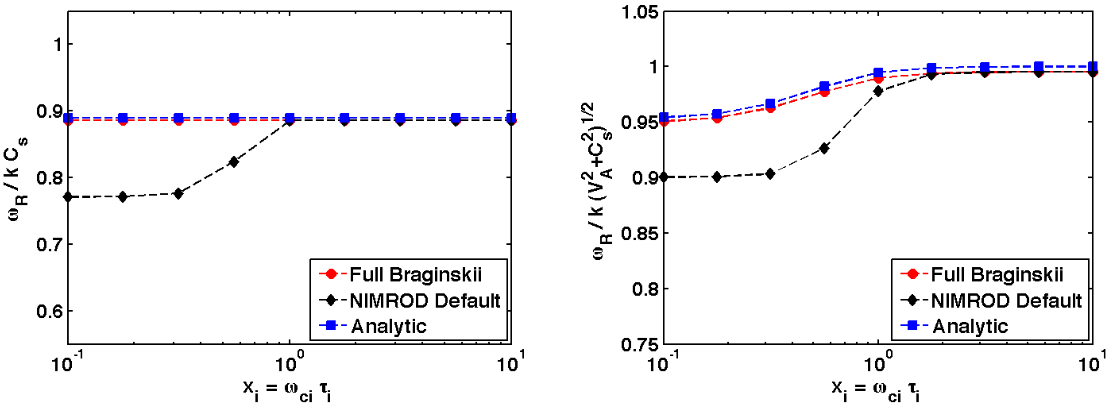

(a) Sound Wave, Re ω (b) Compressional Alfvén Waves, Re ω

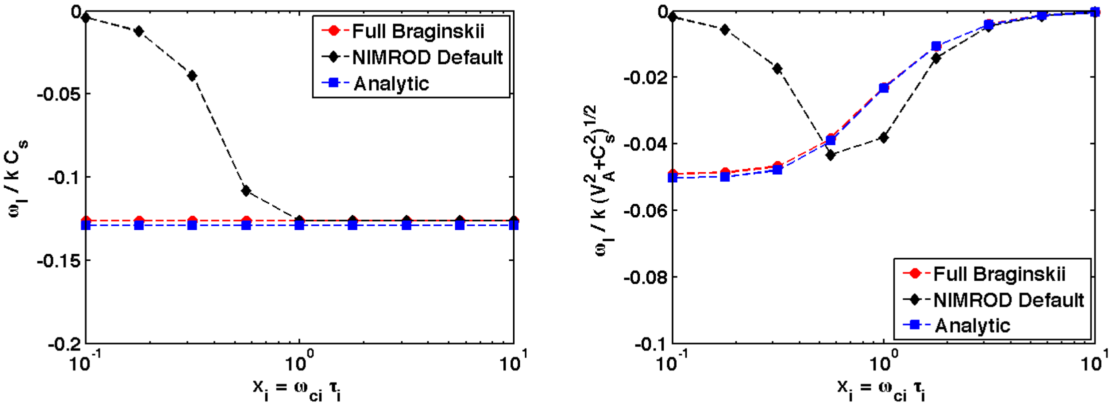

(c) Sound Wave, Im ω (d) Compressional Alfvén Waves, Im ω

Figure A.3: Sound and compressional Alfvén wave dispersion with varying magnetization $\omega_{ci}\tau_i$

Bibliography

[1] S. I. Braginskii. Transport processes in a plasma. *Reviews of Plasma Physics*, 1:205–311, 1965.

[2] C.E. Kessel. Bootstrap current in a tokamak. *Nuclear Fusion*, 34(9):1221, 1994.

[3] John Wesson. *Tokamaks*. Number 118 in International Series of Monographs on Physics. Oxford University Press, New York, third edition, 2004.

[4] Nathaniel J. Fisch. Theory of current drive in plasmas. *Rev. Mod. Phys.*, 59(1):175–234, Jan 1987.

[5] D. R. Sweetman, J. G. Cordey, and T. S. Green. Heating and plasma interactions with beams of energetic neutral atoms. *Philosophical Transactions of the Royal Society of London. Series A, Mathematical and Physical Sciences*, 300(1456):589–598, 1981.

[6] D F H Start, J G Cordey, and E M Jones. The effect of trapped electrons on beam driven currents in toroidal plasmas. *Plasma Physics*, 22(4):303, 1980.

[7] D.Q. Hwang and J.R. Wilson. Radio frequency wave applications in magnetic fusion devices. *Proceedings of the IEEE*, 69(8):1030 – 1043, aug. 1981.

[8] Abhay K. Ram, Abraham Bers, Steven D. Schultz, Vladimir Fuchs, A. Bécoulet, and B. Saoutic. Mode-converted ion-Bernstein waves in tokamaks. Technical Report PFC/JA-95-20, Plasma Fusion Center, Massachusetts Institute of Technology, Cambridge, September 1995.

[9] S. D. Schultz, A. K. Ram, and A. Bers. Mode-converted electron Bernstein waves for heating and current drive in NSTX. In *Proceedings of the 17th Fusion Energy Conference*, number CDP/13, Yokohama, Japan, October 1998. International Atomic Energy Agency.

[10] A Montes and G O Ludwig. Electron Bernstein wave current drive in the start-up phase of a tokamak discharges. *Plasma Physics and Controlled Fusion*, 28(12A):1765, 1986.

[11] P. M. Bellan. Mode-beating model of ac helicity injection. *Phys. Rev. Lett.*, 54:1381–1384, Apr 1985.

[12] P.E. Sieck, T.R. Jarboe, V.A. Izzo, W.T. Hamp, B.A. Nelson, R.G. O'Neill, A.J. Redd, and R.J. Smith. Demonstration of steady inductive helicity injection. *Nuclear Fusion*, 46(2):254, 2006.

[13] T.R. Jarboe, B.S. Victor, B.A. Nelson, C.J. Hansen, C. Akcay, D.A. Ennis, N.K. Hicks, A.C. Hossack, G.J. Marklin, and R.J. Smith. Imposed-dynamo current drive. *Nuclear Fusion*, 52(8):083017, 2012.

[14] R. Raman, B. Nelson, D. Mueller, T. Jarboe, M. Bell, B. LeBlanc, R. Maqueda, J. Menard, M. Ono, M. Nagata, L. Roquemore, and V. Soukhanovskii. Solenoid-free plasma start-up in NSTX using transient CHI. *Journal of Fusion Energy*, 28(2):200–202, June 2009.

[15] T. R. Jarboe, M. A. Bohnet, A. T. Mattick, B. A. Nelson, and D. J. Orvis. Results from current drive experiments on the helicity injected torus. *Physics of Plasmas (1994-present)*, 5(5):1807–1814, 1998.

[16] A. J. Redd, B. A. Nelson, T. R. Jarboe, P. Gu, R. Raman, R. J. Smith, and K. J. McCollam. Current drive experiments in the helicity injected torus (hit-ii). *Physics of Plasmas (1994-present)*, 9(5):2006–2013, 2002.

[17] Masayoshi Nagata, Takashi Kanki, Naoyuki Fukumoto, and Tadao Uyama. The internal magnetic field structures and current density profiles in the helicity injected spherical torus plasma driven by coaxial helicity injection. *Physics of Plasmas (1994-present)*, 10(7):2932–2939, 2003.

[18] D. S. Darrow, M. Ono, C. B. Forest, G. J. Greene, Y. S. Hwang, H. K. Park, R. J. Taylor, P. A. Pribyl, J. D. Evans, K. F. Lai, and J. R. Liberati. Properties of dc helicity injected tokamak plasmas. *Physics of Fluids B: Plasma Physics*, 2(6):1415–1420, 1990.

[19] M. Ono, G. J. Greene, D. Darrow, C. Forest, H. Park, and T. H. Stix. Steady-state tokamak discharge via dc helicity injection. *Phys. Rev. Lett.*, 59:2165–2168, Nov 1987.

[20] D. J. Battaglia. *Non-Solenoidal Tokamak Startup Using Localized Current Sources Near the Outboard Midplane.* PhD thesis, University of Wisconsin–Madison, 2009.

[21] K. E. Thome, J. L. Barr, M. W, Bongard, M. G. Burke, J.A. Cole, R. J. Fonck, E. T. Hinson, A. J. Redd, and G. R. Winz. Improved density control in the PEGASUS toroidal experiment using internal fueling, 2012. Poster presented at

the 55th Annual Meeting of the American Physical Society - Division of Plasma Physics.

[22] J.L. Barr, M.W. Bongard, M.G. Burke, R.J. Fonck, E.T. Hinson, J.M. Perry, A.J. Redd, D.J. Schlossberg, and K.E. Thome. Predictive power-balance modeling of PEGASUS and NSTX-U local helicity injection discharges, 2013. Poster presented at the 55th Annual Meeting of the American Physical Society - Division of Plasma Physics.

[23] P.P Wise, B.L Lesch, H.J.S Muntau, T.P Intrator, R.J Fonck, and G.R Winz. The wisconsin pegasus solenoid. *Physica B: Condensed Matter*, 246-247(0):350 – 352, 1998.

[24] A. C. Sontag, G. D. Garstka, R. J. Fonck, R. J. Schooff, T. A. Thorson, and K. L. Tritz. Diagnostic suite used for magnetohydrodynamics equilibrium reconstruction on the PEGASUS toroidal experiments. *Review of Scientific Instruments*, 72(1):430–430, 2001.

[25] K. Tritz, R. Fonck, M. Reinke, and G. Winz. Tangential soft x-ray imaging for shape and current profile measurements. *Review of Scientific Instruments*, 74(3):2161–2164, 2003.

[26] G.D. Garstka, E.A. Unterberg, S.J. Diem, N.W. Eidietis, R.J. Fonck, B.T. Lewicki, G. Taylor, D.J. Battaglia, M.W. Bongard, M.J. Frost, B.A. Kujak-Ford, B.J. Squires, and G.R. Winz. The upgraded pegasus toroidal experiment. *Nuclear Fusion*, 46(8):S603, 2006.

[27] G Fiksel, A F Almagri, D Craig, M Iida, S C Prager, and J S Sarff. High current plasma electron emitter. *Plasma Sources Science and Technology*, 5(1):78, 1996.

[28] Nicholas Walter Eidietis. *Non-inductive startup of the Pegasus Spherical Torus using localized washer-gun current sources*. PhD thesis, University of Wisconsin–Madison, 2007.

[29] D.J. Battaglia, M.W. Bongard, R.J. Fonck, and A.J. Redd. Tokamak startup using outboard current injection on the pegasus toroidal experiment. *Nuclear Fusion*, 51(7):073029, 2011.

[30] Justin Perry, Jayson Barr, Ray Fonck, Edward Hinson, Benjamin Lewicki, and Aaron Redd. Local helicity injection systems for non-solenoidal startup in the Pegasus Toroidal Experiment, 2013. Poster presented at the 55th Annual Meeting of the American Physical Society - Division of Plasma Physics.

[31] C. R. Sovinec and S. C. Prager. Magnetohydrodynamic simulations of direct current helicity injection for current drive in tokamaks. *Physics of Plasmas*, 3(3):1038–1046, 1996.

[32] X. Z. Tang and A. H. Boozer. Current drive by coaxial helicity injection in a spherical torus. *45th Annual Meeting of the APS Division of Plasma Physics*, 11(5):2679–2687, 2004.

[33] C. R. Sovinec, B. I. Cohen, G. A. Cone, E. B. Hooper, and H. S. McLean. Numerical investigation of transients in the SSPX spheromak. *Phys. Rev. Lett.*, 94(3):035003, Jan 2005.

[34] B. I. Cohen, E. B. Hooper, R. H. Cohen, D. N. Hill, H. S. McLean, R. D. Wood, S. Woodruff, C. R. Sovinec, and G. A. Cone. Simulation of spheromak evolution and energy confinement. *Physics of Plasmas*, 12(5):056106, 2005.

[35] E. B. Hooper, B. I. Cohen, H. S. McLean, R. D. Wood, C. A. Romero-Talamas, and C. R. Sovinec. Nimrod resistive magnetohydrodynamic simulations of spheromak physics. *Physics of Plasmas*, 15(3):032502, 2008.

[36] Mitchell A. Berger and George B. Field. The topological properties of magnetic helicity. *Journal of Fluid Mechanics*, 147:133–148, 1984.

[37] H. K. Moffatt. The energy spectrum of knots and links. *Nature*, 347(6291):367–369, September 1990.

[38] M A Berger. Third-order link integrals. *Journal of Physics A: Mathematical and General*, 23(13):2787, 1990.

[39] Alexander Ruzmaikin and Peter Akhmetiev. Topological invariants of magnetic fields, and the effect of reconnections. *Physics of Plasmas*, 1(2):331–336, 1994.

[40] Peter Akhmetiev and Alexander Ruzmaikin. A fourth-order topological invariant of magnetic or vortex lines. *Journal of Geometry and Physics*, 15(2):95 – 101, 1995.

[41] Mitchell A. Berger. Introduction to magnetic helicity. *Plasma Physics and Controlled Fusion*, 41(12B):B167–B175, 1999.

[42] John M. Finn and Thomas M. Antonsen, Jr. Magnetic helicity: What is it and what is it good for? *Comments Plasma Phys. Controlled Fusion*, 9:111–126, 1985.

[43] Allen H. Boozer. Helicity content and tokamak applications of helicity. *Physics of Fluids*, 29(12):4123–4130, 1986.

[44] Allen H. Boozer. Magnetic helicity and dynamos. *Physics of Fluids B: Plasma Physics*, 5(7):2271–2277, 1993.

[45] M. A. Berger. Inverse Cascades in a Periodic Domain. *Astrophysical Letters and Communications*, 34:225, 1996. Provided by the SAO/NASA Astrophysics Data System.

[46] M. A. Berger. Magnetic helicity in a periodic domain. *J. Geophys. Res.*, 102:2637–2644, 1997.

[47] P. G. Watson and I. J. D. Craig. Helicity dissipation in planar periodic geometries. *Journal of Geophysical Research: Space Physics*, 106(A8):15735–15743, 2001.

[48] Suresh Chandra. The chandrasekhar-kendall functions. *Astrophysics and Space Science*, 136(2):409–412, 1987.

[49] G. J. Rickard. Taylor relaxation of a Gold-Hoyle flux tube. *Astrophysical Journal*, 389:413–420, April 1992.

[50] S. Dasso, C. H. Mandrini, P. Démoulin, and C. J. Farrugia. Magnetic helicity analysis of an interplanetary twisted flux tube. *Journal of Geophysical Research: Space Physics*, 108(A10), 2003.

[51] E. R. Priest and T. G. Forbes. Steady magnetic reconnection in three dimensions. *Solar Physics*, 119:211–214, March 1989.

[52] E. N. Parker. Sweet's mechanism for merging magnetic fields in conducting fluids. *Journal of Geophysical Research*, 62(4):509–520, 1957.

[53] P. A. Sweet. The Neutral Point Theory of Solar Flares. In B. Lehnert, editor, *Electromagnetic Phenomena in Cosmical Physics*, volume 6 of *IAU Symposium*, page 123, 1958.

[54] Masaaki Yamada, Russell Kulsrud, and Hantao Ji. Magnetic reconnection. *Rev. Mod. Phys.*, 82:603–664, Mar 2010.

[55] H. E. Petschek. Magnetic Field Annihilation. *NASA Special Publication*, 50:425, 1964.

[56] Masayuki Ugai and Takao Tsuda. Magnetic field-line reconnexion by localized enhancement of resistivity: Part 1. evolution in a compressible mhd fluid. *Journal of Plasma Physics*, 17:337–356, 6 1977.

[57] Tetsuya Sato and Takaya Hayashi. Externally driven magnetic reconnection and a powerful magnetic energy converter. *Physics of Fluids (1958-1988)*, 22(6):1189–1202, 1979.

[58] Manfred Scholer. Undriven magnetic reconnection in an isolated current sheet. *Journal of Geophysical Research: Space Physics*, 94(A7):8805–8812, 1989.

[59] D. Biskamp. Magnetic reconnection via current sheets. *Physics of Fluids (1958-1988)*, 29(5):1520–1531, 1986.

[60] D. A. Uzdensky and R. M. Kulsrud. Two-dimensional numerical simulation of the resistive reconnection layer. *Physics of Plasmas (1994-present)*, 7(10):4018–4030, 2000.

[61] M. E. Mandt, R. E. Denton, and J. F. Drake. Transition to whistler mediated magnetic reconnection. *Geophysical Research Letters*, 21(1):73–76, 1994.

[62] B. N. Rogers, R. E. Denton, J. F. Drake, and M. A. Shay. Role of dispersive waves in collisionless magnetic reconnection. *Phys. Rev. Lett.*, 87:195004, Oct 2001.

[63] V. V. Mirnov, C. C. Hegna, and S. C. Prager. Two-fluid tearing instability in force-free magnetic configuration. *Physics of Plasmas (1994-present)*, 11(9):4468–4482, 2004.

[64] J. A. Breslau and S. C. Jardin. Global extended magnetohydrodynamic studies of fast magnetic reconnection. *Physics of Plasmas*, 10(5):1291–1298, 2003.

[65] Dmitri A. Uzdensky. Petschek-like reconnection with current-driven anomalous resistivity and its application to solar flares. *The Astrophysical Journal*, 587(1):450, 2003.

[66] E. R. Priest and P. Démoulin. Three-dimensional magnetic reconnection without null points: 1. basic theory of magnetic flipping. *Journal of Geophysical Research: Space Physics*, 100(A12):23443–23463, 1995.

[67] Vyacheslav S. Titov, Gunnar Hornig, and Pascal Démoulin. Theory of magnetic connectivity in the solar corona. *Journal of Geophysical Research: Space Physics*, 107(A8):SSH 3–1–SSH 3–13, 2002.

[68] Eric E. Lawrence and Walter Gekelman. Identification of a quasiseparatrix layer in a reconnecting laboratory magnetoplasma. *Phys. Rev. Lett.*, 103:105002, Sep 2009.

[69] M. G. Linton, R. B. Dahlburg, and S. K. Antiochos. Reconnection of twisted flux tubes as a function of contact angle. *The Astrophysical Journal*, 553(2):905, 2001.

[70] M. G. Linton and S. K. Antiochos. Magnetic flux tube reconnection: Tunneling versus slingshot. *The Astrophysical Journal*, 625(1):506, 2005.

[71] T. J. Bogdan. The turbulent twisted magnetic flux tube gas. *Physics of Fluids (1958-1988)*, 27(4):994–1004, 1984.

[72] James E. Zweibel, Ellen G.; Rhoads. Magnetic merging in colliding flux tubes. *Astrophysical Journal, Part 1*, 440(1):407–414, 1995.

[73] S. Chandrasekhar and L. Woltjer. ON FORCE-FREE MAGNETIC FIELDS. *Proceedings of the National Academy of Sciences of the United States of America*, 44(4):285–289, 1958.

[74] L. Woltjer. A THEOREM ON FORCE-FREE MAGNETIC FIELDS. *Proceedings of the National Academy of Sciences of the United States of America*, 44(6):489–491, 1958.

[75] L. Woltjer. ON HYDROMAGNETIC EQUILIBRIUM. *Proceedings of the National Academy of Sciences of the United States of America*, 44(9):833–841, 1958.

[76] M. D. Kruskal and R. M. Kulsrud. Equilibrium of a magnetically confined plasma in a toroid. *Physics of Fluids*, 1(4):265–274, 1958.

[77] J. B. Taylor. Relaxation of toroidal plasma and generation of reverse magnetic fields. *Phys. Rev. Lett.*, 33(19):1139–1141, Nov 1974.

[78] J. B. Taylor. Relaxation and magnetic reconnection in plasmas. *Rev. Mod. Phys.*, 58(3):741–763, Jul 1986.

[79] A. Bhattacharjee, R. L. Dewar, and D. A. Monticello. Energy principle with global invariants for toroidal plasmas. *Phys. Rev. Lett.*, 45(5):347–350, Aug 1980.

[80] A. Bhattacharjee, R. L. Dewar, and D. A. Monticello. Energy principle with globial invariants for toroidal plasmas. *Phys. Rev. Lett.*, 45(14):1217, Oct 1980.

[81] A. Bhattacharjee and R. L. Dewar. Energy principle with global invariants. *Physics of Fluids*, 25(5):887–897, 1982.

[82] A. Bhattacharjee, A. H. Glasser, Avinash, and J. E. Sedlak. Relaxation of toroidal plasmas. *Physics of Fluids*, 29(1):242–246, 1986.

[83] Eliezer Hameiri and James H. Hammer. Turbulent relaxation of compressible plasmas. *Physics of Fluids*, 25(10):1855–1862, 1982.

[84] Eliezer Hameiri and A. Bhattacharjee. Entropy production and plasma relaxation. *Phys. Rev. A*, 35(2):768–777, Jan 1987.

[85] Simon Candelaresi and Axel Brandenburg. Decay of helical and nonhelical magnetic knots. *Phys. Rev. E*, 84:016406, Jul 2011.

[86] T. H. Jensen and M. S. Chu. Current drive and helicity injection. *Physics of Fluids*, 27(12):2881–2885, 1984.

[87] Jill P. Dahlburg, David Montgomery, Gary D. Doolen, and Leaf Turner. Turbulent relaxation of a confined magnetofluid to a force-free state. *Journal of Plasma Physics*, 37:299–321, 3 1987.

[88] J. P. Dahlburg, D. Montgomery, G. D. Doolen, and L. Turner. Driven, steady-state rfp computations. *Journal of Plasma Physics*, 40:39–68, 7 1988.

[89] Troy Stribling, William H. Matthaeus, and Sanjoy Ghosh. Nonlinear decay of magnetic helicity in magnetohydrodynamic turbulence with a mean magnetic field. *J. Geophys. Res.*, 99:2567–2576, 1994.

[90] U. Frisch, A. Pouquet, J. Léorat, and A. Mazure. Possibility of an inverse cascade of magnetic helicity in magnetohydrodynamic turbulence. *Journal of Fluid Mechanics*, 68:769–778, 3 1975.

[91] A. Pouquet, U. Frisch, and J. Léorat. Strong mhd helical turbulence and the nonlinear dynamo effect. *Journal of Fluid Mechanics*, 77:321–354, 1976.

[92] Eric G. Blackman and George B. Field. Dynamical magnetic relaxation: A nonlinear magnetically driven dynamo. *Physics of Plasmas*, 11(6):3264–3269, 2004.

[93] Eric G Blackman. How spectral shapes of magnetic energy and magnetic helicity influence their respective decay timescales. *Plasma Physics and Controlled Fusion*, 46(2):423, 2004.

[94] X. Z. Tang and A. H. Boozer. Force-free magnetic relaxation in driven plasmas. *Phys. Rev. Lett.*, 94(22):225004, Jun 2005.

[95] X. Z. Tang and A. H. Boozer. Constrained resonance in magnetic self-organization. *Phys. Rev. Lett.*, 95(15):155002, Oct 2005.

[96] C. R. Sovinec, T. A. Gianakon, E. D. Held, S. E. Kruger, D. D. Schnack, and NIMROD Team. Nimrod: A computational laboratory for studying nonlinear fusion magnetohydrodynamics. *Physics of Plasmas*, 10(5):1727–1732, 2003.

[97] NIMROD home page. http://nimrodteam.org.

[98] C. R. Sovinec, J. R. King, and the NIMROD Team. Analysis of semi-implicit algorithm for low-frequency two-fluid plasma modeling. Technical Report 09-13, Center for Plasma Theory and Computation, University of Wisconsin–Madison, 2009.

[99] Xiaoye S. Li and James W. Demmel. SuperLU_DIST: A scalable distributed-memory sparse direct solver for unsymmetric linear systems. *ACM Trans. Math. Softw.*, 29(2):110–140, 2003.

[100] Youcef Saad and Martin H. Schultz. GMRES: A generalized minimal residual algorithm for solving nonsymmetric linear systems. *SIAM Journal on Scientific and Statistical Computing*, 7(3):856–869, 1986.

[101] C. R. Sovinec, A. H. Glasser, T. A. Gianakon, D. C. Barnes, R. A. Nebel, S. E. Kruger, D. D. Schnack, S. J. Plimpton, A. Tarditi, and M. S. Chu. Nonlinear magnetohydrodynamics simulation using high-order finite elements. *Journal of Computational Physics*, 195(1):355 – 386, 2004.

[102] Gilbert Strang and George J. Fix. *An Analysis of the Finite Element Method.* Automatic Computation. Prentice Hall, Edgewood Cliffs, NJ, 1973.

[103] O. C. Zienkiewicz, R. L. Taylor, and J. Z. Zhu. *The Finite Element Method: Its Basis and Fundamentals.* Elsevier/Butterworth-Heinemann, New York, sixth edition, 2006.

[104] Neil A. Gershenfield. *The Nature of Mathematical Modeling.* Cambridge University Press, New York, 1999.

[105] Bengt Fornberg. *A Practical Guide to Pseudospectral Methods.* Cambridge Monographs on Applied and Computational Mathematics. Cambridge University Press, New York, 1998.

[106] M. W. Bongard. *Edge Magnetohydrodynamic Instability Studies in the Pegasus Toroidal Experiment.* PhD thesis, University of Wisconsin–Madison, 2011.

[107] D. J. Battaglia, M. W. Bongard, R. J. Fonck, A. J. Redd, and A. C. Sontag. Tokamak startup using point-source dc helicity injection. *Phys. Rev. Lett.*, 102:225003, Jun 2009.

[108] X. Sun, T. P. Intrator, L. Dorf, J. Sears, I. Furno, and G. Lapenta. Flux rope dynamics: Experimental study of bouncing and merging. *Phys. Rev. Lett.*, 105:255001, Dec 2010.

[109] W. Gekelman, S. Vincena, B. Van Compernolle, G. J. Morales, J. E. Maggs, P. Pribyl, and T. A. Carter. The many faces of shear alfvén waves. *Physics of Plasmas (1994-present)*, 18(5):–, 2011.

[110] T. P. Intrator, X. Sun, G. Lapenta, L. Dorf, and I. Furno. Experimental onset threshold and magnetic pressure pile-up for 3d reconnection. *Nat Phys*, 5(7):521–526, July 2009.

[111] J. B. O'Bryan, C. R. Sovinec, and T. M. Bird. Simulation of current-filament dynamics and relaxation in the pegasus spherical tokamak. *Physics of Plasmas*, 19(8):080701, 2012.

[112] Y-T. Lau and J. M. Finn. Magnetic reconnection and the topology of interacting twisted flux tubes. *Physics of Plasmas (1994-present)*, 3(11):3983–3997, 1996.

[113] J B O'Bryan and C R Sovinec. Simulated flux-rope evolution during non-inductive startup in pegasus. *Plasma Physics and Controlled Fusion*, 56(6):064005, 2014.

[114] J. M. Finn and P. K. Kaw. Coalescence instability of magnetic islands. *Physics of Fluids (1958-1988)*, 20(1):72–78, 1977.

[115] John M. Finn, Carl R. Sovinec, and Diego del Castillo-Negrete. Chaotic scattering and self-organization in spheromak sustainment. *Phys. Rev. Lett.*, 85:4538–4541, Nov 2000.

[116] N.W. Eidietis, R.J. Fonck, G.D. Garstka, E.A. Unterberg, and G.R. Winz. Non-inductive production of st plasmas with washer gun sources on the pegasus toroidal experiment. *Journal of Fusion Energy*, 26:43–46, 2007.